



Brydone, Alistair Stewart (2025) *Nanopatterning titanium and PEEK for orthopaedic implants*. PhD thesis.

<https://theses.gla.ac.uk/84882/>

Copyright and moral rights for this work are retained by the author

A copy can be downloaded for personal non-commercial research or study, without prior permission or charge

This work cannot be reproduced or quoted extensively from without first obtaining permission in writing from the author

The content must not be changed in any way or sold commercially in any format or medium without the formal permission of the author

When referring to this work, full bibliographic details including the author, title, awarding institution and date of the thesis must be given

Enlighten: Theses

<https://theses.gla.ac.uk/>
research-enlighten@glasgow.ac.uk

Nanopatterning titanium and PEEK for orthopaedic implants

By

Alistair Stewart Brydone

Submitted in fulfilment of the requirements for the degree of Doctor of Philosophy

Biomedical Engineering Division

James Watt School of Engineering

College of Science and Engineering

University of Glasgow

Abstract

This project was inspired by research by Dalby and Gadegaard that demonstrated nanopatterning of poly-methyl-methacrylate (PMMA) surfaces can stimulate mesenchymal stromal cells (MSCs) to differentiate into osteoblasts and produce bone mineral *in vitro*. [1] The motivation for this thesis was to adapt and upscale the technology for clinical application, with the aim of fabricating osteogenic implants for orthopaedic surgery, such as intervertebral fusion cages. [2] This translation would initially involve injection mould nanopatterning poly-ether-ether-ketone (PEEK) surfaces. A further objective was to discover methods for fabricating non-planar moulds that could be used in the injection mould nanopatterning process.

Nanoimprint lithography of a novel titanium dioxide precursor sol-gel was performed using flexible polydimethylsiloxane (PDMS) stamps that could conform to non-planar contours of injection mould inlays as a demonstration of the technology. Subsequent injection moulding showed initial success, but the titanium dioxide nanopillars lacked the durability required for repeated moulding cycles.

Nanopatterned PEEK surfaces produced by injection moulding (using electroplated nickel inlays) were assessed to determine whether the nanopatterns exhibited any biological effect upon human bone marrow cells. Initial *in vitro* experiments by Dr Daniel Morrison and a collaborative group in Davos raised concerns regarding cell adhesion on nanopatterned PEEK surfaces and additional work was undertaken to modify PEEK using oxygen plasma treatment. [3] The use of a cell seeding device designed by Dr Paul Reynolds, led to more reliable *in vitro* results as it provided a more favourable environment for cell adhesion.

Due to the opacity and autofluorescence of PEEK, *in vitro* analysis used histological staining with reflected light microscopy and quantitative reverse transcriptase PCR. *In vitro* experimentation revealed that oxygen plasma treatment increased cell adhesion but reduced the bioactive effect of nanopatterning. Although bone marrow cells adhered to the PEEK nanopatterns in small numbers, the cells exhibited a more osteogenic phenotype, demonstrated by relative increased in calcium and phosphate expression.

Nanopatterned PEEK did not achieve the results required for progression to an *in vivo* study. Therefore, surface coating nanopatterned PEEK was considered as an

alternative method to satisfy the objectives of the project. An *in vivo* study was undertaken in collaboration with Nijmegen to study osseointegration of titanium coated injection mould nanopatterned surfaces. Due to intellectual property negotiations, polycarbonate was used rather than PEEK and the NSQ and HEX nanopatterns were not included. The titanium coated nanopatterned implants demonstrated significantly increased bone to implant contact compared to commercially developed grit-blasted acid-etched titanium implants.

With a view to further pre-clinical studies of nanopatterned implants, improved *in vivo* models of osseointegration and osteogenesis in rabbits were developed. These will enable the assessment of novel implants and satisfied the UK Home Office requirements for reduction, refinement and replacement of animal models.

Although not suitable for use in high performance injection mould inlays, the titanium dioxide precursor sol-gel developed for this thesis could be used to directly nanopattern orthopaedic implant surfaces, thus promoting osteogenesis. Furthermore, as demonstrated by the *in vivo* study presented in this thesis, injection mould nanopatterned polymeric implants (such as PEEK) can be modified with an ultra-thin layer of titanium to improve osseointegration.

The work described herein has highlighted that nanopatterning will not necessarily provide the same results in different materials. It does, however, provide further evidence to support the hypothesis that nanopatterning directs cell behaviour by nanotopographical changes in surface chemistry and surface energy which affect cell adhesion.

Acknowledgements

Many thanks to my supervisor Prof. Nikolaj Gadegaard and co-supervisors: Prof. Dominic Meek, Prof. Matthew Dalby, and Prof. Elizabeth Tanner for their many years of support.

Thank you to my friends and colleagues in the Bio-Interface Group: Dr Andrew Greer, Dr Daniel Morrison, Dr Paul Reynolds, Dr Johnny Stormonth-Darling, Dr Iskander Vasiev, Maranda Thomson, Dr Rasmus Petersen, Dr Affar Karimullah, Dr Anwer Saeed, Dr Ali Khokar.

Thank you to everyone in the Centre for Cell Engineering. Special thanks to Prof. Adam Curtis, Prof. Mathis Riehle, Dr Laura McNamara, Carol-Anne Smith, Dr Monica Tsimbouri, and Dr Louisa Lee.

Many thanks to the technical staff in the Engineering Department: Brian Robb, William Monaghan, Ewan Russell.

Thank you, Peter Chung, for your knowledge and guidance in Crystallography.

Thank you, Dr Ross Colquhoun, for your assistance with mechanical testing and FTIR-ATR.

Thank you Prof. Frank Walboomers, Dr Ljupcho Prodanov, and Prof. John Jansen for your expertise and generosity at Radboud University in Nijmegen.

Thank you, Dr Alexandra Poulsson, Dr Edward Rochford and Prof. Geoff Richards for your hospitality at the AO in Davos.

Thank you, Dr Jean Wilson, Christine Stirton and Jim Reilly, at the BHF Cardiovascular Research Centre in Glasgow.

Thank you Prof. Iain McInnes and Diane Vaughan in the Institute of Infection, Immunity and Inflammation in Glasgow.

I wish to thank my clinical colleagues who have offered their time, support and tuition: Mr Andrew Kinninmonth, Prof. Frederic Picard, Mr David Russell, Mr Anthony Reece, Mr Likhith Alakandy, and Mr David Allan.

Finally, thank you to my sponsors: NHS Scotland, Invibio Biomaterials Solutions Ltd., Joint Action, AO Foundation, and Marcus Jarman-Smith.

Table of Contents

Abstract.....	2
Acknowledgements.....	4
List of Tables	10
List of Figures	11
Glossary of Abbreviations	15
Publications arising from this thesis	20
Presentations arising from this thesis	20
Author’s Declaration	22
1 Introduction.....	23
1.1 Thesis outline.....	23
1.2 Orthopaedic biomaterials.....	27
1.3 The ‘ideal’ orthopaedic biomaterial	28
1.4 Titanium and other Metals	31
1.5 PEEK and Polymers	33
1.6 Surface modification of PEEK.....	36
1.7 Cell surface interactions.....	38
2 Fabrication of nanopatterned injection moulding tools.....	45
2.1 Introduction.....	45
2.1.1 Orthopaedic implant fabrication.....	45
2.1.2 Nanopattern generation using electron beam lithography	45
2.1.3 Nanoimprint lithography	48
2.1.4 Injection moulding of nanopatterns.....	50
2.2 Aims and Objectives	51
2.3 Materials and Methods.....	51
2.3.1 Injection mould tool preparation	51

2.3.2	Nanoimprint lithography	53
2.3.3	Topographical analysis.....	56
2.3.4	Injection moulding of nanopatterns.....	58
2.4	Results.....	60
2.4.1	Injection mould tool preparation	60
2.4.2	Nanoimprint lithography of injection mould tools using TiO ₂	65
2.4.3	Injection moulding of nanopatterns using TiO ₂ imprinted mould tools	76
2.5	Discussion	77
2.5.1	Injection mould tool preparation	77
2.5.2	Nanoimprint lithography	78
2.5.3	Injection moulding of nanopatterns.....	82
3	Surface modification and characterisation of poly-ether-ether-ketone	83
3.1	Introduction	83
3.2	Aims and Objectives	83
3.3	Materials and Methods.....	84
3.3.1	Fabrication of injection mould nanopatterned PEEK.....	84
3.3.2	Machining of PEEK	84
3.3.3	Oxygen plasma treatment of PEEK.....	85
3.3.4	Annealing of PEEK.....	85
3.3.5	Surgical application and sterilisation of PEEK.....	85
3.3.6	Water contact angle analysis	86
3.3.7	Scanning electron microscopy	86
3.3.8	Atomic force microscopy	86
3.3.9	X-ray photo electron spectroscopy	86
3.3.10	Fourier transform infra-red spectroscopy with attenuated total reflection	87
3.4	Results.....	88

3.4.1	Commercial PEEK implants and machined PEEK	88
3.4.2	Oxygen plasma treated and nanopatterned PEEK.....	89
3.4.3	Annealed nanopatterned PEEK	94
3.5	Discussion	96
4	Quantifying osteogenesis on PEEK	98
4.1	Introduction	98
4.2	Aims and Objectives	98
4.3	Materials and Methods.....	99
4.3.1	Fabrication of injection mould nanopatterned PEEK	99
4.3.2	Human bone marrow stromal cell isolation and culture	100
4.3.3	Cell staining.....	102
4.3.4	Staining analysis	103
4.3.5	Field Emission-SEM and Energy Dispersive Spectroscopy	105
4.3.6	Gene expression analysis using Reverse Transcriptase Quantitative Polymerase Chain Reaction	105
4.4	Results.....	108
4.4.1	Validation of histological staining using Energy-dispersive analysis	108
4.4.2	Osteogenesis on oxygen plasma treated and injection mould nanopatterned PEEK.....	110
4.4.3	Gene expression on oxygen plasma treated injection mould nanopatterned PEEK.....	116
4.5	Discussion	119
4.5.1	Stromal cell culture.....	119
4.5.2	Nanopatterned PEEK.....	119
4.5.3	Oxygen plasma treated PEEK.....	120
4.5.4	The adhesion-mineralisation paradox	121
4.5.5	Gene expression on oxygen plasma treated injection mould nanopatterned PEEK.....	123

4.5.6	Summary.....	131
5	In vivo osseointegration of Ti coated nanopatterned polymer implants	133
5.1	Introduction	133
5.2	Aims and Objectives	134
5.3	Materials and Methods.....	135
5.3.1	Fabrication of Ti nanopatterned polymer implants.....	135
5.3.2	Fabrication of grit-blasted acid-etched titanium implants.....	135
5.3.3	Implant surface characterisation	136
5.3.4	Surgical technique.....	136
5.3.5	Histological staining.....	137
5.3.6	Histological analysis	138
5.4	Results.....	138
5.4.1	Implant surface characterisation	138
5.4.2	General observations	141
5.4.3	Histological analysis	141
5.5	Discussion	142
6	Design of an <i>in vivo</i> study to assess non-planar bioactive orthopaedic implants	145
6.1	Introduction	145
6.1.1	Modelling the clinical application	145
6.1.2	Animals as bioreactors	146
6.2	Aims and Objectives	147
6.3	Materials and Methods.....	148
6.3.1	Morphometric analysis of rabbit femora	148
6.3.2	Fabrication of prototype nanopatterned PEEK implants.....	149
6.3.3	Mechanical testing of prototype PEEK implants.....	150
6.3.4	Cadaveric implantation using a critical gap defect model of bone regeneration in rabbit femora	150

6.3.5	Cadaveric implantation using an intramedullary model of osseointegration in rabbit femora	151
6.4	Results.....	152
6.4.1	Morphometric analysis of rabbit femora	152
6.4.2	Fabrication of prototype nanopatterned PEEK implants.....	154
6.4.3	Mechanical testing of prototype PEEK implants.....	154
6.4.4	Cadaveric implantation using a critical gap defect model of bone regeneration in rabbit femora	156
6.4.5	Cadaveric implantation using an intramedullary model of osseointegration in rabbit femora	156
6.5	Discussion	157
7	General Discussion.....	160
8	Conclusion and Outlook.....	164
9	References	165
10	Appendix.....	208

List of Tables

Table 1. Characteristics of orthopaedic biomaterials	31
Table 2. Titanium dioxide precursor sol-gel solvents	50
Table 3. Injection moulding parameters	59
Table 4. Hand polished surfaces*	61
Table 5. Chemical-mechanical polishing of titanium	63
Table 6. Surface planarization with TiO ₂ sol-gel	64
Table 7. Mechanical properties of PEEK [104]	Error! Bookmark not defined.
Table 8. Topographic analysis of PEEK spinal implants and machined PEEK	89
Table 9. PCR array of gene expression markers for stem cell differentiation.	107
Table 10. EDS analysis of ARS and von Kossa stains	109
Table 11. Surface properties of Ti nanopatterned implants	139
Table 12. Elemental analysis of Ti nanopatterned implants.....	140
Table 13. Elemental analysis of oxygen plasma treated PEEK	208
Table 14. Gene reference table for PCR array.....	216
Table 15. Gap defect studies in rabbit femora	220
Table 16. Gap defect studies in rabbit tibiae	221
Table 17. Distal femoral and intramedullary implant studies in rabbits	222

List of Figures

Figure 1. Thesis workstream.....	23
Figure 2. Applications of orthopaedic biomaterials.....	29
Figure 3. The chemical structure of poly-ether-ether-ketone.....	34
Figure 4. PEEK spinal implants in vivo.....	35
Figure 5. Chalmers method to assess PEEK crystallinity using ATR-FTIR.....	37
Figure 6. Nanotopographical control of cell adhesion.....	40
Figure 7. Nanotopographical control of cell behaviour.....	42
Figure 8. Nickel mould inlay nanofabrication.....	47
Figure 9. Nanoimprint lithography.....	48
Figure 10. Chemical-mechanical polishing.....	53
Figure 11. Fabrication of reinforced flexible and non-planar PDMS nanoimprint stamps.....	56
Figure 12. Assessment of nanopattern fidelity.....	58
Figure 13. Injection mould nanopatterning process.....	59
Figure 14. Non-planar aluminium injection mould tools.....	61
Figure 15. Hand polished surfaces.....	62
Figure 16. CMP polished titanium grade 2.....	64
Figure 17. Silicon master nanotopography.....	66
Figure 18. Nanopatterned PDMS stamps.....	67
Figure 19. PDMS stamp distortion.....	67
Figure 20. PDMS stamp demoulding.....	68
Figure 21. Thermogravimetric analysis of TiO ₂ precursor sol-gel.....	69
Figure 22. Planar nanoimprinting augmented using O ₂ plasma treatment.....	70
Figure 23. Oxidation of tool materials during annealing.....	71
Figure 24. TiO ₂ nanopatterns on tool materials.....	72

Figure 25. Nanoimprint defects.....	73
Figure 26. TiO ₂ nanopillar fabrication on tool materials.....	75
Figure 27. TiO ₂ nanoimprinting on non-planar aluminium.....	76
Figure 28. Injection moulding using TiO ₂ nanopatterned P20 steel tools.....	77
Figure 29. Injection moulding using TiO ₂ nanopatterned aluminium tools.....	77
Figure 30. TiO ₂ nanoimprinting on aluminium tools	81
Figure 31. AFM analysis of spinal implants and machined PEEK	89
Figure 32. Hydrophobic recovery of oxygen plasma treated PEEK	90
Figure 33. The effect of cleaning, sterilization and handling on oxygen plasma treated PEEK	91
Figure 34. AFM analysis of O ₂ plasma treated PEEK nanopatterns	93
Figure 35. Atomic percentage of oxygen and C=O on plasma treated PEEK	94
Figure 36. AFM analysis of annealed nanopatterned PEEK	96
Figure 37. Absorbance ratio vs. PEEK crystallinity	97
Figure 38. Plasma treatment effect on PEEK wettability	98
Figure 39. Ordered and disordered nanopatterns	102
Figure 40. Ficoll-Paque density gradient separation of mononuclear cells	103
Figure 41. Cell counting using a haemocytometer	104
Figure 42. ARS and VK stain analysis of PEEK substrates	106
Figure 43. CellProfiler image analysis pipeline	107
Figure 44. EDS surface analysis of ARS stained PEEK	111
Figure 45. EDS surface analysis of von Kossa stained PEEK	111
Figure 46. Analysis of ARS stained cells for oxygen plasma optimisation	113
Figure 47. Analysis of von Kossa stained cells for oxygen plasma optimisation.	113
Figure 48. Analysis of ARS stained cells on hydrophobic, hydrophilic and meta-stable nanopatterned PEEK	115

Figure 49. Analysis of von Kossa stained cells on hydrophobic, hydrophilic and meta-stable nanopatterned PEEK	116
Figure 50. Analysis of ARS stained cells on ordered and disordered oxygen plasma treated nanopatterned PEEK	116
Figure 51. Analysis of von Kossa stained cells on ordered and disordered oxygen plasma nanopatterned PEEK.....	117
Figure 52. Gene expression on nanopatterned PEEK.....	119
Figure 53. Genetic characterisation of cells on nanopatterned PEEK.....	120
Figure 54. The adhesion-mineralisation paradox.....	124
Figure 55. Genetic determination of stromal cell fate.....	125
Figure 56. Smurf mediated ossification.....	131
Figure 57. Temporal expression of osteogenic genes.....	134
Figure 58. Revised project workstream.....	135
Figure 59. Surgical implantation of Ti coated polymer implants.....	139
Figure 60. Surface analysis of Ti nanopatterned implants.....	141
Figure 61. X-ray photo-electron spectroscopy of Ti nanopatterned implants.....	142
Figure 62. Histological analysis of osseointegration.....	143
Figure 63. Bone-implant contact of Ti nanopatterned implants with rabbit tibiae	144
Figure 64. PEEK nanopatterned rod.....	150
Figure 65. Fabrication of PEEK implants.....	151
Figure 66. Cadaveric implantation using the critical gap defect model.....	152
Figure 67. Cadaveric implantation using the intramedullary model.....	152
Figure 68. Morphometric study of rabbit femora.....	154
Figure 69. Mechanical testing of PEEK implants.....	156
Figure 70. Proposed analysis of retrograde intramedullary model.....	160
Figure 71. XPS survey scan of PEEK, 0 days after plasma treatment.....	196
Figure 72. XPS survey scans of PEEK, 6 weeks after plasma treatment.....	197

Figure 73. Curve fitting XPS spectra for PEEK, 0 days after O ₂ plasma treatment.....	197
Figure 74. Narrow scan XPS spectra for PEEK, 0 days after O ₂ plasma treatment.....	198
Figure 75. Curve fitting XPS spectra for PEEK, 6 weeks after O ₂ plasma treatment.....	199
Figure 76. Narrow scan XPS spectra for PEEK, 6 weeks after O ₂ plasma treatment.....	200
Figure 77. FTIR analysis of injection moulded and annealed PEEK.....	201

Glossary of Abbreviations

ACTB	Actin beta (Housekeeping gene)
AFM	Atomic force microscopy
ALCAM	Activated leucocyte cell adhesion molecule (<i>syn.</i> CD166)
ALP	Alkaline phosphatase
ANOVA	Analysis of variance
ANPEP	Alanyl aminopeptidase (<i>syn.</i> CD13)
ARS	Alizarin red S (alizarin sodium monosulphate, 3,4-dihydroxy-9,10-dioxo-2-anthracenesulfonic acid sodium salt)
AWCA	Advancing water contact angle
BEEA	2-(2-butoxyethoxy) ethyl acetate
BGLAP	Bone gamma carboxyglutamate protein (<i>syn.</i> OCN or osteocalcin)
BIC	Bone-implant contact
B-ME	Beta mercaptoethanol
BMP	Bone morphogenetic protein
CAD/CAM	Computer aided design / computer aided manufacturing
Cbfa1	Core binding factor alpha 1 (<i>syn.</i> Runx2)
CD	Cluster of differentiation
cDNA	Complementary Deoxyribonucleic Acid
CMP	Chemical-mechanical polisher
CNC	Computer numerical control
COL1A1	Collagen type 1 subunit alpha 1
CT	Computed tomography
DMEM	Dulbecco's modified Eagle's medium
DMSO	Dimethyl Sulphoxide
ECM	Extra-cellular matrix

EDS	Energy-Dispersive X-ray Spectroscopy
EDTA	Ethylenediaminetetraacetic acid
EMEM	Eagle's minimum essential medium
ENG	Endoglin (<i>syn.</i> CD105)
ERK	Extra-cellular signal regulated kinase
FAK	Focal adhesion kinase
FAT	Focal adhesion targeting
FBS	Foetal bovine serum
FLAT	Flat experimental surfaces (<i>syn.</i> PL or planar)
FTIR-ATR	Fourier-transform infrared attenuated total reflection spectroscopy
GAE	Grit-blasted acid-etched
GAPDH	Glyceraldehyde 3-phosphate dehydrogenase (Housekeeping gene)
GDF	Growth differentiation factor
HA	Hydroxyapatite
HCAM	Homing cell adhesion molecule (<i>syn.</i> CD44)
HEPES	(4-(2-hydroxyethyl)-1-piperazineethanesulfonic acid)
HES1	Hairy and enhancer of split 1 transcription factor
HEX	Hexagonal pattern topography
HEY1	Hairy and enhancer of split related with YRPW motif 1 protein
HGF	Hepatocyte growth factor
IPA	Isopropyl alcohol
ITG	Integrin
ITGA6	Integrin subunit alpha 6 (<i>syn.</i> CD49f)
ITGAV	Integrin subunit alpha V (<i>syn.</i> CD51)
ITGAX	Integrin subunit alpha X (<i>syn.</i> CD11c)
ITGB1	Integrin subunit beta 1 (<i>syn.</i> CD29)
JAG1	Jagged canonical Notch ligand 1

KDR	Kinase insert domain receptor (<i>syn.</i> CD309, VEGFR2)
KITLG	Kit ligand gene (<i>syn.</i> Stem cell factor, SCF)
LIF	Leukaemia inhibitory factor
MAPK	Mitogen activated protein kinase
MCAM	Melanoma cell adhesion molecule (<i>syn.</i> CD146)
MEM	Minimum essential medium
MIBK	Methyl Isobutyl Ketone
MMP	Matrix metalloproteinase
MSC	Mesenchymal stromal cell (<i>syn.</i> bone marrow stem cell)
NES	Nestin
NOTCH1	Notch homolog 1
NSQ	Near square topography
NT5E	Ecto-5-prime-nucleotidase (<i>syn.</i> CD73)
OCN	Osteocalcin
OCT4	Octamer-binding transcription factor 4 (<i>syn.</i> POU domain, class 5, transcription factor 1, POU5F1)
PBS	Phosphate buffered solution
PC	Polycarbonate
PCL	Polycaprolactone
PCR	Polymerase chain reaction
PDGFRB	Platelet derived growth factor receptor beta
PDMS	Polydimethylsiloxane
PEEK	Poly-ether-ether-ketone
PL	Planar surface topography (<i>syn.</i> FLAT)
PMMA	Poly-methyl-methacrylate
PP	Polypropylene
PPARG	Peroxisome proliferator activated receptor gamma

PROM1	Promonin 1 (<i>syn.</i> CD133)
PTFE	Polytetrafluoroethylene
PTK2	Protein tyrosine kinase 2 gene (<i>syn.</i> focal adhesion kinase or FAK)
PTPRC	Protein tyrosine phosphatase receptor type C (<i>syn.</i> CD45)
R _a	Arithmetic mean deviation of surface roughness
RAND	Random pattern topography
REX1	Reduced expression protein 1 (<i>syn.</i> ZFP42)
rhBMP	Recombinant human bone morphogenetic protein
RHOA	Rhomboid homolog A
R _{max-min}	Maximum peak height minus minimum height
RMS	Root mean square
RNA	Ribonucleic acid
ROCK	Rho associated coiled coil containing kinase
RPLP0	60s acidic ribosomal protein P0 (Housekeeping gene)
RT-qPCR	Quantitative reverse transcriptase polymerase cell reaction
RUNX2	Runt related transcription factor 2 (<i>syn.</i> Cbfa1)
SD	Standard deviation
SEM	Scanning electron microscopy
SMAD	Small mothers against decapentaplegic homolog
SMURF	SMAD ubiquitin regulatory factor
SOX2	(Sex determining region Y)-box transcription factor 2
SOX9	(Sex determining region Y)-box transcription factor 9
SQ	Square pattern topography
SU-8	Thick film negative photoresist with 8 epoxy groups
TCPS	Tissue culture polystyrene
TERT	Telomerase reverse transcriptase
T _g	Glass-liquid transition temperature

TGF β	Transforming growth factor beta
THY1	Thymocyte differentiation antigen 1 (<i>syn.</i> CD90)
Ti-6Al-4V	Titanium alloy with 6% aluminium and 4% vanadium (<i>syn.</i> grade 5)
UHMWPE	Ultra-high molecular weight polyethylene
VCAM1	Vascular cell adhesion protein 1 (<i>syn.</i> CD106)
VEFGA	Vascular endothelial growth factor A
VEGFR2	Vascular endothelial growth factor receptor 2
UV	Ultraviolet
WAXS	Wide angle x-ray scattering
Wnt	Wingless-Integrated homolog
XPS	X-ray photoelectron spectroscopy

Publications arising from this thesis

Mechanical compatibility of sol-gel annealing with titanium for orthopaedic prostheses. Greer AI, Lim TS, **Brydone AS**, Gadegaard N. *J Mater Sci Mater Med* 2016; 27(1): 21. PMID: 26691162.

Titanium nanofeaturing for enhanced bioactivity of implanted orthopedic and dental devices. Sjöström T, **Brydone AS**, Meek RD, Dalby MJ, Su B, McNamara LE. *Nanomedicine (Lond)*. 2013; 8(1): 89-104. PubMed PMID: 23256494.

Presentations arising from this thesis

Brydone AS, Morrison DSS, Meek RDM, Tanner KE, Dalby MJ, Gadegaard N. Enhanced osteogenesis on PEEK polymer using injection mould nanopatterning. 2nd International PEEK meeting, Washington, USA. April 2015. (Podium).

Brydone AS, Morrison DSS, Meek RDM, Tanner KE, Dalby MJ, Gadegaard N. Enhanced osteogenesis on PEEK polymer using injection mould nanopatterning. Glasgow Meeting of Orthopaedic Research, Glasgow, March 2015. (Podium).

Brydone AS, Prodanov L, Lamers E, Gadegaard N, Jansen JA, Walboomers XF. Enhanced osseointegration on rabbit tibiae using titanium coated nano-patterned implants. Glasgow Meeting of Orthopaedic Research, Glasgow, March 2014. (Podium).

Brydone AS, Prodanov L, Lamers E, Gadegaard N, Jansen JA, Walboomers XF. Increased interfacial bone contact using nano-patterned titanium coated implants in a rabbit femur model. British Orthopaedic Association Annual Congress, Birmingham, October 2013. (Podium).

Brydone AS, Prodanov L, Lamers E, Gadegaard N, Jansen JA, Walboomers XF. Increased interfacial bone contact using nano-patterned titanium coated implants in a rabbit femur model. British Orthopaedic Research Society and Bone Research Society Joint Meeting, Oxford. September 2013. (Poster).

Brydone AS, Morrison DSS, Meek RDM, Dalby MJ, Gadegaard N. Enhanced osteogenesis on PEEK polymer using oxygen plasma treatment. British Orthopaedic Research Society and Bone Research Society Joint Meeting, Oxford. September 2013. (Poster).

Brydone AS, Morrison DSS, Meek RDM, Dalby MJ, Gadegaard N. Enhanced osteogenesis on PEEK polymer using oxygen plasma treatment. Glasgow Meeting of Orthopaedic Research, Glasgow. March 2013. (Podium).

Brydone AS, Morrison DSS. Surface modification of PEEK for orthopaedic applications. Glasgow Orthopaedic Research Initiative, Glasgow. October 2012. (Podium).

Brydone AS, Morrison DSS, Stormonth-Darling J, Meek RDM, Tanner KE, Gadegaard N. Design and fabrication of a 3D nanopatterned PEEK implant for cortical bone regeneration in a rabbit model. A cadaveric pilot study. European Cells and Materials Conference, Davos, Switzerland. June 2012. (Poster).

Author's Declaration

I declare that all the work presented in this thesis has been carried out by me, unless otherwise acknowledged or referred to.

Alistair Stewart Brydone

April 2023

1 Introduction

1.1 Thesis outline

The project workstream, (illustrated in Figure 1) incorporates a wide range of scientific disciplines: nanofabrication, biomaterials, stem cell research, and pre-clinical animal studies. Each step will be presented as an individual chapter with a separate description of methods and materials.

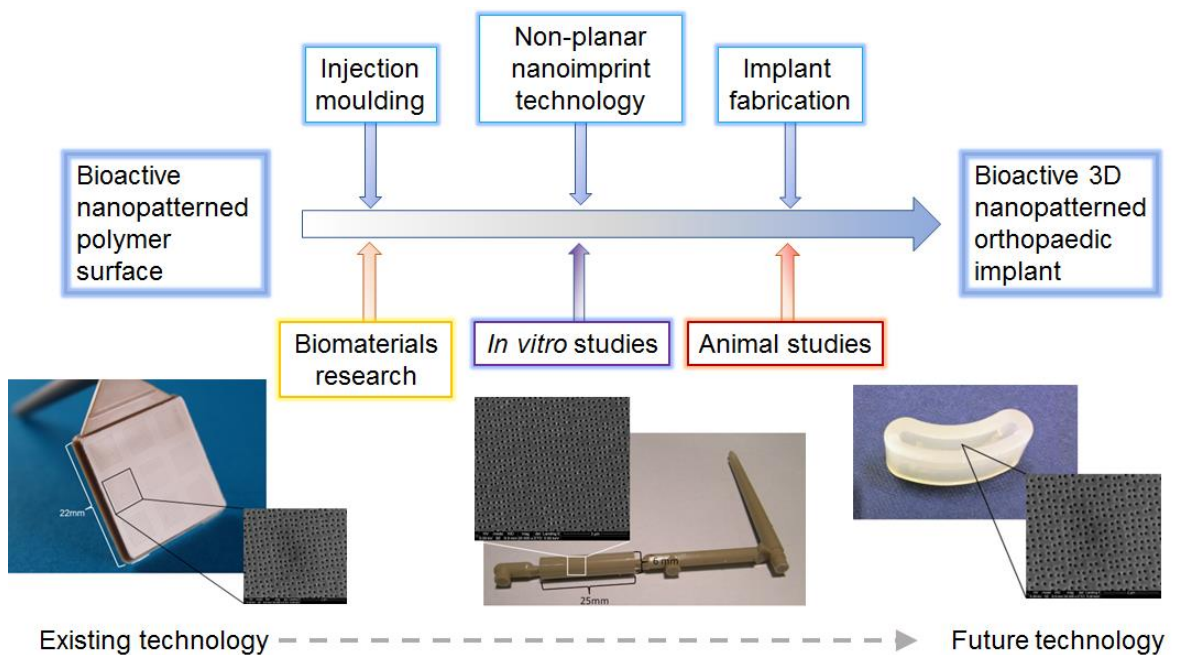


Figure 1. Thesis workstream

This diagram charts the proposed route for this project: starting from the existing technology described by Dalby and Gadegaard,[1, 4] moving towards to a pre-clinical prototype of a bioactive nanopatterned orthopaedic implant.

Chapter 2 details how nanopatterning can be used to modify orthopaedic implants. The aim of this chapter was to fabricate tools for injection moulding nanopatterns on planar and non-planar surfaces for the manufacture of bioactive PEEK implants. This would be achieved via the following objectives:

- Fabricate injection mould tools and inlays using 3D CAD design, traditional machining, hand polishing, and chemical -mechanical polishing;

- Nanopattern injection mould tools using nanoimprint lithography and perform surface analysis;
- Use nanopatterned tools to injection mould cell culture substrates and prototype implants using polycarbonate and PEEK

Chapter 3 characterises injection moulded nanopatterned PEEK and describes further surface modification methods for PEEK.

This would be achieved by analysing the following surfaces:

- Commercially available PEEK implants;
- Machined PEEK surfaces;
- Injection mould nanopatterned PEEK;
- Oxygen plasma treated PEEK;
- Oxygen plasma treated and injection mould nanopatterned PEEK;
- Injection mould nanopatterned and annealed PEEK.

The PEEK surfaces will be analysed using the following methods:

- Water contact angle analysis;
- Field emission scanning electron microscopy (SEM);
- Atomic force microscopy (AFM);
- X-ray photo electron spectroscopy (XPS);
- Fourier transform infrared spectroscopy with attenuated total reflection.

Chapter 4 assesses the in vitro bioactivity of the PEEK surfaces using human bone marrow cells. The aim of this chapter was to explore and optimise the bioactivity of oxygen plasma treated injection mould nanopatterned PEEK by assessing MSC mediated osteogenesis using quantifiable methods.

This would be achieved by using the following objectives:

- Culture MSCs on nanopatterned PEEK surfaces for 6 weeks using five different oxygen plasma treatments to optimise the protocol;
- Assess the validity of Alizarin Red S stain (ARS) and von Kossa stains by co-localising calcium to ARS stained particles and phosphate to von Kossa stained particles using Energy-dispersive X-ray Spectroscopy (EDS);
- Use Alizarin Red S stain (ARS) to identify calcium particles on surfaces and quantify them using microscopy and image analysis software;

- Surfaces will be assessed for % coverage of surface by cells, cell number, and calcium expression;
- Use Von Kossa stain to identify phosphate particles on surfaces and quantify them using microscopy and image analysis software as above;
- Culture MSCs on nanopatterned PEEK surfaces for 6 weeks using the preferred oxygen plasma treatment protocol and analyse using ARS and von Kossa stains.
- Culture MSCs on hydrophobic (untreated), hydrophilic (plasma treated that day) and metastable (aged following plasma treatment) PEEK surfaces for 6 weeks and analyse using ARS and von Kossa stains;
- Culture MSCs on PEEK surfaces for 2 weeks and assess an array of MSC gene expression markers using qRT-PCR.

Chapter 5 describes an *in vivo* assessment of titanium-coated injection moulded nanopatterned polymer surfaces in a rabbit model. The aim of this experiment was to assess the *in vivo* osseointegration of Ti-coated nanopatterned polymer implants and compare to commercially available grit-blasted acid-etched (GAE) titanium surface with proven clinical efficacy.

- Polycarbonate (SQ and RAND) nanopatterning was performed by Prof Gadegaard's Bio-Interface Group in Glasgow.
- GAE implant fabrication and titanium coating of polymer implants was performed by Prof Walboomers Research Group in Nijmegen.
- Surgical implantation and histological preparation were undertaken by Prof Walboomers Research Group in Nijmegen.
- Bone-to-implant contact (%) was assessed using light microscopy.
- The implant surfaces were assessed using SEM, AFM, water contact angle analysis and XPS.

Chapter 6 presents an alternative model for *in vivo* analysis of non-planar implants. The aim of this chapter of the project was to design an animal model to assess the *in vivo* osteogenic bioactivity of a rod-shaped implant. Ideally, it will incorporate the nanopatterned PEEK rod provided by Prof Gadegaard (Figure 64).

After literature review and appreciation of the facilities available in Glasgow, two models using rabbit femora were considered:

- A critical gap segment model to investigate cortical bone regeneration along and around a bioactive implant;
- An intramedullary model to test endosteal osseointegration of both cancellous and cortical bone onto a bioactive implant.

This would be achieved by:

- Conducting a morphometric analysis of rabbit femora;
- Fabrication of prototype implants;
- Mechanical testing;
- Cadaveric implantation.

1.2 Orthopaedic biomaterials

Due to the aging population and the ongoing prevalence of orthopaedic trauma, the need to reconstruct and replace bones and joints is increasing.[5] Bone grafting is frequently required during orthopaedic surgery to restore bone lost or damaged by disease and trauma.[6] Technological improvements in nanofabrication methods used in electronic engineering can potentially be used to create orthopaedic implants that can integrate with, or restore bone tissue.[7]

The first practice of implantation surgery was performed by ancient civilisations who used precious stones and shells to augment or replace teeth.[8] Endosteal implantations were not performed until the nineteenth century, when Themistocles Glück produced a remarkable series of fourteen ivory joint replacements, including hip, wrist, knee and elbow prostheses in 1890.[9, 10] Although highly successful in the short term, all these implants were destined to fail due to deficiencies in antiseptic practice.

In the 1940s, the concept of biocompatible materials was demonstrated for the first time when the lack of an inflammatory or immune response to an exogenous material was considered the most appealing characteristic in the production of implants.[11, 12]

Orthopaedic endo-prostheses (such as joint replacements) must be fixed firmly to bone, as a loose implant may cause pain and/or peri-prosthetic fracture. The creation of a direct biological bond with bone tissue that persists during normal function is known as osseointegration.[13] Even if there is good mechanical stability of an implant initially, as bone is remodelled with time, loosening can occur many years later. This process is known as aseptic loosening and is the most common indication for revision joint replacement in the UK.[14] In the last thirty years, prevention of long term aseptic loosening by improving osseointegration has been of paramount orthopaedic interest.[13]

Bone forms the basic structural framework of vertebrates; it permits function and defines form. It is a living tissue composed of a type 1 collagen framework that is reinforced by hydroxyapatite.[15] Bone is continually re-modelled in response to mechanical and chemical stimuli by osteoblasts, osteoclasts and osteocytes.[16] Movement is generated by muscles that contract to pull bones along a plane of

motion dictated by adjacent articulations. If these bones become diseased or traumatised, they may cease to function adequately and cause disability to the individual affected. Orthopaedic surgery aims to restore function following the damaging effect of disease, and this may require replacing parts of the musculoskeletal system with artificial devices (otherwise known as endoprotheses).

1.3 The 'ideal' orthopaedic biomaterial

Research literature in orthopaedic biomaterials is frequently introduced by a description of the 'ideal biomaterial'. There are some fundamentally desirable properties for an orthopaedic biomaterial (intended for permanent implantation):

Mechanically:

- Resistant to fracture
- Resistant to corrosion
- Comparable to the host tissue

Biologically:

- Compatible with the host tissue
- Sterile
- Hypo-allergenic
- Resistant to infection

Clinically:

- Easy to assess radiographically
- Favourable to handle
- Cost-effective

Consideration of the 'ideal' orthopaedic biomaterial, however, does not exist without a description of the intended application and the particular bone or joint that is affected (Figure 2 **Error! Reference source not found.**). The desired properties of a material are dependent upon the clinical situation and the 'ideal' material would need to respond appropriately to a spectrum of dynamic requirements throughout an individual's life. *In vivo* testing of an orthopaedic biomaterial should also directly relate to the intended clinical application.[17, 18]

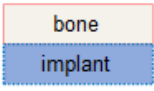
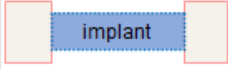
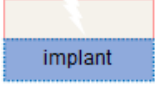
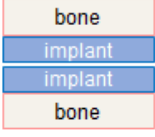
Orthopaedic application	(a) anchorage	(b) regeneration	(c) load bearing	(d) articulation
Schematic				
In vivo model	osseointegration model	osteogenesis gap defect model	fracture healing model	arthroplasty model

Figure 2. Applications of orthopaedic biomaterials

This diagram summarises the main applications required from orthopaedic biomaterials. In orthopaedics, materials are chosen dependent upon the characteristics they possess and how suited they are to a specific purpose.

(a) The most fundamental requirement for an orthopaedic biomaterial is anchorage. This is achieved by using strong materials with a high degree of surface roughness or screws to enable mechanical interlocking.[19]

(b) Gap defects can occur within bone due to trauma, infection or tumours. The ability of the of the human body to heal defects is limited by the size and location of the defect, the vascular supply and the age and well-being of the patient. Bioengineered bone graft substitutes and porous proto-bone frameworks can be used to regenerate bone in these scenarios.

(c) The majority of fractures heal, provided stability of the affected bone is maintained. Fracture fixation plates and intramedullary nails are routinely used in orthopaedic trauma to support fracture fragments until bone healing is achieved. Osseointegration of fracture fixation plates and intramedullary nails is undesirable if future implant removal is required.

(d) Joint replacement articulations usually involve coupling a ‘hard’ material with a ‘soft’ material (such as stainless steel and UHMWPE).[14] Some joints replacements involve the coupling of two ‘hard’ materials (such as ceramic-on-metal hip replacements) and some use only ‘soft’ materials (such as silicone elastomer metacarpo-phalangeal joint replacements).[14]

Throughout the twentieth century, surgeons and engineers have experimented with different metals and polymers to construct implants for bone and joint replacement

(Table 1). To meet the different requirements of orthopaedic implants, the properties of biomaterials can be tailored by blending (e.g., alloys and composites), combining (e.g., coatings and modular components) or physical modification (e.g., polishing and annealing).

An alloy is a metallic mixture of an elemental base metal with other metals or non-metals to create a material with different physical characteristics. The most frequently desired improvements are strength, modulus of elasticity, and resistance to corrosion.[20] The most commonly used alloys in the medical industry are Ti-6Al-4V (also known as titanium grade 5), stainless steel and Co-Cr-Mo.

Titanium and Ti alloys can be used as a coating material to enhance bioactivity of metallic or polymeric implants. It has good bonding properties that can create a strong interface and it can be deposited in different particle sizes to fabricate defined surface topography.

Synthetic hydroxyapatite (HA) has commonly been used for coating orthopaedic implant since the Furlong hip endoprosthesis was introduced in 1985.[21, 22] Despite the advances made, hydroxyapatite coating has not been a panacea for osseointegration and PMMA cemented femoral stems are regaining popularity.[14] Hydroxyapatite coated components fail to function through incomplete osseointegration[23-25], due to resorption or delamination of the coating.[26]

The presence of surface topography at both the macro- and micron-scale is considered essential to ensure good initial mechanical stability via interlocking with tissue to allow subsequent osseointegration. Bone implants are designed to achieve immediate mechanical stability using macro-features such as spikes, ridges, fins, keels, beads, pores, or screw threads. The importance of increasing surface area to improve bone-to-implant contact has been demonstrated by measurement of torque required to remove implants exhibiting different degrees of micron-scale roughness.[27]

If the surface material does not exhibit the desired characteristics, it can be modified using physical treatments such as sand blasting, reactive ion etching, annealing, plasma treatment, and anodization which change the composition at the atomic level. Other physical processing methods such as machining, polishing and moulding, modify the surface while maintaining the chemistry of the material. The

bioactivity of an orthopaedic implant can also be enhanced by coating with a biomaterial that generates a more favourable cell response.

Table 1. Characteristics of orthopaedic biomaterials

	Elastic Modulus (GPa)	Ultimate strength (MPa)	Reference
Bone (femur)	13.6-16.8	68-141 ^t	[28]
	17.6	194 ^c	[29]
Bone (lumbar vertebra)	0.04-0.06	2.7-4.6 ^c	[28]
Ti grade 1 ASTM F67	102.7	240 ^t	[30]
Ti grade 2 ASTM F67	102.7	345 ^t	[30]
Ti-6Al-4V ASTM F1472	110-114	895-930 ^t	[30]
Stainless steel 316L	205-210	465-950 ^t	[31]
PEEK	4.2 [*]	108 [*]	[Technical data from Invibio]

^{*}, ^c Compressive strength, ^t Tensile strength

1.4 Titanium and other Metals

Although titanium was discovered in 1791 it was not purified until 1910 and was not produced in significant quantities until after the second World War.[32] Titanium has gained popularity as an orthopaedic biomaterial due to its high strength and low modulus of elasticity compared to other metallic biomaterials.[20] The biocompatibility of titanium was further demonstrated in the 1960s when Brånemark used titanium dental implants to introduce the concept of osseointegration i.e. biological bonding of bone with a biomaterial).[33, 34]

Commercially pure Ti (Cp Ti) is available in four grades which are defined according to increasing oxygen content (grade 4 has 0.4% oxygen).[31] The TiO₂ oxide layer that develops on titanium and Ti alloys imparts excellent corrosion resistance, but low shear resistance and therefore poor wear characteristics.[31] Cp Ti, typically has a single-phase alpha microstructure, whereas Ti-6Al-4V has a biphasic alpha–

beta microstructure stabilised by aluminium and vanadium which significantly increases the yield and ultimate strength.[31]

Ti-based alloys have also been developed to fabricate 3D porous scaffolds by rapid prototyping, allowing the emergence of patient specific implants.[35-39]

Nitinol is an alloy of nickel and titanium which exhibits the properties of 'shape memory' and 'super elasticity' due to a reversible solid-state phase transformation known as martensitic transformation. The parent shape is formed by heating to 500°C to form the austenite phase. When the alloy is cooled it transforms to a martensite phase. If the alloy is deformed in the martensite phase it can be returned to its austenitic parent shape by re-heating. This property has been harnessed by TiNi memory staples which once implanted undergo transformation into a contracted shape and compresses the bones together.[40]

Titanium based alloys continue to be developed with theoretical advantages over Ti-6Al-4V and other alloys. For example, titanium nitride and titanium niobium nitride joint replacements have undergone clinical trials, but the outcomes have been poor.[41-44]

The 300 series of stainless steels (e.g., 316, 316L and 304) are most commonly used in biomedical applications.[45] Corrosion resistance is increased with the addition of chromium in type 304 stainless steel and molybdenum in type 316 stainless steel.[45] Austenite-stabilizing elements (primarily nickel, but also manganese and nitrogen) are added to steel (an alloy of iron and carbon) to achieve its primary face-centred cubic crystalline structure.[31]

The cobalt-chrome alloys are desirable as orthopaedic bearing surfaces due to its hardness and wear resistance when compared to titanium and stainless steel. Co-Cr alloys can be divided into castable alloys and hot-forged or wrought alloys. Vitallium (Co-28Cr-6Mo, ASTM F75 alloy), introduced by Venable and Stucke in 1936, is moulded into orthopaedic implants using investment casting. In this process the alloy is melted to 1350-1450°C and pressurised into ceramic moulds. Hot forging involves re-shaping the alloy at lower temperatures to increase yield and tensile strength. High revision rates of hip replacements with Co-Cr bearing surfaces and evidence of toxicity of wear related metal ions led to the majority of these products being withdrawn from the market.[46]

Ceramicised metals have become popular in orthopaedics, particularly as bearing materials in joint replacements. Clinical experience with alumina oxide and then zirconia in the 1980s, has led to hot isostatically press sintered zirconia toughened alumina (commercially known as Biolox).[47] Ceramic dental implants have been developed for implantation in bone, however ceramic implants designed for orthopaedic implantation in the metatarso-phalangeal joint proved far less successful.[48, 49]

Tantalum metal can be fabricated into 80% porous orthopaedic implants with a trabecular bone-like microstructure which have demonstrated bone ingrowth and improved fixation in vivo.[50]

1.5 PEEK and Polymers

Polymers provide an alternative to metals for orthopaedic applications. The use of polymers in orthopaedics was pioneered by Smith-Peterson , who used Bakelite, pyroxylin (nitrocellulose) and Pyrex to make implants.[51] Polymethylmethacrylate (PMMA, originally patented by Otto Röhm as Plexiglas in 1933) [52] was used by the Judet brothers to fabricate a monobloc femoral head and neck replacement. The initial design was revised, however, to incorporate a reinforcing steel rod after the implants fractured during clinical use.[53-56] Following this, PMMA gained popularity as 'bone cement' when Gottfried Roth, a dental technician, discovered that mixing milled PMMA with its monomers created a mouldable putty-like material.[52, 57][57] PMMA remains widely used in orthopaedics to 'cement' endoprostheses onto bone, although its lack of mechanical strength limits its value as an implant material.

PEEK (poly-ether-ether-ketone, as shown in Figure 3), approved for medical implantation in 1998, is a relatively new and versatile polymer with characteristics that are well suited for use as an orthopaedic implant material.[5, 58, 59]

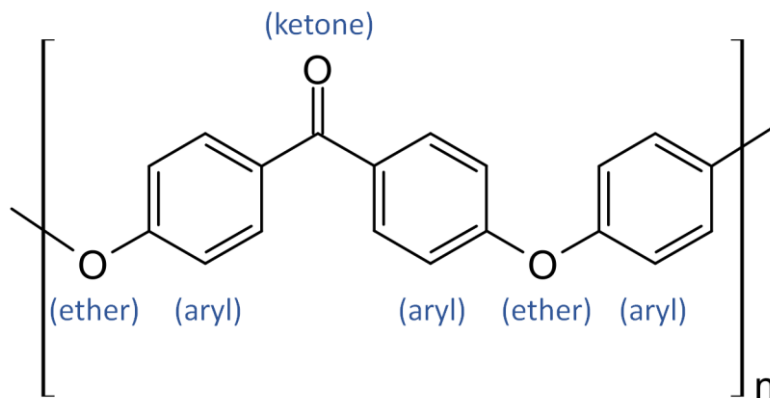


Figure 3. The chemical structure of poly-ether-ether-ketone

PEEK is a semi-crystalline thermoplastic polymer consisting of aryl groups connected by ketone- or ether- groups.

PEEK has similar mechanical properties to bone which maintains the body's normal biomechanics to minimise bone resorption around the implant.[60] PEEK is also radiolucent, which helps monitor *de novo* bone formation adjacent to the implant and causes no artefact on magnetic resonance or computed tomographic imaging.[2] X-ray markers (such as tantalum or barium sulphate) can be added to PEEK to help monitor the position of implants *in vivo* if desired.[61]

PEEK is commonly used to make inter-vertebral 'cages' used for spinal fusion (Figure 4). The cage restores the appropriate distance between the vertebral bodies after the damaged intervertebral disc material has been excised. Bone graft is implanted into the PEEK cage and the space between the vertebrae to encourage bone-to-bone fusion between the vertebral bodies. As PEEK is radiolucent (unlike titanium), plain x-rays can be used to check for successful inter-vertebral fusion.

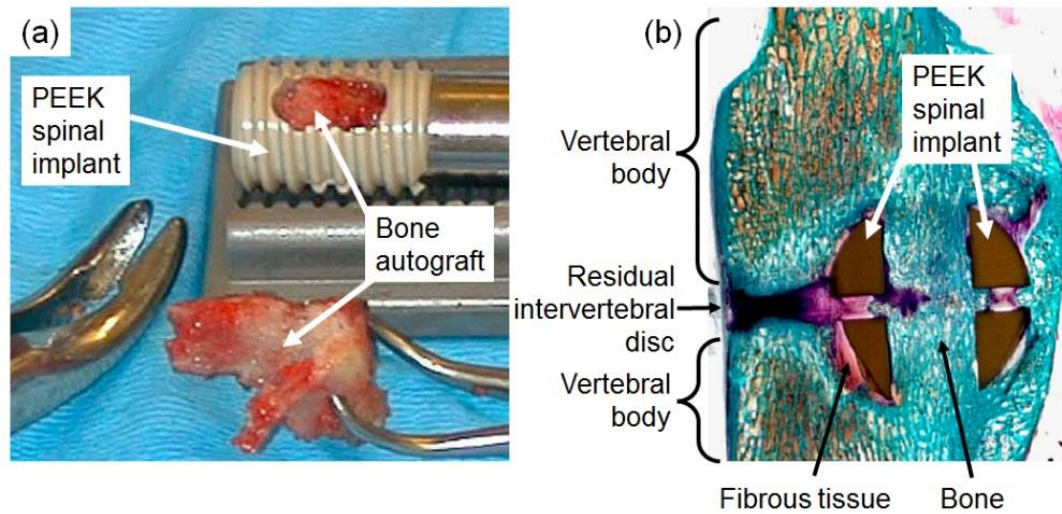


Figure 4. PEEK spinal implants in vivo

(a) This photograph shows threaded hollow PEEK spinal implants (known as intervertebral fusion cages) being filled with bone autograft before it is inserted into the space between two vertebral bodies during an in vivo study in goats. (b) Nuclear trichrome staining of undecalcified sections after 6 months show that the PEEK spinal implant has been inserted into the intervertebral space after removal of the intervertebral disc (cartilage stains dark purple). Fusion has occurred between the vertebral endplates (indicated by trabecular blue/green stained tissue in the region within the PEEK implant). Due to a lack of bioactivity the PEEK implant has become encapsulated with fibrous connective tissue (pink). Images reproduced and modified with permission from [62].

PEEK-on-PEEK spinal disc replacements have been introduced with the intention of maintaining spinal motion.[63] They are not currently designed to osseointegrate and implant migration is therefore possible.[62]

PEEK is also used to fabricate interference screws and bone anchor screws used in ligament reconstruction surgery, cranial reconstruction plates and fracture fixation plates.[64] It has previously been trialled as a material for use as acetabular cups and femoral stems, but the bio-inert nature of PEEK has limited its clinical success.[65] With the use of modern fabrication techniques, it may be possible to modify the surface of PEEK implants to make them bioactive, thereby enabling osseointegration by stimulating cells to produce bone tissue.

The characteristics of PEEK have made it a desirable material for engineering purposes and surgical devices.[5] Specialised grades of PEEK have been

developed for different applications, i.e. radio-opaque PEEK, reinforced PEEK and low viscosity (LT3) PEEK for injection moulding (Table 2 **Error! Reference source not found.**).

Table 2. Mechanical properties of PEEK [61]

<i>Property</i>	<i>Units</i>	<i>PEEK Optima LT1 (Vitrex 450G)</i>	<i>PEEK Optima LT3 (Vitrex 150G)</i>
<i>Tensile Strength (ISO 527)</i>	<i>MPa</i>	100	105
<i>Tensile elongation (ISO 527)</i>	<i>%</i>	20	30
<i>Flexural modulus (ISO 178)</i>	<i>GPa</i>	4	4.1
<i>Flexural strength (ISO 178)</i>	<i>MPa</i>	170	130
<i>Melt flow index</i>		3.4	36.4
<i>Molecular weight</i>	<i>M_n</i>	115,000	83,000
<i>Crystalline melt temperature</i>	<i>°C</i>	343	343
<i>Glass transition temperature</i>	<i>°C</i>	143	143

Although PEEK was specifically designed for injection moulding, surgical implants are often fabricated from PEEK using subtractive manufacturing methods, such as sawing, drilling and milling. By changing the cutting tool dimensions, speed and path different topographies and surface finishes can be easily be applied.

1.6 Surface modification of PEEK

Plasma is considered the fourth state of matter and is created by energising gas. Plasma treatment involves the exposure of a material to plasma and is frequently used in industry to promote adhesion between two surfaces and in cell engineering to enhance cell adhesion to tissue culture polystyrene (TCPS). Two step NH₃ and H₂ plasma treatment of PEEK has been shown to support murine osteoblast differentiation and, oxygen plasma treatment has been shown to improve human osteoblast differentiation.[3, 66]

The most readily observed physical effect of plasma treatment is a change in the wettability of the surface. This can be measured by the water contact angle that exists at the tri-phase boundary of solid, liquid and gas (i.e., PEEK, deionised water and air). The advancing water contact angle is measured as an enlarging droplet of water dynamically wets a surface and can quantify the hydrophobicity (tri-phase

angle $> 90^\circ$) or hydrophilicity (tri-phase angle $< 90^\circ$). The receding contact angle is assessed as the water is withdrawn from the surface and demonstrates how adherent a material is to water. The chemical modifications that result from plasma treatment are dynamic; they usually diminish with time and may be affected by cleaning, sterilisation and surface contact.[67-70]

Annealing can be used to increase the crystallinity of injection moulded PEEK.[71] PEEK is biphasic and is typically 30-40% crystalline within an otherwise amorphous state.[71] The amorphous state exhibits a glassy appearance, has less mechanical strength and reduced chemical resistance. Annealing causes PEEK polymer units to elongate in a symmetrical linear fashion without side branching. As the polymer chain length increases, they fold to form lamellae and become more closely packed.[71]

Fourier transform infrared spectroscopy with attenuated total reflection (ATR-FTIR) is a non-destructive, rapid method of assessing the surface crystallinity of PEEK. [71-73] The ratio of absorbance peaks $1305\text{ cm}^{-1}/1280\text{ cm}^{-1}$ and $970\text{ cm}^{-1}/952\text{ cm}^{-1}$ are compared to data derived from wide angle x-ray scattering (WAXS) to calculate crystallinity of PEEK by the Chalmers method (Figure 4).

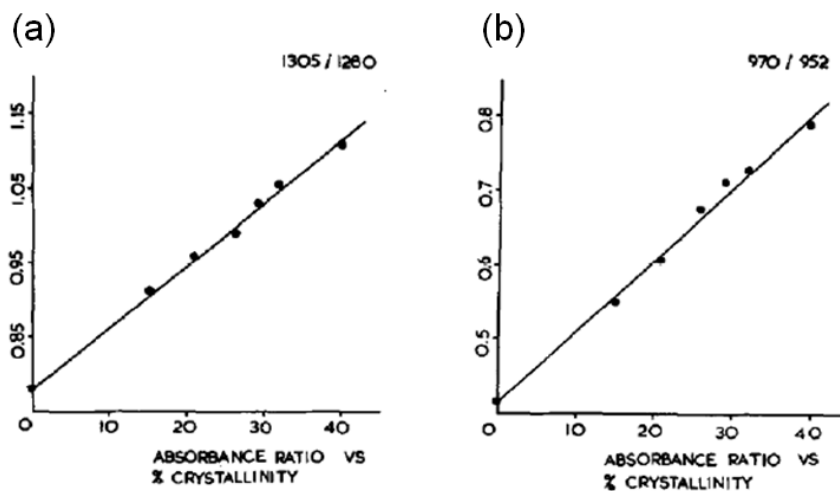


Figure 4. Chalmers method to assess PEEK crystallinity using ATR-FTIR

Chalmers identified direct linear relationships between (a) the $1305\text{ cm}^{-1}/1280\text{ cm}^{-1}$ and (b) the $970\text{ cm}^{-1}/952\text{ cm}^{-1}$ absorption index band ratio and PEEK crystallinity as determined by WAXS. Reproduced with permission from [72]

Gamma irradiation (most commonly 2.5 MRads or 25 kGy) is used to sterilise orthopaedic implants.[74] Gamma radiation affects surface energy, and the

resultant accelerated degradation of ultra-high molecular weight polyethylene is well documented in the orthopaedic literature.[75, 76]

1.7 Cell surface interactions

Many reports have shown increased bone response to roughened materials [77, 78], other authors have demonstrate no change [79], and some have found a reduced cellular response.[80] This may be due to under appreciation of the heterogeneity of such mechanically generated random surface topographies.

Porous surfaces have typically been designed with spaces greater than 100 μm to allow bone ingrowth, thus facilitating osseointegration.[50] Topography may aid in stabilisation of fibrin clot and extracellular matrix proteins to enable osteoprogenitor cells to become associated with the implant (contact guidance).[81, 82]

Protein surface interactions are influenced by material properties such as surface energy, polarity, charge, and topography.[83, 84] The conformation of adsorbed proteins is determined by attractive Coulomb's force and Van-der Waals interactions.

Fibronectin, an extracellular matrix protein, attains a globular conformation with a diameter of 16-35 nm on hydrophobic surfaces and a linear confirmation with a diameter of 2 nm and a length of 120 -180 nm on hydrophilic surfaces.[85-88]

Cellular anatomy is measurable by the nanometer and osteoblasts have been shown to react to features as small as 10 nm in diameter.[89] Bone tissue is characterized by a hydroxyapatite with an average organic grain size of 10-50 nm, and extracellular matrix proteins such as type 1 collagen with fibril diameters of 45-60 nm.[90] Cells membrane projections called filopodia with 50-100 nm diameter tips are thought to sense surfaces for suitable molecular adhesion sites.[91-93] The role of filopodia in cell migration and cell adhesion is difficult to elucidate as they are a transient structure and part of a dynamic process.

Cell adhesions are peripherally located anchor sites between a cell and the underlying substrate and play the key role in a cell's response to a surface. Connections are usually made between integrins (transmembrane receptor proteins) and proteins that have adhered to the surface.[94] Surface ligands (binding molecules) such as collagen, fibronectin and vitronectin are present in human body fluid and foetal bovine serum (FBS, a common component of cell culture medium)

and become bound to surfaces on initial contact. Cells therefore interact with arrangements of proteins on a surface rather than the surface directly.

Integrins exist in a bent closed (inactive) conformation and become extended open when activated.[95, 96] Super-resolution fluorescence microscopy has demonstrated integrin adhesion complex architecture consisting of FAK, paxillin, talin, vinculin, zyxin, vasodilator-stimulated phosphoprotein (VASP) and α -actinin.[97, 98]

When mechanical force is applied to the talin molecule from integrins, it unfolds to permit vinculin and actin binding, which strengthens and matures the adhesion complex.[98, 99] The maturation and coalescence of integrin adhesion complexes lead to actin polymerization and the formation of actin stress fibres which increases tension and stability within the cell.[100, 101]

Nascent adhesions formed in the broad protrusion at the leading edge of the cell (known as the lamellipodium) develop into focal complexes, focal adhesions, super mature focal adhesions and fibrillary adhesions.[102, 103, 105] These structures can be defined separately by morphology, spatial location and molecular composition but they are considered to be phases in a continuum of surface-cytoskeleton interaction during cell migration.[106]

Increased integrin clustering and FA formation subsequently facilitates increased actin polymerization and cytoskeletal tension via Rho GTPase, focal adhesion kinase (FAK) and mitogen-activated protein kinase (MAPK) signalling.[107-110] Integrin adhesion maturation also induces downstream cell responses involving the recruitment and activation of signalling proteins such as FAK, paxillin, proto-oncogene tyrosine-protein kinases (SRC) for extracellular signal-related kinases (ERK). [111-114]

To initiate cell adhesion, integrins bind to their peptide ligands and then cluster to form focal adhesions that stimulate actin polymerisation. If the space between integrins is more than 70nm apart, focal adhesions do not cluster, actin polymerisation does not occur, and cell adhesion is prevented.[115-119] As such, if the space between potential surface adhesion sites in the x, y or z direction is increased beyond 50–60nm then focal adhesion formation, actin polymerisation and cell adhesion is impaired.[115, 120, 121].

Research in our institution has shown that nanotopography affects the size, orientation and distribution of focal adhesions.[120, 122] Focal adhesions are preferentially established on raised nanofeatures such as pillars, islands or the spaces between pits (Figure 6).

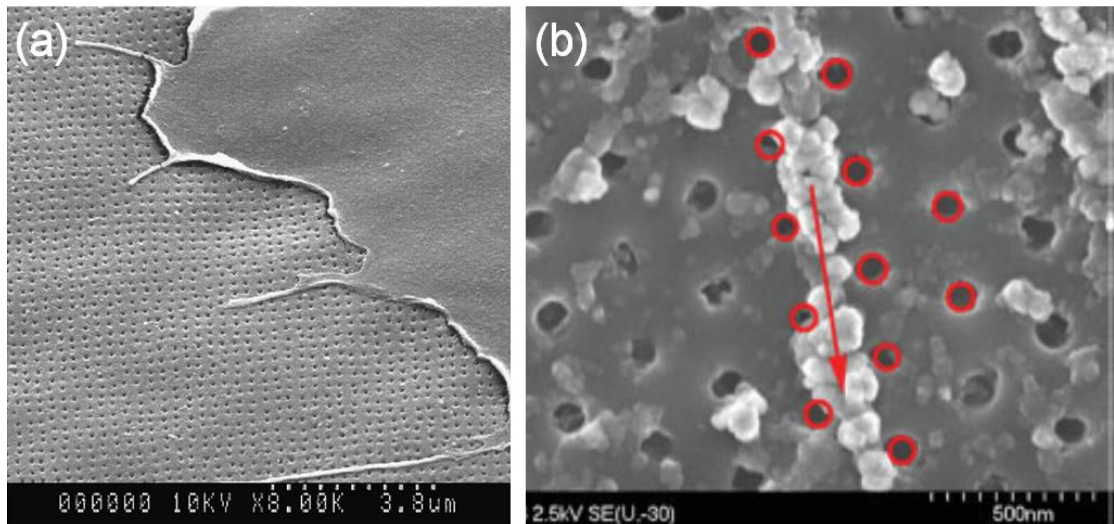


Figure 6. Nanotopographical control of cell adhesion

Human osteoblasts cultured on NSQ developed a larger number of super mature focal adhesions (10-20 μm) compared to the FLAT, SQ and HEX surfaces.[120] Image (a) from [7]. Image (b) from [122].

Mesenchymal stromal cells (MSCs) are found in bone marrow and have the ability to differentiate into osteoblasts, fibroblasts, adipocytes, chondrocytes, muscle cells, and nerve cells.[123-126] *In vitro*, this differentiation can be driven by the use of growth factors, such as dexamethasone for osteoblastic differentiation, insulin for adipocytogenesis, and hydrocortisone for myocytogenesis.

In vivo, an implant surface may exert an effect on cell behaviour, such as inducing multipotent cells to differentiate towards a committed osteoblastic lineage, or inhibiting differentiation, thus maintaining pluripotency. To enable successful osseointegration of orthopaedic implants, osteoinduction of surrounding MSCs to form osteoprogenitor cells and osteoblasts is the key goal as these cells will produce bone tissue and form a mechanically sound interface between the host and the implant. If cells were unintentionally stimulated to become adipocytes, they would form fat cells which have little mechanical integrity. Similarly, connective or fibrous tissue produced by fibroblasts is elastic and will not form a stable interface with orthopaedic implants.

Before differentiation, MSCs stabilize their adhesions to prevent locomotion.[127] Osteoblasts require highly stable adhesions and a large amount of intracellular tension to support their phenotype.[125, 128, 129] Osteospecific differentiation (versus adipogenic differentiation) of MSCs is directly related to cellular spreading, whereas reduced cellular adhesion with deactivation of FAK induces adipospecific differentiation.[128, 130] These characteristics illustrate the importance of surface topography to osteoblasts and some surfaces cannot sustain the cytoskeletal framework necessary for osteoblasts to function.[125, 129].

MSC multipotency can be retained with a moderate degree of intra-cellular tension, but if the cytoskeleton is disrupted, adipogenesis is initiated.[131] These observations suggest that high adhesion nanotopographies should be employed if osteospecific differentiation is desired and low adhesion nanotopographies will reduce differentiation and maintain the MSC phenotype [132].

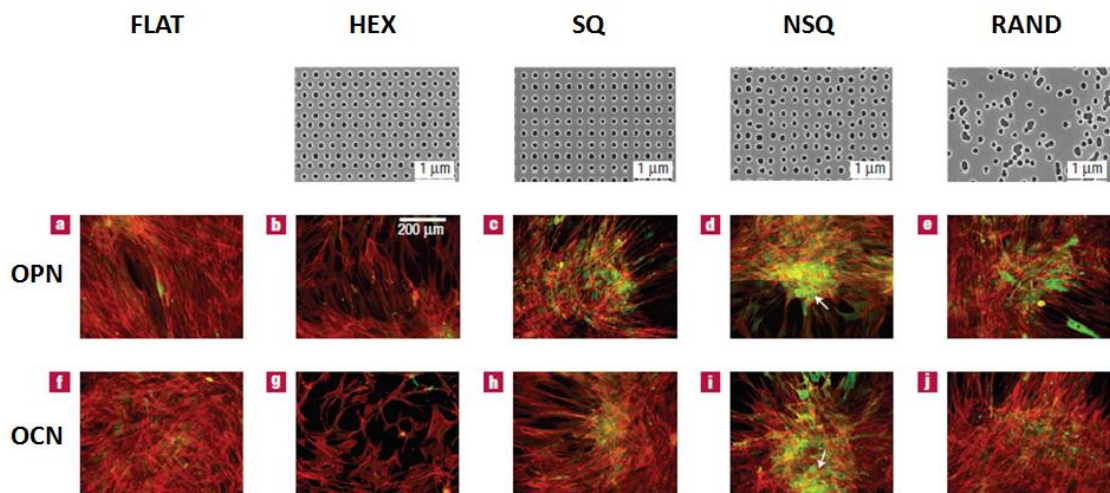


Figure 7. Nanotopographical control of cell behaviour

In this experiment Stro-1 enriched human MSCs were cultured on arrays of nanopits (120nm diameter, 100nm depth) with an ordered (HEX or SQ), disordered (NSQ) or random (RAND) pattern made from polymethylmethacrylate (PMMA).[1] MSCs cultured on NSQ, SQ and RAND produced bone specific proteins (OPN and OCN), whereas the planar control (FLAT) and HEX substrates had negligible amounts of bone cell markers and appeared to maintain a bipolar fibroblastic-like appearance. Image adapted from [1].

Nanotopography has been shown to stimulate cell differentiation with similar effects to exogenous growth factors. When cultured on a surface of nanopits in a disordered (or near-square i.e. NSQ) square pattern, MSCs expressed high levels of bone cell

markers comparable to MSCs cultured on planar substrates with osteogenic growth factors (dexamethasone and ascorbic acid)(Figure 7).

Titanium, aluminium and stainless steel spontaneously form oxide on the surface. Anodisation can be used to tailor the composition and morphology of the oxide film at the nano-scale. Titania nanotubes can be formed in the range of 10-100 nm by changing the voltage, solvents or temperature used for the anodisation process.[133-136] The interaction between oxide growth and dissolution can form the nanotubes into self-arranged arrays.[137] Park et al. demonstrated that stem cell responses could be modulated by changing the diameter of nanotubes.[133]

A study into the response of human MSCs to TiO₂ nanopores showed that adhesion, elongation, and differentiation of the cells was affected by increasing the diameter of the pores from 30 nm to 100 nm.[134] The 30nm pores had a higher number of adherent cells with a rounded morphology, whereas the 100nm pores resisted adhesion and the cells developed an elongated morphology.[134]

Cell-specific changes were identified using Ti-based substrates 70 nm nanoporous surfaces which induced osteoblast and fibroblast adhesion and alignment along the pores, whereas macrophages remained oval-shaped and sparsely distributed. [138]

Osteogenic differentiation of the cells was observed to occur on the 100 nm TiO₂ pores, with negligible amounts of osteogenic markers observed on TiO₂ nanopores of 50 nm diameter or less.[134] SEM showed that unidentified extra-cellular matrix (ECM) aggregates formed a blanket across the sub-50nm diameter tubes. When the diameter was increased above 50 nm, aggregates only formed around the rim of the nanopore. Modulation of adhered proteins in this manner could potentially create different topographical cues to the MSCs.

Titania nanotubes with a variable diameter of approximately 50-100 nm arranged in a disordered pattern fabricated by Bjursten et al. were implanted onto the surface of a rabbit's tibiae. Subsequent results demonstrated a significantly greater pull-off force was required to dislodge the nanopatterned surface compared to a grit-blasted Ti surface (which was rougher at the micron-scale). Also, a greater bone to implant contact was observed on the nanopatterned titania implants.[139]

Direct comparisons of surfaces are hindered as many different parameters can affect the success of the implant, such as device design, geometry and surgical technique which varies between products. A meta-analysis of implants from four

studies was used to compare machine-turned surfaces to roughened machined surfaces.[140-143] They found no statistically significant clinical difference in the number of early failures, but the roughened surfaces were correlated with an increased incidence of peri-implant inflammation.[140]

The methods used for fabricating nanoscale topographies are now being utilized to create bioactive titanium implants for commercial distribution.

A number of titanium dental implants that have undergone surface modification to exhibit random nanoscale roughness are commercially available.[69, 144-150] *In vitro*, bone cells respond to very specific nanoscale surface mechanotransductive cues and the use of random nanoscale roughness can potentially generate a non-mineralised fibrous layer on the implant surface and lead to loosening *in vivo*. [1, 100]

OsseoSpeed surface (Astra Tech AB, Molndal, Sweden) has microscale variations created by grit blasting titania (TiO₂) and nanoscale features produced by hydrofluoric acid etching.[145, 146] *In vitro*, the Osseospeed surface with nanoscale features caused greater expression of the osteoblast markers Runx, Osterix, alkaline phosphatase, and bone sialoprotein. In a canine model, there was increased bone identified at the interface between the Osseospeed titanium implant treated with hydrofluoric acid compared to a similar implant treated with grit blasting alone. [139, 140] An *in vivo* experiment using rabbits compared OsseoSpeed implants with titanium implants which are smooth at the nanoscale, and failed to detect any statistical difference between the bone-implant contact ratios after 2 weeks (36.0 vs 47.4% respectively).[151-154]

Nanotite (BIOMET 3i Implant Innovations, Palm Beach Gardens, Florida) are dental implants made from titanium alloy coated with 50-100 nm calcium phosphate nanoparticles using discrete crystalline deposition [141]. In a rat tibia model, bone ingrowth was 27% (CpTi) and 30% (Ti alloy) for the metals with nanotopography compared to 12% (CpTi) and 17% (Ti alloy) for the unmodified and surfaces [142]. The Nanotite surface was further investigated by Orsini et al. and subsequent histologic analysis revealed a bone-implant contact of $19 \pm 14.2\%$ for the control implant (without nanofeatures) and $32.2 \pm 18.5\%$ for the Nanotite implants.[155] Goene et al. reported on the clinical application of Nanotite implants and found a significant increase ($p < 0.01$) in the bone-implant contact in the experimental implants and observed an increase in bone healing at 4 and 8 weeks.[156]

SLActive implants are made by coarse grit-blasting Ti, followed by acid-etching to create nanostructures, nitrogen cleaning and immersion in isotonic NaCl solution to prevent hydrophobic recovery.[157, 158] The nanostructured implants have demonstrated greater bone to implant contact in dog mandibles and greater resistance to pull-out in rabbit tibiae.[158, 159]

Superhydrophilic SLActive treatment of Roxolid (15% zirconium and 85% titanium alloy) implants was determined to be superior to hydrophobic implants and surfaces without nanostructures.[160]

A number of groups have produced nanopores on type 316 stainless steel with diameters of less than 100 nm to 345 nm.[161-166] Rodriguez-Contreras et al. considered the anodised stainless steel surfaces to favour the proliferation of osteoblast cells over fibroblast cells.[167]

2 Fabrication of nanopatterned injection moulding tools

2.1 Introduction

2.1.1 Orthopaedic implant fabrication

Orthopaedic implants are manufactured by using a combination of additive and subtractive manufacturing processes and are carefully controlled using CAD/CAM (computer-aided design/computer aided-manufacture) techniques and CNC (computer numerically controlled) machines.[168] Casting (an additive process) is the traditional method for producing metallic components, such as orthopaedic prostheses. It involves pouring heated liquid metal into the internal cavity of a mould. The metal hardens when it cools and then the mould is separated to allow removal of the shaped metal. The shaped metal cast then undergoes secondary machining using cutting tools such as lathes and drills to remove excess metal and apply detailing before it undergoes surface finishing or polishing.[168]

The use of an automated injection moulding machine offers the most cost-effective fabrication process when large numbers of components are required.[169] This technique requires more sophisticated tooling and machinery compared to traditional moulding. Each stage of the moulding process is accurately monitored and controlled to allow enable optimisation of the process. Importantly, for the purposes of this project, it allows for the accurate replication of nanopatterns on an industrial scale.[170]

Fused deposition modelling, selective electron beam melting, selective laser melting, selective laser sintering, and inkjet printing are further examples of modern manufacturing methods that can be used to produce medical implants but they lack the precision to fabricate detailed nanotopography.[168]

2.1.2 Nanopattern generation using electron beam lithography

Nanolithography is the study and fabrication of nanoscale structures. Using this technology nanostructures of 10-20 nm in size (the same width as a collagen fibre)

can be fabricated.[171] The nanostructures fabricated using nanolithography have been described as grooves, ridges, pillars, pits, tubes, and needles.[172]

Electron beam (or E-beam) lithography allows the fabrication of nanostructures of any desired geometry in any pattern or shape. Unlike other forms of nanolithography, E-beam lithography, can generate ordered, disordered and random nanopatterns. The process involves directing a beam of electrons onto a resist layer using a digital template to create a pattern of exposure within the surface. Depending on the resist material used, the electron beam can either break the polymer chains rendering it soluble to the developing solvent (i.e., a positive resist) or cause polymerisation, leaving it insoluble to the solvent (i.e., a negative resist). The remaining resist layer is used as a mask to allow selective etching of the unprotected areas of the surface using reactive gases. Figure illustrates how this process can be combined with electroplating to fabricate the nanopatterned nickel mould inlays used in this project.





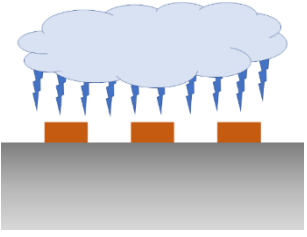
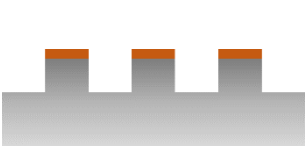

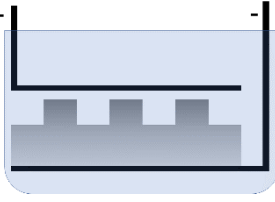
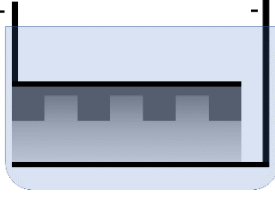

1.  A resist layer is spun onto a clean silicon wafer for a specific time and at a chosen speed (rpm) to achieve the desired thickness.
2.  The desired pattern is created using design software. The desired electron beam dose is chosen. The wafer is mounted into the electron beam lithography tool and the program is run.
3.  The electrons target the chosen areas of the nanopattern which causes bonds to form within the (negative) resist layer.
4.  The wafer is removed from the e-beam tool and the unexposed resist is developed away using solvents.
5.  The pattern is etched into the substrate using reactive ion etching. High energy gas plasma created between electrodes within a vacuum chamber attacks the substrate until the desired etch depth is reached. The substrate coated with resist is protected from the process.
6.  After reactive ion etching, the nanopattern will be etched into the substrate to the desired depth. The resist layer may have diminished in thickness but it will usually persist on top of the nanofeatures.
7.  The remaining resist is then removed with solvents and/or plasma etching to leave a nanopatterned silicon wafer.
8.  The e-beam generated nanopattern then needs to be transferred to a material suitable for injection mould nanofabrication. Nickel electroplating creates a negative copy of the nanopatterned silicon wafer.
9.  Nickel is deposited directly onto the nanopatterned silicon wafer. The subsequent process of removing the nanopatterned nickel shim from the wafer is often damaging and usually prevents the silicon wafer from being used again.
10.  After cleaning and characterisation using microscopy, the nanopatterned nickel shim is ready to be mounted in the injection moulding machine.

Figure 8. Nickel mould inlay nanofabrication

2.1.3 Nanoimprint lithography

Nanoimprint lithography (Figure 9) is a technique in which a nanopattern can be transferred from one material to another by using a stamp to directly deform a resist layer through contact.[173] This method provides a low cost, high output method, and up-scalable method of transferring electron beam generated nanopatterns to machine parts or orthopaedic endoprotheses.

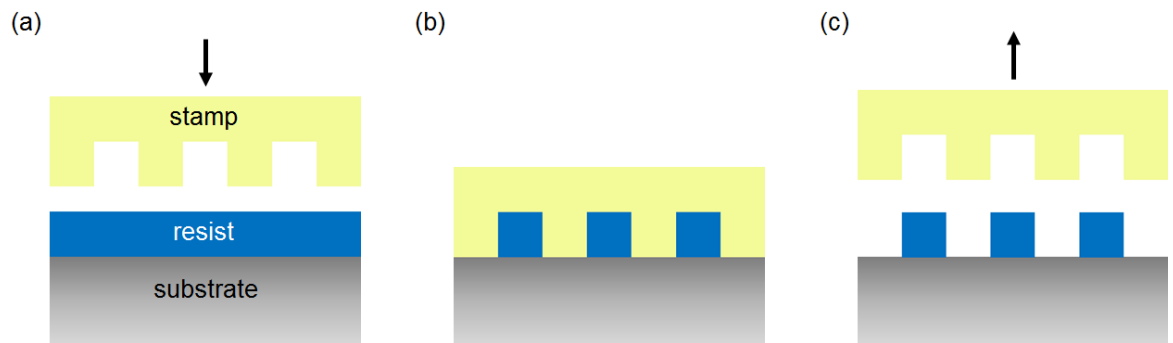


Figure 9. Nanoimprint lithography

(a) After appropriate preparation, a resist layer is applied to the substrate.

(b) The stamp is brought into contact with the resist layer which conforms to the topography of the stamp. Additional pressure can be applied during the stamping process. The resist is allowed to cure (this can be initiated or accelerated using heat).

(c) The stamp is removed to reveal a negative copy of the stamp nanotopography in the underlying resist layer.

To create a specific desired final nanotopography, consideration must be given to the physical properties of the materials involved and the conditions in which the process is undertaken. Small variations in these parameters can lead to changes in the height, diameter and shape of the resultant nanostructures, and can affect the overall transfer quality of the nanotopography.

To adequately prepare the substrate for nanolithography it is essential to start with a perfectly flat (planar) and clean surface. Planarization can be achieved using a number of methods and these can be additive or subtractive in nature.

Liquid layers can be added onto the surface and smoothed by spin coating. The liquid can then be solidified by thermal or ultra-violet curing to make a new planar surface. A common problem with this method is that a mismatch in mechanical

properties – particularly thermal expansion – can lead to separation at the interface between the two materials.

A more promising method of planarization for this project involves subtraction of the surface roughness by abrasive mechanical or chemical-mechanical methods, as it will create a more uniform surface than an equivalent substrate planarized by a spin-coated layer, and it will also be less susceptible to stress cracking that can occur due to mismatch of thermal expansion properties when using two materials.

Silicon wafers undergo chemical/mechanical polishing to have minimal surface roughness before use in the microelectronics industry. Chemical-mechanical polishing involves pressing the substrate against a polishing pad or platen while adding an abrasive and corrosive chemical slurry (usually a colloid – microscopic insoluble particles dispersed in water). The substrate is held onto a carrier or chuck by a vacuum or hydrostatic pressure. Potentially the rotatory speed, the downward pressure and the back pressure of the carrier can be adjusted. An increase in the speed and downward pressure will increase the volume of material that is removed, whereas the back pressure can be used to create a flatter surface from the centre to the edge of larger wafers.

A novel titanium dioxide precursor sol gel (after work by Yoon *et al.*, Richmond *et al.*, and Greer *et al.*[174-176]) was developed within our research group for use as a nanoimprint resist in this project. Uniquely, this contained 2-(2-butoxyethoxy) ethyl acetate (22BEEA) and 1-hexanol (50:50 w/w) (Table 3) to reduce the vapour pressure and increase the working time for imprinting. This is especially important when fabricating thin films and using ‘step-and-repeat’ pattern replication (in which the process is repeated multiple times over a surface to create a larger patterned area).[177]

As per Yoon *et al.*, polydimethylsiloxane (PDMS) was used as the stamp material. PDMS is a transparent biocompatible silicone elastomer that conforms to micro and nanotopography and is extensively used in lithography.[178] The modulus can be altered by adjusting the proportions of the pre-polymer (base) and cross-linker (curing agent), and alternatively, hexanol can be added to reduce the viscosity. [178, 179] The flexibility of PDMS offers the potential for creating stamps that conform to non-planar surfaces to allow 3D nanoimprinting.[179-183]

Table 3. Titanium dioxide precursor sol-gel solvents

Solvent	Vapour Pressure	Boiling point	Reference
<i>Ethanol</i>	<i>44.60 mmHg (20°C)</i>	<i>78°C</i>	<i>Yoon et al.[175]</i>
<i>2-Methoxyethanol</i>	<i>6.17 mmHg (20°C)</i>	<i>124°C</i>	<i>Richmond et al.[174]</i>
<i>1-Hexanol</i>	<i>1.00 mmHg (25.6°C)</i>	<i>157°C</i>	<i>Greer et al.[176]</i>
<i>22BEEA</i>	<i>0.04 mmHg (20°C)</i>	<i>240 °C</i>	

2.1.4 Injection moulding of nanopatterns

Injection moulding is an automated mechanical process that involves using a large mechanical screw combined with thermostatically controlled heaters to melt materials and insert them into a mould with pressure.[59] The material conforms to the internal shape of the mould, then freezes and is ejected from the machine as a finished moulded part in a cycle that lasts less than 30 seconds. Moulding of orthopaedic implants using injection moulding potentially offers increased precision and throughput compared to other traditional methods such as casting or machining. The separate stages of the process can be accurately monitored and controlled to enable optimisation and reproducibility.

Nanopatterned inlays have been used in the injection moulding machine to automatically reproduce nanopatterns in thermoplastic polymers.[184] Combining this technology with ‘step-and-repeat’ nanoimprint lithography, introduces the possibility of manufacturing of larger scale nanopatterned mould tools.[185] With the further addition of advanced soft lithography techniques, the non-planar tools exhibiting nanopatterns required for this project can potentially be fabricated.[180]

Injection moulding of nanopatterns has been used extensively in Glasgow to fabricate nanopatterns in polystyrene and polycarbonate for *in vitro* biological experimentation.[186] Poly-ether-ether-ketone (PEEK) was specifically designed for injection moulding and it benefits from a rapid and reliable state change from liquid to solid during the freezing stage which allows the production of precise surface architectures.[59] It is already prevalent as a biomaterial in the orthopaedic industry for use in spinal implants, screws and bone anchors, and offers an ideal biomaterial for use in this project.[2, 64, 65]

Unlike conventional manufacturing methods, injection moulding presents an exciting opportunity to create novel PEEK orthopaedic implants that exhibit bioactive surface nanopatterns.

2.2 Aims and Objectives

The aim of this chapter was to fabricate tools for injection moulding nanopatterns on planar and non-planar surfaces for the manufacture of bioactive PEEK implants.

This would be achieved via the following objectives:

- Fabricate injection mould tools and inlays using 3D CAD design, traditional machining, hand polishing, and chemical -mechanical polishing;
- Nanopattern injection mould tools using nanoimprint lithography and perform surface analysis;
- Use nanopatterned tools to injection mould cell culture substrates and prototype implants using polycarbonate and PEEK

2.3 Materials and Methods

2.3.1 Injection mould tool preparation

2.3.1.1 Design

Bespoke tool inserts or inlays (24.8 mm x 24.8 mm x 10 mm and 2 mm radius) were designed to fit an existing injection mould tool which has a cavity of 25 mm x 25 mm x 10 mm and 2 mm radius rounded corners. Moulds for the fabrication of nanopatterned *in vitro* cell substrates, non-planar *in vivo* implants and prototype orthopaedic devices: a concave dome; a convex dome and a bone anchor were created. 3D models of the tools were created in Rhinoceros® CAD/CAM software. 0.1 mm clearances were incorporated into the design to prevent the tool insert sticking in the backplate.

2.3.1.2 Machining

1 mm titanium grade 2 plate (William Gregor Ltd., London, UK) was cut into 24.8 mm x 24.8 mm pieces with 2 mm radius rounded corners using industrial waterjet

cutting (JetCut Ltd., Glasgow, UK). Titanium grade 1 (10 mm thickness), Ti-6Al-4V (10 mm), stainless steel 304 (10 mm), and P20 tool steel (10 mm) (Harrison Special Steels Ltd., Riccal, UK) tools were prepared using CNC machining in the University of Glasgow Workshop. Aluminium 6084 (Clickmetal, Romsey, UK) (also 24.8 mm x 24.8 mm pieces with 2 mm radius rounded corners) was prepared using CNC machining in the Bio-Interface Group laboratory. Yellow brass (RS Components Ltd., Corby, UK) substrates were cut using a guillotine and the corners were filed by hand. The 3D model design files (.3dm) were converted to CNC toolpath g-code files using madcam software. For planar mould tools a 3 mm straight, ended mill was used with a X-Y speed of 2 mm/sec and a Z height drop of 0.5mm. Millcool (Hexol FR9) water-based metalworking fluid was used as lubricant and cleaning agent during machining. A 2-mm ball nosed mill was used to cut the non-planar surfaces.

2.3.1.3 Planarization

The surfaces were planarized to prepare them for nanoimprinting. Hand polishing was performed using 400, 600, and 1200 grit silicon carbide abrasive paper (RS Components Ltd., Corby, UK). The surfaces were then polished using a flat ended felt bob fitted to a mini rotary tool and Kemet 6-KD, Kemet 3-KD, and Kemet 1-KD diamond paste (Kemet International Ltd., Maidstone, UK) successfully until a mirror finish was obtained. The samples were then wiped clean with cleanroom paper, and ultrasonically solvent cleaned in acetone, methanol, and isopropyl alcohol (IPA) before being rinsed in deionised water and dried using filtered nitrogen.

Planarization of inlays was also undertaken using the Logitech Orbis Standing CMP (chemical/mechanical polishing) System (Logitech Ltd., Glasgow, UK) (Figure 10). The flat surface and the edges of the sample were initially hand ground using 600 grit silicon carbide abrasive paper. The samples were then ultrasonically solvent cleaned in acetone, methanol, and IPA, and then rinsed in deionised water before being loaded into the CMP machine. The polishing platen was set at 60 or 160 rpm, the sample carrier was set at 40, 60, or 120 rpm, the downward load was 1, 5, or 9 psi, and the duration of polishing was 5, 10, 15, 20, 25, or 30 mins. SF-1 alkaline colloidal silica polishing slurry (Logitech Ltd., Glasgow) was used with and without the addition of 6% hydrogen peroxide (Fisher Scientific UK Ltd., Loughborough, UK).[187, 188]

After chemical/mechanical polishing, samples were sonicated in 2.45% tetramethylammonium hydroxide solution (TMAH, Microposit MF-321 Developer, Shipley Company, Marlborough, MA, USA) for 5 mins, rinsed in deionised water and ultrasonically solvent cleaned in acetone, methanol, and IPA before being finally rinsed in deionised water and dried using filtered nitrogen. TMAH is silicon etching and cleaning solution used to remove any remaining silica particles from the surfaces.[187, 188]

Planarization was separately undertaken using a novel titanium dioxide precursor sol-gel described previously (Table 3). This was applied after initial hand polishing and ultrasonic cleaning.

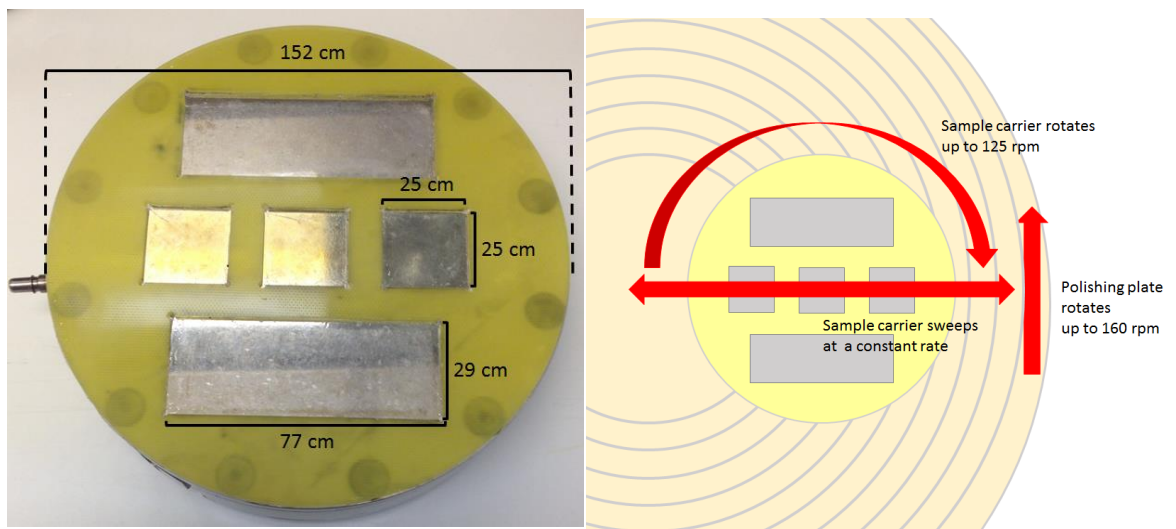


Figure 10. Chemical-mechanical polishing

A carrier template designed to hold small inlays (25 x 25 mm) and larger slide-shaped inlays (29 x 77 mm) was commissioned from Logitech Ltd. The carrier and polishing platen rotate and the carrier constantly sweeps from the inside to the outside of the polishing platen whilst applying up to 9 psi of down load on the samples.

2.3.2 Nanoimprint lithography

Nanopillared master stamps were fabricated in silicon with the assistance of my colleague Dr Andrew Greer. 1 mm silicon wafer was cut into 15 mm pieces and ultrasonically solvent cleaned in acetone, methanol and IPA, rinsed in deionised water and dried using filtered nitrogen. Elvacite[®] 2041 PMMA resist (Lucite International Specialty Polymers & Resins, Newyton Aycliffe, U.K.) was spun onto the silicon and soft baked at 180°C for 1 hour. The nanopattern design for this stamp was an ordered array of 200 nm diameter circles with a centre-to-centre pitch of 300

nm covering a square area of 10 x 10 mm and was created using L-edit software. The nanopattern was generated by cross-linking the PMMA resist using a Vistec Gaussian Vector Beam 6 (100kV) electron beam lithography tool.

Following exposure, the negative-tone PMMA resist was developed in 1:2.5 MIBK:IPA solution, rinsed in IPA and cleaned in O₂ plasma at 20W for 1 min at 0.2 mbar. Thereafter, 60 nm of NiCr was evaporated onto the remaining PMMA using a Plassys MEB 550S tool to create an etch mask. The samples were dry etched for 240 s, 300 s, and 400 s with a mixture of C₄F₈ and SF₆ gases using a Surface Technology Systems Reactive Ion Etch tool. The depth of the chrome etch was analysed using atomic force microscopy (AFM) before it was removed by sonicating for 2 min in ceric ammonium nitrate and nitric acid. The remaining PMMA resist was removed using 50°C acetone, and the nanopillared Si stamp was ultrasonic cleaned in acetone, methanol, IPA, and deionised water.

The Si stamps were silanized by vapour deposition of Trichloro (1H, 1H, 2H, 2H-perfluoro-octyl) silane (Sigma Aldrich, Gillingham, U.K.) to create a hydrophobic non-adherent surface. This was achieved by, firstly, plasma treating the Si masters in O₂ for 1 min at 100W at 0.2 mbar. They were then transferred to a glass dish and, with nitrogen venting, 50 µl of trichloro-silane was added periphery of the dish, which was covered and heated to 150°C. Once the trichloro-silane had vaporised the stamps were allowed to cool to room temperature.

The TiO₂ precursor sol-gel was prepared, firstly, by mixing 2-(2-butoxyethoxy) ethyl acetate 4.6 ml, 1-hexanol 2.77 ml (Sigma Aldrich, Gillingham, U.K.), and deionised H₂O 0.10 ml and stirring for one hour. Then, diethanolamine 0.96 ml and titanium (IV) butoxide (Ti (OBU)₄) 3.4 ml (Sigma Aldrich, Gillingham, U.K.) were added and the solution was stirred for 2 hours in a temperature and humidity controlled clean room. The TiO₂ sol-gel was analysed using thermo-gravimetric analysis using a 2°C/min ramp up to maximum temperature.

Reinforced flexible and non-planar hybrid polydimethylsiloxane (PDMS) nanoimprint stamps were fabricated using 10 parts base to 1 part crosslinker (Sylgard® 184, Dow Corning Corporation, Barry, U.K.)(Figure 11).

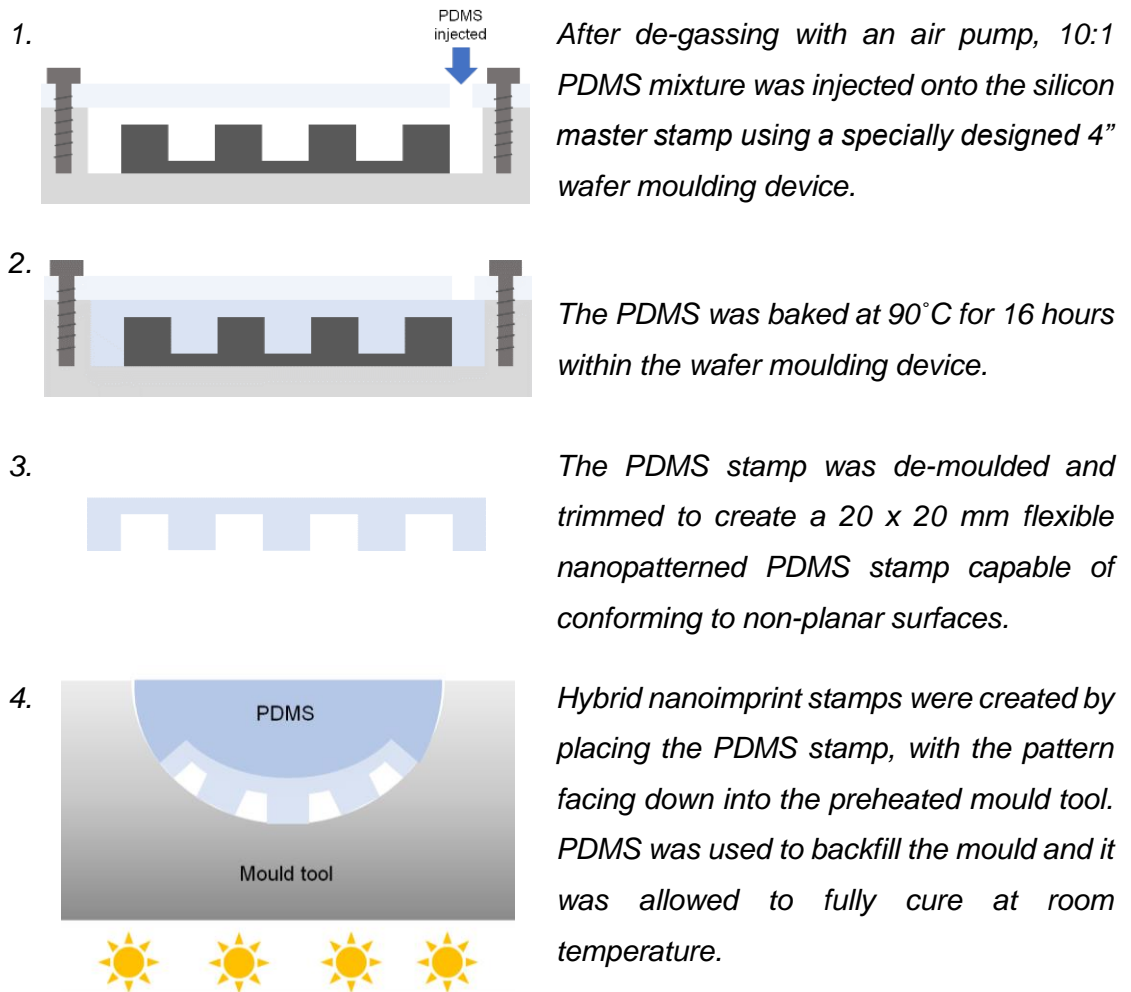


Figure 11. Fabrication of reinforced flexible and non-planar PDMS nanoimprint stamps.

Schematic demonstrating the methods used to create thin flexible and hybrid PDMS stamps for nanoimprinting.

Oxygen plasma treatment (PlasmaPrep5 barrel asher, GaLa Instrumente GmbH, Bad Schwalbach, Germany) was used to modify pattern transfer between the PDMS nanopatterned stamp and the substrates. The substrates and PDMS received 20W for 30 s (0.2 mbar), 100W for 30 s (0.2 mbar) or no plasma treatment.

TiO₂ sol-gel was either spun onto the nanopatterned PDMS stamp at 10,000 rpm for 7 s or spun onto the substrate at 10,000 rpm for 7 s. These spin parameters have previously been found to create a titanium dioxide layer which is approximately 100 nm thick after annealing. The substrates were aluminium, brass, titanium grade 1, titanium grade 5, titanium Ti-6Al-4V alloy, stainless steel and P20 tool steel as described previously. After spinning, the nanopatterned PDMS stamps were

immediately pressed onto the substrate. Air bubbles that arose between the PDMS and the underlying substrate were squeezed out. A glass slide was placed on top and held in position with gentle pressure using a 'pocket' nano-imprinter device.[189] The PDMS and substrates were baked at 90°C or 120°C before demoulding of the PDMS. The PDMS stamps were retained for analysis and were not reused.

The nanoimprinted mould tools were annealed in a furnace: Al, Ti, Ti-6Al-4V, and stainless steel was annealed at 500°C (ramp to 500°C in 4 h (2°C/min), then held for 30 mins), then cooled to room temperature gradually; P20 steel tool was annealed at 500°C, 500°C in an argon chamber, and 300°C using a 2°C/min temperature ramp.

2.3.3 Topographical analysis

Before analysis, samples were ultrasonically cleaned in acetone, methanol, IPA, and rinsed in deionised water, before being dried in filtered nitrogen.

Scanning electron microscopy (Hitachi S-4700, Hitachi Ltd., Warrington UK) was used to analyse the surfaces before imprinting and after annealing. CellProfiler open-source software was used to assess the fidelity of pattern transfer [190]. SEM analysis of PDMS stamps was performed after sputtering with a 9 nm layer of AuPd.

Atomic force microscopy (Veeco Dimension 3100, Veeco Instruments Inc., Cambridge, UK) with a pyramidal cantilever tip in tapping mode was used to attain 3D profiles of the surfaces. In each case at least 3 locations were randomly analysed on at least 3 samples. Gwyddion 2.26 open-source software was used to measure surface dimensions.[191] Further image analysis was achieved using ImageJ open-source software.[192] Height profiles were also analysed using a Veeco Dektak 6M Height Profiler (Veeco Instruments Inc., Cambridge, UK) during optimising of the process.

SEM images were analysed using CellProfiler Software to count the number of pillars that were successfully transferred from the original silicon master (Figure). The nanopattern transfer fidelity was calculated as the percentage of the successfully replicated nanostructures. A successfully replicated nanostructures had a roundness ratio >0.9 and was not in contact with any surrounding structures.

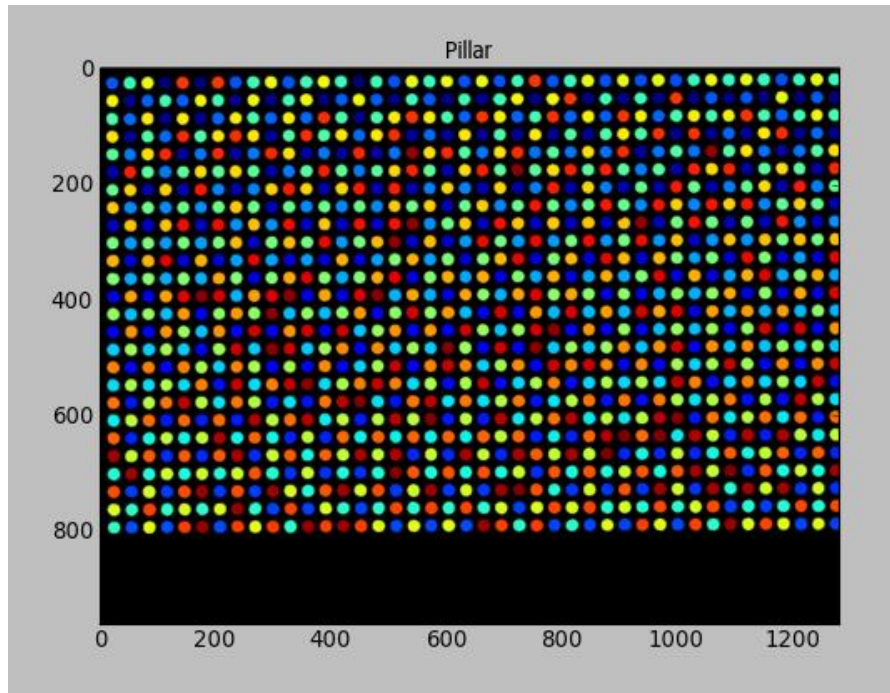


Figure 12. Assessment of nanopattern fidelity

CellProfiler automatically recognised nanostructures as areas of different intensity based upon threshold parameters set by the user. This image highlights 448 nanostructures from a SEM image (10K magnification) and indicates a successful pattern transfer. The roundness ratio was assessed using the following equation (in which 1 is a perfect circle and 0 is a highly non-circular shape): $\text{Roundness} = 4\pi \times \text{Area} / \text{Perimeter}^2$

2.3.4 Injection moulding of nanopatterns

Polycarbonate (PC)(Makrolon OD2015), PEEK LT1 Optima, PEEK LT3 Optima (Invibio Ltd., Thornton-Cleveleys, U.K.), and polypropylene (PP)(Capilene E 50 E, Carmel Olefins Ltd., Israel) were used in an Engel Victory 28 hydraulic injection moulding machine (Engel GmbH, Schwertberg, Austria)(Figure , Table 4).

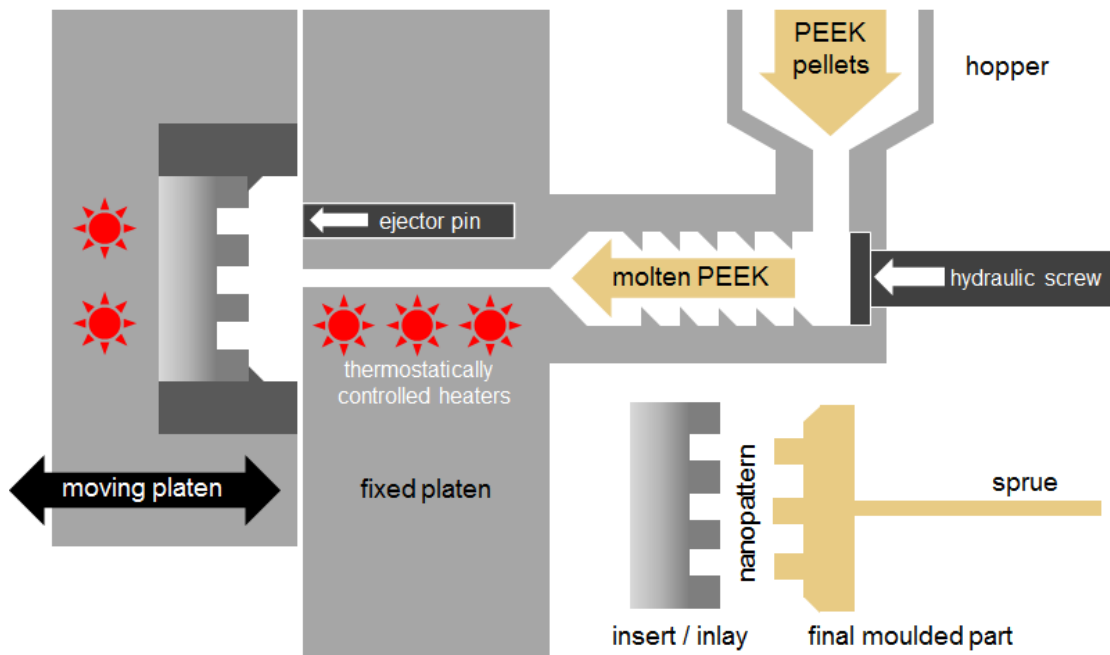


Figure 13. Injection mould nanopatterning process

Polymer pellets (e.g., PEEK) were inserted into the hopper and transferred into the mould cavity by a large mechanical screw. The polymer was heated beyond the melting point (360°C for PEEK) and the temperature was carefully controlled to optimise the moulding conditions. The material conforms to the internal dimensions of the mould cavity and the platens separate, so the moulded part can be ejected from the machine. The moving platen then returns to re-seal the mould in readiness for another shot of polymer. A sprue of PEEK remains attached at the end of the process and was snapped off before use.

The thermostats for the mould tool and the separate heating elements were set to the desired level (Table 4). The system was purged by loading the hopper with 750 g of undried PC and plasticising it through the screw at 250°C. Vacuum dried PC was added to the hopper and plasticised at 280°C. The mould tool was inserted into the injection moulding machine. Vacuum dried PEEK was loaded into the hopper and the temperature was increased to the desired level and plasticised.

The desired injection speed and holding pressure were selected (Table 4). The nozzle was then cleaned and the platens were closed to allow hydraulic pressure to build up and moulding was commenced. Initially semi-automatic mode was used to confirm satisfactory part quality before switching to automatic mode.

The injection mould parts were ejected from the machine and collected in a clean container. The sprue was removed and the nanopatterned samples were packaged into vacuum sealed bags.

Table 4. Injection moulding parameters

<i>Polymer (brand)</i>	<i>Nozzle temp (°C)</i>	<i>Tool temp (°C)</i>	<i>Injection speed (cm³ s⁻¹)</i>	<i>Holding pressure (bar)</i>	<i>Cooling time (s)</i>	<i>Shrinkage (%)</i>	
<i>PC (Makrolon OD 2015)</i>	280	80	50	1000	5	0.6	[193]
<i>PEEK (Optima LT1)</i>	380	370	50	1000	5	1.2	[194]
<i>PEEK (Optima LT3)</i>	380	370	50	1000	5	1.3	[194]
<i>PP (Capilene E 50 E)</i>	230	40	50	1000	5		

2.4 Results

2.4.1 Injection mould tool preparation

2.4.1.1 Machining

Planar injection mould tools were machined in aluminium, brass, P20 tool steel, titanium grade 1, titanium grade 2, Ti-6Al-4V alloy, and stainless steel. Non-planar mould tools were created by machining hemi-cylindrical and hemispherical shapes (Figure 14).

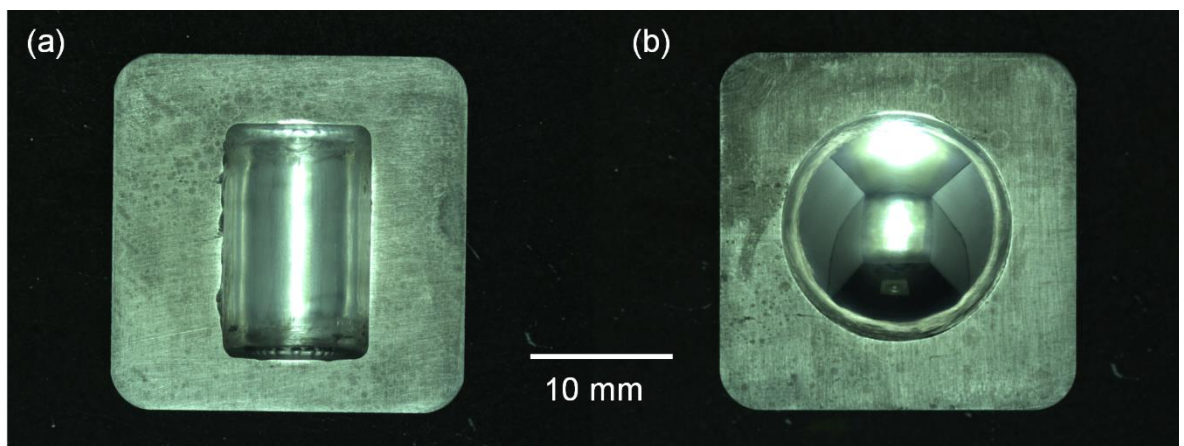


Figure 14. Non-planar aluminium injection mould tools

Photographs of non-planar injection mould tools machined in aluminium. (a) Hemi-cylindrical and (b) hemispherical mould tool inserts were designed to represent simple orthopaedic devices.

2.4.1.2 Planarization: Hand polishing mould tools

A planar and uniform mirror finish was achievable in all tool materials by hand polishing. In this series of results (Figure 15 and Table 5), the lowest Ra was achieved on stainless steel. Each sample took approximately 30 minutes to reach a consistent standard.

The finish achieved by hand polishing is subject to variability and dependent on technique and duration. It was considered necessary to achieve a $R_{\max-\min}$ of less than 200 nm for subsequent nanoimprinting and this was achieved reliably in aluminium, brass, stainless steel, and P20 tool steel. Titanium grade 1, titanium grade 2 and Ti-6Al-4V alloy, however, had $R_{\max-\min}$ that approached or exceeded 200 nm, particularly when a larger surface area was analysed.

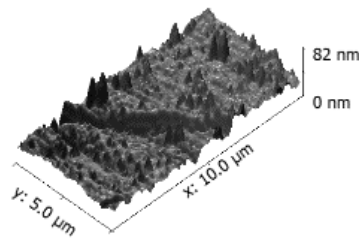
Table 5. Hand polished surfaces*

	R_a (nm)	R_{ms} (nm)	$R_{max-min}$ (nm)
Stainless Steel	6.1	8.05	81.51
Aluminium	9.1	12.0	102.1
P20 Steel	9.7	12.7	100.6
Titanium grade 1	10.8	14.7	160.1
Ti-6Al-4V alloy	14.0	20.7	192.4
Brass	17.3	20.9	128.3
Titanium grade 2	19.5 [†]	26.2 [†]	284.5 [†]

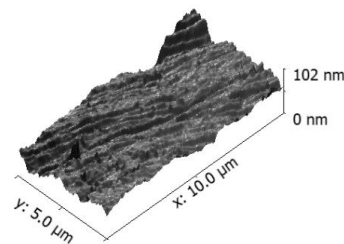
*These are representative examples rather than statistically average samples.

[†]This sample (g) was taken using a 60 x 60 μm rather than a 5 x 10 μm .

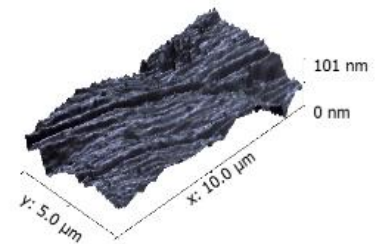
(a) Stainless steel



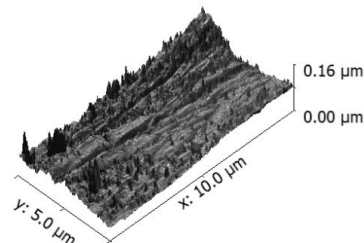
(b) Aluminium



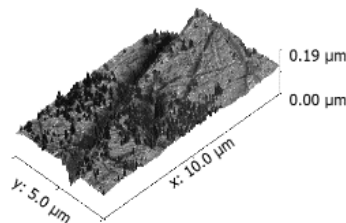
(c) P20 steel



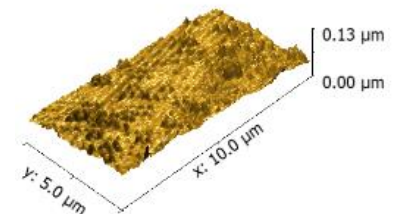
(d) Titanium grade 1



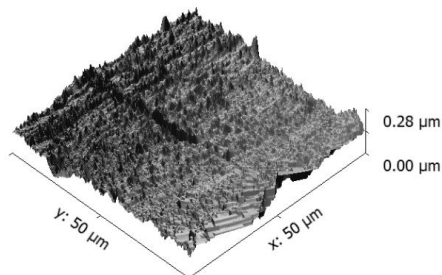
(e) Ti-6Al-4V alloy



(f) Brass



(g) Titanium grade 5

**Figure 15. Hand polished surfaces**

Polishing of metallic surfaces using a hand operated mini rotary device reduced $R_{max-min}$ to < 200nm in a 50 μm^2 area (a to f), but when larger (2500 μm^2) areas (g) were analysed the surface finish was considered inadequate for nano-imprinting.

2.4.1.3 Planarization: Chemical-mechanical polishing mould tools

To improve planarization, chemical-mechanical polishing was undertaken. The protocols were optimised for titanium grade 2 by adjusting the parameters as shown in Table 6. The surface roughness of a silicon wafer is shown as the gold standard target to achieve.

Increased duration of polishing from 5 mins to 30 mins reduced the surface roughness (R_a) from 28.3 nm to 3.0 ± 0.7 nm. Increasing the downward load to 9 psi (maximum) improved R_a (9.9 ± 6.5 nm) compared to 1 psi and 5 psi (50.9 ± 30.4 nm and 14.6 ± 12.5 nm respectively). An increase in both the speed of the carrier and plate from 60/60 rpm to 125/160 rpm and polishing duration from 30 to 60 mins reduced R_a from 3.0 ± 0.7 nm to 2.2 ± 0.1 nm. Increased carrier speed led to increased volume of material removed from the surface. This was observed to cause fouling of the previously polished surfaces and could also lead to unwanted release of the sample from the carrier.

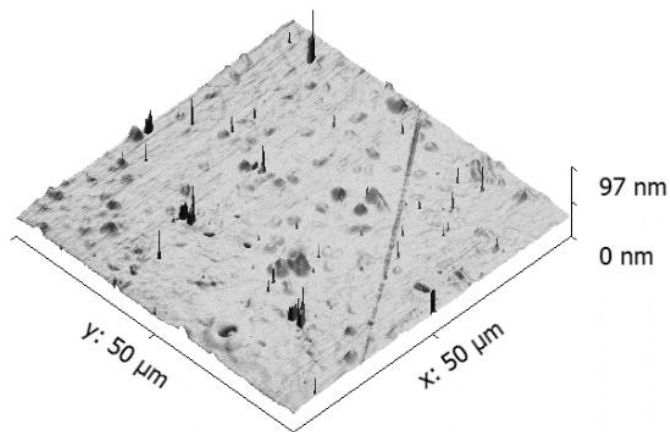
The slurry rate was increased from 50 to 200 mls/min and this did not improve the surface roughness. A 50:50 v/v mixture of SF-1 colloidal slurry and 6% H_2O_2 was used at a rate of 50 mls/min, but the results were noticeably poor with numerous surface defects evident. Once again, the material loss at the surface was excessive and this approach was consequently abandoned.

Protocol 6 (in Table 6) which used a carrier speed of 60 rpm, a plate speed of 60 rpm with a load of 9 psi for 30 mins, and a slurry rate of 50 mls/min was therefore chosen as the preferred method of surface planarization.

Different methods of cleaning the samples after polishing were also trialled (see protocols 6, 9 & 10 in Table 6): A_5 cleaning method (ultrasonic wash in acetone for 5 mins, methanol for 5 mins, isopropyl alcohol for 5 mins, rinsed in deionised water and dried using filtered nitrogen); A_{30} cleaning method (as A_5 but acetone washed for 30 mins instead of 5 mins); and M cleaning method (ultrasonic wash in microposit (97-98% H_2O , 2.45% tetramethylammonium hydroxide) for 5 min before cleaning as per A_5). The use of microposit for cleaning following the CMP (protocol 10 in Table 6) marginally reduced the surface roughness to provide the most planarized surface (R_a 2.5 ± 0.7 nm, RMS 3.8 ± 1.2 nm, and $R_{max-min}$ 120.1 ± 30.2 nm of a $50 \mu m^2$ area of titanium grade 2).

Table 6. Chemical-mechanical polishing of titanium

No.	Carrier speed (rpm)	Plate speed (rpm)	Time (min)	Load (psi)	Slurry rate (mls/min)	Slurry	Cleaning method	R_a (nm)	RMS (nm)	$R_{max-min}$ (nm)
Si	-	-	-	-	-	-	A ₅	2.2 ± 0.9	2.7 ± 1.2	35.1 ± 17.3
1	60	60	20	1	200	SF-1	A ₅	50.9 ± 30.4	89.9 ± 32.6	731.6 ± 214.2
2	60	60	20	5	200	SF-1	A ₅	14.6 ± 12.5	27.8 ± 20.1	720.0 ± 426.4
3	60	60	5	9	200	SF-1	A ₅	28.3	57.9	609.8
4	60	60	10	9	200	SF-1	A ₅	12.7	18.6	284.1
5	60	60	20	9	50	SF-1	A ₅	9.9 ± 6.5	14.3 ± 8.8	253.1 ± 112.2
6	60	60	30	9	50	SF-1	A ₅	3.0 ± 0.7	6.2 ± 2.5	184.6 ± 61.1
7	60	60	30	9	200	SF-1	A ₅	6.9	14.7	509.7
8	125	160	60	9	50	SF-1	A ₅	2.2 ± 0.1	4.03 ± 0.3	151 ± 6.9
9	60	60	30	9	50	SF-1	A ₃₀	15.4	21.4	377.4
10	60	60	30	9	50	SF-1	M	2.5 ± 0.7	3.8 ± 1.2	120.1 ± 30.2



Parameter	Value
R_a	1.48 nm
Rms	2.24 nm
$R_{max-min}$	96.68 nm

Figure 16. CMP polished titanium grade 2

AFM image of Ti polished for 30 mins (protocol 10 in Table 6), then ultrasonically cleaned in microposit for 5 mins, acetone for 5 mins, methanol for 5 mins, isopropyl alcohol for 5 mins, rinsed in deionised water and dried in nitrogen.

2.4.1.4 Surface planarization with titanium dioxide sol-gel

Further attempt at planarization was attempted by using TiO₂ precursor sol-gel on CMP polished titanium grade 2. As shown in Table 7, the use of TiO₂ precursor sol gel (which was also spun and stamped using planar PDMS) did not reduce the surface roughness to a sufficient level appropriate for subsequent nanoimprinting. As the surfaces coated with TiO₂ precursor sol-gel were rougher than the those prepared by CMP alone (R_a 62.8 ± 36.2 vs. 2.5 ± 0.7), the sol-gel was not used as a method of planarization.

Table 7. Surface planarization with TiO₂ sol-gel

<i>Material</i>	R_a	<i>RMS</i>	$R_{max-min}$
<i>Si</i>	2.2 ± 0.9	2.7 ± 1.2	35.1 ± 17.3
<i>Ti</i>	2.5 ± 0.7	3.8 ± 1.2	120.1 ± 30.2
<i>Ti – TiO₂</i>	62.8 ± 36.2	103.8 ± 36.2	756.8 ± 295.1

2.4.2 Nanoimprint lithography of injection mould tools using TiO₂

2.4.2.1 Silicon master nanofabrication

The primary silicon master was reactive ion etched for 196 seconds. Initial post-annealing imprints onto aluminium using this stamp created TiO₂ nanopillars of approximately 67 nm height. Nanopillars of >100 nm were required in order to create bioactive 100 nm deep nanopits in the injection moulded parts, and so the fabrication process was modified.

Subsequent silicon masters were reactive ion etched for 300 seconds to create taller Si pillars (with the intention of making deeper pits in the PDMS stamps), taller TiO₂ pillars and deeper pits in the final polymer). After etching and removal of the chrome mask, Si pillars were 690 nm tall, 135± 3 nm wide at the top and 215± 4 nm wide at the base (Figure 17).

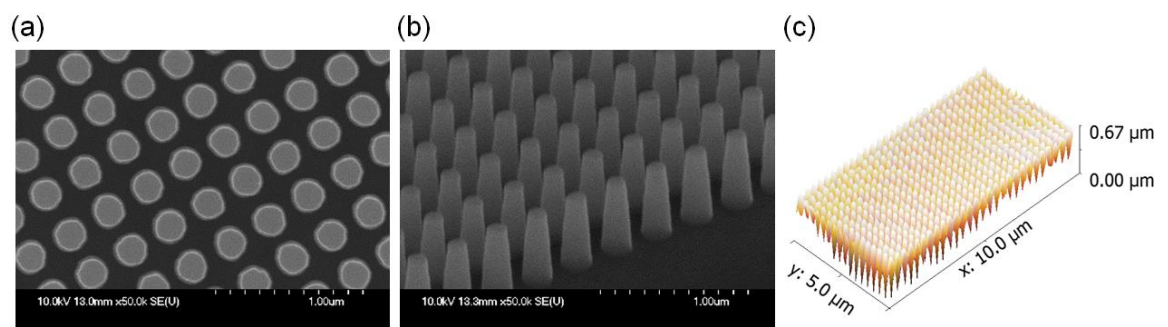


Figure 17. Silicon master nanotopography

SEM images (a) and (b) and AFM image (c) of the 300 s etched silicon master used to create the subsequent nanopitted PDMS stamps.

2.4.2.2 PDMS stamp fabrication

The PDMS moulds cast from the silicon master usually exhibited excellent pattern transfer and pit definition (Figure 8). Initially, the nanopits observed in the PDMS stamps appeared distorted (Figure). This was addressed by using a 1:10 PDMS mixture and curing the PDMS at 90°C to reduce the flexural modulus. Increasing the PDMS curing time, however, created issues with inadequate demoulding of the PDMS stamp from the silicon master (Figure 20).

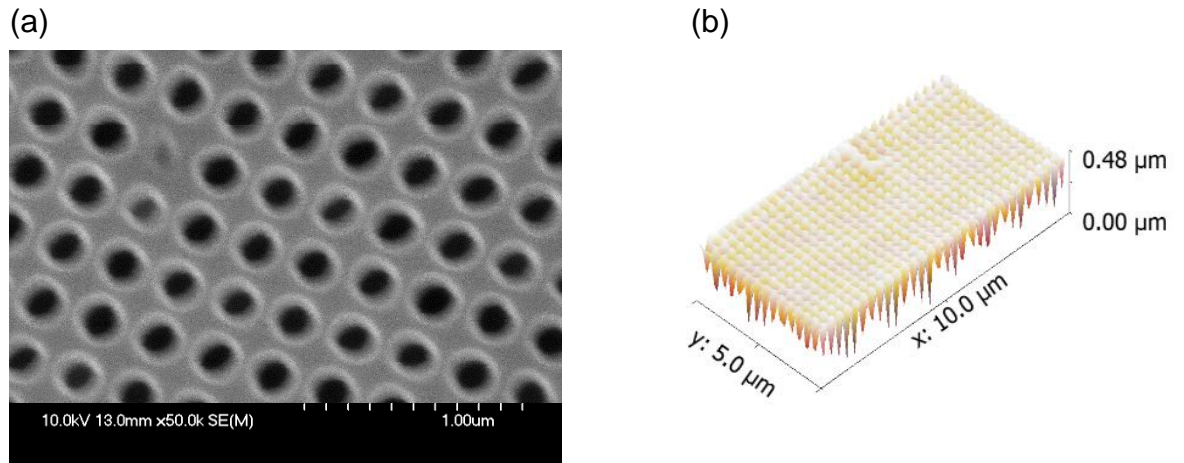


Figure 18. Nanopatterned PDMS stamps

The silicon nanopillars successfully created multiple nanopitted PDMS stamps for subsequent nano-imprinting. The images above show SEM (a) and AFM (b) images of a typical PDMS mould taken from the silicon (300 s) master stamp (Figure 17). SEM and AFM demonstrated successful pattern transfer. The PDMS pit depth appeared to be less than the silicon master pillar height (480 nm, rather than 690 nm).

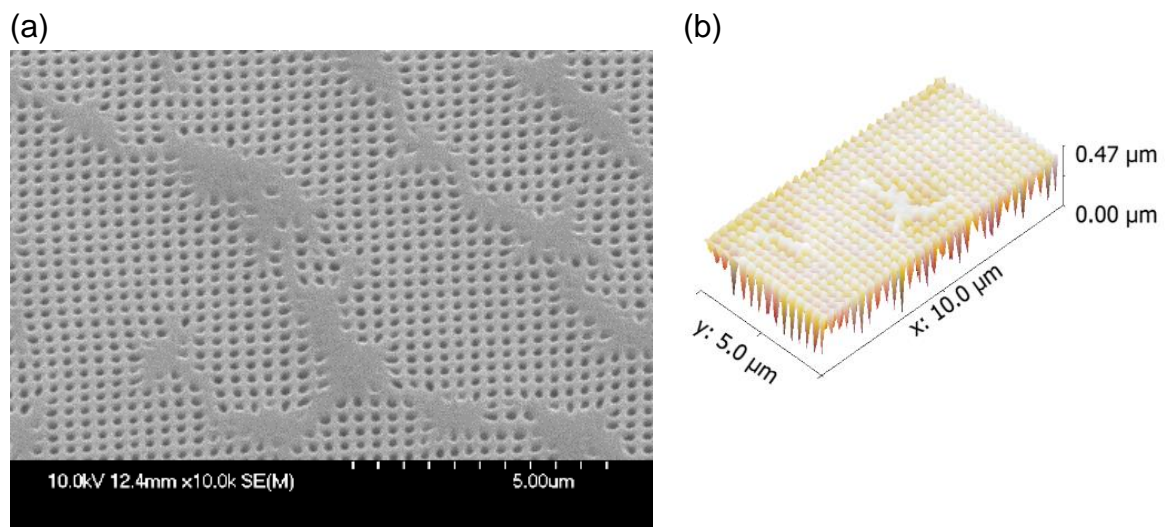


Figure 19. PDMS stamp distortion

This SEM image (a) and AFM image (b) show a re-occurring feature observed in PDMS stamps. Areas that should be covered in nanopits instead show flat, linear, featureless areas in which the opening pores to the nanopits have closed. This feature was more readily apparent when a (softer) 20:1 PDMS mixture was used or when PDMS was cured for reduced times. Improved pattern fidelity was achieved by curing the PDMS for 16 hours at 90°C before demoulding.

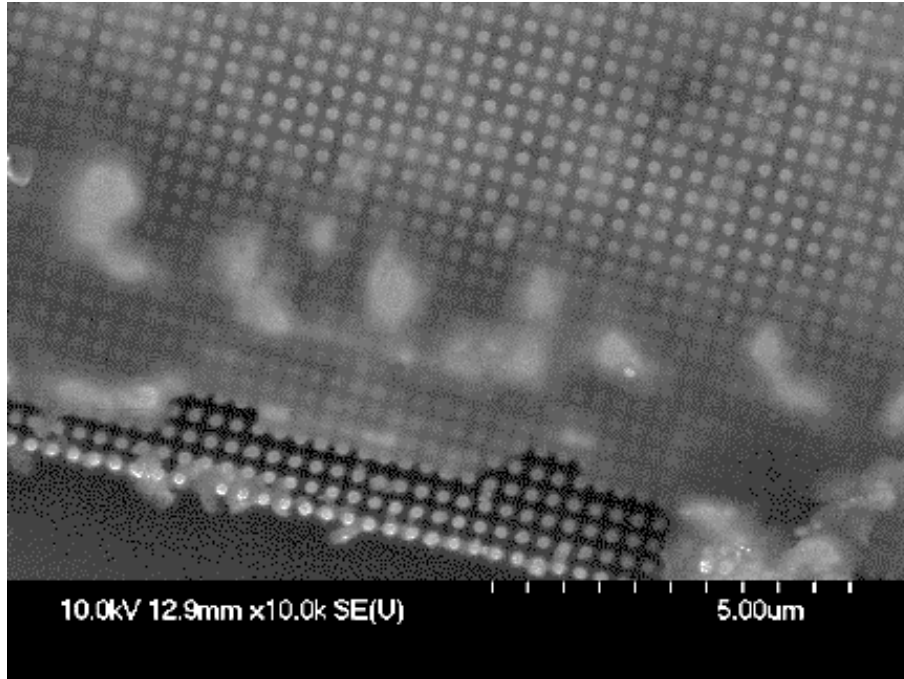


Figure 20. PDMS stamp demoulding

After repeated PDMS mouldings, the fidelity of the nanopattern in the silicon master could become obscured. This appears to be caused by PDMS retention between the Si nanopillars which obscures the nanotopography, as shown in this SEM image, it is likely due to inadequate demoulding causing delamination of the PDMS.

2.4.2.3 Thermogravimetric analysis

Before developing methods for curing and annealing the TiO₂ precursor sol-gel, thermogravimetric analysis was undertaken to better understand the behaviour of this novel nanoimprint resist during heating (Figure 21).

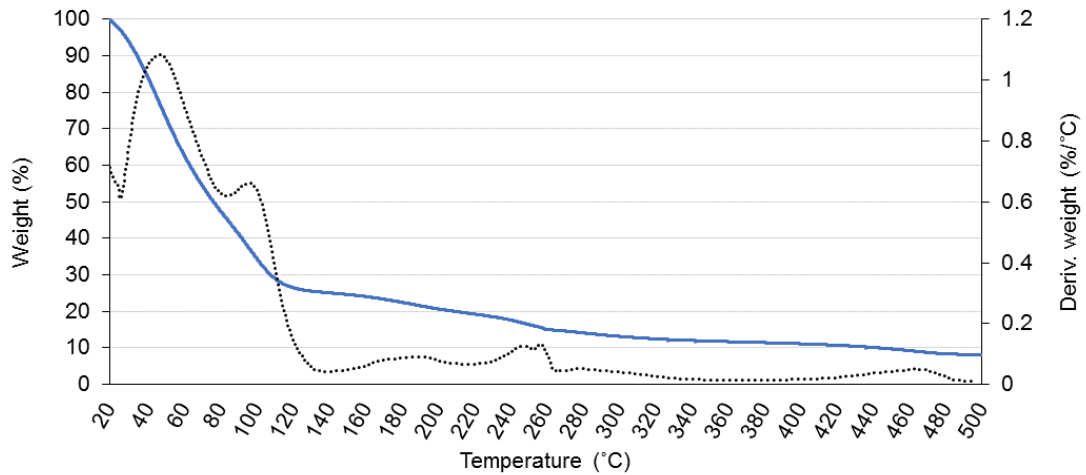


Figure 21. Thermogravimetric analysis of TiO₂ precursor sol-gel

Thermogravimetric analysis of the titanium dioxide precursor sol-gel revealed that it underwent a phase transition at approx. 120°C and approx. 260°C. At 500°C, the sol-gel has lost 91.9% of its initial weight. This suggests that the sol-gel should be cured appropriately at 120°C to permit successful demoulding.

2.4.2.4 Macroscopic pattern transfer

The initial results of nanoimprinting highlighted issues with transfer of the TiO_2 precursor sol-gel from the PDMS stamp onto the tool materials. Large areas failed to transfer and the underlying tool material was visible (as shown in Figure 22 (a)). This suggested an imbalance between adhesion and demoulding, and so, oxygen plasma treatment was used to modify the wettability of the materials in order to enhance adhesion and nanopattern transfer onto the tool materials (Figure 22).

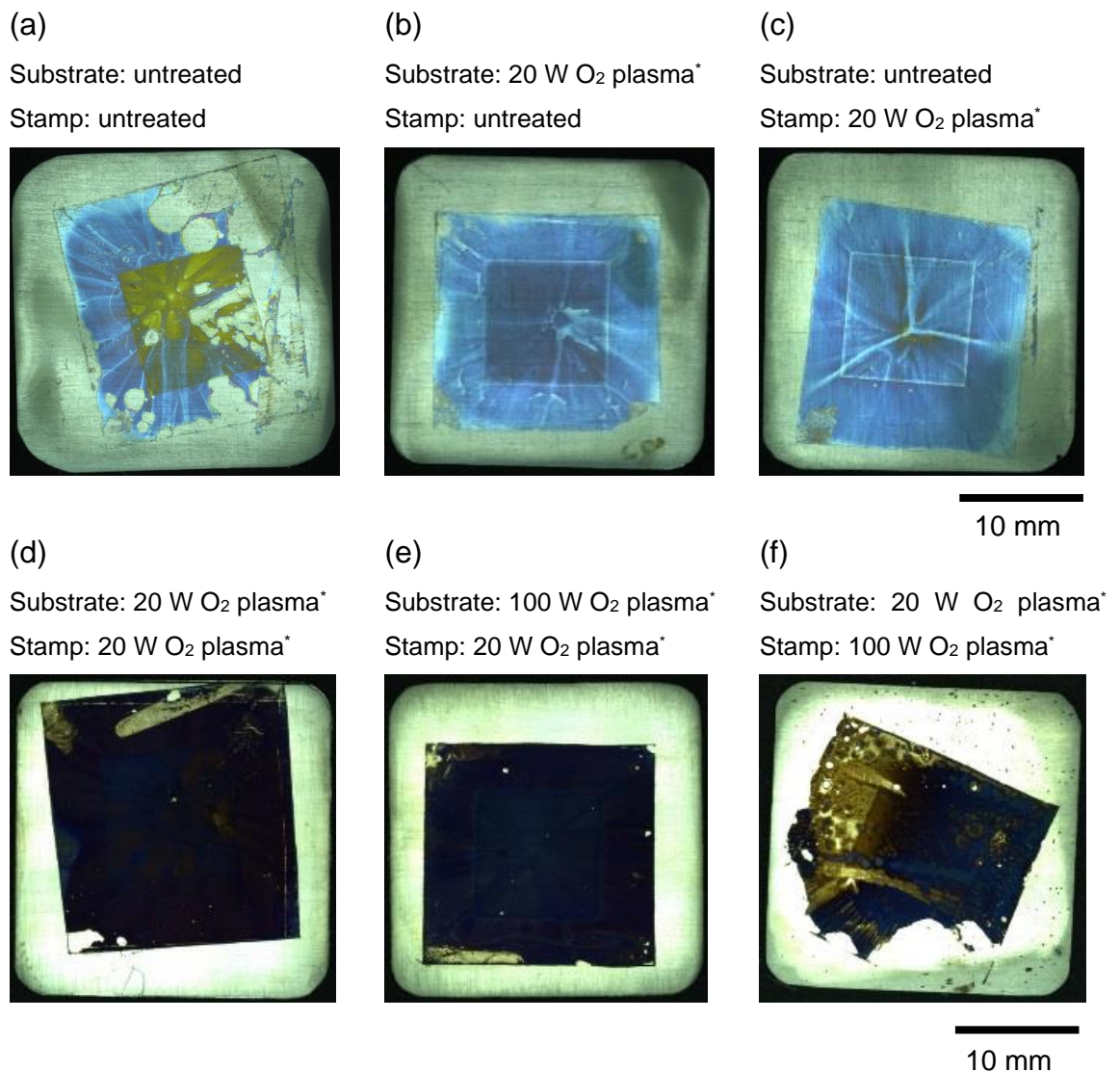


Figure 22. Planar nanoimprinting augmented using O_2 plasma treatment

*All oxygen plasma treatment was conducted at 0.2 mbar for 30 s and the TiO_2 precursor sol-gel was applied to the substrate before being spun. The PDMS stamps were ~ 20 x 20 mm in size with a 10 x 10 mm nanopatterned central area and a planar margin. Macroscopic damage caused by instrumentation during demoulding of the PDMS stamp is observed in (d), (e) and (f). When 100 W O_2 plasma was used on the PDMS stamp (f) it became adherent to the tool material during curing and broke apart during demoulding.

The uniformity of the nanopatterned area was improved by oxygen plasma treatment of either the tool material or the PDMS stamp. This indicated that oxygen plasma treatment influenced nanopattern transfer at the macroscale level.

After demoulding, the nanoimprinted tool materials were annealed in a furnace. This caused unwanted oxidation of the surface in brass and P20 tool steel (Figure 23). Subsequently P20 tool steel was annealed at 300°C to prevent this problem, whilst all other tool materials were annealed at 500°C. Brass tools did not exhibit nanopatterned titania and were not analysed further.

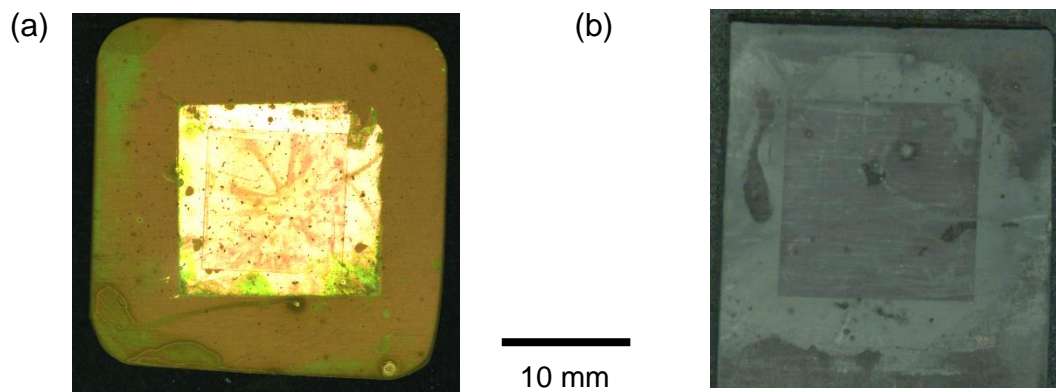


Figure 23. Oxidation of tool materials during annealing

The surface of brass (a) and tool steel (b) became heavily oxidised after annealing at 500°C. Similar results were obtained after reducing the temperature ramp to 1°C/min and annealing in an argon atmosphere. Thereafter, P20 tool steel was annealed at 300°C (1°C/min temperature ramp) to prevent this oxidation reaction.

2.4.2.5 Analysis of TiO₂ nanopatterns on planar mould tools

Aluminium, P20 tool steel, stainless steel, titanium grade 1, and Ti-6Al-4V (also referred to as titanium grade 5 alloy) were successfully patterned with TiO₂ nanopillars (Figure 24).

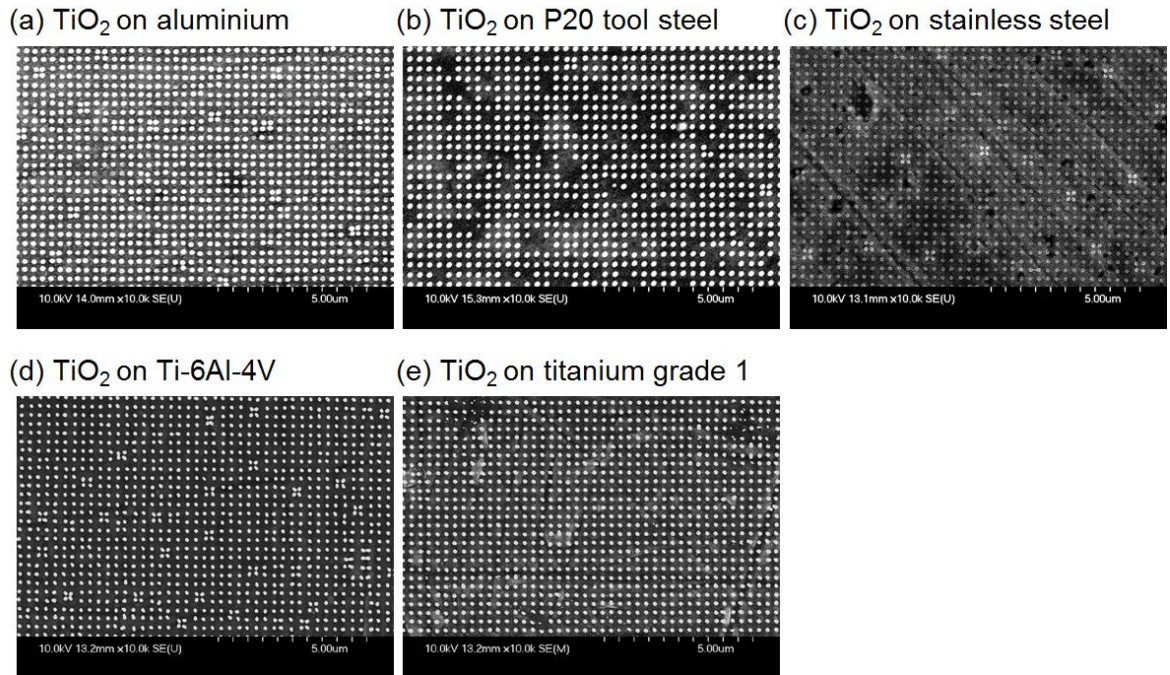
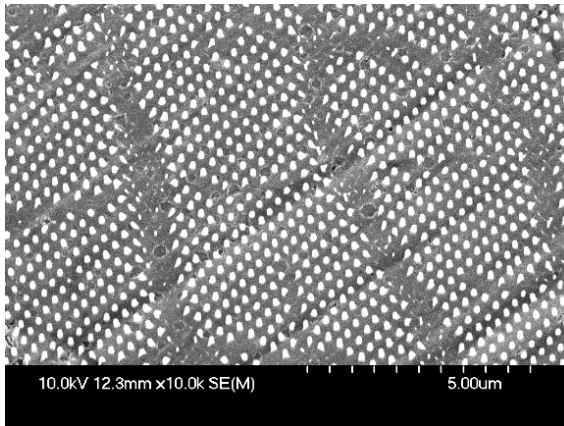


Figure 24. TiO₂ nanopatterns on tool materials

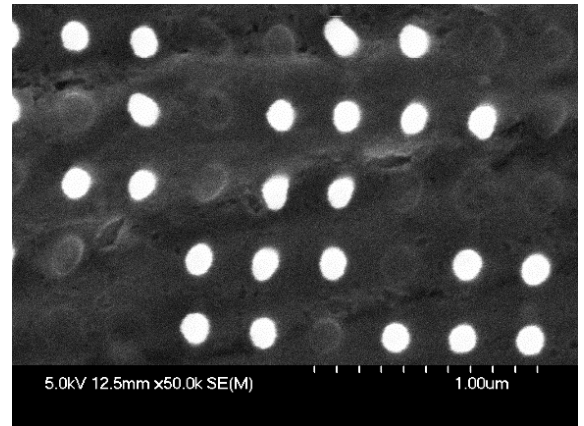
TiO₂ nanopatterns on (a) aluminium, (b) P20 tool steel, (c) stainless steel, (d) titanium grade 1, and (e) Ti-6Al-4V alloy as shown using SEM.

SEM identified areas of defective pattern transfer (Figure 25). These were attributed to PDMS stamp deformation, demoulding problems, or thermal stress cracking caused by annealing. Irregular linear areas lacking nanopillars, approximately 200 nm wide were found on the TiO₂ surface. These were morphologically comparable to those seen in the PDMS mould before nanoimprinting. Furthermore, a 30-degree tilt and demonstrates angled nanopillars adjacent to the linear defect. This suggests that the nanopits within the PDMS mould have collapsed together, closing off the opening of the pits and deviating the position of adjacent nanopits.

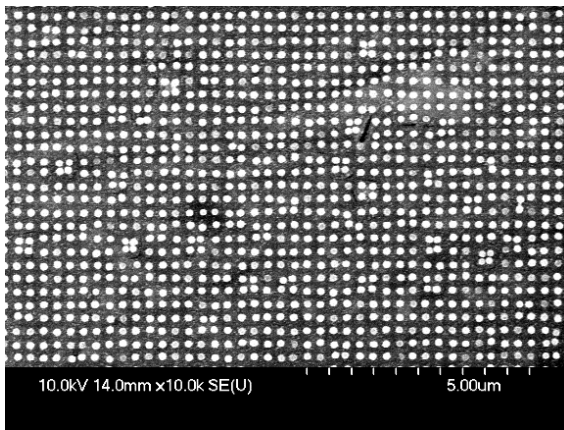
(a) Lines



(b) Missing pillars



(a) Clover leaves



(b) Cracking

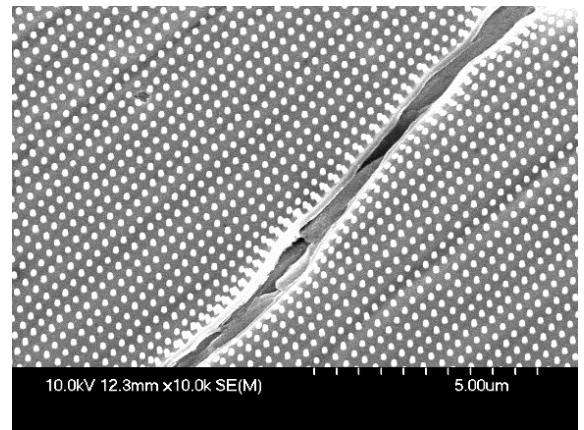


Figure 25. Nanoimprint defects

These SEM images demonstrate defects that were observed in the annealed TiO_2 nanopatterns.

(a) This SEM was taken with a 30-degree tilt and demonstrates angled nanopillars adjacent to the linear defect.

(b) Nanopillars could be removed or significantly reduced in height if the TiO_2 precursor sol-gel pillar remained in the PDMS nanopit after demoulding.

(c) Groups of four nanopillars could merge together to create what resembled a four-leaf clover. This clover leaf deformity was not observed on either the silicon master or the PDMS stamp.

(d) Thermal stress cracking was occasionally observed in the TiO_2 layer caused by annealing.

Absent or short nanopillars were caused by inadequate demoulding in which the TiO₂ precursor sol-gel remained within the PDMS nanopit mould rather than adhere to the substrate.

Groups of four nanopillars were observed merged together to create a structure that resembled a four-leaf clover. This clover leaf deformity was not observed on either the silicon master or the PDMS stamp, which suggested it was caused by adhesion of the unannealed pillars after demoulding.

Cracks were occasionally observed in the TiO₂ layer post annealing. These were attributed to thermal stress cracking and were more prevalent when the sol-gel spin layer was >300 nm pre-annealing.

AFM was then used to determine the height of the nanopillars on each of the different tool materials.

Figure 26 clearly shows that nanopillar height can be increased by spinning the sol-gel onto the PDMS stamp before imprinting on Al, T1, T5 and SS. Furthermore, oxygen plasma treatment of the PDMS stamp increases the post annealed height of nanopillars in all cases, whether the sol-gel was spun onto the PDMS or not. Pillars less than 100 nm in height are unsuitable for use as mould tools in this project.

The quality of the nanopattern transfer was quantified by counting the number of nanopillars that were well demarcated and circular. 100% nanopattern transfers were observed on some tool materials (aluminium and titanium (grade 5) alloy), but most samples sustained a 25-50% of loss of nanopillars (as shown in Figure 26). Each of the four different processes and five different materials exhibited variability in terms of the number of nanopillars successfully fabricated. Spinning the sol-gel onto the PDMS stamps before nano-imprinting resulted in similar levels of pattern transfer compared to spinning the sol-gel onto the substrate first. Overall, the proportion of pillars fabricated onto P20 substrates was less than other the other tool materials.

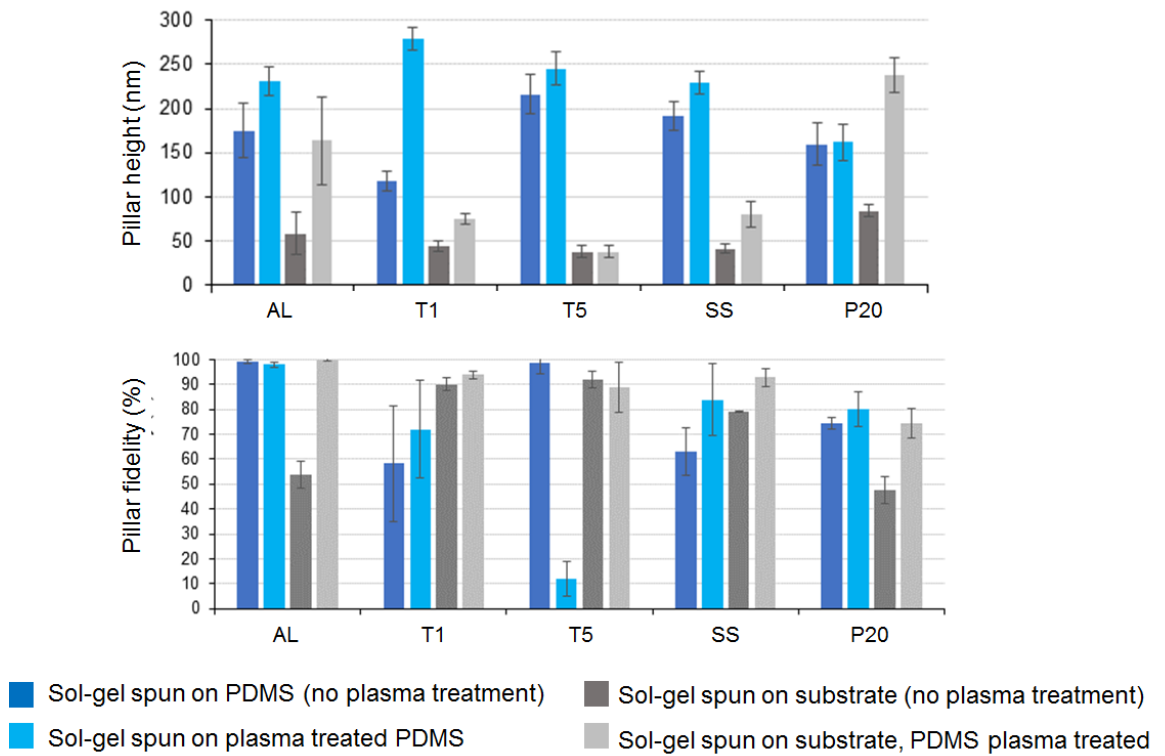


Figure 26. TiO_2 nanopillar fabrication on tool materials

These graphs show the final pillar height and the proportion of pillars successfully fabricated (i.e., pillar fidelity) for each tool material using four different processes. Aluminium (AL), grade 1 titanium (T1), grade 5 titanium alloy (T5) and stainless steel (SS) were annealed at 500°C. P20 tool steel was annealed at 300°C.

2.4.2.6 Analysis of TiO₂ nanopatterns on non-planar mould tools

Once the process had been sufficiently developed on planar tool materials, non-planar mould tools were fabricated in aluminium and nanoimprinted using the TiO₂ precursor sol-gel (Figure).

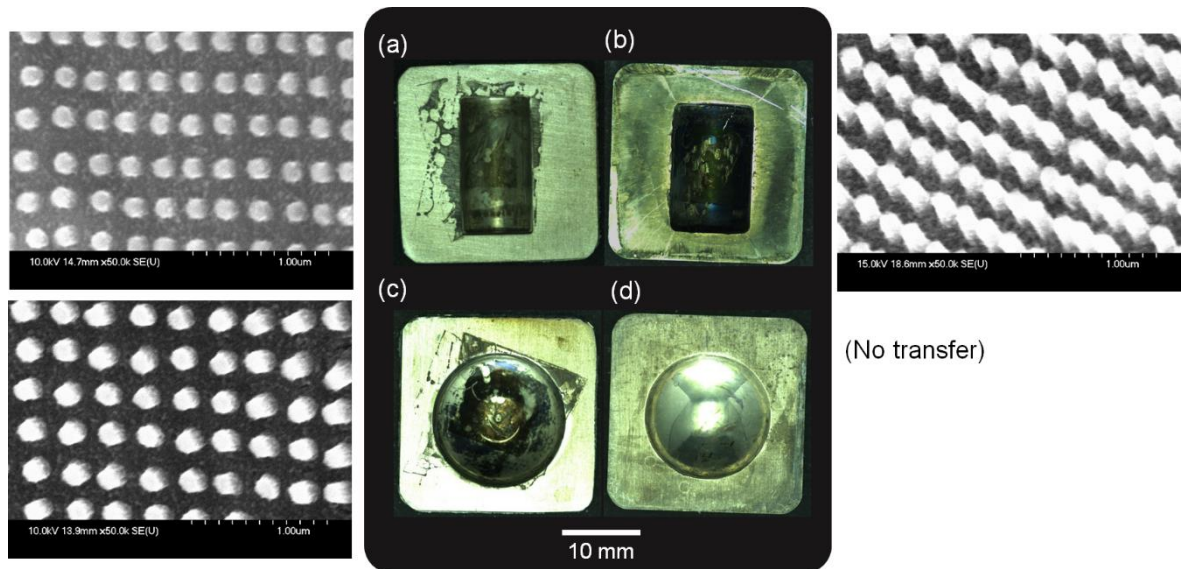


Figure 27. TiO₂ nanoimprinting on non-planar aluminium

The hemi-cylinder (a), and hemisphere (c) were imprinted with a TiO₂ precursor sol-gel coated PDMS stamp. The thin nanopatterned reinforced PDMS stamp was planar, but very flexible. The half-cylinder (b), and hemisphere (d) were imprinted using a non-planar hybrid PDMS stamp after the TiO₂ precursor sol-gel was spun onto the aluminium.

Nanopillars were successfully transferred to the hemi-cylinders (a) and (b) and hemisphere (c) as shown in the SEM images. All these images were taken without tilting the sample; the angle of the nanopillars reflects the slope on which the TiO₂ is patterned. The pattern failed to transfer to the second hemisphere (d).

Handling of very thin PDMS stamps was problematic as they were inherently fragile and had a propensity to tearing when lifted. Thin nanopatterned PDMS stamps were thereafter reinforced with an aluminium foil backing to increase strength and improve handling. Hybrid non-planar PDMS stamps were also produced by placing a thin nanopatterned PDMS stamp (face down) in the base of the aluminium mould and backfilling with PDMS (as in Figure). The resultant non-planar PDMS mould then featured a nanopatterned surface, which improved handling of the stamp, but created unreliable pattern transfer (Figure 27 (d)).

2.4.3 Injection moulding of nanopatterns using TiO₂ imprinted mould tools

Injection moulding was undertaken using TiO₂ nanopatterned mould tools fabricated using nanoimprint lithography. Fifty polymeric parts were moulded using a P20 steel tool (Figure 28) and an aluminium tool (Figure 29). The results from the limited moulding run demonstrated that the titania nanopillars were quickly degraded by the injection moulding process.

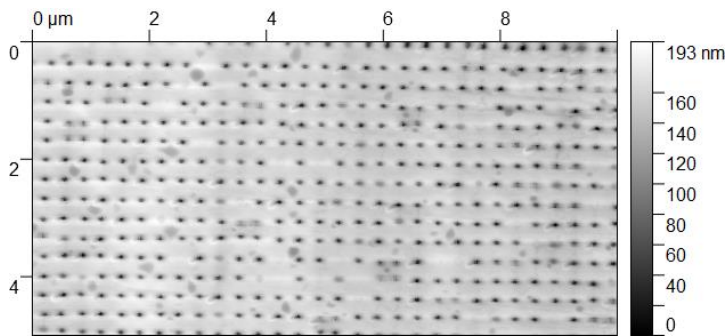


Figure 28. Injection moulding using TiO₂ nanopatterned P20 steel tools

This AFM image of injection mould nanopatterned PC demonstrates translation of the nanotopography. When compared to the original Si nanopattern, nanopits of > 100 nm depth were fabricated in 75.8% of desired positions. The P20 steel mould tool used in this run featured 161.6 ± 20.8 nm nanopillars. The depth of nanopits in the subsequent polymeric nanopattern replicates was 107.6 ± 11.4 nm.

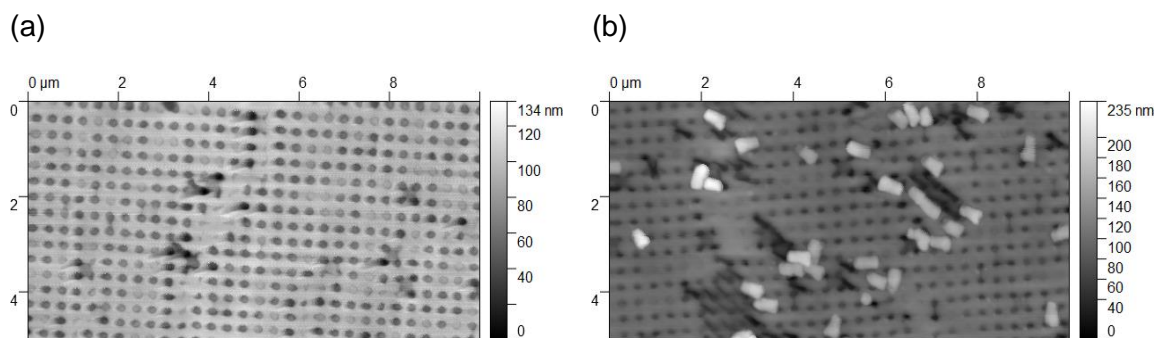


Figure 29. Injection moulding using TiO₂ nanopatterned aluminium tools

These AFM images show satisfactory nanopattern fabrication at the start of the run (a) with > 100 nm depth nanopits successfully formed in 94.2% of the time. Towards the end of the run (b), broken nanopillars became prevalent on the surface and the nanopattern transfer rapidly deteriorated.

2.5 Discussion

2.5.1 Injection mould tool preparation

Preparation of the material surface for nanoimprinting and electron beam lithography is necessary to achieve satisfactory results. Excessive roughness in the surface of the material before nanoimprinting will be translated into the final nanotopography. In this project an $R_{\text{max-min}}$ of < 200 nm was considered the maximum roughness parameter that the TiO_2 precursor sol-gel could cover effectively. The underlying topography following planarization with CMP could still be observed in the nanopatterned titania indicating an inability for this sol-gel to correct nanoscale surface irregularity and the importance of good surface planarization. Increasing the thickness of the TiO_2 precursor sol-gel layer was not undertaken as thermal stress cracking was observed at pre-anneal thicknesses of more than 300 nm.

Aluminium, brass, stainless steel, P20 steel, titanium, and Ti-6Al-4V / titanium (grade 5) alloy were chosen as substrate materials as they were initially considered appropriate for tool making. Aluminium and brass, are relatively soft materials which permitted easy CNC machining, but also predisposed to deformation and a lack of durability when used in the high-pressure environment of the injection moulding machine.

Sheet or plate metal inherently has microtopography introduced by rollers used in the manufacturing process. This research demonstrates that these surfaces can be suitably prepared for nanofabrication by hand polishing. Hand polishing is inexpensive and can be adapted to polish more complex non-planar and three-dimensional surfaces such as mould tools. Chemical-mechanical polishing has the advantages of being completely automated, reproducible and not requiring any manual labour. In our institution, however, it is limited to polishing flat surfaces which was essential for this project.

It was not possible to use the CMP machine for preparing the mould tools as it accepted samples with a maximum height of 2 mm. Thicker mould tools were therefore polished by hand using a rotary felt bob. This led to slight variation in the height of the mould tools from one side to another, which could potentially cause flashing and malfunction in the injection moulding machine.

Magnetic metals deviate the electron beam when used in an electron beam writer or in a scanning beam electron microscope. Materials used in nanofabrication should, ideally, be non-magnetic. The P20 steel used in this project is magnetic, which caused difficulties in obtaining SEM images. Stainless steel is austenitic (also known as a gamma phase non-magnetic allotrope of iron) but can become slightly magnetic due to ferrite and martensite impurities. There were issues obtaining SEM images of titania on stainless steel, but the P20 steel was more troublesome. For nanofabrication purposes, it is also preferable that elemental metals or metalloids are used for the purposes of simplifying the etching process. If an alloy is used (e.g., Ti-6Al-4V) the gases used in the etch process may react differently to the separate Ti, Al and V elements causing them to be removed from the substrate at different rates, causing an uneven finish.

2.5.2 Nanoimprint lithography

2.5.2.1 PDMS nanoimprinting using TiO₂ precursor sol-gel

In nanoimprinting, when a resist layer is applied onto a substrate, if the thickness of this layer does not exceed the maximum peak to trough distance the substrate topography will remain evident following spin coating. Also, if the resist becomes viscous or partially cures at room temperature (a feature common to sol-gels) it may not completely fill the trough features in the tool material. In this project, the TiO₂ precursor sol-gel was applied with a 7 second spin coat at 10,000 rpm. Reduced spin speed or duration created thicker layers of the sol-gel, but these were prone to thermal cracking during annealing.

For the purposes of transferring this technology to three dimensional surfaces, it was initially preferable to spin the Ti sol-gel onto the PDMS mould before using the inherent flexibility of the PDMS mould to conform to a non-planar surface. It is, however, possible to spin the Ti precursor sol-gel directly onto the non-planar substrates before imprinting with the PDMS stamp. The centrifugal forces acting on the sol-gel will increase as the fluid moves away from the rotational axis of spin, made it difficult to create a uniform thickness in this manner. An alternative method could be the deposition of the sol gel by spraying.

The composition of the PDMS mould is essential for a good quality pattern transfer. A PDMS mix of twenty parts base PDMS to one-part cross-linker was initially used to produce a flexible PDMS stamp. The nanopattern, however, was not retained properly due to collapse of the nanopit opening pores caused by the increased flexural modulus of the PDMS. Similarly, this could occur if the PDMS was baked at temperatures below 90°C or for less than four hours.

During the nanoimprinting process, the TiO₂ was occasionally removed with the PDMS stamp during demoulding. This indicated the sol-gel adhered more readily to the nanopatterned area of the PDMS stamp than the mould tools. This resulted in areas on the mould tools that lacked titania coating. Failure of pattern transfer could have also been caused by loss of TiO₂ sol-gel from the PDMS stamp due to liquid run-off as the stamp was being inverted or evaporation in the time period prior to imprinting.

Pattern transfer was improved by using oxygen plasma treatment of the PDMS stamp (to improve stamp wetting and reduce sol-gel run-off) and the tool material (to increase adhesion) thus validating the previous observations.

Distinct colour variation was observed in the titania nanopatterned areas after annealing. Light reflected from the aluminium underlying the sol-gel causes interference with light reflected from the surface. The colour of the titania indicates the thickness and uniformity of the oxide layer of titanium (Figure 30).

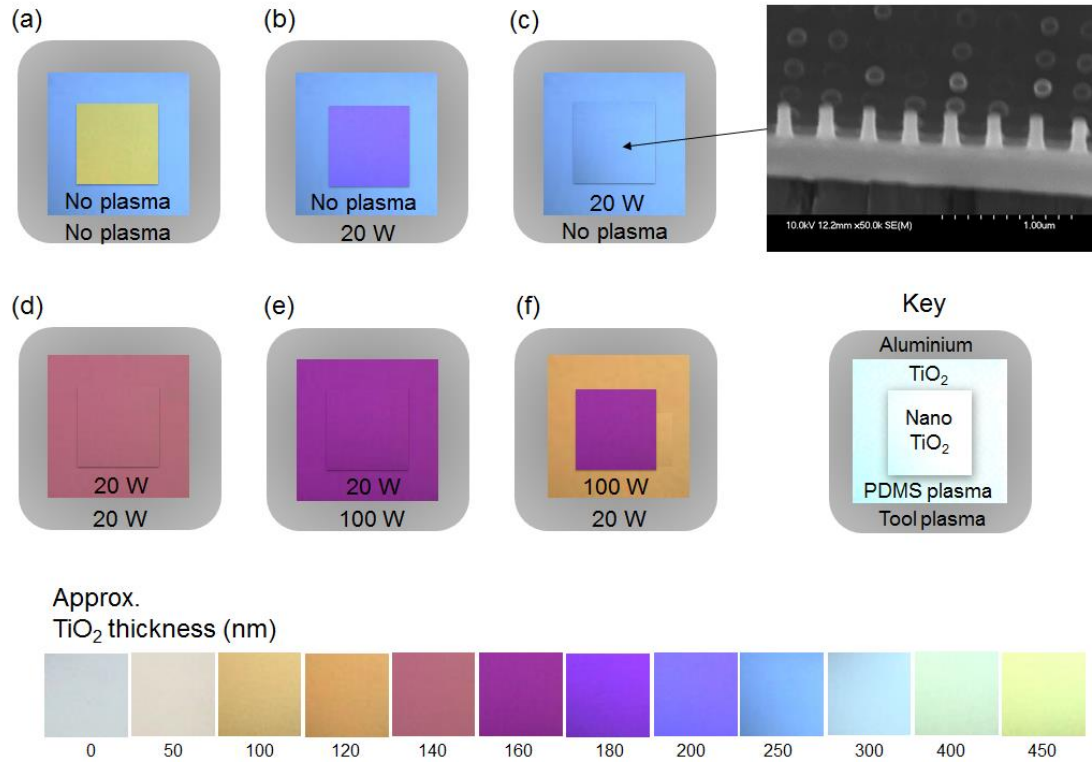


Figure 30. TiO_2 nanoimprinting on aluminium tools

This schematic is an interpretation of the results demonstrated in Fig. 22 and illustrates the effect of oxygen plasma treatment on TiO_2 nanoimprinting of aluminium tools. Plasma was applied to the PDMS stamp and/or the aluminium tool (in the doses shown above). The central area in each diagram (a) to (f) represents nanopatterned TiO_2 and the marginal area is flat TiO_2 .

The samples that demonstrated little colour differential between the nano- TiO_2 and TiO_2 areas (Figure 30(b) to (e)) also exhibited poor nanopattern transfer (as determined by % of nanopillars successfully fabricated). The colour of the TiO_2 can also be used to estimate the thickness of the layer.[195] The annealed thickness of TiO_2 of the samples (Figure 30(a) to (e)) appear to be between 120 and 300 nm according to the known colour variations in titania.[195] This is supported by SEM of (c) shown above which demonstrates a TiO_2 layer (not including the nanopattern) of approximately 300 nm. Samples in which there is a more striking colour differential between the nano- TiO_2 and TiO_2 areas (Figure 30 (a) and (f)) were found to have good nanopattern transfer with nanopillars of approx. 150 nm.

AFM analysis revealed that nanopillar height was increased if the sol-gel was spin coated on an oxygen plasma treated PDMS stamp before nanoimprinting onto the tool material. The increased wettability caused by the oxygen plasma allows the sol-

gel to penetrate deeper into the PDMS pores, increasing the height of the resultant nanopillars. Conversely, oxygen plasma treatment of the metal substrate reduced the height of the nanopillars. This demonstrates that if given one master stamp featuring nanostructures: oxygen plasma treatment can be used to tailor the height (or depth) of titania nanostructures as desired without needing to fabricate a new master.

This work has demonstrated that planar and non-planar tool materials can be successfully nanopatterned with TiO_2 . Two key issues predominate the TiO_2 nanoimprinting process:

Firstly, surface cracking was observed with sol-gel thicknesses of $>300\text{nm}$. This necessitates very small margins of error when considering fabricating large tools. The material to be patterned with TiO_2 must have nominal roughness, which is difficult to achieve in three dimensions.

Secondly, the physical interaction between PDMS, the TiO_2 precursor sol-gel and the metal substrate creates many potential outcomes. Increased wettability of the metal substrate may prevent the sol-gel from entering the pores in the PDMS stamp. Conversely, increased PDMS wettability may break-off nanopillars, or delaminate the sol-gel entirely. Finally, the effect of these nanopatterns on wettability and adhesion is still, as yet, not fully understood.

2.5.2.2 Annealing of TiO_2 nanopatterns

Titanium dioxide has distinct mineral forms which each have different crystal structures: anatase, rutile and brookite. Initially the sol-gel exists in an amorphous state, but as temperature increases (as in annealing) carbon is released, and the proportion of crystalline titanium dioxide will increase.[176] From thermogravimetric analysis (Figure 21Figure), we can extrapolate that carbon is predominantly removed from the amorphous sol-gel at 265°C , permitting the transition to anatase titania.[176] Annealing the sol-gel at 265°C may permit phase transition, whilst maximising nanostructure height and permitting the use of materials (such as PEEK) that have a T_g around 300°C .

As the Ti sol-gel is annealed by heating, it important that the underlying substrate is not inappropriately affected by this process. Metals are readily oxidised by heating and the topography generated by the resultant oxide may have a detrimental effect

on the nanoimprinted pattern. Previous work has identified 500°C as the preferred temperature to completely remove carbon and transition from amorphous to anatase titania.[174] Heating of P20 tool steel and brass to 500°C caused the formation of an oxide layer with microtopography that obscures the nanotopography. Subsequent P20 steel samples were annealed at 300°C, and although the TiO₂ was not fully annealed it successfully injection moulded PC. Aluminium and titanium were not affected by this problem as they spontaneously reactive with atmospheric oxygen and form a thin passivation layer of oxide (~5 nm) which protects against uncontrolled oxidation during annealing.[196, 197]

2.5.3 Injection moulding of nanopatterns

Nanopatterns were successfully fabricated on tools using a novel TiO₂ precursor sol-gel and transferred to polymeric replicates using injection moulding. This represents a proof-of-concept project and further work is required to produce durable mould tools.

During injection moulding PEEK is heated to temperatures approaching 400°C. It was therefore decided to use brass, stainless steel, P20 tool steel, commercially pure titanium, and titanium (grade 5) alloy (Ti-6Al-4V) as they are physically stable at high temperatures. SU-8 has previously been used to rapidly prototype injection mould inlays but it will degrade at 400°C, making it unsuitable for injection moulding PEEK.[198]

Furthermore, the mould tools must be strong enough to cope with the injection pressure applied. Unfortunately, silicon, a favoured substrate for nanofabrication, is susceptible to fracture when using as injection mould inlays or tools. The reduced hardness of aluminium compared to titanium and steel made it very amenable to CNC machining. When subjected to the high pressures within the injection moulding machine, however, the backside of the inlays deformed making aluminium an unsuitable tool material.

For the purposes of tooling and nanofabrication, commercially pure titanium (titanium grade 1) provided the best option as a nanoimprint substrate. Its purity makes it more compatible with nanofabrication processes that involve reactive gases and solvents as the surface is more likely to have a consistent reaction compared to alloyed metals.

3 Surface modification and characterisation of poly-ether-ether-ketone

3.1 Introduction

As a biomaterial, PEEK is considered to be biocompatible and bio-inert.[199] While osteogenesis can occur in anatomical regions near PEEK, direct bone bonding (i.e. osseointegration) does not occur. This enables the formation of a fibrous and flexible interfacial layer which can predispose to unwanted movement of the implant. It is hypothesised that the surface of PEEK can be modified to support mesenchymal stromal cell (MSC) mediated osteogenesis *in vitro*, and this will translate to osseointegration *in vivo*.

Having successfully nanopatterned PEEK using injection moulding, the surfaces will be examined in detail within this chapter and comparisons are made to commercially available PEEK surfaces. Previous cell culture experiments have demonstrated restricted cell adherence of mesenchymal stromal cells (MSCs) to the PEEK surfaces and so further methods of surface modification of PEEK have been explored with the overall aim of creating an osteogenic PEEK surface.

3.2 Aims and Objectives

The aim of this chapter was to characterise the physical and chemical nature of PEEK surfaces.

This would be achieved by analysing the following surfaces:

- Commercially available PEEK implants
- Machined PEEK surfaces
- Injection mould nanopatterned PEEK
- Oxygen plasma treated PEEK
- Oxygen plasma treated and injection mould nanopatterned PEEK
- Injection mould nanopatterned and annealed PEEK

The PEEK surfaces were analysed using the following methods:

- Water contact angle analysis
- Field emission scanning electron microscopy (SEM)

- Atomic force microscopy (AFM)
- X-ray photo electron spectroscopy (XPS)
- Fourier transform infrared spectroscopy with attenuated total reflection (FTIR-ATR)

3.3 Materials and Methods

3.3.1 Fabrication of injection mould nanopatterned PEEK

The PEEK surfaces (LT1 and LT3 Optima, Invibio Biomaterials Solutions Ltd, Thornton-Cleveleys, U.K.) used in the subsequent two chapters were made using electron beam lithography, nickel electroplating, and injection mould nanopatterning.[184, 200] For these nanostructures, the resist was reactive ion-etched into silicon to form an array of 120 nm diameter and 100 nm depth nanopits in a disordered or near-square (NSQ) and an ordered square (SQ) pattern. 50 nm of NiV was sputter coated onto the silicon, and 0.3 mm nickel inlays (with nanopillars) were generated by electroplating (DVDNorden A/S, Denmark). The nickel inlays were cleaned in acetone, IPA, methanol, deionised water, dried using filtered N₂ and inserted into an injection mould tool to create numerous negative copies (with nanopits) using injection mould nanopatterning (Victory 28, Engel GmbH, Schwertberg, Austria). Planar or FLAT PEEK samples were also fabricated to use as controls.

3.3.2 Machining of PEEK

Four commercially available examples of PEEK implants were donated by three different companies (the company identities have not been provided to protect intellectual property rights). A machined PEEK surface used for commercial demonstration was provided by Invibio Biomaterial Solutions Ltd.

Machined PEEK samples were fabricated using a CNC engraving-milling machine (AutoGrav, Wesseling, Germany) and electric milling motor (Kress 1050 FME, Kress-Elektrik & Co GmbH, Germany), at 29,000 rpm with a 2 mm flat milling cutter (YG-1, U.S.A.) at 2 mm/sec feed rate controlled with AutoGrav software. Cutting templates were designed on Rhinoceros 4.0 3D CAD package (Robert McNeel & Associates, U.S.A.) with a madCAM 4.3 plug-in.

3.3.3 Oxygen plasma treatment of PEEK

The PEEK surfaces were plasma treated (PlasmaPrep 5, GaLa Instrumente GmbH, Bad Schwalbach, Germany) at 20°C at 200 W and 0.2 mbar O₂ for 0, 30, 60, 120, 300 or 600 seconds. PEEK substrates were sealed in air-tight containers before use. To assess the long-term stability of oxygen plasma treatment, samples were also stored submerged in deionised water and were analysed for up to one-year post treatment.

3.3.4 Annealing of PEEK

Post process annealing was achieved by heating the samples at the designated temperature (150°C, 200°C, 250°C or 300°C) for 5 mins with a 2°C/min ramp increase.

3.3.5 Surgical application and sterilisation of PEEK

3.3.5.1 Surface cleaning

To investigate the effect that laboratory methods of surface cleaning had upon oxygen plasma treated PEEK surfaces, triplicate surfaces were separately treated with air drying, rinsing in deionised water or ethanol disinfection. Air drying was performed by projecting pressurised filtered room air onto the surface for 10 seconds. Triple filtered Millipore deionised water (Merck Life Science UK Limited, Gillingham, U.K.) or 70% ethanol was used to wash the treated and untreated surfaces by submerging in the fluid for 5 mins before allowing the surfaces to air dry.

3.3.5.2 Steam autoclaving

The substrates were transferred to stainless steel slide holders, sealed into autoclave pouches and steam autoclaved at 134°C for 3.5 mins using the same protocol as NHS Greater Glasgow & Clyde [personal communication].

3.3.5.3 Gamma irradiation

The substrates were sealed in autoclave pouches and transferred to Quality Laboratories, Johnson & Johnson Ltd, Livingston for gamma irradiation using 30 kGy.

3.3.5.4 Surgical handling

For the handling experiments: either a sterile surgical glove (Biogel, Mölnlyke Healthcare Ltd., Oldham) or a sterile non-woven cotton gauze swab (Shermond, Bunzl Retail & Healthcare Supplies Ltd., Middlesex) was placed under a 10 N weight and placed gently onto the test surface for 5 s and removed.

3.3.6 Water contact angle analysis

Water contact angle measurements were taken using a telescopic goniometer with video capture CAM100 software (FTS Technologies/Attension, Manchester, UK) equipped with a Gilmont syringe and a 24-gauge flat-tipped needle. The probe fluid was deionised water purified using a Millipore Milli-Q system (Merck Life Science UK Limited, Gillingham, U.K.). Video capture was used to calculate a mean advancing and receding angle for each drop of water. The mean angle measurements of three separate water drops on different parts of the surface was calculated to give the figures stated in the results.

3.3.7 Scanning electron microscopy

Field emission scanning electron microscopy (S-4700, Hitachi High Technologies America Inc., USA) was also used to characterise the surface topography after sputtering a 9 nm thick AuPd layer.

3.3.8 Atomic force microscopy

Atomic force microscopy (Dimension 3100, Veeco, Cambridge, UK) with a silicon cantilever tip in tapping mode was used to profile the surfaces. In each case at least 3 locations were randomly analysed on at least 3 samples and $5 \times 10 \mu\text{m}$ areas were analysed using Gwyddion 2.26 software to measure surface roughness (R_a , RMS, and $R_{\text{max-min}}$).

3.3.9 X-ray photo electron spectroscopy

X-ray Photoelectron Spectroscopy (XPS) was carried out in a SAGE 100 system (Specs GmbH, Germany). Base pressure in the analysis chamber was approximately 2e^{-7} mbar. The X-ray source was $\text{MgK}\alpha$ operated at an anode voltage of 12.5 kV and 250 W power. Spectra were recorded at a take-off angle of 90° . The pass energy for the hemispherical analyser was 50 eV for survey scans, and 15 eV

for high resolution scans. Spectra were analysed using casaXPS software (Casa Software Ltd., Teignmouth, U.K.), and atomic composition was determined by integration of peak areas using a standard Shirley background. Due to time constraints and technical issues, single measurements were performed at each time point (day 0 and day 42/week 6).

3.3.10 Fourier transform infra-red spectroscopy with attenuated total reflection

Fourier transform infrared spectroscopy with attenuated total reflection (FTIR-ATR) was performed using a Perkin Elmer Spectrum One FTIR Spectrometer with a Universal ATR Sampling Accessory and Spectrum software version 5.0.1 (PerkinElmer, Inc., U.S.A.). The ATR crystal was diamond/thallium-bromiodide (C/KRS-5) with a penetration depth up to 2 μm . The exposed diameter of the crystal was 1.33 mm giving a sample area of around 1.39 mm^2 . 32 scan accumulations were used at a resolution of 4 cm^{-1} .

3.4 Results

3.4.1 Commercial PEEK implants and machined PEEK

Analysis of the surfaces of commercially available PEEK spinal implants revealed a micro rough surface, with no discernible machining marks (such as the grooves observed in the samples (e) and (f) (Figure 31), suggesting that they had undergone further processing.

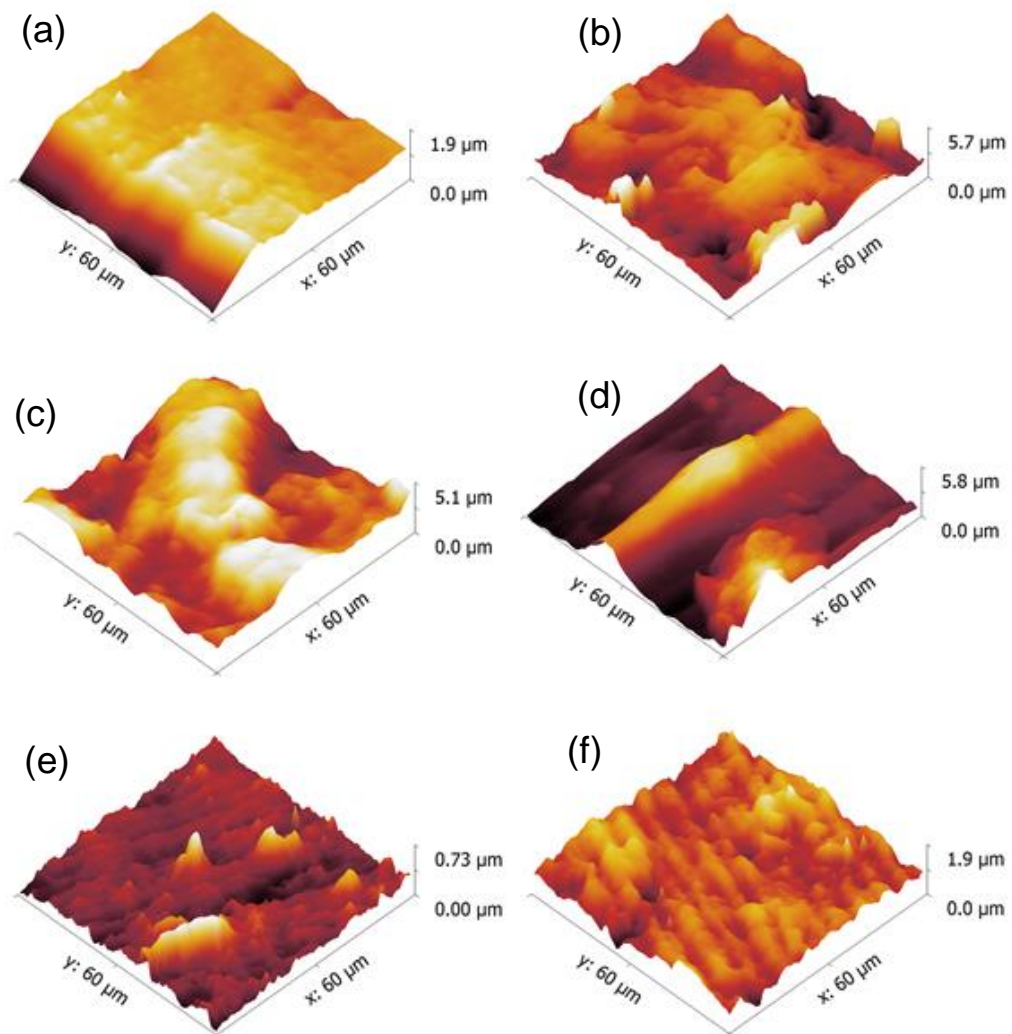


Figure 31. AFM analysis of spinal implants and machined PEEK

The AFM images (a) to (d) demonstrate the surface topography of commercially available PEEK implants designed for spinal applications and currently used clinically in the EU. A PEEK surface provided by Invibio Biomaterial Solutions Ltd. is shown in (e). The surface shown in (f) was fabricated by CNC milling for this project.

The roughness parameters indicated increased surface roughness compared to simple machining (Table 8).

Table 8. Topographic analysis of PEEK spinal implants and machined PEEK

	<i>Implant</i> A	<i>Implant</i> B	<i>Implant</i> C	<i>Implant</i> D	<i>Machined</i> A	<i>Machined</i> B
R_a (nm)	280 ± 53	751 ± 37	461 ± 265	646 ± 252	335 ± 7	288 ± 179
RMS (nm)	390 ± 81	937 ± 59	596 ± 276	797 ± 305	422 ± 19	356 ± 219
$R_{max-min}$ (µm)	3.3 ± 1.5	5.5 ± 0.2	4.5 ± 0.7	4.5 ± 1.1	2.7 ± 0.6	2.6 ± 1.0
$Area$ (µm ²)	3685 ± 37	4380 ± 421	3829 ± 33	3885 ± 228	3851 ± 66	3771 ± 97

3.4.2 Oxygen plasma treated and nanopatterned PEEK

3.4.2.1 Water contact angle analysis of oxygen plasma treated and nanopatterned PEEK

NSQ and SQ nanopatterned PEEK samples were assessed, and compared to FLAT and machined PEEK using water contact angle analysis. This revealed that FLAT and NSQ PEEK had similar advancing water contact angles (AWCA) ($93.0^\circ \pm 4.3^\circ$ and $92.4^\circ \pm 3.5^\circ$ respectively) and receding water contact angles ($49.7^\circ \pm 8.3^\circ$ and $48.3^\circ \pm 4.3^\circ$ respectively). SQ nanopatterned PEEK had an increased AWCA ($99.1^\circ \pm 3.0^\circ$) and similar receding water contact angle ($47.9^\circ \pm 6.0^\circ$). Machined PEEK had the highest advancing water contact angle ($108.7^\circ \pm 3.1^\circ$) and lowest receding water contact angle ($23.2^\circ \pm 4.5^\circ$).

When samples were analysed over 12 weeks, it became apparent that hydrophobic recovery occurred in the oxygen plasma treated surfaces (Figure 32). These results were derived from the testing of the same samples and demonstrate that the wettability of PEEK following oxygen plasma treatment diminishes with time (and testing).

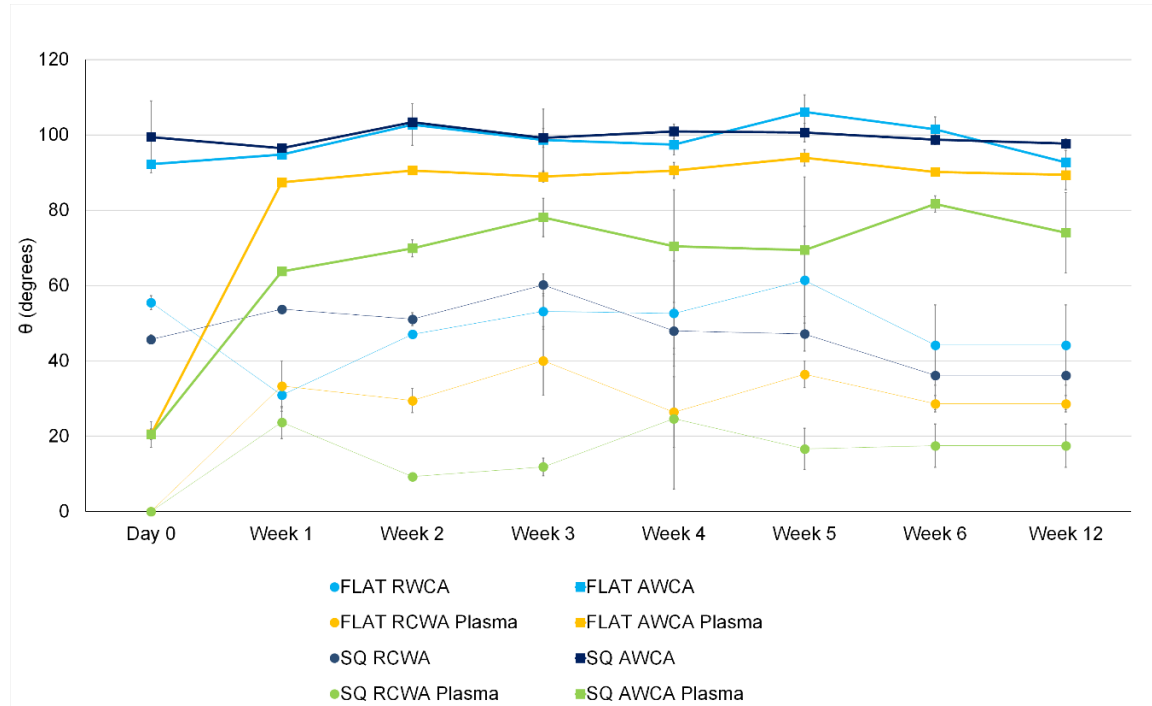


Figure 32. Hydrophobic recovery of oxygen plasma treated PEEK

This graph depicts the change in advancing (AWCA) and receding (RCWA) water contact angles on FLAT and SQ PEEK with time following 2mins of oxygen plasma treatment compared to untreated PEEK. At the end of the 12-week period of this experiment the oxygen plasma treated samples remained relatively more hydrophilic than the untreated samples.

As before, untreated FLAT and SQ PEEK have a similar AWCA. Interestingly, there is a trend towards SQ nanopatterned PEEK retaining a more hydrophilic nature 2 to 12 weeks following oxygen plasma treatment (and successive testing) compared to the equivalent FLAT samples.

It has been determined that oxygen plasma treatment exerts both a topographical and chemical change in PEEK. The chemical change can be monitored using water contact measurements and these measurements have been observed to change with time. For oxygen plasma treatment to be) (considered as a potential surface treatment for surgical implants it is essential to develop further understanding of how the chemical effect of the treatment is affected by other factors involved in manufacturing, sterilization and surgical implantation. Therefore, water contact angle measurements were performed before and after cleaning, sterilizing and handling the surfaces to determine whether these processes affected the chemical

effect of oxygen plasma treatment. Figure 33 illustrates that the use of compressed air, sterilizing with gamma irradiation and contact with surgical gloves has little effect on the advancing water contact angle. Washing with deionized water or ethanol, autoclave sterilization and contact with a gauze swab induced hydrophobic recovery i.e., reversed the chemical effect of oxygen plasma treatment.

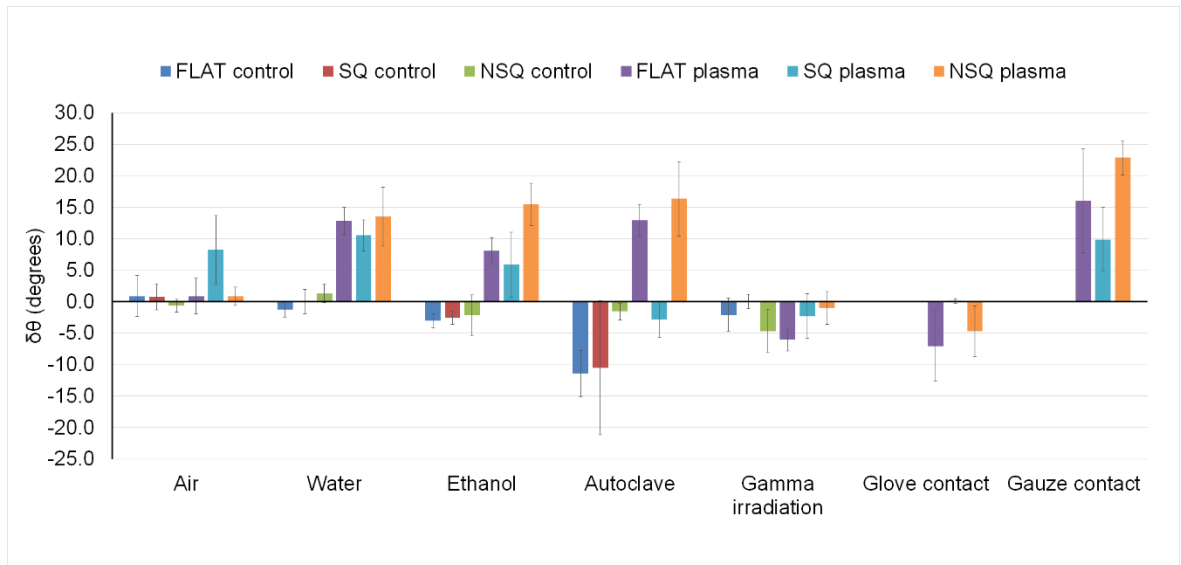


Figure 33. The effect of cleaning, sterilization and handling on oxygen plasma treated PEEK

This graph shows whether hydrophobic recovery of oxygen plasma treated FLAT, NSQ and SQ nanopatterned PEEK was induced by different methods of cleaning, sterilization and surgical handling.

3.4.2.2 AFM analysis of O₂ plasma treated PEEK nanopatterns

Planar samples of injection moulded PEEK were treated with oxygen plasma treatment (200 W at 0.2 mbar) for 120, 300 or 600 seconds and compared using AFM. The results show that there was negligible increase in the R_a (1.8 ± 1.1 for untreated PEEK, compared to 3.7 ± 2.6 for 120 s and 2.1 ± 0.5 300 s oxygen plasma treated samples). Oxygen plasma treatment created peaks and valleys of approximately 20 nm height and depth upon the previously planar surfaces (Figure 34).

Nanopits had a mean depth of 67 nm, with an opening width of 158 nm and base width of 58 nm (Figure 34). Oxygen plasma treatment for 60 s or more resulted in decreased depth, increasing opening width and increased base width. This also had the effect of reducing the area between the nanopits.

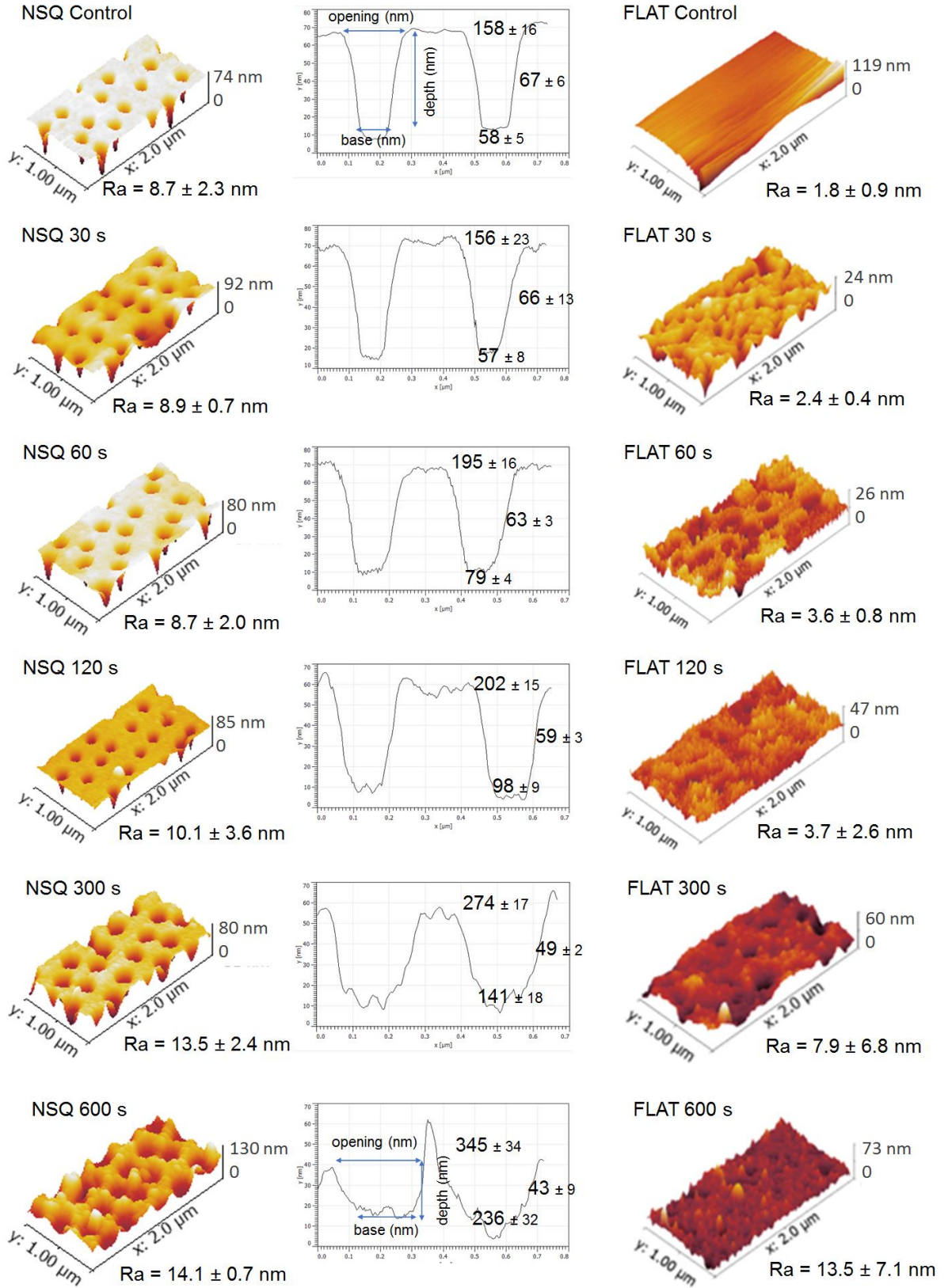


Figure 34. AFM analysis of O₂ plasma treated PEEK nanopatterns

AFM analysis demonstrates the marked effect of oxygen plasma treatment on planar and nanopatterned PEEK surfaces.

3.4.2.3 XPS analysis of O₂ plasma treated nanopatterned PEEK

The XPS data derived from the wide-scan survey spectra for PEEK shows that oxygen plasma treatment increases the atomic percentage of oxygen (at. % O₂) at the surface. 30 seconds of plasma treatment increased at. % O₂ from 12.9% to 19.9%. and the maximum at. % O₂ was detected on the sample treated for 600 seconds (Figure 35).

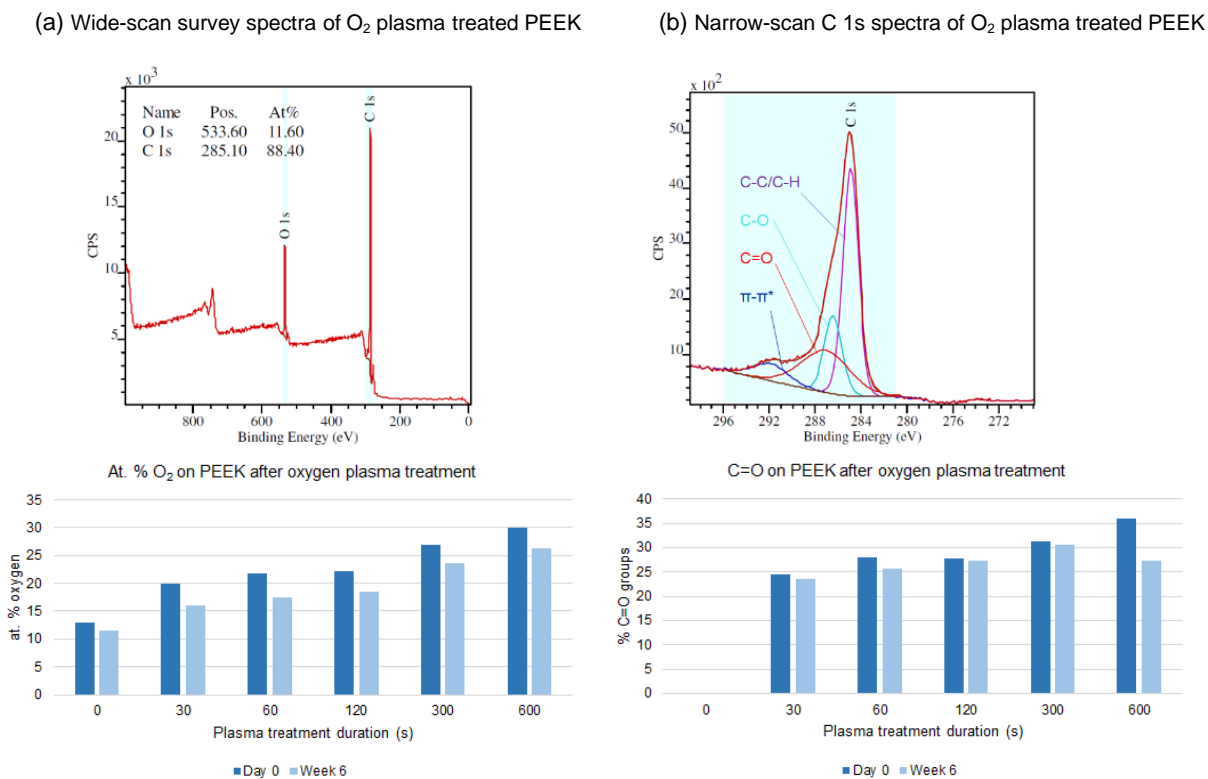


Figure 35. Atomic percentage of oxygen and C=O on plasma treated PEEK

X-ray photoelectron spectroscopy surveys of oxygen plasma treated nanopatterned PEEK demonstrated that oxygen plasma treatment increased the at. % O₂ and carbonyl/diether (C=O) binding. SD for each time point are not shown as single measurements were performed. Results are provided to illustrate the trend observed.

After 6 weeks in dry storage the at. % O₂ decreased in all samples, but still remained higher than untreated PEEK (Figure 35). The data from the narrow-scan spectra (Appendix) provides the proportion of carbon atoms at the surface that are bound as hydrocarbons, alcohols or carbonyl groups. Oxygen plasma treatment increases the percentage of carbonyl (C=O) groups from 17.6% up to 36.0% after 600 seconds (Figure 35). Oxygen plasma also causes a decrease in the π - π^* shake-up satellite after 120 seconds of treatment (Appendix). Full recovery of this feature occurred on

the 120 s and 300 s samples after 6 weeks of dry storage and partial recovery occurred on the 600 s plasma treated PEEK surface.

3.4.3 Annealed nanopatterned PEEK

PEEK was annealed to determine the effect of temperature upon the nanotopography (Figure 36) and ATR-FTIR was used to assess changes in surface crystallinity (Figure 37) .

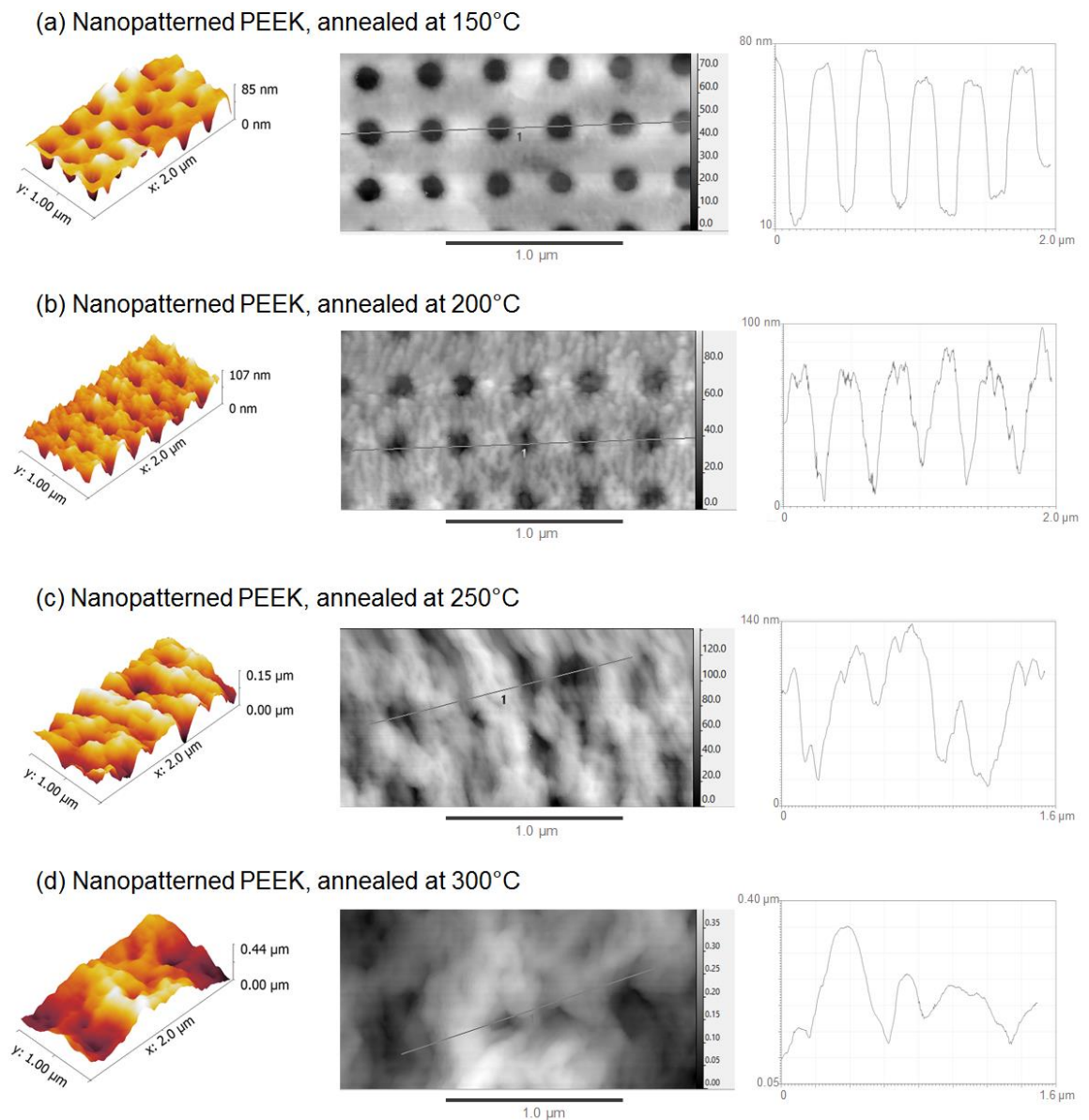


Figure 36. AFM analysis of annealed nanopatterned PEEK

Nanopatterned PEEK was annealed at (a) 150°C, (b) 200°C, (c) 250°C, and (d) 300°C for 5 mins. AFM analysis shows that no discernible surface modification occurs at 150°C (a). At 200°C (b) the surface appears roughened, but the pit topography remains intact. At

250°C (c) there is loss of the distinctive nanopattern, although some pits are retained. At 300°C (d) PEEK is beginning to melt, with complete loss of nanofeatures.

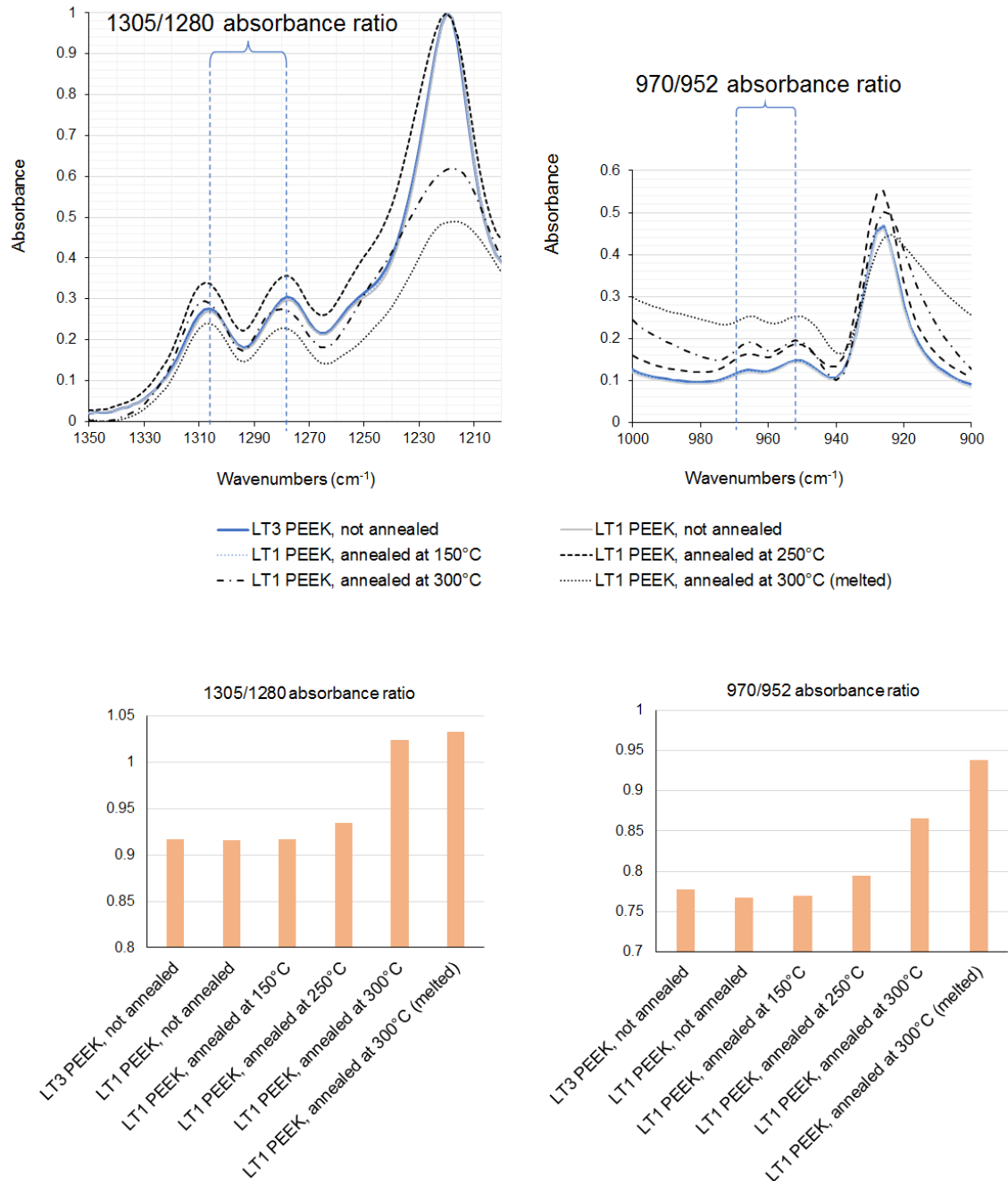


Figure 37. Absorbance ratio vs. PEEK crystallinity

The absorption ratios derived from ATR-FTIR spectral bands can be extrapolated to determine the crystallinity of PEEK when compared to WAXS data (as per the Chalmers method (**Error! Reference source not found.5**)). The complete ATR-FTIR spectral bands are shown in the Appendix.

ATR-FTIR was performed on injection moulded LT1 (standard viscosity) and LT3 (low viscosity) PEEK. The spectra (Figure) illustrates difference between the un-annealed and annealed PEEK samples. The changes in the intensity of the absorbance peaks at 1305 cm^{-1} , 1280 cm^{-1} , 970 cm^{-1} , 965 cm^{-1} , and 952 cm^{-1} are evidence of increased crystallinity of PEEK.[72, 201, 202] Figure 37 also demonstrates how annealing PEEK is associated with changes in the relative intensity of absorbance bands $1305\text{ cm}^{-1}/1280\text{ cm}^{-1}$ and $970\text{ cm}^{-1}/952\text{ cm}^{-1}$ which indicated an increase crystallinity in samples annealed at 250°C or more.

3.5 Discussion

Surface analysis of the PEEK implants demonstrated that the surface of the commercial implants had been roughened after machining, but they exhibited no nanotopography. Nanopatterning of PEEK in this project was successfully achieved by injection moulding using nanopatterned nickel inlays. The TiO_2 sol-gel inlays fabricated previously in this project did not produce satisfactory replicates.

Oxygen plasma treatment of PEEK created hydrophilicity which diminished with time; until, a moderately hydrophilic or meta-stable situation developed (Figure). This occurs due to alterations in the free energy available at the surface and relates to atomic changes which were identified using XPS. Although significant topographical changes were observed in the nanopatterns, these (according to popular theories) were not capable of causing the dramatic changes observed in surface wetting.

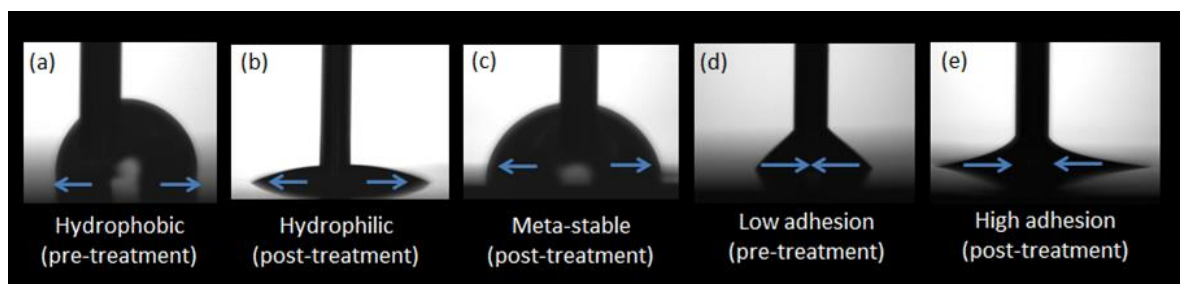


Figure 38. Plasma treatment effect on PEEK wettability

The effect of oxygen plasma on surface wetting is shown with the AWCA ((a) to (c)). The receding contact angle measures solid-liquid adhesion and is measured by withdrawing the

water drop ((d) and (e)). This is a dynamic measurement and the arrows indicate the direction of water movement.

Modifications of Young's equation by Cassie & Baxter and Wenzel are often used to predict the water contact angle of a porous or rough surface.[203-205] Recent authors refer to the advancing or receding fluid-solid-vapour (i.e., triphase) interface as a dynamic boundary line rather than one dictated by the already wetted surface.[206-208] This allows for the concept of line tension caused by nanoscale features which cause apparent 'pinning' of the tri-phase interface.[208] Disruption of this tri-phase balance may explain why NSQ patterned PEEK does not follow the recognised models of surface wetting. Early attempts at injection moulding demonstrated that insufficient heating led to amorphous rather crystalline PEEK. Furthermore, injection moulded low viscosity LT3 PEEK was lighter and therefore 'appeared' more crystalline. Annealing (i.e., heating above the glass transition temperature (143°C for PEEK)) was used to increase the crystallinity of PEEK as this could potentially improve the surface characteristics for stromal cell culture.

ATR-FTIR showed a marginal increase in the crystallinity at 250°C, but 300°C was required to effect a significant change (**Error! Reference source not found.36**). At 300°C a shift in the carbonyl stretching frequency from 1653 cm⁻¹ (typical of amorphous PEEK[209]) to 1648 cm⁻¹ (typical of crystallised PEEK was observed).[201]

The degradation response of PEEK nanostructures to increasing temperature has not previously been demonstrated. Nanostructures were retained up to 200°C, but at 250°C pattern fidelity was lost (Figure). The degradation of the PEEK nanostructures coincided with the increase in crystallinity, which demonstrated that annealing could not be used as a method of modifying nanopatterned PEEK.

The use of ATR-FTIR confirmed that it could be employed in a rapid and non-destructive manner as a quality control device if surface crystallinity was essential for the normal function of the product.

4 Quantifying osteogenesis on PEEK

4.1 Introduction

In this chapter, the PEEK surfaces modified by injection mould nanopatterning and oxygen plasma treatment as described in Chapter 3 are assessed by directly culturing MSCs on the surfaces and analysing for the products of osteogenesis.[1, 3] *In vitro*, MSCs will not synthesise bone tissue, but will potentially differentiate into osteoblasts which exhibit characteristic gene markers and produce bone mineral.

Due to the auto-fluorescent nature of PEEK, histological stain reaction was used to assess for markers of osteogenesis, and quantitative reverse transcriptase polymerase chain reaction qRT-PCR experiments were performed to assess the relative expression of stromal cell marker genes to characterise their behaviour and phenotype.

The MSCs are isolated from the proximal femoral bone marrow cavity of humans undergoing hip replacement surgery. Mononuclear cells are isolated from the bone marrow samples using Ficoll density gradient and cultured onto tissue culture polystyrene. The adherent cells are considered osteoprogenitor cells or mesenchymal stromal cells and the non-adherent cells are discarded.[210] As this cell population is potentially heterogeneous and, in an effort to reduce variability between patient donors, commercially available Promocell MSCs were used for the qRT-PCR experiment.

Osteogenesis is a dynamic process involving the temporal regulation of gene expression in the first 7-20 days, before mineralisation is observed from approximately day 28.[211] It was therefore decided to assess for gene expression on day 14 and mineralisation on day 42.

4.2 Aims and Objectives

The aim of this chapter was to explore and optimise the bioactivity of oxygen plasma treated injection mould nanopatterned PEEK by assessing MSC mediated osteogenesis using quantifiable methods.

This was achieved by using the following objectives:

- Culture MSCs on nanopatterned PEEK surfaces for 6 weeks using five different oxygen plasma treatments to optimise the protocol;
- Assess the validity of Alizarin Red S stain (ARS) and von Kossa stains by co-localising calcium to ARS stained particles and phosphate to von Kossa stained particles using Energy-dispersive X-ray Spectroscopy (EDS);
- Use Alizarin Red S stain (ARS) to identify calcium particles on surfaces and quantify them using microscopy and image analysis software;
- Surfaces will be assessed for % coverage of surface by cells, cell number, and calcium expression;
- Use Von Kossa stain to identify phosphate particles on surfaces and quantify them using microscopy and image analysis software as above;
- Culture MSCs on nanopatterned PEEK surfaces for 6 weeks using the preferred oxygen plasma treatment protocol and analyse using ARS and von Kossa stains.
- Culture MSCs on hydrophobic (untreated), hydrophilic (plasma treated that day) and metastable (aged following plasma treatment) PEEK surfaces for 6 weeks and analyse using ARS and von Kossa stains;
- Culture MSCs on PEEK surfaces for 2 weeks and assess an array of MSC gene expression markers using qRT-PCR.

4.3 Materials and Methods

4.3.1 Fabrication of injection mould nanopatterned PEEK

The nanopatterned nickel master inlays (NSQ, SQ, and HEX) were fabricated using electron beam lithography and electroplating in a previously described technique (Figure).[200] FLAT samples were also fabricated to provide control surfaces as shown in Figure 39. Injection mould nanopatterned PEEK surfaces were produced using PEEK Optima LT1 (standard viscosity) (Invibio Biomaterials Solutions Ltd., Thornton-Cleveleys, UK) and oxygen plasma treated as previously described. PEEK substrates were disinfected with 70% (v/v) ethanol and dried with filtered compressed air before being used for cell culture.

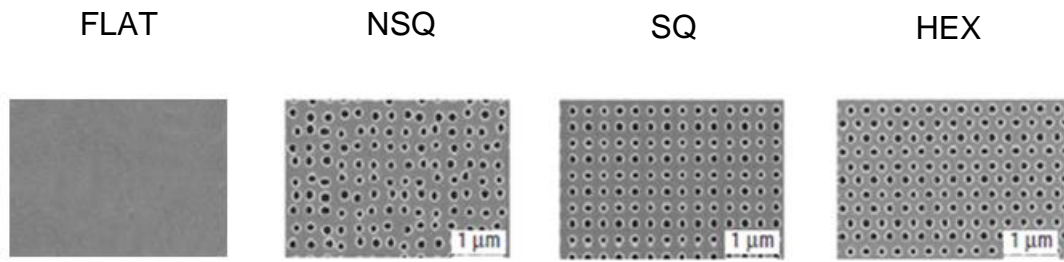


Figure 39. Ordered and disordered nanopatterns

This shows the nanopatterned nickel inlays used in this chapter: FLAT (planar at the nanoscale), NSQ (near-square pattern), SQ (ordered square pattern) and HEX (hexagonal pattern). The pillars were 120 nm in diameter and 100 nm high, with a mean centre-centre distance of 300 nm in all patterns. (Image adapted from [1]).

4.3.2 Human bone marrow stromal cell isolation and culture

Human bone marrow cells were harvested from the proximal femur of patients undergoing primary hip replacement operations at the Southern General Hospital (NHS Greater Glasgow & Clyde), Queen Elizabeth University Hospital (NHS Greater Glasgow & Clyde) and the Golden Jubilee National Hospital (NHS National Waiting Times Centre) following appropriate Ethical Approval and documented informed patient consent. After broaching the proximal femoral canal, bone marrow was collected in a 20 ml syringe and transferred to a container with 20 ml of transfer medium.

Transfer medium was made by filtering: phosphate buffered solution 200 ml, EDTA 0.6 g, 0.2 $\mu\text{g/ml}$ fungizone, 67 U/ml penicillin-streptomycin, 66 mg/ μl streptomycin (Sigma-Aldrich, Dorset, UK) into a sterile bottle. The pH was adjusted to 7.2, and stored in 20 ml aliquots at 20°C until use.

MSCs were isolated from the bone marrow sample using Ficoll-Paque PREMIUM 1.073 density gradient (GE Healthcare Life Sciences, Bucks, UK) (Figure 40). The liquid portion of the bone marrow sample was pipetted equally into two centrifuge tubes and spun at 400 g for 5 mins. The cell clots were resuspended in 10 ml of transfer medium. 5 ml of Ficoll-Paque was added to two centrifuge tubes. Each bone marrow sample (mixed with transfer medium) was carefully layered on top of the Ficoll-Paque without allowing it to mix. The Ficoll-Paque density gradient was spun for 45 mins at 400 g.

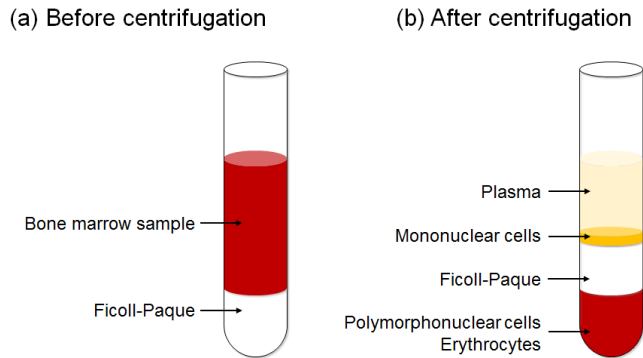


Figure 40. Ficoll-Paque density gradient separation of mononuclear cells

The use of Ficoll-Paque is a simple and reliable method of separating the cellular components of bone marrow according to density.

After centrifugation high density polymorphonuclear cells (neutrophils, eosinophils, erythrocytes) were at the bottom of the tube, having passed through the Ficoll-Paque layer (Figure 39). Mononuclear cells (lymphocytes, monocytes, platelets) settled on the Ficoll-Paque layer as the 'buffy coat', and were pipetted into a separate container.

Complete culture medium was made by filtering: D5671 Dulbecco's modified Eagle's medium (DMEM) with 10% (v/v) foetal bovine serum (FBS)(Sigma-Aldrich, Dorset, UK), 1% (v/v) minimal essential amino acids (Gibco, Life Technologies, Paisley, UK), 1% (v/v) sodium pyruvate (Sigma-Aldrich, Dorset, UK), 1% (v/v) L-glutamine 200 mM (Sigma-Aldrich, Dorset, UK), and 0.2 µg/ml fungizone, 67 U/ml penicillin-streptomycin, 66 µg/ml streptomycin (Sigma-Aldrich, Dorset, UK). Culture medium was stored in a sterile non-vented bottle at 5°C and used within a week.

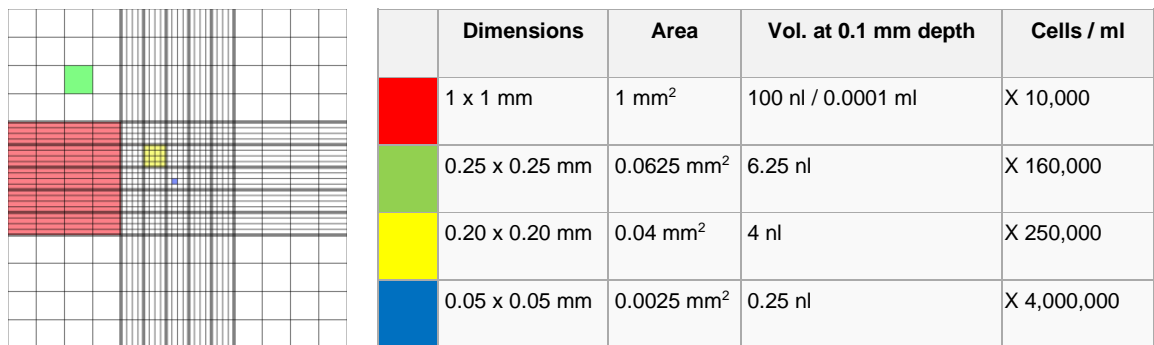
20 ml of complete culture medium was added to the mononuclear cells (or 'buffy coat') and they were transferred to sterile vented polystyrene tissue-culture flasks (TCPS) (Dow Corning) in a humidified atmosphere of 5% CO₂ at 37°C.

The culture medium was changed after 48 hours, then three times weekly until required. Non-adherent or dead cells were removed with the culture medium, so, after several changes of media, the predominant cell type were adherent mononuclear cells, i.e., mesenchymal stromal cells (MSCs).

MSCs were seeded at passage 1 to 3. The culture medium was removed from the culture flask and the cell sheet was washed in 10% HEPES buffer three times to remove any proteins that would reduce the efficacy of the detachment solution.

Trypsin-EDTA cell detachment solution was warmed to 37°C and 2.5 ml was added to each cell flask. The flasks were gently agitated, and cell detachment was monitored using a light microscope. After 5 mins, culture medium was added to the flask to deactivate the detachment buffer. The cell suspension was centrifuged for 5 mins at 1400 rpm. The supernatant was removed, and the cells were re-suspended in 10 ml of culture medium.

50 µL of the cell suspension was transferred to a haemocytometer (Figure 41). The number of cells in one 0.04 mm² area was counted and multiplied by 250,000 to determine the cell concentration.



	Dimensions	Area	Vol. at 0.1 mm depth	Cells / ml
	1 x 1 mm	1 mm ²	100 nl / 0.0001 ml	X 10,000
	0.25 x 0.25 mm	0.0625 mm ²	6.25 nl	X 160,000
	0.20 x 0.20 mm	0.04 mm ²	4 nl	X 250,000
	0.05 x 0.05 mm	0.0025 mm ²	0.25 nl	X 4,000,000

Figure 41. Cell counting using a haemocytometer

The cell concentration was assessed using a haemocytometer and the mixture was diluted with culture medium to attain a concentration of 80,000 cells/ml.

500 µl (40,000 cells) of cell suspension was added to each substrate using cell seeding devices provided by Reynolds et al. (Patent no. WO/2014/064449).[212] The substrates were put into an incubator for one hour to permit cell attachment. After an hour the cell seeding device was removed and 8 ml of 37°C complete culture medium was added. The culture medium was changed three times a week.

4.3.3 Cell staining

Cell staining was performed as a quantitative method of assessing bone mineral production. Confocal microscopy of PEEK was not considered a viable option due to immunofluorescence of the surface.[213]

After six weeks in culture, the cells were fixed in 4% (v/v) paraformaldehyde and 2% (w/v) sucrose phosphate buffered saline (PBS) solution at 37°C for 30 mins.

Cells were stained using alizarin red S (alizarin sodium monosulphate, ARS) to detect calcium particles and the von Kossa technique was used to detect phosphate particles.

Alizarin red staining is a standard histological method for identifying calcium phosphate.[214] It chelates with calcium to form a bright red birefringent alizarin – calcium complex to enable visual detection of mineralization in vitro.[214]

To stain the cells using ARS, the fixed cells were washed using ice-cold 1x phosphate buffered saline (PBS) and 40mM ARS (Sigma-Aldrich, Dorset, UK) was added for 60 minutes. Samples were washed thoroughly using deionised water and dried using filtered compressed air and left in a hot room overnight.

Von Kossa originally described using silver nitrate solution to bind phosphate and create a yellow-silver precipitate in 1901.[215] It was later appreciated that exposure to UV light resulted in reduction of the precipitate into metallic silver.[215]

For the von Kossa technique, the fixed cells were washed three times in deionised water and 5% silver nitrate solution (Sigma-Aldrich, Dorset, UK) was added. The substrates were placed under a UV light for 30 mins. The silver nitrate solution was removed, and 5% sodium thiosulphate solution (Sigma-Aldrich, Dorset, UK) was added. The cells were rinsed in tap water and nuclear fast red (Sigma-Aldrich, Dorset, UK) (a nuclear counter stain) was added for 2 mins. The cells were then washed in deionised water and dried using filtered compressed air.

ARS and silver nitrate do not exclusively bind to calcium and phosphate respectively, but, for brevity, dark red ARS stained particles are referred to as calcium and dark brown von Kossa stained particles are referred to as phosphate.

4.3.4 Staining analysis

25 images of each sample were taken using a Leica DM750M polarising optical microscope (Leica Microsystems, Milton Keynes, UK) (Figure 42). The microscope images were analysed using CellProfiler® software (Figure 43) to standardise the brightness and contrast, and threshold the image appropriately to identify the weakly stained objects (cells) from strongly stained objects (calcium or phosphate particles).[216, 217] The software was used to calculate: (1) % of the surface covered with cells; (2) total cell number; (3) mean expression (i.e., surface area with positive staining) of calcium or phosphate particles (in pixels).[218]

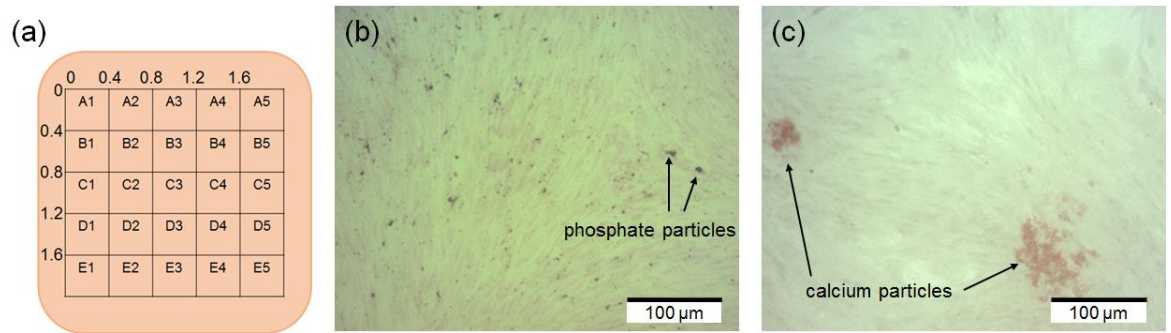


Figure 42. ARS and VK stain analysis of PEEK substrates

(a) 25 images of each PEEK surface were recorded based on a grid structure from A1 to E5. The microscope stage was moved blindly in 0.4 mm increments to avoid bias and achieve a representative sample of > 50% of each surface. (b) ARS staining demonstrates cell nuclei in pink and calcium particles in dark red. (c) Von Kossa staining allows the identification of cell nuclei (stained pink by nuclear fast red) and phosphate particles identified by the dark brown deposits of metallic silver.

The original images were converted to grayscale and the colour was inverted. Due to the discrepancy in illumination of the image from the centre to the periphery caused by the reflectiveness of the sample surface, an elliptical correction function was employed to create uniform contrast between objects and the background.

After smoothing the images with a Gaussian filter, an adaptive threshold strategy (which partitions each image into separate tiles to account for variability) and a Two-class Otsu thresholding method were used to identify primary objects (cell nuclei) between 10-400 pixels in size. Clumped objects were distinguished using the Laplacian of Gaussian method with an automatic Gaussian smoothing filter, and dividing lines were drawn using object intensity. Secondary objects (cell bodies) were identified using the propagation method from the previously identified primary objects (cell nuclei). All experiments were performed in triplicate and single-factor ANOVA, two-factor ANOVA with replication, and two-tailed Student's T-test were used to determine statistical significance between samples.

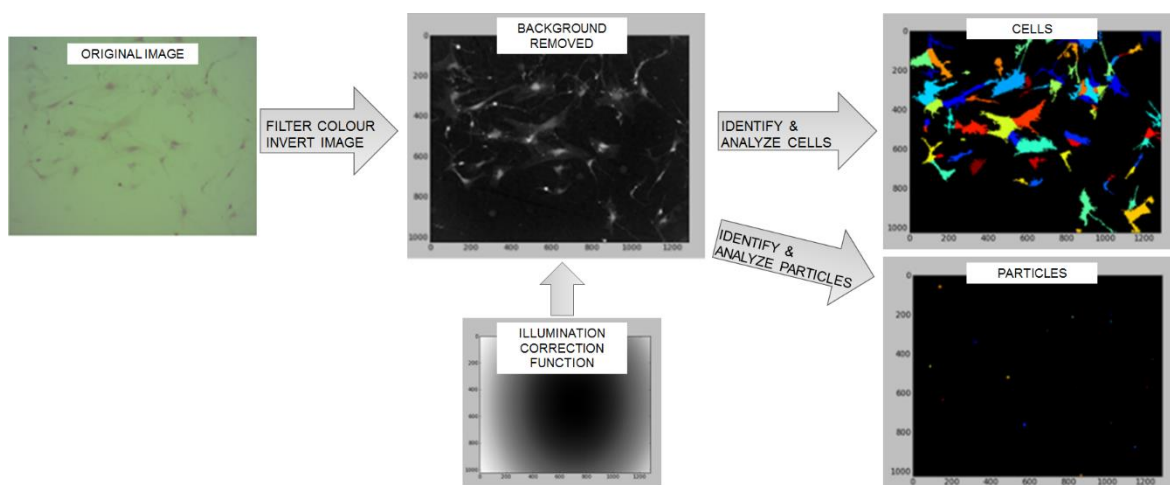


Figure 43. CellProfiler image analysis pipeline

Each of the 25 images captured from each PEEK sample were entered into CellProfiler. An image processing pipeline was designed to allow automatic image correction and analysis as shown above.

4.3.5 Field Emission-SEM and Energy Dispersive Spectroscopy

Field emission scanning electron microscopy was performed by a Zeiss Sigma microscope with Zeiss Gemini in-lens electron optical column operated using Zeiss SmartSEM software (Carl Zeiss Ltd., Cambridge, UK). Energy dispersive spectroscopy (EDS) was achieved using an X-Max Silicon Drift EDS Detector operated using AZtec software (Oxford Instruments, Oxford, UK).

4.3.6 Gene expression analysis using Reverse Transcriptase Quantitative Polymerase Chain Reaction

With prolonged time in culture, the genes associated with the maintenance of multipotency such as *CD105*, *CD271*, and *CD166* are deactivated. Human mesenchymal stromal cells (MSCs) derived from human bone marrow supplied by Promocell GmbH, Heidelberg, Germany were used for these gene expression experiments as they undergo quality control measures using flow cytometric analysis of gene expression, e.g. *HCAM (CD44)*, *CD45*, and *Endoglin (CD105)* and differentiation assays for adipogenic, osteogenic, and chondrogenic lineages are performed for each lot under culture conditions.[219]

NSQ PEEK and FLAT PEEK substrates were oxygen plasma treated (PlasmaPrep 5, GaLa Instrumente GmbH, Bad Schwalbach, Germany) for 120 s at 200W in 0.2

mbar O₂. 20,000 Promocell MSCs were seeded onto meta-stable oxygen plasma treated PEEK surfaces (advancing contact angle between 60° and 100°) using cell seeder devices as described previously. Complete Dulbecco's modified Eagle's medium was changed 3 times weekly for 2 weeks.

After 14 days in culture the cells were lysed and the RNA was extracted. Five PEEK samples were combined to create one biological replicate.

Cell freeze mixture (50% FBS, 30% DMEM, 20% Dimethyl sulfoxide (DMSO)) was added 1:1 to the cell mixture and the cells were stored at -70°C. Alternatively, the cells can be lysed while still adherent to the test substrate. The disadvantage of that method is that it is not possible to achieve an accurate cell count.

Cells were defrosted, centrifuged, washed in PBS and transferred to new RNase-free polypropylene centrifuge tubes. These were centrifuged at 300 x *g* for 5 minutes to pellet the cells and the supernatant was removed by aspiration.

The RNA was isolated using a Qiagen RT² HT First Strand Kit (96) within a clean laboratory area. 10 µl of 14.3 M β-mercaptoethanol (β-ME) was added to 1 ml of RLT buffer. 600 µl of β-ME / RLT buffer was added to the cell pellet in each tube and vortexed to mix. The lysate was then pipetted into the QIAshredder spin column which was put into a 2 ml vial and centrifuged for 2 mins at full speed. 600 µl of 70% ethanol was added to the lysate, mixed by pipetting and transferred to a RNeasy spin column (in a 2 ml collection tube) and centrifuged at ≥ 8000 x *g* (≥ 10,000 rpm) for 15 s. The flow-through was discarded and 700 µl of RW1 buffer was added to the spin column and centrifuged briefly to wash the spin column membrane. A 20% RPE buffer / ethanol solution (v / v) was made and 500 µl of this solution was added to the spin column and centrifuged briefly to wash the spin column membrane. 500 µl of the RPE buffer / ethanol solution was added to the spin column once again and centrifuged at ≥ 8000 x *g* (≥ 10,000 rpm) for 2 mins. The spin column was then transferred to a new 2 ml collection tube and centrifuged for a further 1 min. The spin column was then transferred to a 1.5 ml collection tube and 50 µl of RNase-free water was added to the spin column membrane and centrifuged at ≥ 8000 x *g* (≥ 10,000 rpm) for 1 min.

The GE2 buffer and BC4 reverse transcriptase mix were taken from -20°C storage, thawed on ice and briefly centrifuged. 6 µl of GE2 buffer was added to each of the 96 wells in the six Qiagen RT² Profiler™ Mesenchymal Stem Cell PCR array plates

(QIAGEN Ltd., Manchester, UK). 8 µl of RNA solution was added to each of the 96 wells in the six array plates as shown in Table 9.

Table 9. PCR array of gene expression markers for stromal cell differentiation.

	1	2	3	4	5	6
A	<i>ABCB1</i>	<i>ACTA2</i>	<i>ALCAM</i>	<i>ANPEP</i>	<i>ANXA5</i>	<i>BDNF</i>
B	<i>CD44</i>	<i>COL1A1</i>	<i>CSF2</i>	<i>CSF3</i>	<i>CTNNB1</i>	<i>EGF</i>
C	<i>FZD9</i>	<i>GDF15</i>	<i>GDF5</i>	<i>GDF6</i>	<i>GDF7</i>	<i>GTF3A</i>
D	<i>IGF1</i>	<i>IL10</i>	<i>IL1B</i>	<i>IL6</i>	<i>INS</i>	<i>ITGA6</i>
E	<i>KITLG</i>	<i>LIF</i>	<i>MCAM</i>	<i>MMP2</i>	<i>NES</i>	<i>NGFR</i>
F	<i>PPARG</i>	<i>PROM1</i>	<i>PTK2</i>	<i>PTPRC</i>	<i>RHOA</i>	<i>RUNX2</i>
G	<i>TBX5</i>	<i>TERT</i>	<i>TGFB1</i>	<i>TGFB3</i>	<i>THY1</i>	<i>TNF</i>
H	<i>ACTB</i>	<i>B2M</i>	<i>GAPDH</i>	<i>HPRT1</i>	<i>RPLP0</i>	<i>HGDC</i>

	7	8	9	10	11	12
A	<i>BGLAP</i>	<i>BMP2</i>	<i>BMP4</i>	<i>BMP6</i>	<i>BMP7</i>	<i>CASP3</i>
B	<i>ENG</i>	<i>ERBB2</i>	<i>FGF10</i>	<i>FGF2</i>	<i>FUT1</i>	<i>FUT4</i>
C	<i>HAT1</i>	<i>HDAC1</i>	<i>HGF</i>	<i>HNF1A</i>	<i>ICAM1</i>	<i>IFNG</i>
D	<i>ITGAV</i>	<i>ITGAX</i>	<i>ITGB1</i>	<i>JAG1</i>	<i>KAT2B</i>	<i>KDR</i>
E	<i>NOTCH1</i>	<i>NT5E</i>	<i>NUDT6</i>	<i>PDGFRB</i>	<i>PIGS</i>	<i>POU5F1</i>
F	<i>SLC17A5</i>	<i>SMAD4</i>	<i>SMURF1</i>	<i>SMURF2</i>	<i>SOX2</i>	<i>SOX9</i>
G	<i>VCAM1</i>	<i>VEGFA</i>	<i>VIM</i>	<i>VWF</i>	<i>WNT3A</i>	<i>ZFP42</i>
H	<i>RTC</i>	<i>RTC</i>	<i>RTC</i>	<i>PPC</i>	<i>PPC</i>	<i>PPC</i>

84 genes in total were assayed on 6 array plates (3 for FLAT PEEK and 3 for NSQ PEEK). Further information regarding the genes is provided in the Appendix.

The plates were sealed with foil and transferred to an orbital shaker for 10 minutes. The foil seal was removed and 6 µl of the BC4 solution (RT master mix) was added to each well. The plates were sealed with new foil and transferred to the orbital shaker for 10 minutes. The plate was transferred to the thermal cycler for reverse transcription. The thermal cycler was set to heat to 42°C for 15 minutes, 95°C for 5 minutes, then cooled to 4°C. The array plates were kept at this temperature until run in the real-time PCR machine to identify the genes shown in Table 9.

Log₂ transformed fluorescence signal to cycle number was analysed to yield the Ct number. Samples were referenced to GAPDH and gene expression on NSQ was compared to FLAT using log₂(fold change) to identify up- and down-regulation. (Fold change = $2^{-\Delta\Delta Ct + SD}$).

4.4 Results

4.4.1 Validation of histological staining using Energy-dispersive analysis

Energy-dispersive analysis (EDS) was used to assess the validity of ARS and von Kossa staining at identifying calcium and phosphate (i.e. phosphorus). Surface mapping was conducted with FE-SEM, and positively or negatively stained areas were examined with spectral analysis (Figure 44).

EDS analysis confirmed that areas stained positive with ARS (3,4-dihydroxy-9,10-dioxo-2-anthracene-sulfonic acid) contained more calcium and phosphorus than surrounding areas. This validated the ARS staining method used in this chapter as quantitative proxy measure of calcium identification.

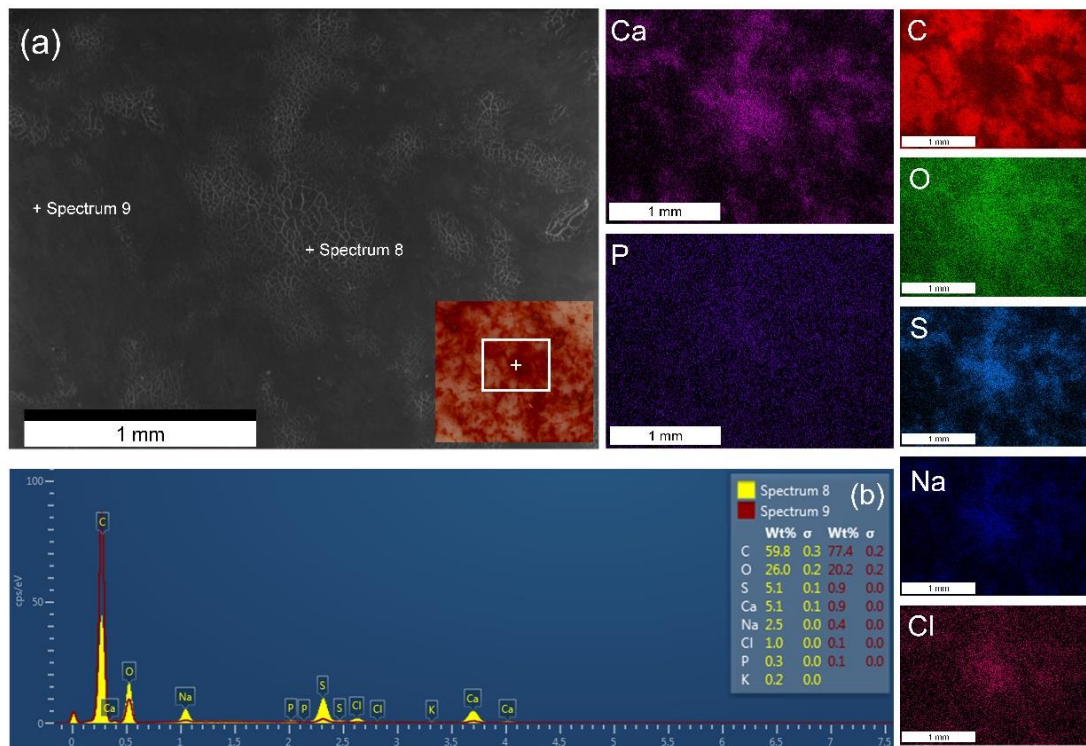


Figure 44. EDS surface analysis of ARS stained PEEK

An area of dense ARS staining was identified using light microscopy (inset picture). EDS surface mapping demonstrates that calcium (Ca) co-localised to areas that were positively stained. Comparative spectral analysis (a) of positively (Spectrum 8) and negatively (Spectrum 9) stained areas showed increased atomic weight of Ca, O, S, Na, P, and K (b).

EDS surface mapping identified minimal phosphorus (and no calcium) on von Kossa stained samples (Figure). There was no difference was in percentage atomic weight of P between positive and negatively von Kossa stained regions. EDS analysis of von Kossa stained samples demonstrated that Ag particles co-localised to areas of phosphorus expression.

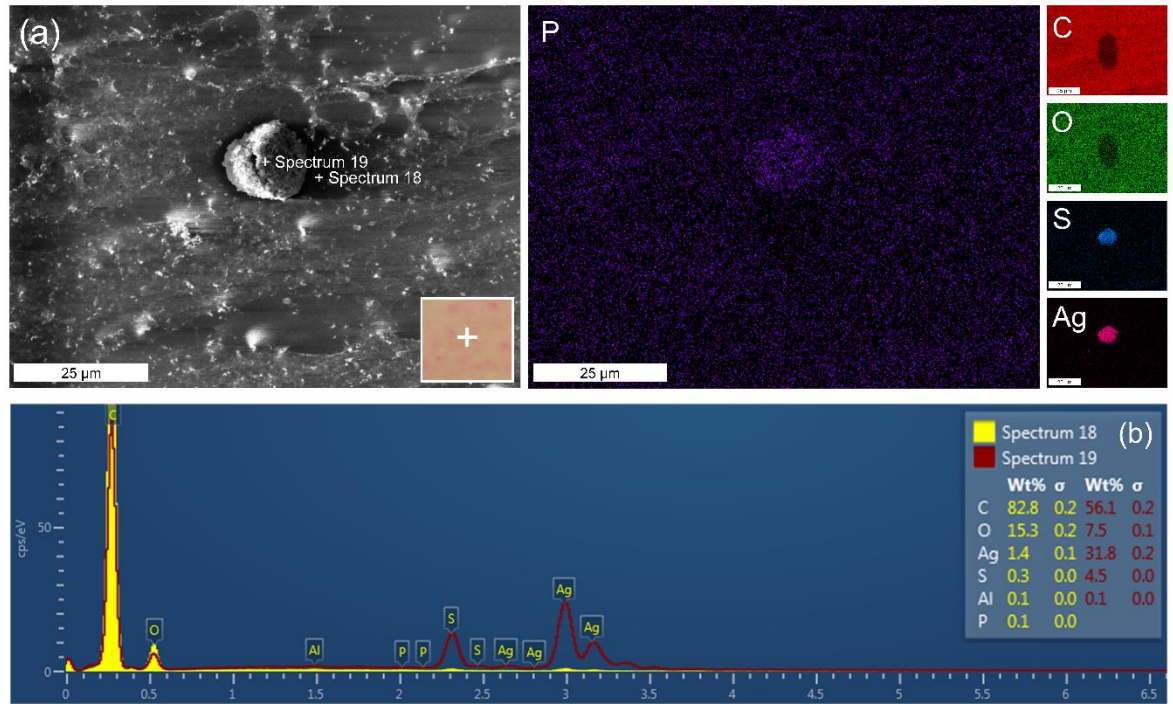


Figure 45. EDS surface analysis of von Kossa stained PEEK

Surface mapping of von Kossa stained cells on PEEK using EDS demonstrated distinct silver particles (Ag) in keeping with positively stained particles. Although the mapping appeared to show an increased concentration of phosphorous (P) in the particles, spectral analysis (a) and (b) revealed the proportional weight of P in these areas was negligible.

Table 10. EDS analysis of ARS and von Kossa stains

Area	Elemental content (wt%)									
	Ca	P	C	O	S	Na	K	Ag	Al	Cl
ARS+	4.3 ± 0.9	0.3 ± 0.1	61.6 ± 2.6	26.7 ± 0.6	4.2 ± 1.0	2.2 ± 0.4	0.1 ± 0.1	-	-	-
ARS-	0.7 ± 0.15	0.03 ± 0.06	58.4 ± 35.2	18.8 ± 1.2	0.7 ± 0.2	0.4 ± 0.1	-	-	-	-
VK+	-	0.1 ± 0.1	53.1 ± 6.5	9.6 ± 3.1	2.3 ± 1.0	-	-	30.8 ± 8.5	0.2 ± 0.1	2.4 ± 2.9
VK-	-	0.1 ± 0.2	77.3 ± 4.7	16.4 ± 1.1	0.5 ± 0.2	-	-	2.3 ± 2.4	0.1 ± 0.2	0.2 ± 0.3

4.4.2 Osteogenesis on oxygen plasma treated and injection mould nanopatterned PEEK

4.4.2.1 Optimisation of oxygen plasma treatment protocol

To determine a preferred protocol for use in subsequent cell cultures and RT-qPCR studies, the osteogenic potential of nanopatterned PEEK samples treated with five different doses of oxygen plasma was compared to untreated controls (Figure 46 and Figure 47).

The ARS stained PEEK surfaces exposed to oxygen plasma were found to have an increased cell-surface coverage and number of cells compared to untreated NSQ and FLAT surfaces (Figure). The mean calcium expression on NSQ PEEK was not increased, but fewer cells were identified on the sample, and the relative calcium expression per cell was increased (Figure 46).

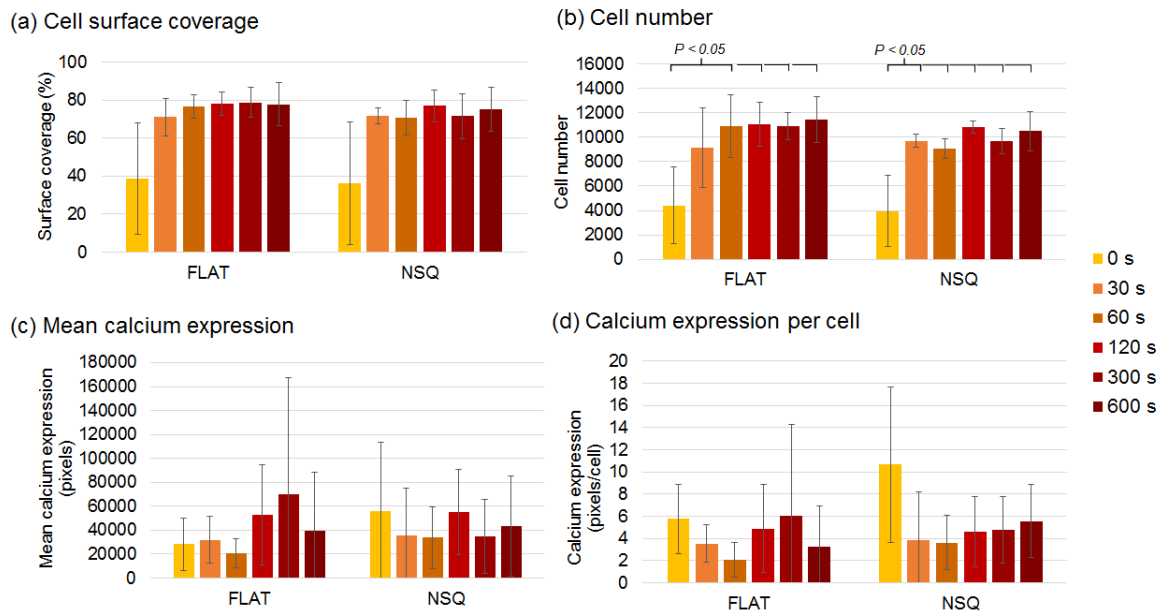


Figure 46. Analysis of ARS stained cells for oxygen plasma optimisation

ARS staining of cells on FLAT and NSQ nanopatterned PEEK surfaces revealed that all surfaces exposed to oxygen plasma exhibited increased cell-surface coverage (a) and cell numbers (b). There was no significant difference in total (c) or relative (d) calcium expression between different durations of oxygen plasma treatment. Calcium expression per cell on untreated surfaces was increased compared to oxygen plasma treated surfaces (d). Error bars represent one standard deviation. Single factor ANOVA (no plasma treatment vs plasma treatment revealed significant variance, and so two-tailed Student's T-test was performed between samples.

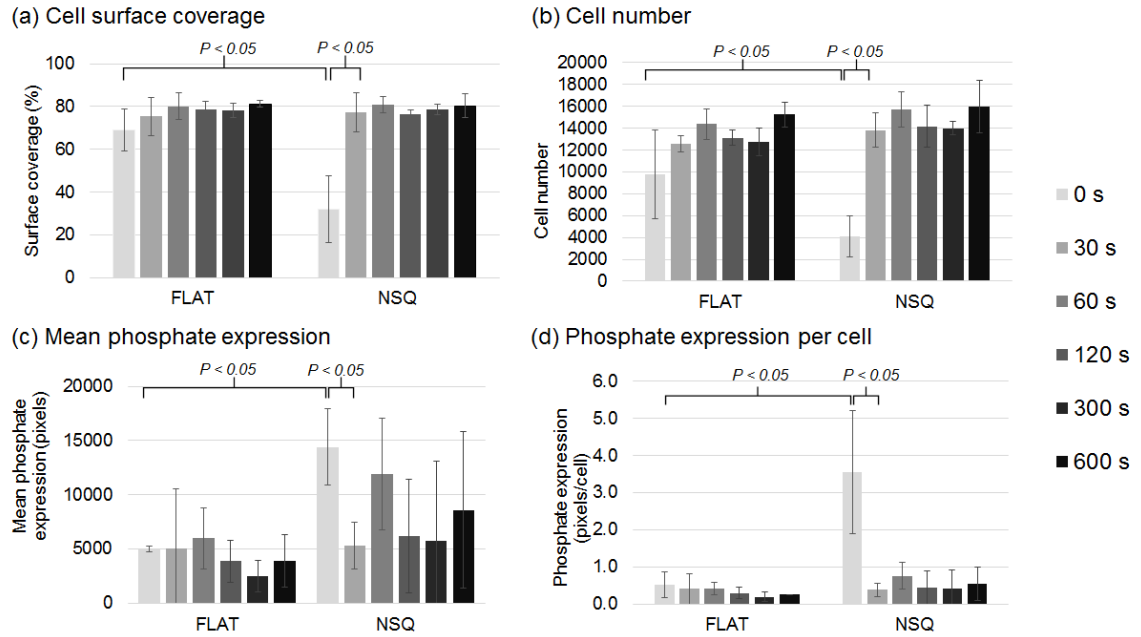


Figure 47. Analysis of von Kossa stained cells for oxygen plasma optimisation.

Von Kossa staining of FLAT and NSQ surfaces in this experiment revealed that oxygen plasma treatment increased cell-surface coverage (a) and cell numbers (b) on NSQ surfaces. Overall, mean phosphate expression (c) was increased on NSQ surfaces, but this was not statistically significant. The relative phosphate expression per cell was significantly increased on untreated NSQ compared to FLAT and oxygen plasma treated NSQ (d) ($P < 0.05$). Error bars represent one standard deviation. Two-tailed Student's T-test was used to compare samples.

From these results using both ARS and von Kossa staining, it was clear that oxygen plasma treatment of PEEK increased cell-surface coverage and the overall cell number (Figure). There was no significant correlation between the duration of plasma treatment (30 s to 600 s) and cell-surface coverage, cell number, calcium, or phosphate expression. Significantly fewer MSCs were identified on untreated NSQ PEEK, but the mean calcium and phosphate expression was similar and therefore the relative calcium and phosphate expression was markedly increased (Figure 46 and Figure 47).

These experiments revealed no discernible difference in cell behaviour between surfaces exposed to oxygen plasma for 30 s and surfaces exposed for 600 s (Figure and Figure). AFM analysis has previously shown a topographical change to PEEK nanopatterns with increasing exposure to oxygen plasma. It was decided that 120 s

of plasma treatment (at 200W in 0.2 mbar O₂) would be used in subsequent experiments.

4.4.2.2 Hydrophobic, hydrophilic and metastable PEEK

In the following experiments, MSCs were cultured on hydrophobic, hydrophilic, and meta-stable PEEK surfaces. From results described previously, PEEK surfaces experience hydrophobic recovery following oxygen plasma treatment (Figure). This experiment examined whether a differential response was exerted by hydrophilic (i.e., AWCA <60°) PEEK surfaces compared to meta-stable (AWCA 60-100°) PEEK surfaces. Both surfaces had been previously treated with 2 mins of 200W O₂ plasma treatment, but the hydrophilic PEEK surfaces (AWCA <60°) were seeded immediately after oxygen plasma treatment, meta-stable PEEK surfaces (AWCA 60-100°) were stored for 12 weeks before seeding, and hydrophobic PEEK surfaces (AWCA of 90-100°) remained untreated. The contact angles of each surface were tested before cell culture. As before, cells were assessed at 6 weeks using ARS (Figure 48) and von Kossa staining (Figure 49).

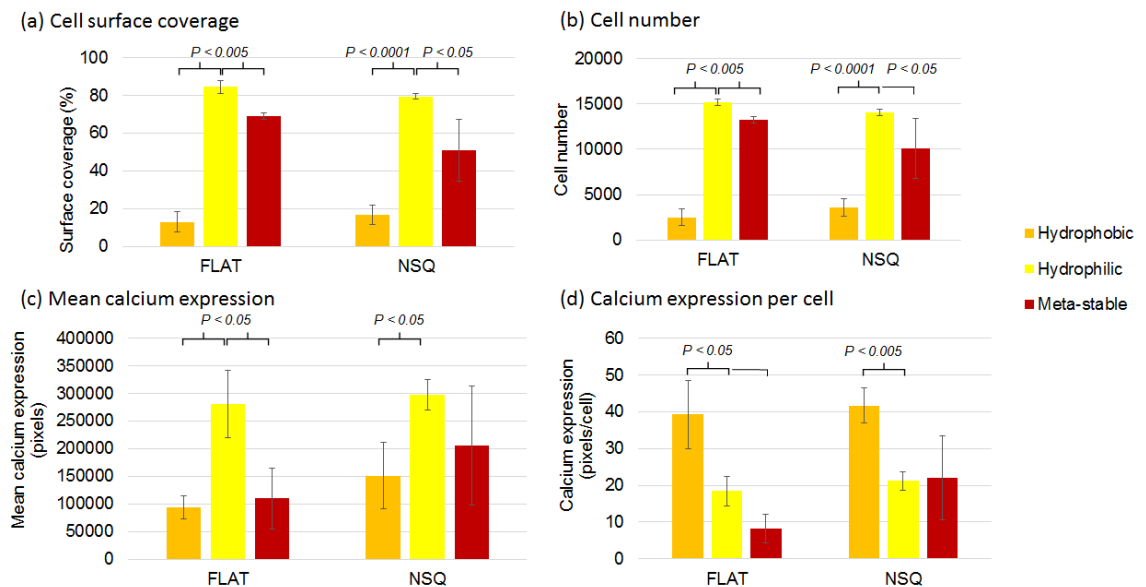


Figure 48. Analysis of ARS stained cells on hydrophobic, hydrophilic and meta-stable nanopatterned PEEK

Hydrophobic, hydrophilic and meta-stable PEEK surfaces were compared using ARS staining. Error bars represent one standard deviation. Two-factor ANOVA with replication indicated significant variance ($P < 0.05$) and so two-tailed Student's *T*-tests were used to compare individual samples.

Hydrophilic PEEK surfaces (both FLAT and NSQ) demonstrated an increased cell-surface coverage, cell number and mean calcium expression compared to meta-stable and hydrophobic PEEK surfaces ($P < 0.05$) (Figure 48).

In this experiment, cell surface coverage and cell number were markedly reduced on the hydrophobic FLAT and NSQ PEEK samples. The relative calcium expression was increased on hydrophobic FLAT and NSQ PEEK surfaces compared to the hydrophilic and meta-stable surfaces.

Similarly, to the ARS staining method, the von Kossa technique (Figure) detected a significantly larger proportion of cell-surface coverage and number of cells on hydrophobic PEEK surfaces compared to hydrophilic or meta-stable PEEK ($P < 0.05$).

No statistical difference was observed in this experiment between hydrophilic and meta-stable PEEK surfaces. The largest expression of phosphate was recorded on hydrophobic NSQ PEEK, but due to variability the difference was not statistically significant.

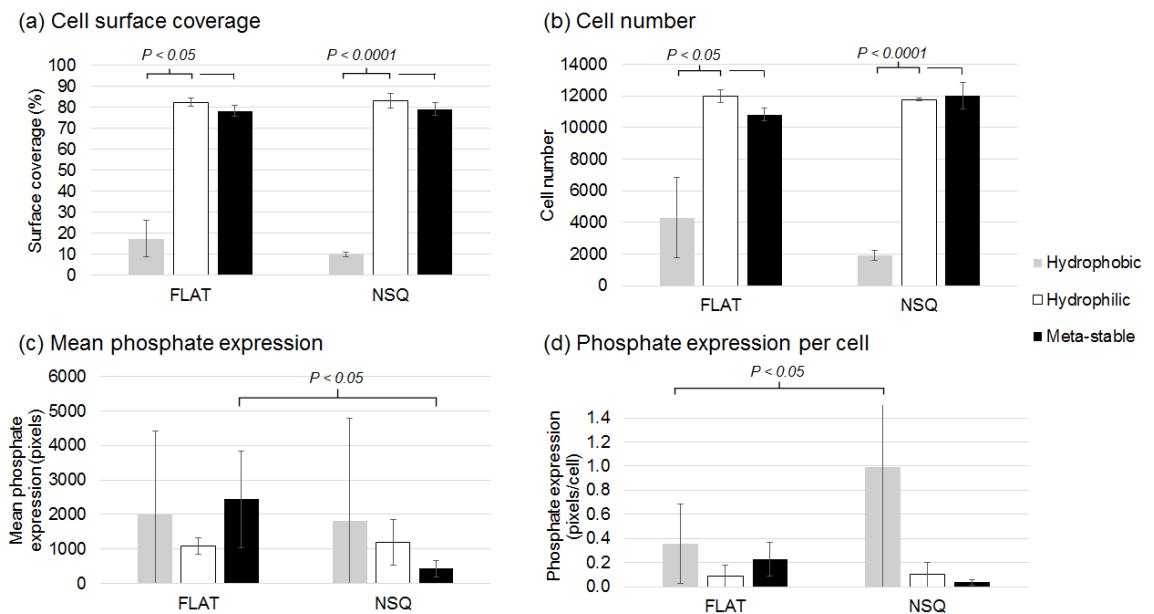


Figure 49. Analysis of von Kossa stained cells on hydrophobic, hydrophilic and meta-stable nanopatterned PEEK

Hydrophobic, hydrophilic and meta-stable PEEK surfaces were compared using von Kossa staining. Error bars represent one standard deviation. Two-tailed Student's *T*-test was performed to compare samples.

4.4.2.3 Ordered and disordered nanopatterned PEEK

This experiment was designed to confirm whether the disordered NSQ nanopattern exerted a differential effect on cell behaviour compared to ordered SQ and HEX nanopatterns (with or without oxygen plasma treatment). Oxygen plasma treatment was performed for 2 mins (as described previously) and the surfaces were allowed to age post-treatment (i.e., meta-stable) before use. As before, expression of calcium and phosphate was assessed with ARS (Figure 50) and von Kossa stains (Figure 51).

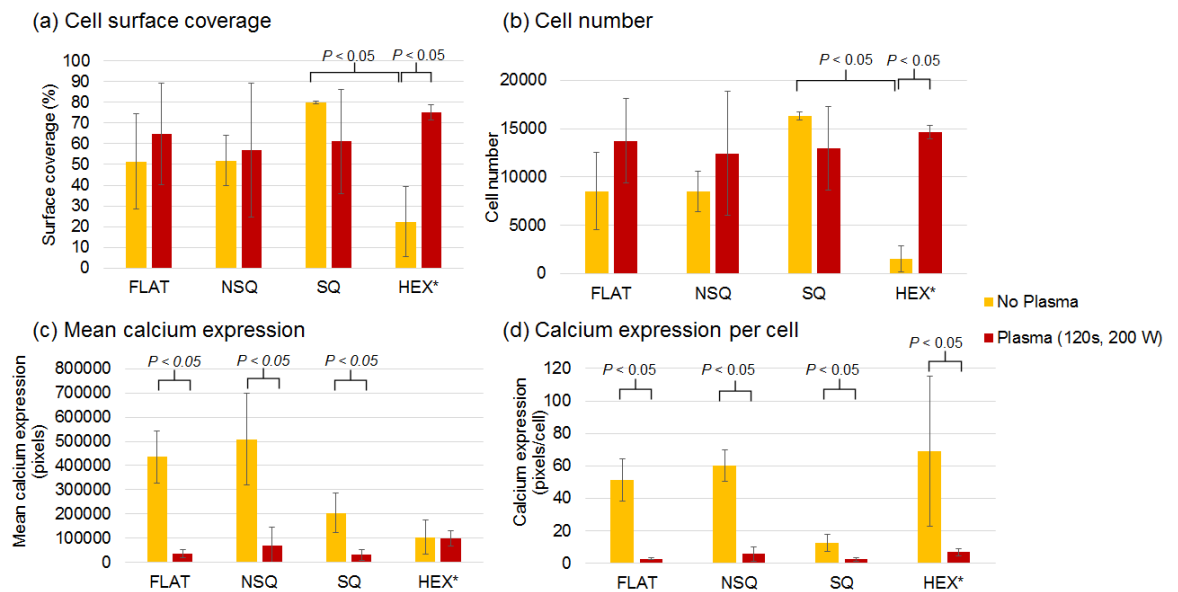


Figure 50. Analysis of ARS stained cells on ordered and disordered oxygen plasma treated nanopatterned PEEK

FLAT, NSQ, SQ and HEX surfaces (with or without 120 s of oxygen plasma treatment) were compared using ARS staining. *The HEX surfaces featured a 10 x 10 mm nanopatterned area that was bounded by a planar margin whereas the NSQ and SQ samples were nanopatterned over the entire 25 x 25 mm surface. Error bars represent one standard deviation. Two-factor ANOVA with replication confirmed significant variance between samples and so two-tailed Student's T-test was performed.

In this experiment, oxygen plasma treatment did not significantly affect cell-surface coverage or cell numbers (approximately 10000 cells) on FLAT, NSQ, or SQ PEEK surfaces ((a) and (b)). Significantly fewer cells were present on untreated HEX (compared to FLAT, NSQ and SQ surfaces) and a significant increase in surface coverage and cell number was observed after oxygen plasma treatment ($P < 0.05$) (Figure 50).

Calcium expression was relatively pronounced on untreated FLAT, untreated NSQ and untreated HEX surfaces. Untreated NSQ and FLAT surfaces had an increased mean calcium expression compared to SQ ($P < 0.05$). Oxygen plasma treatment significantly reduced calcium expression on all surfaces ($P < 0.05$).

A differential cell response was also observed on untreated SQ, with a significantly decreased expression of calcium (per cell) compared to FLAT, NSQ, and HEX surfaces ($P < 0.05$) (Figure 51).

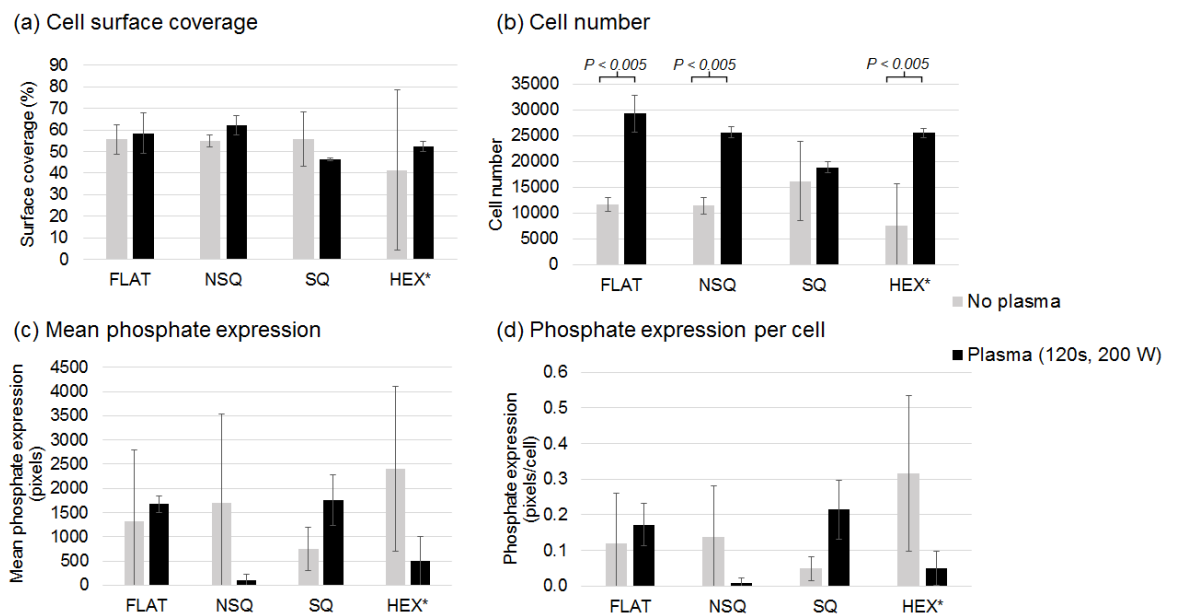


Figure 51. Analysis of von Kossa stained cells on ordered and disordered oxygen plasma nanopatterned PEEK

FLAT, NSQ, SQ and HEX surfaces (with or without 120 s of oxygen plasma treatment) were compared using ARS staining. In this experiment oxygen plasma treatment did not increase cell-surface coverage (a), but did increase cell numbers (b) on FLAT, NSQ and HEX surfaces. There was variability observed in phosphate expression (c and d), as demonstrated by the large error bars (+/- 1 SD). Two-tailed Student's T-test was performed to compare samples.

Phosphate expression was relatively pronounced on FLAT, untreated NSQ, untreated HEX, and plasma treated SQ PEEK surfaces. Decreased phosphate expression was observed on untreated SQ compared to FLAT, NSQ and HEX surfaces. Oxygen plasma treatment of SQ surfaces increased phosphate expression.

4.4.3 Gene expression on oxygen plasma treated injection mould nanopatterned PEEK

84 genes in total were assayed using the RT-qPCR arrays. From the total of 504 tests (84 genes x 6 array plates) there were 440 hits and 64 misses (a Ct cut-off was set at 35 cycles). The up- and down regulation of gene expression (calculated as log₂fold change) is shown in Figure 52 and 53.

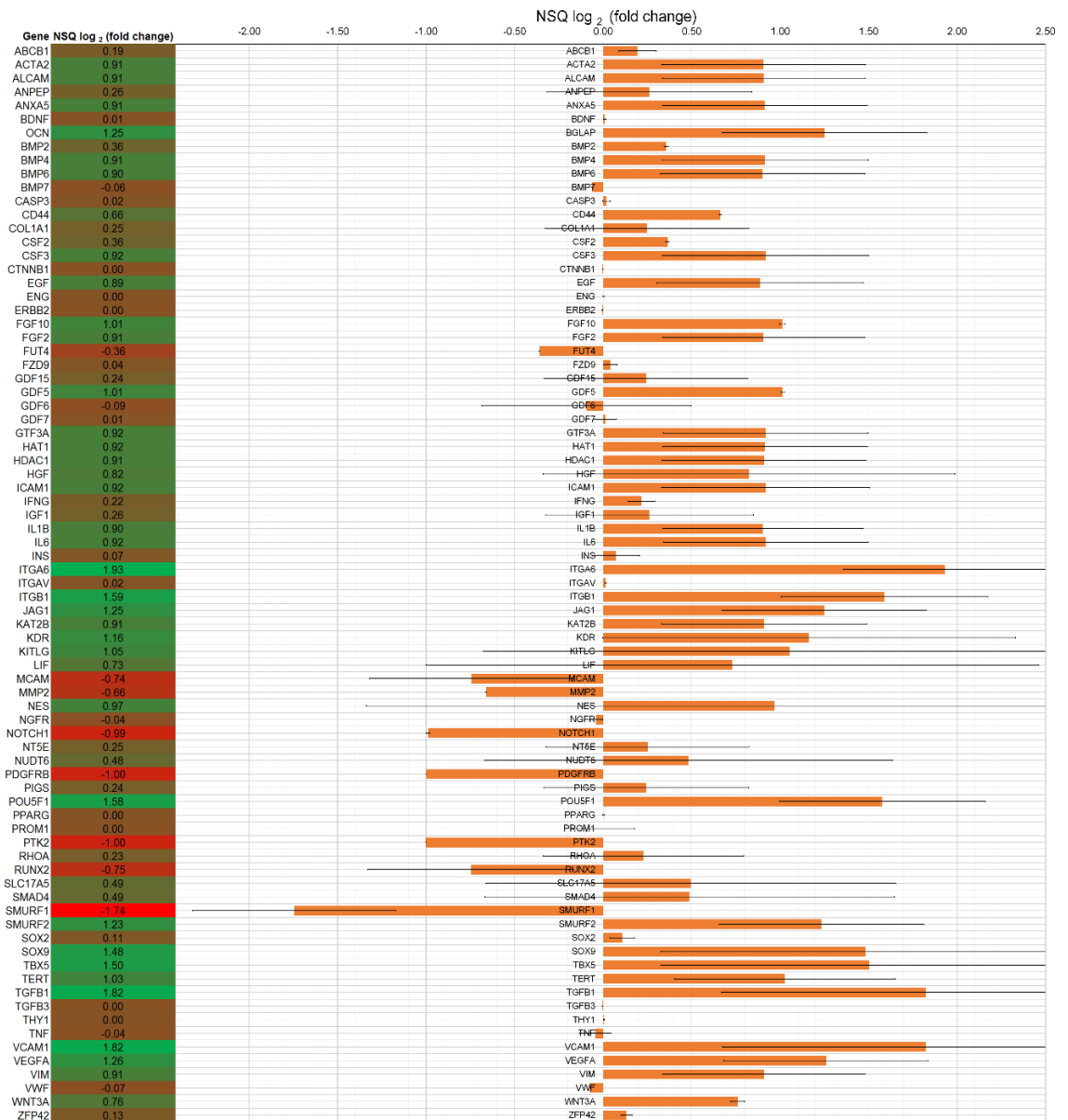


Figure 52. Gene expression on nanopatterned PEEK

This chart displays the (log₂) fold change of gene expression on NSQ compared to FLAT PEEK. The errors bars represent ± 1 S.D. Ct(NSQ). Ct values were normalised to GAPDH.

The haematopoietic markers *CD11c (ITGAX)* and *CD45 (PTPRC)* were not identified on either NSQ or FLAT surfaces. Three other genes (*FUT1*, *IL10*, and *HNF1A*) were excluded from further analysis due to insufficient transcription in at least one of the samples.

No difference in the MSC gene markers *CD73 (NT5E)*, *CD90 (THY1)*, and *CD105 (ENG)* was identified between NSQ and FLAT surfaces. *CD146 (MCAM)* expression was down regulated on NSQ (0.74 ± 0.01). Gene expression of *CD51 (ITGAV)*, and *CD271 (NGFR)* were similar on both surfaces. *CD309 (KDR or VEGFR)* and *VEGFA* expression was upregulated on NSQ (1.16 ± 0.60 and 1.26 ± 0.59 respectively).

CD140b (associated with myofibroblastic cells) was down regulated on NSQ (-1.00 ± 0.01). [220] The multipotency maintenance genes *CD29 (ITGB1)*, *CD44 (HCAM)*, *CD49f (ITGA6)*, *CD106 (VCAM1)*, *CD166 (ALCAM)*, *CD339 (JAG1)*, *LIF*, *TERT*, *NES*, *OCT4 (POU5F1)*, *SOX2*, and *REX1 (ZFP42)* were upregulated on NSQ. *ITGB1 (CD29)* and *ITGA6 (CD49f)* expression on NSQ was 1.59 ± 0.58 and 1.93 ± 0.01 respectively. *CD44 (HCAM)*, *CD106 (VCAM1)*, *CD166 (ALCAM)* expression on NSQ was 0.66 ± 0.57 , 1.82 ± 0.01 , 0.91 ± 0.01 respectively. *CD339 (JAG1)*, *LIF*, *TERT* and *NES* expression on NSQ was 1.25 ± 0.60 , 0.73 ± 0.00 , 1.03 ± 0.11 , 0.97 ± 0.01 respectively. *OCT4 (POU5F1)*, *SOX2* and *REX1 (ZFP42)* expression on NSQ was 1.58 ± 0.57 , 0.11 ± 0.02 , and 0.13 ± 0.03 respectively. *NOTCH1* was significantly down regulated on NSQ (0.99 ± 0.02).

RUNX2 (also known as Runt-related transcription factor 2 and core-binding factor subunit alpha-1) was significantly down-regulated on NSQ (-0.75 ± 0.01). *BGLAP* (or *OCN*) which encodes for osteocalcin, a bone specific marker of mineralisation, was significantly upregulated on NSQ (1.25 ± 0.58). The expression of osteogenesis related genes *BMP2*, *BMP4* and *COL1A1* was similar on both surfaces (0.36 ± 0.57 , 0.91 ± 0.01 , 0.25 ± 0.58 respectively).

Chondrogenesis markers *SOX9* and *GDF5* were upregulated on NSQ (1.48 ± 0.58 and 1.01 ± 0.01). No significant change was observed in expression of the chondrogenesis markers *BMP7* and *GDF6* (-0.06 ± 0.06 and -0.09 ± 0.01).

The adipogenesis marker *PPARG* (peroxisome proliferator-activated receptor gamma) was identified equally on the two surfaces.

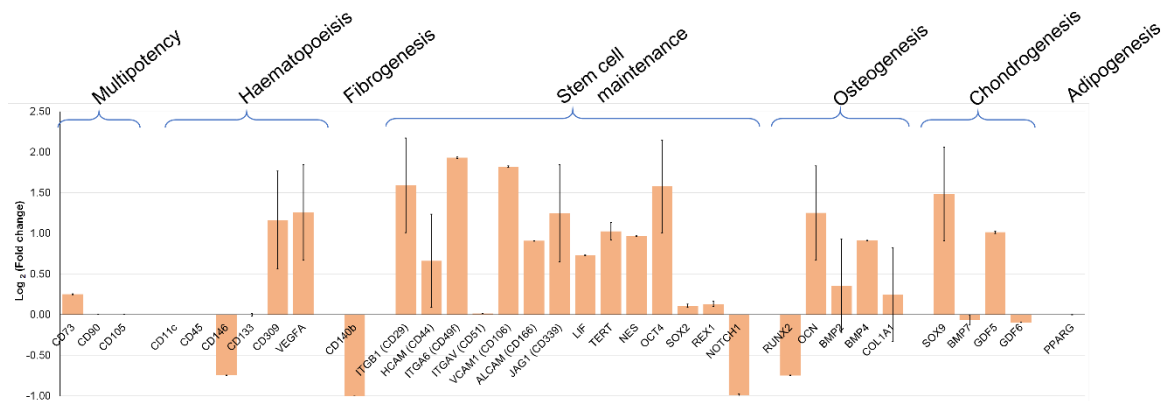


Figure 53. Genetic characterisation of cells on nanopatterned PEEK

The genes identified in the PCR array can be grouped into functional roles according to cell lineage. Some markers can be expressed by cells of more than one lineage. There is considerable overlap between osteogenesis and chondrogenesis markers. Error bars are ± 1 S.D. of Ct(NSQ).

4.5 Discussion

4.5.1 Stromal cell culture

Preliminary cell culture experiments of mesenchymal cells on PEEK identified difficulties with cell-surface adhesion. Micro-mass seeding was the standard approach for transferring cells onto surfaces in our laboratory. This involved carefully pipetting a specific volume of cell mixture (0.5 ml) directly onto the surface whilst ensuring all the sample is retained on the surface and not allowed to run-off the sides. The samples would then be incubated for 2 hours, to allow cell adhesion, before adding additional culture medium. Micro-mass seeding resulted in an irregular heterogeneous distribution of cells and were more susceptible to becoming detached.

This problem was overcome when a cell seeding device was designed and patented by another member of our research group. Once this was employed in this project, a uniform distribution of cells was observed and less cell detachment encountered.

4.5.2 Nanopatterned PEEK

The bioactivity of nanopatterned PEEK (NSQ, SQ and HEX) was investigated to determine if the MSC response was comparable to other polymers (e.g., polycarbonate (PC), polymethylmethacrylate (PMMA), and polycaprolactone (PCL)).

An increased number of cells were detected on the SQ nanopatterned PEEK surfaces compared to FLAT, NSQ and HEX (Figure (b)). This reflects previous findings on PC and PMMA that have demonstrated the propensity for SQ nanotopography to maintain MSCs in a multipotent phenotype capable of prolific replication.[1, 131]

A markedly reduced number of cells were seen on HEX nanopatterned PEEK (Figure (b)). The HEX nanotopography has previously been identified to have a non-adhesive or anti-fouling property.[1] This effect appears to be reproducible in PEEK, and is dramatically reversed following oxygen plasma treatment.

NSQ nanotopography has previously been described as osteoinductive when fabricated in polymethylmethacrylate (PMMA) and polycarbonate.[1] In this project, NSQ demonstrated increased relative expression of calcium compared to FLAT and SQ PEEK using ARS stain, but the difference was not statistically significant.

Staining for phosphate expression using the von Kossa technique provided more variable results. Concerns have previously been published regarding the ability of von Kossa staining to identify phosphate *in vitro*.^[221] Indeed, small amounts of phosphorus were identified in this project using EDS and so the highly stained areas featuring black silver deposits may not, therefore, provide accurate quantification of mineralisation.

4.5.3 Oxygen plasma treated PEEK

Oxygen plasma treatment of PEEK increased cell number and cell-surface coverage, but did not increase calcium and phosphate expression (relative to the number of cells identified). The optimisation experiments (Figure and Figure) demonstrated that all doses of oxygen plasma (from 6 kJ to 120 kJ) exhibited a similar cellular effect.

The hydrophilic nature of oxygen plasma treated PEEK diminishes with time (as shown in Figure) and after approximately 6 weeks the AWCA increases to 60-90° and the surfaces were considered 'meta-stable'. Hydrophilic PEEK (i.e., the cells were seeded within hours of plasma treatment and the AWCA was < 60°) had significantly more calcium expression than hydrophobic or meta-stable PEEK due to the larger number of cells present on the surface. Surprisingly, hydrophobic PEEK appeared to significantly increase the relative calcium expression per cell (but the overall expression was reduced due to fewer adherent cells).

It was hypothesised that meta-stable PEEK would increase cell adhesion and prevalence compared to untreated (i.e., hydrophobic) PEEK. As demonstrated in graphs (a) and (b) in Figures 48 and 49, meta-stable PEEK (with AWCA 60-90°) did indeed permit increased cell adhesion and prevalence, but the mean (calcium and phosphate) mineralisation and mineralisation per cell was not reliably improved. Therefore, hydrophobic recovery of oxygen plasma treated PEEK had a detrimental effect on the surface bioactivity.

4.5.4 The adhesion-mineralisation paradox

It is apparent from these experiments that a direct relationship exists between wettability, cell adhesion and proliferation and an indirect relationship exists between wettability and mineralisation. This corresponds to studies that identified that MSCs need to achieve a high-tension phenotype with elongated cell adhesion complexes incorporating vinculin and talin before they can differentiate into mineral producing cells

Increased surface wettability may allow focal adhesions to form more easily, and may allow less mature adhesions to exist without needing to upregulate additional scaffolding proteins, such as vinculin and talin.[128, 222] This is likely to diminish the drive towards osteoblastic differentiation. Alternatively, increased surface wettability may alter the landscape of adherent proteins, thus providing alternative binding sites for integrin transmembrane receptors.

It is clear, therefore, that an inverse relationship exists between cell adhesion/proliferation and cell differentiation/mineralisation to which surface wettability is the determinant factor (Figure).

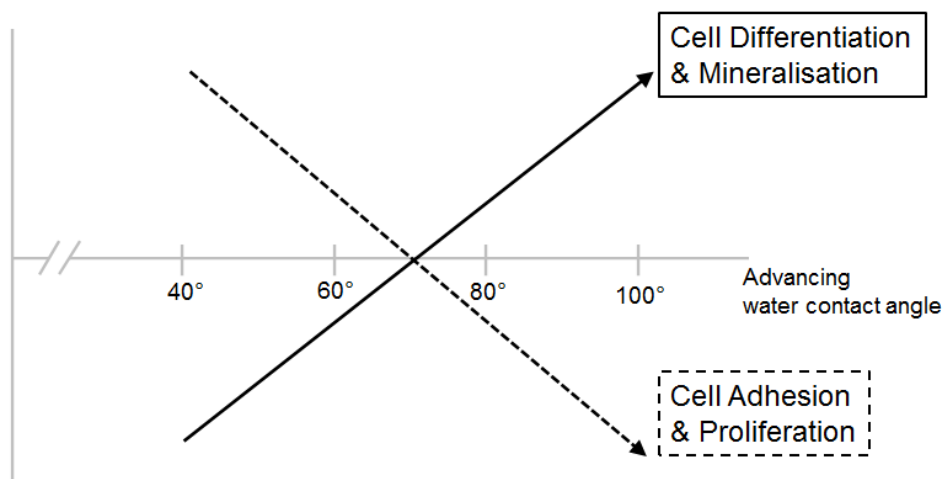


Figure 54. The adhesion-mineralisation paradox

Mesenchymal stromal cells do not adhere well to injection moulded (i.e., hydrophobic) PEEK. The majority of cells that successfully attach, however, appear to favour osteogenesis. If the AWCA of PEEK is decreased using plasma treatment, cell adhesion and proliferation on the surface will increase, but the cells will be less osteogenic and more fibroblastic in behaviour.

Nanotopography, may be able to augment this relationship by altering the adhesion potential of a surface. Cells are less likely to form adhesions to proteins at the bottom of nanopits, and, as such, nanotopography reduces the available binding regions yet still allows focal adhesions to form.[223] This modulation of focal adhesions appears to be the stimulus for changing cell behaviour.

PEEK does not behave exactly like other polymers, such as PC, PMMA, and PCL. It appears that materials exhibit a fundamental capability for cell adhesion (vs differentiation), which is likely based on chemical composition and surface wettability. The results in this project demonstrate that the bioactivity of nanotopography is dependent upon surface wettability, and is diminished by oxygen plasma treatment.

The same principles, however, are observed between the different materials:

- SQ nanopatterning of PEEK (like PC) can increase MSC proliferation [70];
- HEX nanopatterning of PEEK (like PMMA) decreases MSC adhesion [72]; and
- NSQ nanopatterning increases MSC mineralisation (like PMMA and PCL).[1, 131, 211]

4.5.5 Gene expression on oxygen plasma treated injection moulded nanopatterned PEEK

4.5.5.1 Stromal cell determination

Mesenchymal stromal cells (MSCs) are multipotent cells capable of differentiating into cells that can generate skeletal tissue and the corresponding vascular, lymphatic and neural networks. Gene expression occurs dynamically within the cell niche, and cells may switch between different progenitor types before developing into a fully committed cell lineage (Figure).

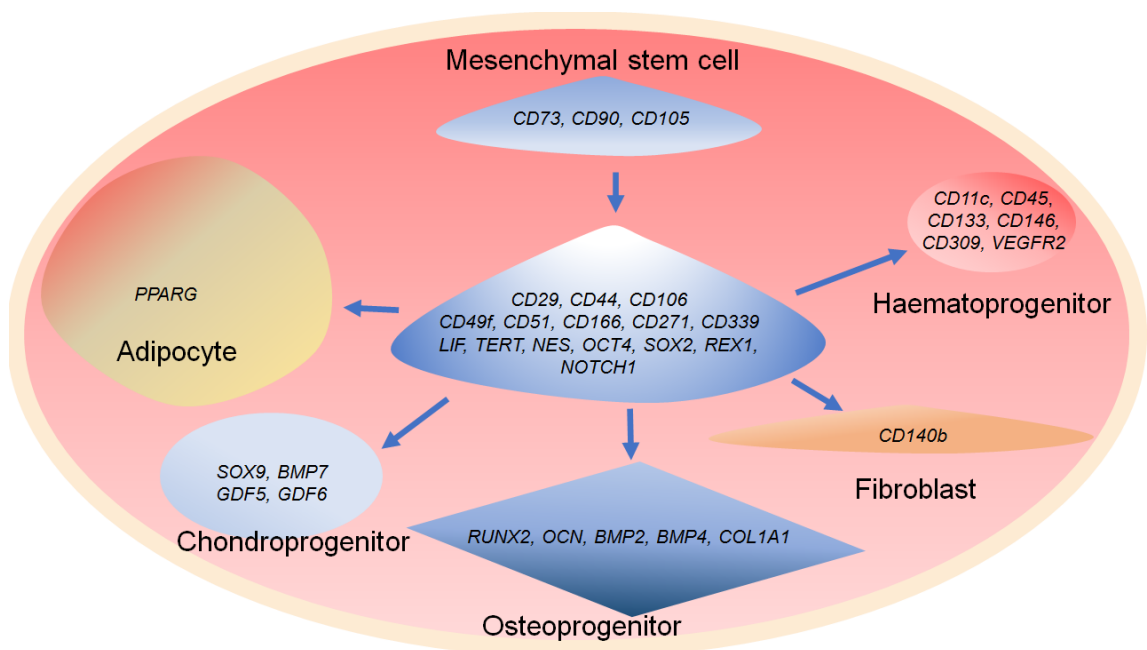


Figure 55. Genetic determination of stromal cell fate

Gene expression determines mesenchymal cell fate and provides a method of identification. This diagram illustrates how the genes investigated in this project relate to different cell types present in the bone marrow niche.

Positive expression of *CD73* (*NT5E*), *CD90* (*THY1*) and *CD105* (*ENG*) is considered a fundamental characteristic of a multipotent MSC.[224, 225] *CD73*, *CD90*, and *CD105* were expressed widely across both surfaces indicating that, after 2 weeks on the PEEK surfaces, cells had maintained their multipotent nature.

CD29 (*ITGB*), *CD44*, and *CD106* (*VCAM1*) have been used as markers to isolate sub-populations of multipotent MSCs.[226, 227] The cell markers *CD49f* (*ITGA6*), *CD51* (*ITGAV*), *CD166* (*ALCAM*) and *CD271* (*NGFR*) have identified sub-

populations of MSCs with useful characteristics, whilst not fulfilling the criteria for multipotency.[228-231] In cultured MSCs, *CD44* expression is normally low (< 5%), and expression of *CD106* and *CD166* is high, but variable.[232, 233] Continued expression of these markers suggests the multipotent stromal cell phenotype is maintained after 2 weeks on both surfaces.

4.5.5.2 Haematopoietic cells

MSCs may differentiate into haematopoietic cells which express the stromal cell markers *CD11c* (*ITGAX*), *CD45* (*PTPRC*), *CD133* (*PROM1*) and *CD309* (*VEGFR2* or *KDR*).[234, 235] The lack of expression of *CD11c*, *CD45*, and *CD133* in this experiment indicates that the cells are not being stimulated to form haematopoietic cells.

MCAM (also known as *CD146*) is a marker of MSCs and endothelial cells and a decrease *MCAM* expression is associated with MSC differentiation.[236, 237] A previous study has demonstrated *CD271⁺/CD146⁺* expression is associated with perivascular cells (i.e. endothelial cells), and *CD271⁺/CD146⁻* expression (i.e. downregulation of *MCAM*) is associated with bone lining cells (i.e. osteoprogenitors).[212, 238] The downregulation of *MCAM* observed in this study suggests increased differentiation on NSQ.

CD309 (also known as vascular endothelial growth factor receptor 2, *VEGFR*) and its ligand *VEGFA* play the predominant roles in vasculogenesis and angiogenesis, and, are essential for osteogenesis.[239-243] *In vivo* deletion of *Vegfr2* in mice osteoblastic cells causes a decrease in the number of osteoprogenitor cells and reduced bone density.[244] Another study showed that *Vegfr2* deletion increases osteoblast maturation and mineralisation during intramembranous ossification.[245] *In vitro*, *Vegfr2*-deficient osteoblasts increase mineralisation, whereas *Vegfr2*-deficient bone marrow cells decrease mineralisation.[245] This demonstrates that *VEGFR2* is important for maintaining osteoprogenitor survival and proliferation, by inhibiting terminal maturation. Indeed, when activated by *VEGFA*, *VEGFR2* activates *Smad7*, which inhibits *Runx2* expression.[246]

4.5.5.3 Stromal cell maintenance

After 2 weeks of culture on NSQ PEEK (relative to FLAT PEEK) there was upregulation of markers associated with maintaining MSC pluripotency: *LIF*, *TERT*,

NES, *POUF51* (*OCT4*), *ZFP42* (*REX1*), *SOX2*, and *JAG1* (*CD339*). These genes maintain the multipotent cell niche which allows cell populations to rapidly expand in number before differentiating. [231, 247-252]

POU5F1 encodes for Oct4 transcription factor; overexpression leads to proliferation and primes the cell for differentiation. [253-256] *REX1* also regulates the stromal cell niche, but it responds to Oct4 and Sox2 protein levels and can inhibit *NOTCH1* expression.[257-260]

Notably, *NOTCH1* was the only stromal cell maintenance gene to be downregulated on NSQ. *NOTCH1* regulates endochondral ossification using Jagged1, Notch target genes HES1 and HEY1, and the osteogenesis master gene, *RUNX2*. [261-263] Continuous Notch signalling (as simulated *in vitro* by adenoviral Jagged1) inhibits osteoblast and chondroblast differentiation to maintain a pool of proliferating progenitor cells. [264, 265] Suppression of Notch signalling by selective knockout of *Jag1* in osteoprogenitor cells, reduces endochondral ossification, increases osteoblast maturation and increases bone mass in mice. [266, 267] Jagged1 (also known as CD339) is the most influential of the five Notch ligands and mutations in *JAG1* cause Alagille syndrome through the lack of Jagged1-Notch signalling. [268] Patients usually exhibit butterfly vertebrae, characteristic facial dysmorphism with hypoplasia of the mandibular condyles and nasal cartilages, and pathological fractures due to diminished Notch mediated endochondral ossification.

Rat calvarial cell studies have shown that Notch signalling pathways are affected by surface nanotopography and wettability, and that inhibition of Notch signalling enhances osteoblastic differentiation of mesenchymal stromal cells cultured on Ti substrates. [269, 270] Furthermore, osteoblast differentiation was increased by DAPT (a Notch inhibitor) and was decreased by bexarotene (a Notch agonist) on the Ti-Nano surfaces as demonstrated by the *Opn* and *Alp* gene expression, *RUNX2* protein expression, and ALP activity. [271] The gene and protein expression of Hes1 was modulated by DAPT and Bexarotene in cells grown on Ti-Nano while the gene expression of *Hey1* and *Hey2* was not affected by surface topography.

Dynamic changes in Notch signalling were identified in a mouse model comparing tibial fractures (endochondral ossification) and calvarial defects (intramembranous ossification). [272] During endochondral ossification, Notch1, Jag1 and Hes1 exhibit parallel profiles of expression that increase up to day 10 post fracture. [272] During

intramembranous ossification, Notch1 expression decreases, before normalising at day 20 post fracture, whilst Jag1 and Hes1 levels increase.[272] The differential pattern of Notch signalling recorded during intramembranous ossification (i.e. Notch1 decreases as Jag1 increases) was also seen by MSCs on NSQ in this project. This suggests that NSQ was stimulating intramembranous rather than endochondral ossification.

4.5.5.4 Fibroblastic differentiation

PDGFRB (CD140b) encodes for the beta receptor for platelet derived growth factor (PDGFR- β) which engages with the MAPK pathway, and leads to cell growth, differentiation and migration.[273] PDGFR- β is associated with $\alpha\beta3$ integrin, which binds with vitronectin and fibronectin and links to the actin cytoskeleton via focal adhesion kinase.[274] Upregulation of PDGFR- β in myofibroblasts contributes to the formation of liver and renal fibrosis and soft tissue cancers.[275]{Chang, 2018 #5177, 276]

4.5.5.5 Chondrogenesis

BMP7 (also known as osteogenic protein-1) has been marketed in a recombinant form as an osteogenic growth factor.[277] Increasingly, research demonstrates that it promotes a chondrogenic phenotype in MSCs; and also stimulates osteogenic markers so likely has an important role in endochondral ossification.[278-282]

GDF5 and *GDF6* (formally known as BMP14 and BMP13 respectively) are growth factors and members of the BMP-TGF β superfamily important for skeletal development; particularly chondrogenesis.[283-286] Abnormalities of these genes in humans cause severe chondrodysplasia.

SOX9 is important for maintaining proliferating chondroblastic cells. *In vitro*, when *SOX9* expression decreases, cells lose their matrix-forming abilities, hypertrophy, and favour deposition of collagens type I and X, rather than collagen type II.[264] *SOX9* has previously been shown to increase on NSQ nanopatterned polymer and an increase was also observed in this project.[287] This would suggest that the NSQ nanopattern is also activating the endochondral ossification pathway.

Upregulation of *COL1A1* is considered an indication of osteoblastic differentiation; although chondrocytes and adipocytes also express the gene.[288] *In vitro*, within a

cell aggregate, chondroprogenitors switch from expressing *COL1A1* to *COL2A1*, but the peripheral cells continue to express *COL1A1*. [289-291]

4.5.5.6 Osteoblastic differentiation

RUNX2 is instrumental for osteogenesis by promoting osteoprogenitor proliferation and inhibiting differentiation during intramembranous ossification. *RUNX2* also has an important role in endochondral ossification by inhibiting chondroprogenitor differentiation. [292] Homozygous *Cbfa1* null mice do not produce a skeleton and are non-viable. [293, 294]

Haploinsufficiency of *RUNX2* by mutations on chromosome 6p21 causes cleidocranial dysplasia, a syndrome that disproportionally affects bones formed by intramembranous ossification (e.g. the distal clavicle). [295, 296]

RUNX2 expression occurs in a temporal manner over the first two weeks in culture: peak levels occur on day 5 and expression diminishes by day 14. [211] *Runx2* expression identifies cells of the osteoblast lineage and induces expression of the bone markers osteocalcin and collagen $\alpha 1$ in the early stages of bone formation. [297-299] Mice transfected with defective *Runx2* had reduced osteoblasts, but had normal expression of collagen $\alpha 1$ and osteocalcin, indicating that *Runx2* is not required for bone maturation. Indeed, the transgenic mice had an age-related increase in compact bone that featured densely and regularly packed collagen fibrils with increased mineralisation. [300] Conversely, overexpression of *Cbfa1/Runx2* in mice at the collagen $\alpha 2$ promoter led to fragility fractures due to excessive proliferation of immature osteoblasts and a deficiency in mature osteocalcin-expressing osteoblasts. [301] The relative down-regulation of *RUNX2* on NSQ surfaces at 2 weeks seen in this project suggests that the genetic switch from proliferation to differentiation has already occurred. [211, 302]

Smad (Mothers against decapentaplegic homolog) protein binding occurs within the TGF β /BMP, Notch, Wnt/ β -catenin, Mitogen-activated protein kinase (MAPK), and NF- κ B signalling pathways and is an essential part of osteogenesis. Smurf1 and Smurf2 are Smad ubiquitin regulatory factors that control Smad expression. [303] Smurf1 ubiquitinates and degrades the BMP-specific receptor Smads (Smad1 and Smad5) thus inhibiting *Runx2* activity. [304] Smurf1 can also inhibit *Runx2* directly or by binding through co-activators. [305-308] Overexpression of Smurf1 in murine

osteoblasts suppressed osteoblast differentiation and bone formation, while *Smurf1*-deficient mice developed age related increased bone mass.[307, 309]

Whilst *Smurf1* controls intramembranous ossification, upregulation of *Smurf2* coincides with endochondral ossification and mineralisation of ColX. *Smurf2* ubiquitinates BMP and TGF β receptor Smads (Smad1, Smad2, Smad3 and Smad5).[310, 311] Regulation of Smads is an important mechanism by which to control osteogenesis. A previous study of MSCs on NSQ50 has shown *SMAD1* and *SMAD5* to be highly expressed relative to planar controls at day 5.[211] Suppression of Smad5 activity has been shown to inhibit osteogenic differentiation and decrease Runx2.[312] Overexpression of Smad5 induces osteoblast differentiation in C2C12 MSCs.[313-315]

A differential expression was observed between the *SMURF* genes, with *SMURF1* expression decreased (-1.74 ± 1.72) and *SMURF2* increased (1.23 ± 0.01) on NSQ. With downregulation of *SMURF1*, the intramembranous ossification pathway is initiated and with upregulation of *SMURF2*, the endochondral ossification pathway is suppressed. The ongoing maintenance of a multipotent cell niche is supporting osteoprogenitor proliferation and the downregulation of *RUNX2* is pushing the osteogenesis axis towards terminal osteoblast differentiation (Figure 56).

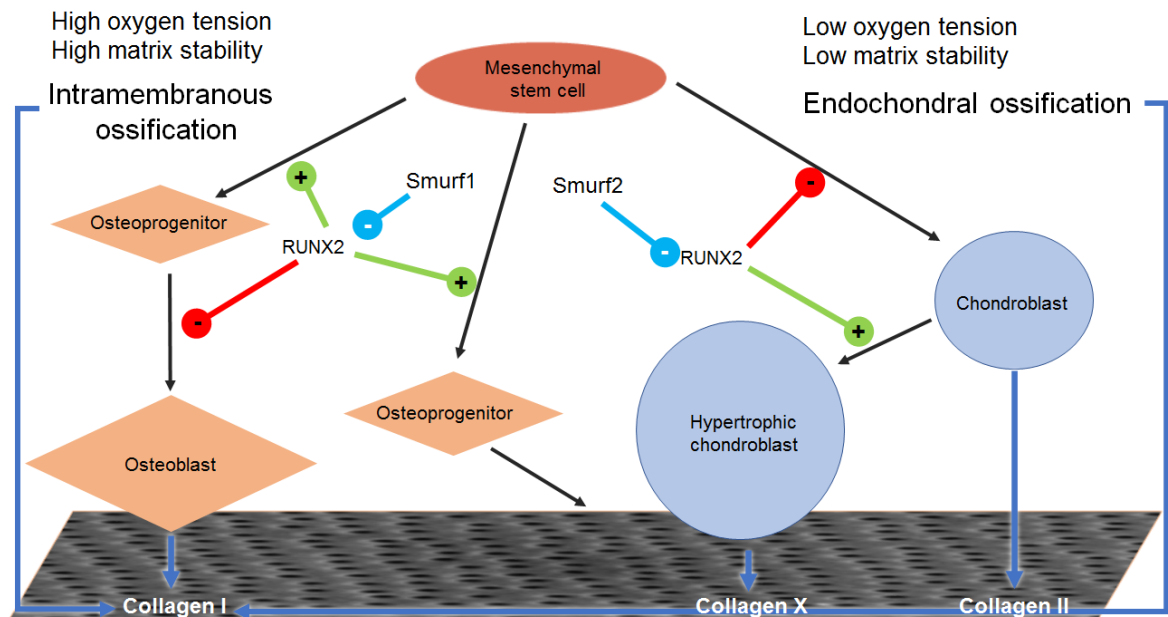


Figure 56. Smurf mediated ossification

Smurf1 mediates intramembranous ossification and Smurf2 (along with Notch signalling) controls endochondral ossification.[272, 304] Downregulation of Smurf2 and Notch signalling and upregulation of OCN suggests that NSQ is inducing intramembranous ossification.

In the early stages of bone healing, bone morphogenic protein 2 (BMP2) up-regulates transcription of the osteoblast related 'MASNSL' isoform of Runx2 via activation of Smad5 and stimulates Runx2 acetylation.[309, 316, 317] BMP2 also activates the MAPK cascades such as extracellular signal-regulated kinase 1/2 (ERK1/2), p38, and c-Jun NH2-terminal kinase 1/2 (JNK1/2) pathways which have important roles in regulating osteogenic differentiation.

BMP2, BMP4, BMP6 and BMP7 promote osteogenesis and also regulate osteoclastogenesis.[318] BMP2 and BMP6, are the most potent inducers of osteogenic markers and matrix mineralisation, and recombinant forms of BMP2, BMP4 and BMP6 have been used in clinical applications to induce bone healing.[319-323] After the initial enthusiasm for rhBMP2 in spinal surgery, complications have been observed.[324] Heterotopic bone formation occurs if rhBMP2 elutes into adjacent structures.[325] Bone resorption has been observed as rhBMP2 creates a proliferating osteoid matrix of low mechanical integrity, and vertebral collapse may result if the spine is not surgically stabilised.[326, 327]

COL1A1 encodes the pro- α 1(I) chain of type I collagen which is the major constituent of bone and *COL1A1* is expressed predominantly by MSCs of the

osteoblastic lineage.[288] Mutations in this gene cause musculoskeletal disorders such as Ehlers-Danlos syndrome and osteogenesis imperfecta.

4.5.5.7 Adipogenesis

PPARG (peroxisome proliferator-activated receptor gamma) is a type II nuclear receptor that is essential for adipogenesis.[328] *PPARG* proteins can repress *Runx2* by directly binding the Runt domain or indirectly without binding.[329, 330]. No difference in *PPARG* expression was identified between the surfaces.

4.5.5.8 Extra-cellular matrix interaction

Cells adhere to extra-cellular matrix proteins via transmembrane receptor known as integrins.[331] Integrins form intracellular focal adhesions with the microfilamentous actin cytoskeleton. Intermediate filament proteins, such as vimentin and talin, can form additional bonds between integrins and the cytoskeleton in response to physical stimuli like topographical variations in the ECM or mechanical stress.[331] The modulation of focal adhesions in this manner can trigger signalling pathways to influence gene transcription and cell behaviour.

There are 18 alpha units and 8 beta subunits of integrin which can combine to form 24 different heterodimers in humans.[332] Specific integrin heterodimers may bind to a number of different extra-cellular matrix proteins, thus creating overlapping roles. For example, inhibition of $\beta 3$ and $\beta 5$ integrin subunits affects *RUNX2* expression in MSCs, but individual blockage of either subunit has no effect.[211] In contrast, the $\beta 1$ integrin subunit assembles with 12 different α chain partners and knockout of $\beta 1$ integrin in mice is lethal at the preimplantation stage.[333] Collagen type I (which is predominant in bone) binds to integrins $\alpha 1\beta 1$ and $\alpha 2\beta 1$.[332] Cartilage-specific deletion of $\beta 1$ integrin gene in mice causes severe chondrodysplasia characterized by a distorted collagen fibrillar network and decreased proliferation of chondrocytes.[334]

The PCR array used in this project analysed the expression of genes encoding for $\alpha 6$, αv , αx , and $\beta 1$ integrin subunits. *ITGAX* expression was not identified, and there was no difference identified in *ITGAV* expression. *ITGB1* (*CD29*) and *ITGA6* expression were upregulated on NSQ.

Integrin $\alpha 6$ subunits dimerize with $\beta 1$ or $\beta 4$ chains, and these heterodimers bind to laminin or collagen. Deletion of integrin $\alpha 6$ in mice leads to a lethal phenotype with

cerebral malformations and severe skin blistering [19]. Integrin $\alpha 6$ is upregulated by Oct4 and Sox2 and causes dephosphorylation of FAK.[229, 335]

$\alpha \beta 1$ binds to fibronectin and $\alpha \beta 3$ and $\alpha \beta 5$ bind to vitronectin.[336] In a previous study investigating MSC behaviour on NSQ, *ITGAV* was upregulated, at day 5 on cells cultured on PCL.[211]

The expression of integrin encoding genes is a dynamic process that is affected by the existing ECM environment and *de novo* ECM production. An inverse relationship has previously been observed between ECM protein production and integrin gene expression.[336] Less adherent surfaces may upregulate integrin subunits to facilitate adequate cell-ECM attachment.[336]

VIM encodes for the intermediate filament protein, vimentin, which forms dynamic focal adhesions used for cell motility. It is thought that vimentin-based adhesions can respond to nanotopography and regulate subsequent cell behaviour through interaction with integrins and cell-signalling pathways.[337] *VIM* was upregulated on NSQ (0.91 ± 0.01).

PTK2 encodes for protein tyrosine kinase 2, which is better known as focal adhesion kinase, or FAK. FAK is an important part of the Rho-ROCK signalling pathway involved in osteoid mineralisation.[338] Focal adhesion kinase appears to be a supplementary component of focal adhesions, that is dynamically recruited in response to topography induced integrin clustering.[339] FAK can bind directly to the tail of β integrin sub-units, and to talin and paxillin via its FAT domain.[222, 340] FAK was downregulated on NSQ (-1.00 ± 0.01).

4.5.6 Summary

It has been shown in this chapter that oxygen plasma treatment can be used to increase MSC surface coverage on planar and nanopatterned PEEK surfaces. Oxygen plasma treatment can increase overall expression of bone minerals *in vitro* as a result of increased cell adhesion and prevalence but it does not stimulate osteogenesis.

Analysis of mineral production from cultures of MSCs on nanopatterned PEEK demonstrated that: the SQ nanopattern increases MSC prevalence; HEX

nanopattern of PEEK decreases cell adhesion; and NSQ nanopatterning may increase mineralisation. Oxygen plasma treatment diminishes the effect of nanopatterning.

NSQ nanopatterning in PEEK promotes expression of stromal cell maintenance genes and may stimulate intramembranous ossification via inhibition of Notch signalling (Figure).

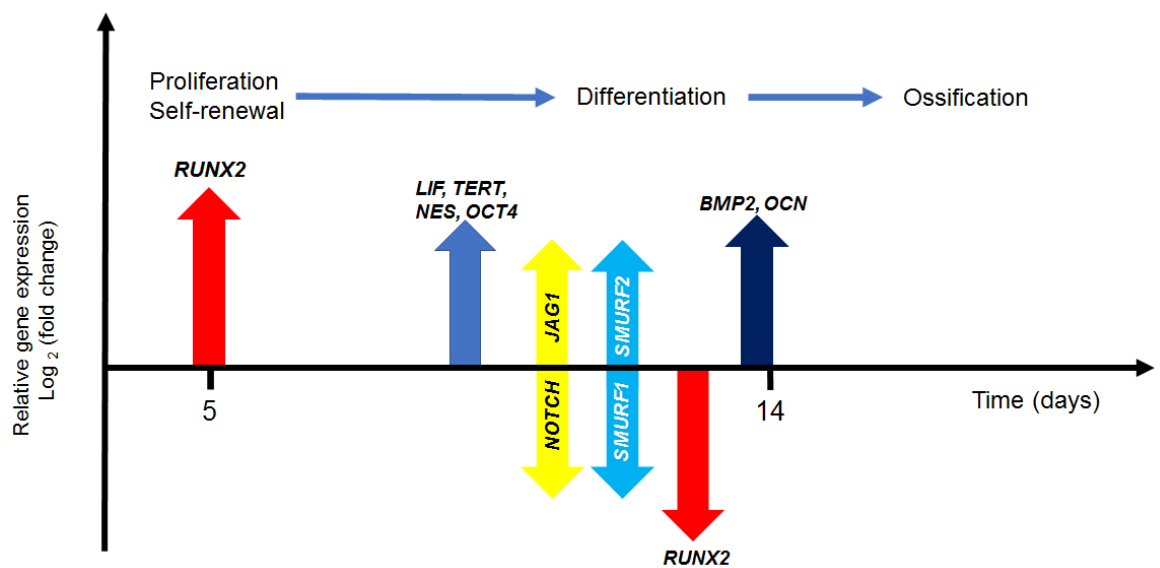


Figure 57. Temporal expression of osteogenic genes

Runx2 is expressed early in osteogenesis and becomes down-regulated at day 14 to permit differentiation and induce ossification with upregulation of BMP2 and OCN. Differential expression within the Notch signalling pathway and the Smurfs is associated with intramembranous ossification and may provide an upstream genetic switch towards differentiation.

5 In vivo osseointegration of Ti coated nanopatterned polymer implants

5.1 Introduction

It is assumed that *in vitro* osteogenesis on implant surfaces translates to *in vivo* osseointegration, but bone is a complex multicellular vascularised tissue that responds to mechanical loading and animal studies are a necessary component of investigating bioactive implants. Failure of osseointegration leads to aseptic implant loosening, the most common reason for revision of orthopaedic implants.[14] It is well recognised that interfacial inconsistencies between bone and PMMA cement mantles promote acetabular loosening.[14] Similar mechanisms of osteolysis may occur in other orthopaedic implants, and a tight bone to implant interface is desired to prevent mechanical attrition from fluid and shear forces.[341, 342]

As previously shown, the bioactivity of PEEK can be modified using injection mould nanopatterning and oxygen plasma treatment. Nanopatterning appeared to exert an effect on cell behaviour, but due to the unfavourable surface energy of PEEK, the effects on osteogenesis are unsatisfactory. An alternative approach to impart bioactivity onto nanopatterned PEEK would be to apply a thin film surface coating. The technology already exists within our laboratory to apply an ultra-thin (< 20 nm) titanium layer. This final modification would potentially enable the initial project objectives to be met (Figure 58).

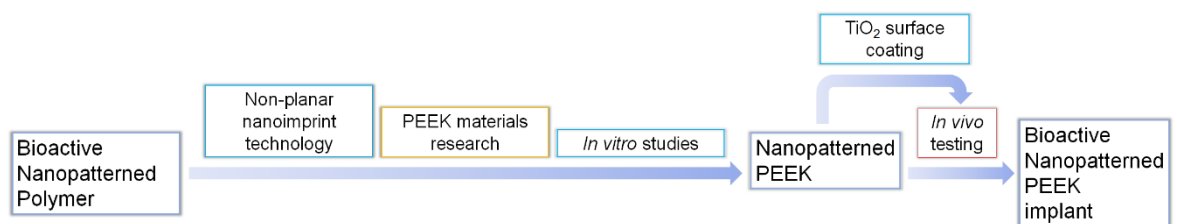


Figure 58. Revised project workflow

To meet the original aims of the project, TiO_2 surface coating was used as a method of creating a bioactive injection mould nanopatterned polymer implant.

In this study, osseointegration of Ti-coated nanopatterned implants were compared to a clinical implant generated by grit-blasting and acid-etching. Due to legal restrictions relating to intellectual property and project permits, the NSQ and HEX

nanopattern and PEEK could not be used. Consequently, SQ and RAND nanopatterns were used and injection moulded polycarbonate surfaces were used as a substitute for PEEK in the following *in vivo* experiment. Due to time constraints, further *in vitro* testing could not be undertaken. There was, however, sufficient *in vitro* and *in vivo* results supporting the use of titanium nanopatterned surfaces to proceed with the animal study in Radboud University, Nijmegen. The *in vitro* application of both the SQ and RAND nanopatterns is demonstrated in Titanium, aluminium and stainless steel spontaneously form oxide on the surface. Anodisation can be used to tailor the composition and morphology of the oxide film at the nano-scale. Titania nanotubes can be formed in the range of 10-100 nm by changing the voltage, solvents or temperature used for the anodisation process.[133-136] The interaction between oxide growth and dissolution can form the nanotubes into self-arranged arrays.[137] Park et al. demonstrated that stem cell responses could be modulated by changing the diameter of nanotubes.[133]

5.2 Aims and Objectives

The aim of this experiment was to assess the *in vivo* osseointegration of Ti-coated nanopatterned polymer implants and compare to commercially available grit-blasted acid-etched (GAE) titanium surface with proven clinical efficacy.

- Polycarbonate (SQ and RAND) nanopatterning was performed by Prof Gadegaard's Bio-Interface Group in Glasgow.
- GAE implant fabrication and titanium coating of polymer implants was performed by Prof Walboomers Research Group in Nijmegen.
- Surgical implantation and histological preparation were undertaken by Prof Walboomers Research Group in Nijmegen.
- Bone-to-implant contact (%) was assessed using light microscopy.
- The implant surfaces were assessed using SEM, AFM, water contact angle analysis and XPS.

5.3 Materials and Methods

5.3.1 Fabrication of Ti nanopatterned polymer implants

The polymer implants used in this study were made using injection mould nanopatterning as described previously.[184, 200]. The nanopattern was initially designed using L-edit software and electron beam written into a positive tone resist. The resist was developed and the nanopattern was reactive ion-etched into silicon to form an array of 120nm diameter and 100 nm depth nanopits in an ordered square (SQ) or random (RAND) pattern. 50 nm of Ni–V was sputter coated onto the silicon nanopatterns, and 0.3 mm nickel inlays (with nanopillars) were generated by electroplating. The nickel inlays were cleaned and inserted into an injection mould tool to create negative polycarbonate (Makrolon OD2015, Covestro UK Ltd., Cheshire) copies (with nanopits) using injection mould nanopatterning (Victory 28, Engel GmbH, Schwertberg, Austria).

Nanopatterned polycarbonate surfaces were uniformly coated with a 20 nm layer of titanium by radio frequency magnetron sputtering (ESM-100, Edwards, Crawly, United Kingdom) at a pressure of 5×10^{-3} mbar and a power of 100 W for 10 minutes. Thickness was confirmed using atomic force microscopy (Nanoscope IIIa, Veeco, Santa Barbara, California). The Ti coated polymer was cut into 5 mm discs using a diamond coated core drill. Petroleum jelly was used as a protective layer for the nanopatterned surface during cutting. SQ and RAND implants were ultrasonically cleaned using isopropanol and deionised water. Before surgery, the implants were autoclaved at 120°C for 15 min.

5.3.2 Fabrication of grit-blasted acid-etched titanium implants

Commercially pure titanium (grade 2) (Thyssen Krupp, Veghel, Netherlands) was grit-blasted and acid-etched (GAE) using 50 μm Al_2O_3 grit, followed by 90 seconds of etching in a solution of 37% acetic acid, 96% sulfuric acid, and water (1:1:1). The titanium was cut into 5 mm discs using electric discharge machining with a 150 mm diameter cutting wire in deionised water (EDM, Charmilles, Switzerland). Petroleum jelly was used as a protective layer for the modified surface during cutting. GAE implants were cleaned ultrasonically in 10% nitric acid, followed by acetone, isopropanol, and deionized water. Before surgery, the implants were autoclaved at 120°C for 15 min.

5.3.3 Implant surface characterisation

Field emission scanning electron microscopy (S-4700, Hitachi High Technologies America Inc., USA) was used to characterise the surface nanotopography.

Atomic force microscopy (Dimension 3100, Veeco, Cambridge, UK) with a pyramidal cantilever tip in tapping mode was used to profile the surfaces. In each case at least 3 locations were randomly analysed on at least 3 samples and 50 μm^2 areas were analysed using Gwyddion 2.26 software was used to measure surface roughness.

Water contact angle measurements were taken using a telescopic goniometer with CAM100 software (FTS Technologies/Attension, Manchester, UK) equipped with a Gilmont syringe and a 24-gauge flat-tipped needle. The probe fluid was deionised water purified using a Millipore Milli-Q system. At least three advancing and receding contact angle measurements were taken from each sample.

X-ray Photoelectron Spectroscopy (XPS) was carried out in a SAGE 100 system (Specs GmbH, Germany). Base pressure in the analysis chamber was approximately $2 \cdot 10^{-7}$ mbar. The X-ray source was $\text{MgK}\alpha$ operated at an anode voltage of 12.5 kV and 250 W power. Spectra were recorded at a take-off angle of 90° . The pass energy for the hemispherical analyser was 50 eV for survey scans, and 15 eV for high resolution scans. Spectra were analysed using casaXPS software, and atomic composition was determined by integration of peak areas using a standard Shirley background.

5.3.4 Surgical technique

A previously described rabbit model of cortical osseointegration was adopted.[343-345] Local approval was obtained (licence no. RU-DEC #2010-028) and all experiments followed national or institutional guidelines for the care and use of animals, and food and water were provided *ad libitum*. 12 New Zealand White adult female rabbits aged 6 months and weighing 3000-3500 g were used. They were sedated with 100 $\mu\text{g}/\text{kg}$ dexmedetomidine and 10 mg/kg ketamine and subsequently intubated and anaesthetised using an inhalation mixture of isoflurane, oxygen and nitrous oxide.

The overlying hair was clipped and the skin was prepared with iodine. A 5 cm skin incision was made to approach the anterior proximal tibial diaphysis (Figure 59).

The underlying fascia and periosteum were incised and retracted. Two pilot holes were created using a trephine drill. A uniformly flat bone surface was created using a 6 mm diameter grinding tool.

The implants were placed within the osseous defect and covered with a polytetrafluoroethylene (PTFE) cap (Plastics One, Roanoke, VA). The implants were held adjacent to the tibia using a pre-formed 40 mm reconstruction plate and five 1.25 mm diameter, 3 mm long screws. Tissues were sutured closed in separate layers. After randomisation, discs were implanted bilaterally in each rabbit (i.e., 4 implants were used per rabbit and 48 implants were used in total).

The rabbits received 20 µg/kg Temgesic, 500 µg/kg Antisedan, and antibiotics for 5 post operative days. Initially, the surgical wounds were examined on a daily basis. Weight, behaviour, and overall health conditions were monitored during the whole study period.

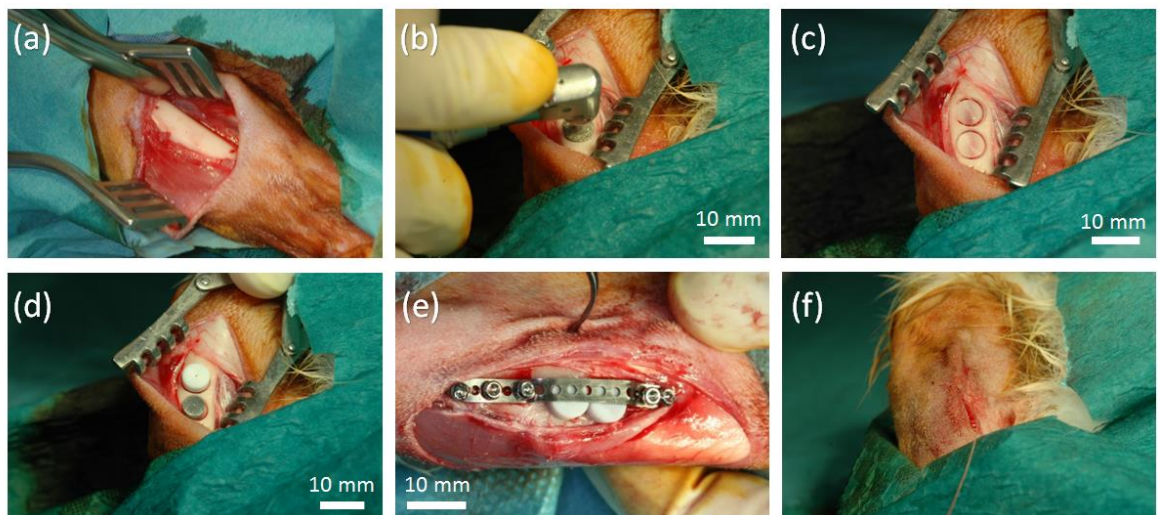


Figure 59. Surgical implantation of Ti coated polymer implants

(a) After preparation of the skin with iodine the proximal tibia was exposed and the periosteum retracted under sterile conditions. (b) A rotary grinder was used to create two flat bone surfaces (c). (d) The implants were inserted into the excavations and a PTFE cap was placed on top. (e) A 40 mm reconstruction plate was used to hold the implants in place against the bone and the layers were closed (f).

5.3.5 Histological staining

Tibiae were harvested after 4 or 8 weeks of implantation. Surrounding soft tissues were removed and each tibia was fixed in 4% formaldehyde for 5 days, dehydrated

in a graded series of ethanol, and embedded in methyl methacrylate. After polymerization, 10 μm non-decalcified sagittal cross sections of the tibia and implants were cut using a modified diamond bladed microtome saw technique and stained with methylene blue/basic fuchsin.[346, 347]

5.3.6 Histological analysis

Digitally stitched 20x images from optical microscopy (Axio Imager Microscope Z1, Carl Zeiss Micro Imaging GmbH, Germany) were assessed and the bone-implant contact (BIC) percentage was measured. The images were imported into Image J software.[348] A linear measurement was made of bone in contact with the implant without fibrous tissue interposition and this was divided by the total length of the implant to determine the % BIC. Quantitative measurements were conducted for three sections per implant. Statistical analysis was performed in Microsoft Excel. BIC percentages were compared using un-paired Student's T test.

5.4 Results

5.4.1 Implant surface characterisation

Scanning electron microscopy and atomic force microscopy revealed the different surface nanotopographies (Figure 60). GAE featured irregular peaks and troughs creating an increased micro-roughness. The SQ surface exhibited nanopits with the characteristic ordered square pattern with 300 nm periodicity. The nanopits had enlarged in diameter from the original 120 nm master. The RAND surface demonstrated a random distribution of nano-pits which have slightly reduced diameter from the original 120 nm master. There appeared to be a larger inter-pit surface area available on the RAND surface.

The highest peaks analysed in the GAE surface approached 5 μm and the roughness (S_a) was 571 ± 266 nm. The SQ and RAND surface, however, were flat at the micro-scale as only the nanopattern contributed to the roughness of the surfaces. Consequently, the roughness (S_a) of SQ and RAND was 12 ± 3 nm. The depth of the nanopits were 54 ± 5 nm (SQ) and 61 ± 6 nm (RAND).

The advancing water contact angle was measured at $82.1 \pm 6.7^\circ$ for GAE and $84.5 \pm 3.0^\circ$ for SQ. The receding water contact angle was $8.7^\circ \pm 1.2$ and $8.0 \pm 1.2^\circ$ respectively. X-ray photoelectron spectroscopy was performed and the results are

shown in Figure 61, Table 11 and Table 12. This shows that Ti was present at the implant surface (16.0% in GAE, 17.7% in SQ, and 22.6% in RAND). As predicted, oxygen and carbon also form a substantial proportion of the surface layer. Ti oxidises readily to form a layer of titanium dioxide and carbon is frequently attracted to any surface exposed to atmospheric conditions. The main difference between the surfaces demonstrated by XPS is that the GAE implant surface comprises 6.8% aluminium, derived from the grit-blasting process.

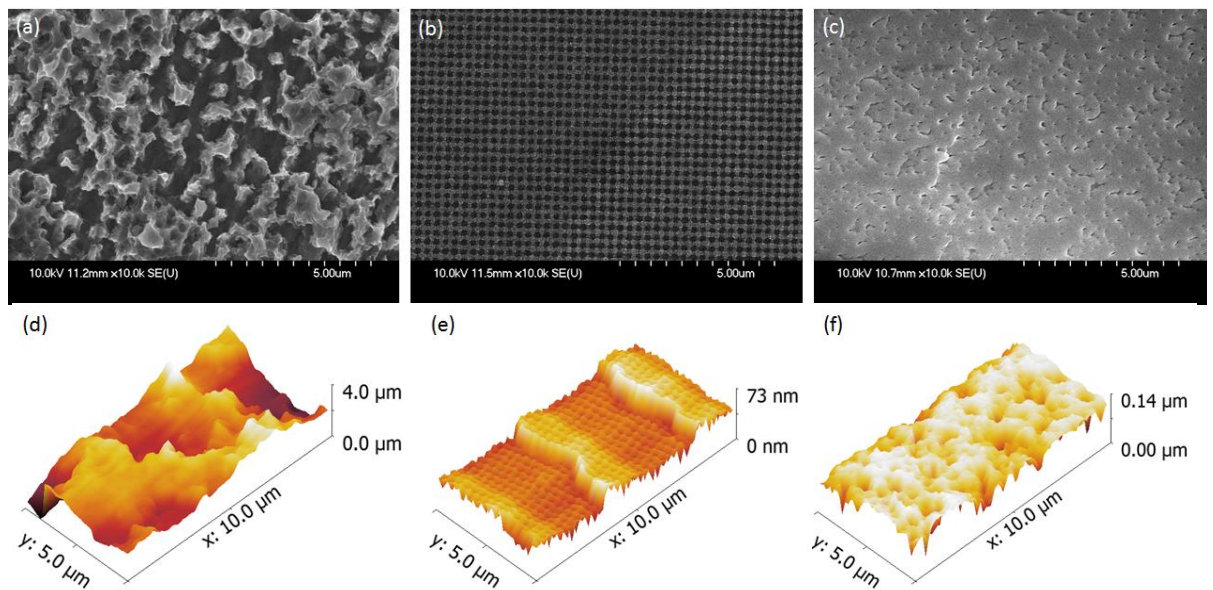


Figure 60. Surface analysis of Ti nanopatterned implants

Scanning electron microscopy (a to c) and atomic force microscopy (d to f) of the surfaces revealed a marked difference in the topography of the surfaces. The grit-blasted acid etched (GAE) surface exhibited an irregular microtopography and showed numerous peaks and troughs (a and d). The SQ surface had an ordered square array of nanopits of 200 nm diameter and a centre-centre distance of 300 nm. There also appeared to be a tidemark with a periodicity of approximately 2 μm (b and e). The RAND surface comprised a random arrangement of nanopits, which connected to adjacent nanopits to create elongated trenches.

Table 11. Surface properties of Ti nanopatterned implants

S_a (nm)	R_q (nm)	$R_{max-min}$ (nm)	Surface area (μm^2)

GAE	571 ± 266	697 ± 319	3757 ± 979	50
SQ	12 ± 1	15 ± 1	88 ± 6	50
RAND	12 ± 1	14 ± 2	124 ± 23	50

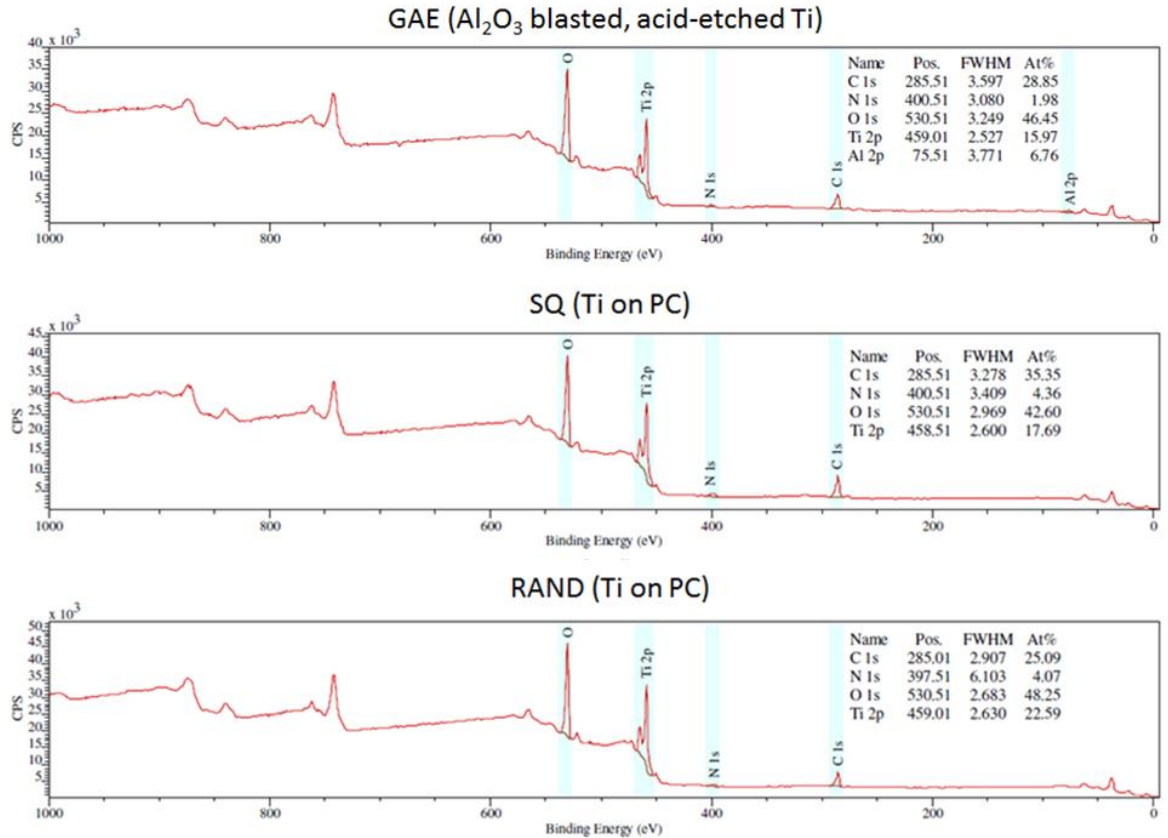


Figure 61. X-ray photo-electron spectroscopy of Ti nanopatterned implants

Chemical analysis shows a similar elemental composition of the three implants involving C, N, O, and Ti. Due to the grit-blasting process GAE also has 6.8% Al.

Table 12. Elemental analysis of Ti nanopatterned implants

	Elemental composition (at%)				
	C 1s	N 1s	O 1s	Ti 2p	Al 2p
Binding energy (eV)	285.5	400.5	530.5	459.0	75.5
GAE	28.9	2.0	46.5	16.0	6.8
SQ	35.4	4.4	42.6	17.7	0
RAND	25.1	4.1	48.3	22.6	0

5.4.2 General observations

Following surgery all animals were in good health and all wounds closed without adverse tissue reactions. 12 implants from the 4-week stage and 23 implants from the 8-week time point were successfully retrieved, embedded, sectioned and stained. Unfortunately, due to periprosthetic fractures, the original plans for mechanical testing were abandoned.

5.4.3 Histological analysis

The implants analysed after 4 weeks *in vivo* showed the PTFE caps were still in position and remodelled bone (dark red) could be easily distinguished from more mature bone (pink) (Figure 62). There was direct bone to implant contact in all groups, although intervening fibrous tissue and gapping was observed between the implant and bone in some cases.

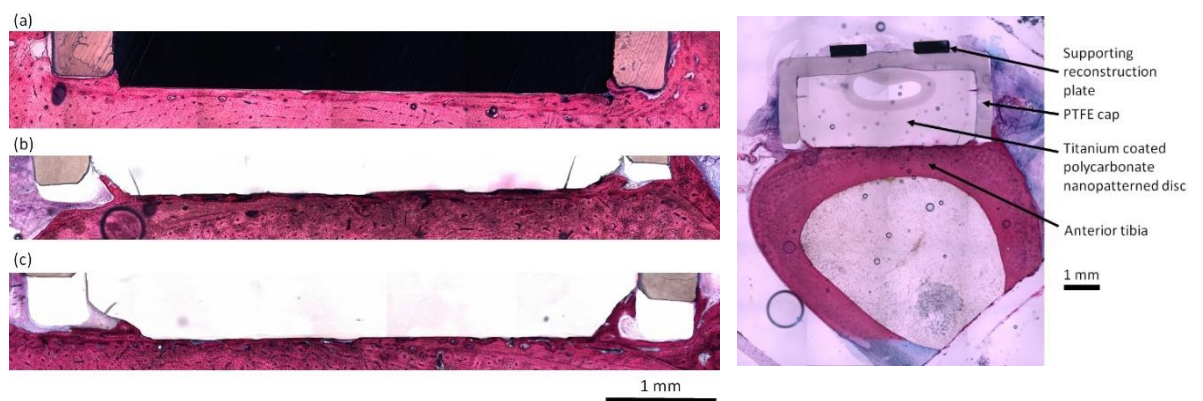


Figure 62. Histological analysis of osseointegration

20x automatically stitched digital images were used to assess bone to implant contact. These sections are representative of samples taken after 8 weeks *in vivo*: (a) GAE, (b) SQ, and (c) RAND. Histology and BIC was also assessed at 4 weeks. The GAE implant appears black as the 10 μm . thick sample allows no transmitted light to pass through, whereas the body of the SQ and RAND implants are polycarbonate which are transparent. The 20 nm titanium coating is not visible by optical microscopy. (d) A cross section of the tibia with implant, cap and plate in place. Bone tissue is stained pink and fibrous tissue appears blue.

At 4 weeks the mean bone to implant contact (BIC) was $37 \pm 20\%$ for GAE ($n = 4$), $59 \pm 11\%$ for SQ ($n = 2$), and $53 \pm 30\%$ for RAND ($n = 4$). At 8 weeks, an increased BIC was observed on the SQ and RAND nanopatterned compared to the GAE implants (Figure 62). The BIC was calculated as $55 \pm 16\%$ for GAE ($n = 5$), $80 \pm 18\%$ for SQ ($n = 6$), and $76 \pm 9\%$ for RAND ($n = 8$) (Figure 63). The difference in

mean BIC between GAE and SQ and GAE and RAND were statistically significant ($P < 0.05$).

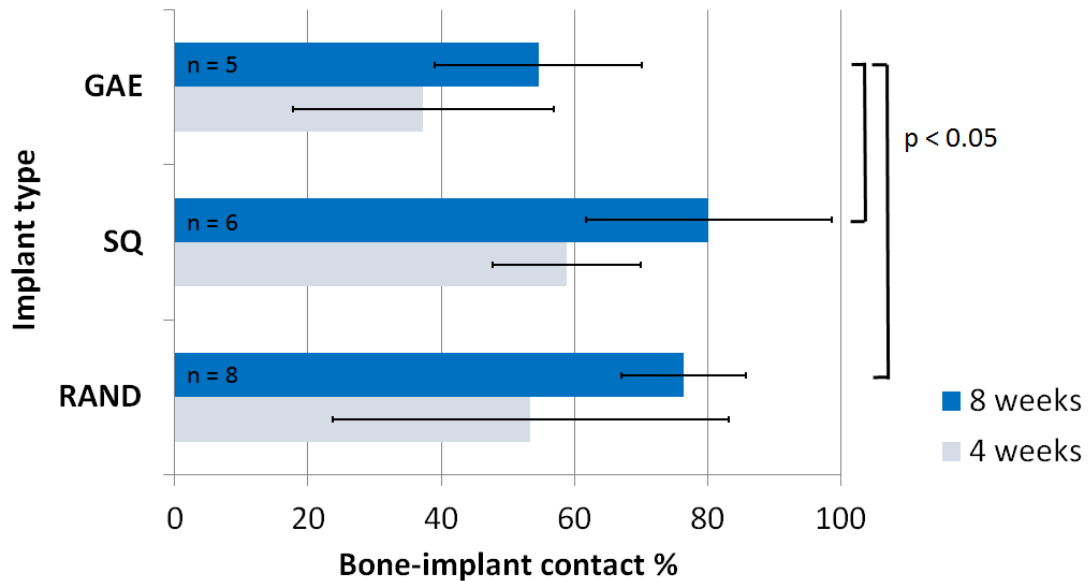


Figure 63. Bone-implant contact of Ti nanopatterned implants with rabbit tibiae

Histological analysis demonstrates an increase in BIC in all implant types from 4 to 8 weeks. There is an increased BIC on the nanopatterned SQ and RAND implants compared to GAE at both 4 and 8 weeks.

5.5 Discussion

XPS and water contact angle analysis has shown similarities between the three surfaces in elemental composition and wettability. GAE surfaces, however, contained 6.8% aluminium embedded by the grit-blasting process. Furthermore, the body of the SQ and RAND implants were moulded from polycarbonate, whereas the GAE implants were grade 2 titanium.

Young's elastic modulus of polycarbonate is 15-20 GPa and grade 2 titanium is 105 GPa.[349] Rabbit cortical bone has a Young's modulus of 13 ± 2 GPa (determined by nanoindentation), or 7 ± 1 GPa (calculated using three-point bending of the intact femur).[350, 351] The reduced modulus of the nanopatterned polymeric implants may have provided an advantageous environment for osseointegration.[352]

The most pronounced discrepancy between the surfaces was identified by surface analysis using AFM and SEM. GAE implants have a very irregular surface and an increased mean surface roughness. This provides a mechanical advantage as it enables interlocking with the porous bone surface and interfacial stability is a pre-

requisite for successful bone generation in clinical practice.[353] SQ and RAND implants were smooth at the micro-scale and, from this perspective, may have been at a disadvantage. The stability achieved by the reconstruction plate used to secure the implants to the bone may have negated the advantage of micro-roughness.

There is a direct linear relationship between surface roughness and tensile load required to remove implants.[354] Tensile pull-off testing is useful measure of osseointegration which was not performed in this study due to the unfortunate loss of test subjects. A previous study using the same animal model assessed the interfacial resistance of titanium dioxide blasted titanium implants to a tensile force and found that increasing the roughness (R_a) from 1.12 to 3.79 significantly increased the force required to remove the implant from 3.24 N to 25.28 N respectively.[345]

There is a less pronounced relationship between surface roughness and BIC. A review of sixteen *in-vitro* studies exploring this association found that increased surface roughness is correlated with increased BIC in 15 out of 16 studies.[354] Increased BIC was observed with both the SQ and RAND nanopatterned surfaces, however the S_a was only 12 nm. This result challenges the commonly held belief that surface roughness is required for osseointegration.

It has been reported that surface features can prevent cell adhesion by the disruption of focal adhesions.[1, 115] It is possible that the roughness of the GAE implants has disrupted the formation of focal adhesions and reduced bone to implant contact. Despite the lack of micro-roughness the SQ and RAND nanopatterns may have permitted the development of focal adhesions as observed *in vitro*. [122, 287, 355] It is important to note that nanotopography can be combined with micro-topography to create surface fractality if desired.

Results using the rabbit model described here have been published by several groups and provide interesting comparators.[345, 356, 357] Using Ti-6Al-4V discs (mean R_a 1.9 μm), Mathieu *et al.* found the BIC to be $27 \pm 19\%$ after 7 weeks and $69 \pm 8\%$ after 13 weeks.[358] Ellingsen *et al.* used titanium oxide blasted titanium implants with and without fluoride modification and found the BIC to be $35 \pm 14\%$ vs. $26 \pm 8\%$ at 4 weeks and $39 \pm 11\%$ vs. $31 \pm 6\%$ at 12 weeks respectively.[357] Rønold *et al.* compared seven different TiO_2 powders and found that surface treatment with 45-55 μm grains provided the highest BIC ($71 \pm 14\%$) after 10 weeks

in vivo.^[343] When compared to these studies assessing interfacial surface contact using the same experimental design it is clear that the Ti nanopatterned polymer implants used in this study produced outstanding results ($80 \pm 18\%$ for SQ and $76 \pm 9\%$ for RAND at 8 weeks).

This rabbit model assesses osseointegration on the periosteal aspect of cortical bone. It is model is well suited to investigate the cortical response of bone to a planar biomaterial surface and provides easy access for implant retrieval. Several fractures unfortunately occurred, and there were inadequate test subjects to proceed with mechanical testing. Alternative animal models may provide useful analysis of the cancellous or endosteal bone response to non-planar biomaterials.

6 Design of an *in vivo* study to assess non-planar bioactive orthopaedic implants

6.1 Introduction

It has been demonstrated in Chapter 2 that bioactive nanopatterns can be applied to non-planar surfaces. Future *in vitro* studies will provide additional insights into the genetic and molecular mechanism of osteogenesis and will allow optimisation of surface design, but analysing cell behaviour on non-planar surfaces presents some difficulties. As described previously, a bespoke cell seeding device was required to achieve adequate and uniform distribution of cells on planar PEEK surfaces. Non-planar surfaces would require additional bespoke seeding devices to achieve similarly reproducible results. Ancillary devices are also required to hold and rotate samples to achieve uniform imaging of cylindrical surfaces. Due to the design of standard AFM cantilevers, it is impossible to profile small concave surfaces as the tip cannot reach the surface. *In vivo* analysis removes some of these problems and is a clinically more relevant method of assessing osseointegration on non-planar surfaces.

The animal model used in Chapter 5 is designed to investigate osseointegration of planar surfaces on the periosteal aspect of cortical bone. For the development of future orthopaedic implants, it is necessary to also consider cancellous bone and the endosteal environment. This chapter investigates alternative animal models that can be used to assess the osteogenic response of non-planar implants.

The animal model must:

- enable comprehensive histological and mechanical testing;
- be achievable with the facilities available in our institution;
- respect the 3 r's (Replacement, Reduction, Refinement).

6.1.1 Modelling the clinical application

The clinical application is the primary consideration when designing an *in vivo* experiment to test the efficacy of an orthopaedic biomaterial. Ideally the prototype implant would be implanted in an animal that most closely resembles humans in terms of morphometric anatomy and physiology. Primates are rarely used in animal

research and the implant may have to be scaled down in accordance with the anatomy of smaller animals.

To properly test orthopaedic implants, the loading conditions in the animal model should replicate the clinical scenario. The femora and tibiae of quadrupedal mammals provide useful models of cortical, cancellous, endosteal and periosteal bone. The bones are orientated and used in a similar manner to humans, although there are important histological differences.

Histologically, rabbit bone is comparable to human bone as it is osteon-dense with Haversian systems approximately 50 to 250µm in diameter.[359] Porcine bone is comprised of sheets of plexiform bone with irregular Haversian systems which is histologically distinct from human bone.[360, 361] The cortical bone of mature sheep and goats also consists of both plexiform and dense Haversian tissue.[362] Consideration must be given to how the speed or quality of bone growth may differ in animals according to their sex, age, health and nutrition.

6.1.2 Animals as bioreactors

Alternatively, if the bioactivity of a test material is the primary concern, animals can be used as *in vivo* bioreactors to measure the bone response. The choice of model is principally led by the type of bone response that is to be assessed: osseointegration or osteogenesis; intramembranous or endochondral; cortical or cancellous; endosteal or periosteal. Bones commonly used as *in vivo* bioreactors are the cranial bones of mice and rats (for intramembranous ossification) and the tibiae and femora of rats and rabbits (for endochondral ossification).

To test osteogenesis and bone regeneration *in vivo*, a critical gap defect is created by resecting bone and the experiment assesses the ability of bone to regrow into the defect. A critical gap is a defect of both bone and periosteum that will not heal spontaneously in the animal's lifetime. The size is specific to the species (and sometimes breed) of the animal, but, for a segmental defect in a long bone, normally equates to a length 2–2.5 times the diameter of the bone.[363] If the periosteum is not removed, bone regeneration is nearly always complete.[363] A small number of studies have adopted a gap defect model to investigate osteogenesis in the rabbit femur or tibia (Table 15 and Table 16, Appendix).

To test osseointegration *in vivo*, the implant must be held onto, or within the bone. Endosteal osseointegration, relevant for most arthroplasty implants, can be assessed by inserting implants into the intramedullary canal (i.e. marrow cavity) of long bones.[364] This procedure can be combined with an osteotomy (i.e. surgical fracture) to investigate fracture healing (Table 17, Appendix). Rod shaped implants correspond to the near circular cross-sectional morphology of long bones and provide a useful platform to demonstrate nanopatterning on a curved surface.

If the biomaterial can be fabricated into a screw device, osseointegration onto cortical, cancellous, periosteal and endosteal bone can be investigated and the implant should inherently incorporate sufficient stability without needing to be additionally stabilised. Unfortunately, this project was not able to achieve injection mould nanopatterning onto the threads of a screw device and so only experimental models suited to cylindrical or rod-shaped implants were considered.

6.2 Aims and Objectives

The aim of this chapter of the project was to design an animal model to assess the *in vivo* osteogenic bioactivity of a rod-shaped implant. Ideally, it will incorporate the nanopatterned PEEK rod provided by Prof Gadegaard (Figure).

After literature review and appreciation of the facilities available in Glasgow, two models using rabbit femora were considered:

1. A critical gap segment model to investigate cortical bone regeneration along and around a bioactive implant;
2. An intramedullary model to test endosteal osseointegration of both cancellous and cortical bone onto a bioactive implant.

This will be achieved by:

1. Conducting a morphometric analysis of rabbit femora;
2. Fabrication of prototype implants;
3. Mechanical testing;
4. Cadaveric implantation.

6.3 Materials and Methods

6.3.1 Morphometric analysis of rabbit femora

24-week-old New Zealand White Rabbit cadavers of known weight were procured from the British Heart Foundation Cardiovascular Research Centre in Glasgow. All rabbits were in good health during life and had cardiac tissue removed immediately after death as part of an unrelated study. Both femurs were dissected from the fresh cadaver. The length of each femur was measured using digital callipers from the most proximal part of the femoral head to the most distal part of the femoral condyle. Each femur was then sectioned (starting from the distal end) into seven 10 mm segments using a handsaw. The cross-sectional dimensions of the most proximal end of each 10 mm section were measured using digital callipers. External anterior-posterior (A-P) and medial-lateral (M-L) distances and internal anterior-posterior and medial-lateral were recorded.

6.3.2 Fabrication of prototype nanopatterned PEEK implants

Prototypical PEEK implants were fabricated using a combination of injection mould nanopatterning and machining. LT3 PEEK pellets (Invibio Biomaterials Solutions Ltd.) were used in the Engel victory 28 injection moulding machine. A nanopatterned mould insert designed by Prof Gadegaard was used to fabricate 25 mm long PEEK rods with a 6 mm diameter (Figure 64 and 65). Implants were fabricated according to the results from the morphometric analysis of rabbit femurs.

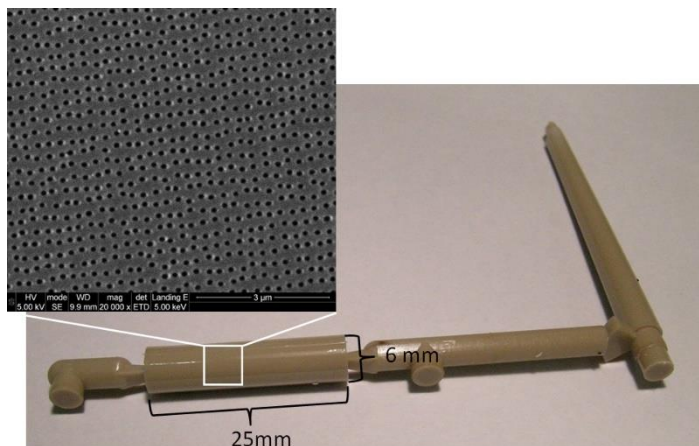


Figure 64. PEEK nanopatterned rod

A 6 mm diameter nanopatterned PEEK rod featuring NSQ nanotopography around the entire circumference (designed and fabricated by Prof Gadegaard).

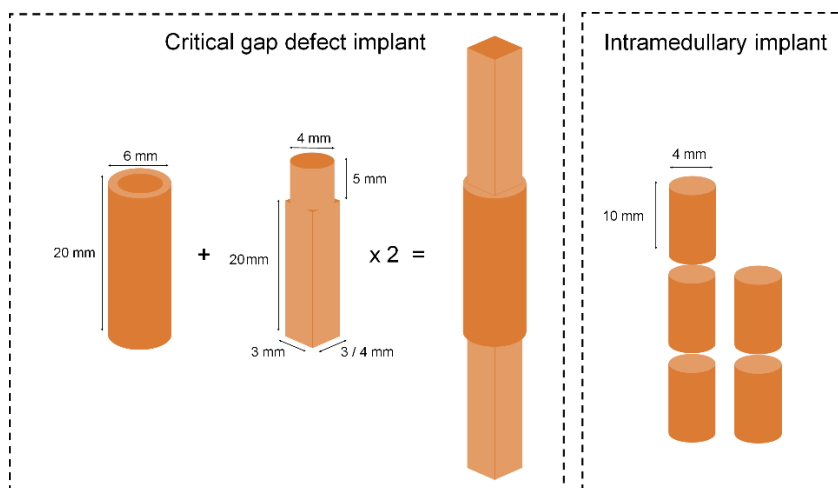


Figure 65. Fabrication of PEEK implants

Diagram showing the construction of the implants by machining two stems and attaching them to the PEEK rod.

6.3.3 Mechanical testing of prototype PEEK implants

3-point bending strength of 5 implants was calculated using a Dartec servo hydraulic testing machine. The crosshead speed was 1 mm/min and force was applied in an anterior to posterior direction at the midpoint of the PEEK rod. The distance between the support beams (lower anvils) was 40 mm. The load-deformation data was obtained and transferred to MS Excel.

6.3.4 Cadaveric implantation using a critical gap defect model of bone regeneration in rabbit femora

24-week-old Male New Zealand White Rabbit cadavers from the British Heart Foundation Cardiovascular Research Centre in Glasgow were used for trial surgery. A lateral approach was used to expose the anterior and lateral aspect of the femur from the greater trochanter proximally to the lateral condyle distally. The midpoint between the greater trochanter and the lateral femoral condyle was marked. Transverse osteotomies were made in the femur 10 mm proximal and distal to this point to remove a 20 mm femoral segment using a hand-held saw. The PEEK implant was positioned into the osteotomy gap (Figure 66).

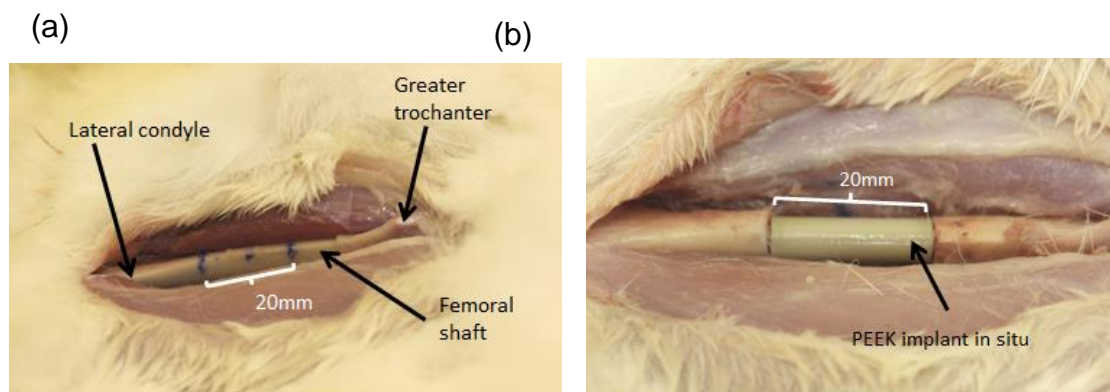


Figure 66. Cadaveric implantation using the critical gap defect model

Photo (a) shows preparation of the femur for a segmental resection of a critical gap defect. The midpoint between the greater trochanter and lateral femoral condyle was marked and marks for the osteotomies were made 10 mm cranial and 10 mm caudal to the midpoint of the femur. The osteotomies were made using a hand saw and a 20 mm segment of bone (and periosteum) was resected. In (b) the PEEK implant was inserted into the segmental gap defect and the cranial and caudal stems of the implant have been inserted into the intramedullary cavity.

6.3.5 Cadaveric implantation using an intramedullary model of osseointegration in rabbit femora

A 30 mm midline incision was made through the skin overlying the patella (Figure 67). The retinaculum lateral to the patella was incised, and the knee joint was opened. The patella was dislocated medially to expose the trochlear groove. An entry point was created in the trochlear groove and extended into the intramedullary canal using a hand drill. PEEK rods were inserted into the distal intramedullary canal with thumb pressure.

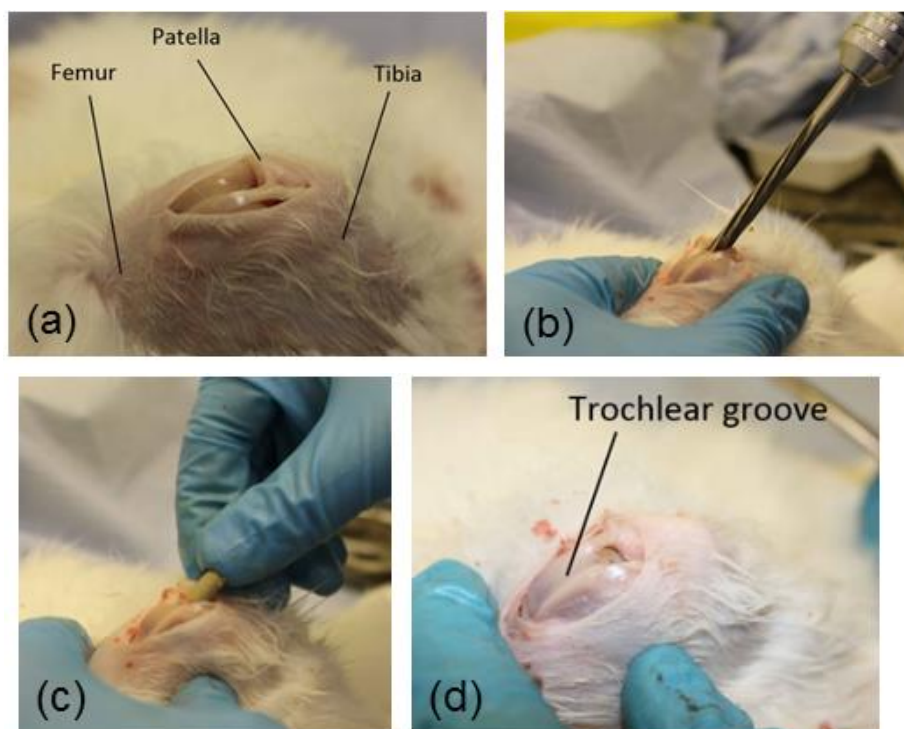


Figure 67. Cadaveric implantation using the intramedullary model

(a) A longitudinal skin incision was made over the distal femur and the lateral retinacular fibres were partially detached from the patella. The patella was dislocated medially to allow access to the trochlear part of the patella-femoral joint.

(b) An entry point was created in the trochlear groove in line with the femoral shaft.

(c) Each rod implant is inserted into the intramedullary canal using thumb pressure.

(d) The rods were advanced beyond the trochlear groove.

6.4 Results

6.4.1 Morphometric analysis of rabbit femora

12 femurs from 6 rabbits were analysed. The rabbits were, male, 24 weeks old and the mean total body weight was 3.0 ± 0.2 kg. Naturally, there was negligible difference in size between left and right femurs in the same rabbit. The mean total femoral length was 102.1 ± 0.4 mm. There was no significant difference between the lengths of any femurs measured.

As shown in Figure 68 the diameter of the femoral shaft increased in a cranial to caudal direction. The smallest femur had an internal anterior-posterior diameter of 3.81 mm and an internal medial-lateral diameter of 3.58 mm. Nevertheless, it was possible to insert a 4 mm diameter metal rod at least 50 mm into all femoral canals, indicating there was no significant femoral bowing.

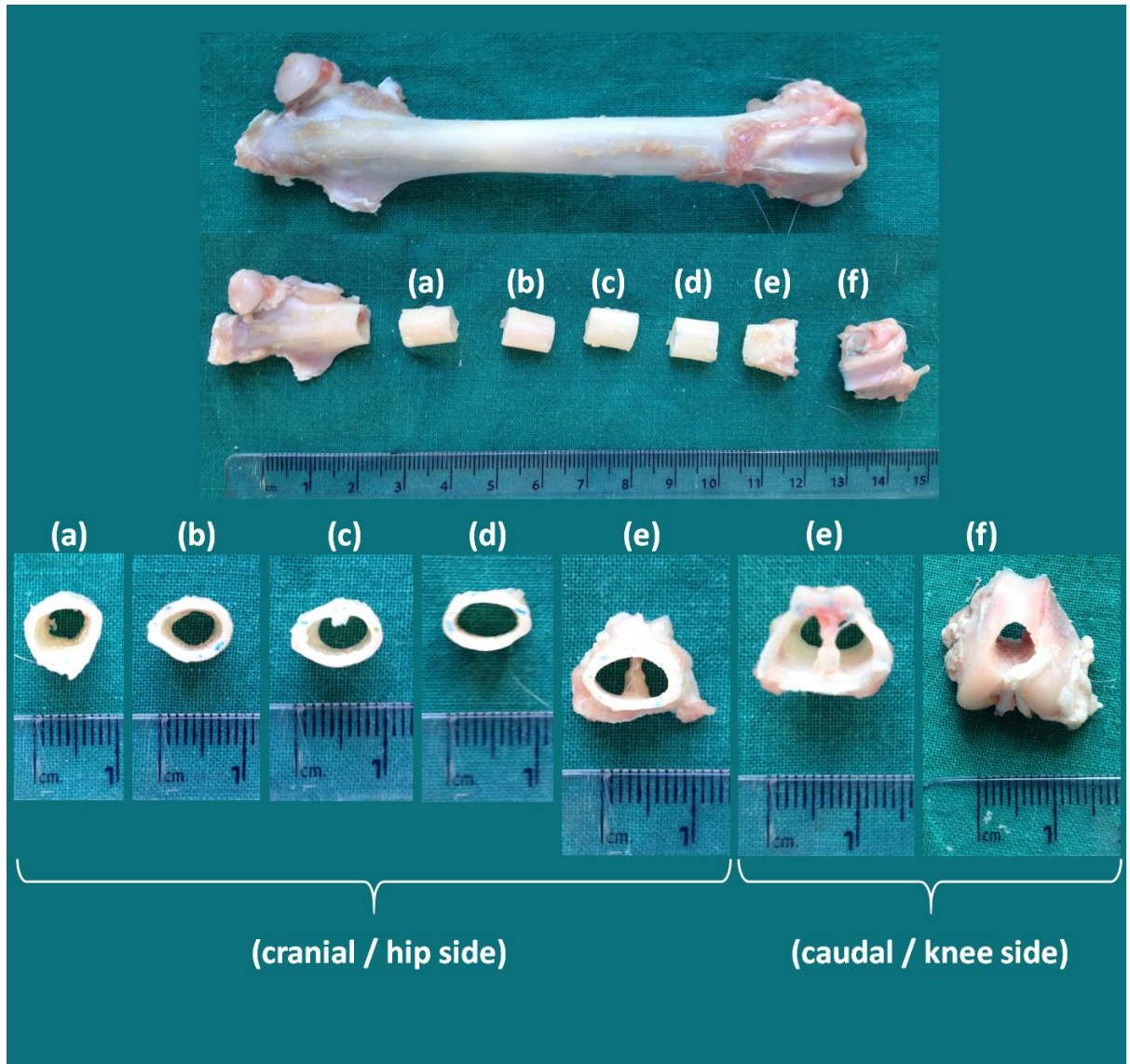


Figure 68. Morphometric study of rabbit femora

Analysis of cadaveric rabbit femora showed that the proximal femur is more circular in cross section, whereas the distal femur is wider in a medial to lateral direction and the bone becomes trapezoidal at the knee level. The femoral shaft dimensions were consistent for approximately 40 mm ((a) to (d)). The smallest intramedullary width was the most cranial section (a) with a mean anterior-posterior diameter of 4.71 ± 0.81 mm.

6.4.2 Fabrication of prototype nanopatterned PEEK implants

6.4.2.1 Critical gap defect implants

Cortical bone replacement implants were designed to fit within a critical gap defect in rabbit femurs. The construct comprised of a cranial and caudal intramedullary stem for insertion into the femoral marrow cavities. The two stems were attached to either end of the test implant which matched the length of the critical gap defect.

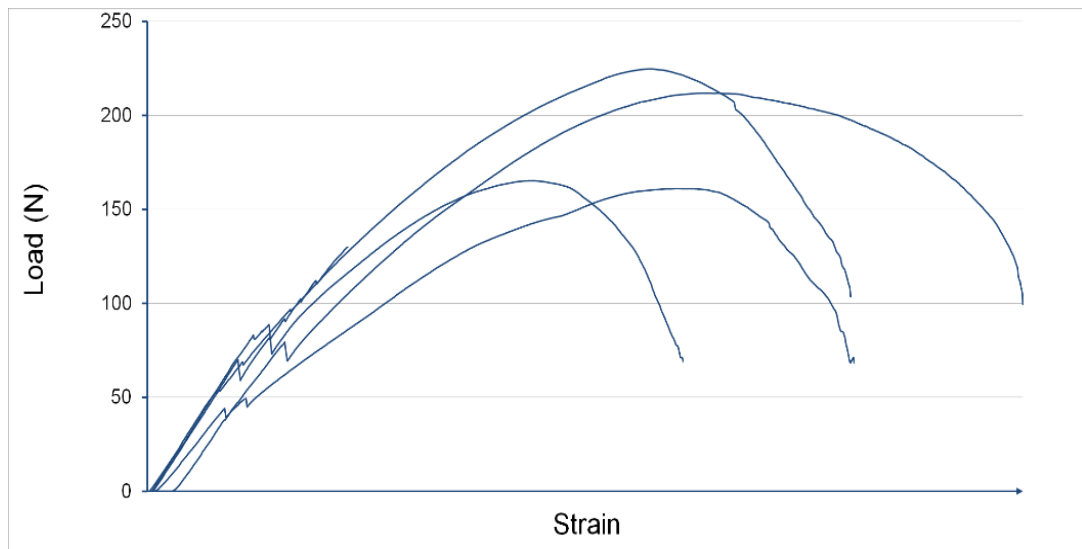
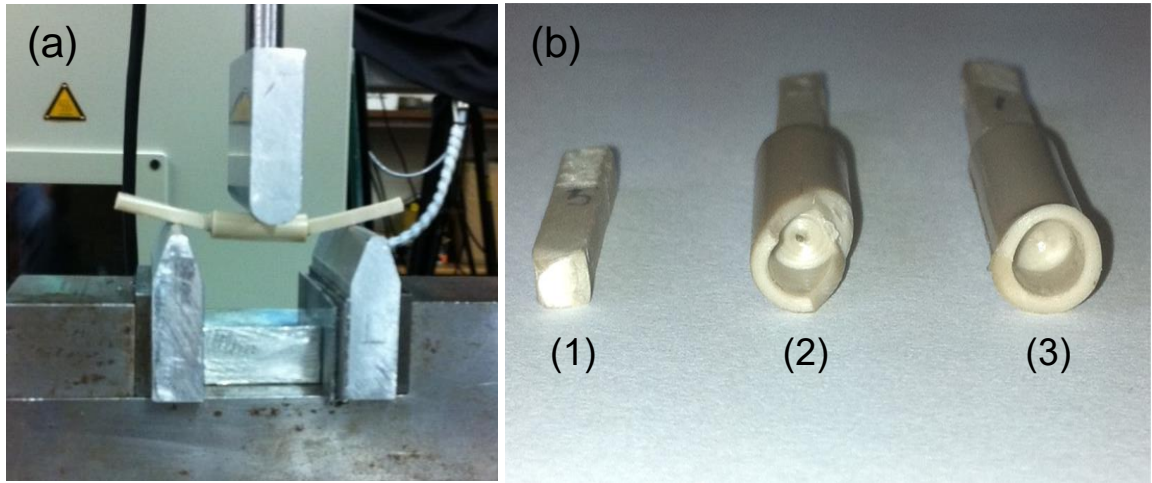
From the morphometric analysis it was decided to make the cranial stem 3 x 3 mm and the caudal stem 4 x 3 mm. The stems were 20 mm long, regular four-sided shapes (Figure 65) and were made with cylindrical plugs that inserted into equivalent sockets drilled into the PEEK rod. The three components of the implant were fixed together using cyanoacrylate resin.

6.4.2.2 Intramedullary implants

Intramedullary implants were designed to be inserted in a retrograde manner (i.e., through the trochlear groove in the knee) into the femoral cavity. The existing 6 mm nanopatterned rod was greater than the mean diameter of the rabbit femora and so 4 mm diameter rods were machined as prototype implants for the intramedullary model of endosteal osseointegration (Figure 65).

6.4.3 Mechanical testing of prototype PEEK implants

A three-point bending test was performed to determine the flexural strength of five PEEK implants designed for the critical gap segment model (Figure 69). Four implants failed due to excessive deformation of the socket rim in the PEEK rod and 1 implant failed due to breakage of one of the stem plugs. A minimum of 129.9N and a maximum of 224.7N was applied to cause implant failure. The mean flexural strength was 178.5 ± 39.0 N.



Implant no.	1	2	3	4	5	Mean
Flexural strength (N)	224.7	165.3	129.9	161.0	211.8	178.5 \pm 39.0

Figure 69. Mechanical testing of PEEK implants

A three-point bending test (a) to determine the load at failure (as shown in graph) to determine the flexural strength (as represented by the load at failure) of the PEEK implants (shown in table). The three modes of failure are shown in image (b): (1) stem fracture; (2) socket fracture; (3) socket deformation causing stem detachment.

6.4.4 Cadaveric implantation using a critical gap defect model of bone regeneration in rabbit femora

Nanopatterned PEEK rods were inserted into a gap defect in cadaveric rabbit femora (Figure 66). This showed that insertion of the pre-assembled implant into the osteotomy gap required an excessive distracting force which could cause nerve or vascular injury to the living animal. Alternatively, one of the stems was fixed *in-situ* using cyanoacrylate resin. It was not possible to achieve satisfactory stability (i.e., resistance to distraction and torsion forces) in the cadaver models by simply press-fitting the cranial and caudal stems. It was clear from trial cadaveric implantation that further methods of stabilising the femur *in vivo* are required.

6.4.5 Cadaveric implantation using an intramedullary model of osseointegration in rabbit femora

Sub-patella trans-trochlear intramedullary implantation of PEEK prototype implants was achieved in the cadaver trial. A 4 mm diameter osteotomy was created in the trochlear groove and extended into the intramedullary canal using a hand drill. A blunt 4 mm metal rod was inserted carefully by hand to ensure the canal was of an adequate width to accept the PEEK implants.

Each of the 10 mm long PEEK rods were carefully inserted with thumb pressure until the distal end of the final rod was believed to be within the epiphyseal cancellous bone. Up to six 10 mm long 4 mm diameter PEEK rods could be inserted into the intramedullary canal of each rabbit femur. Intramedullary reaming or drilling did not aid the procedure as it did not effectively increase the internal diameter of the femoral canal and risked causing fracture.

6.5 Discussion

The group of New Zealand white rabbits examined for the morphometric study had predictable femoral anatomy with little variation between subjects. The 6 mm diameter nanopatterned PEEK rod fabricated by Prof Gadegaard could be tested using the critical gap defect model or, alternatively, it could be inserted approximately 5 mm into the distal femur as a plug implant (Figure 67).

All of the stemmed PEEK prototype implants failed at the interface between the stem and the rod. Four of the implants had deformation of the 1 mm wide rim of PEEK into which the stem inserted. The remaining sample failed at the base of the 3 mm diameter proximal stem. This indicates that the mean load to failure could be increased by increasing the width of the PEEK rim.

In one study, the raw flexural strength of rabbit femurs was approximately 152.0 ± 15.7 MPa (reduced to 109.4 ± 16.9 MPa after drug treatment).[365] In a study using a composite compression and bending force, cadaveric femurs withstood 201.2 N of force applied to the femoral head, whilst osteotomised femurs with combined intramedullary and external fixation failed at 91.8 N, and osteotomised femurs that were plated failed at 47.6 N.[366] These figures are comparable to the mean load to failure of the stemmed PEEK implants. To further investigate this critical gap defect model, a compression force could be applied to the head of a femur with an implant inserted. This would create a compression load and bending moment at the osteotomy site.

A large amount of soft tissue distraction was required to insert the gap defect implants if they were pre-assembled. This was avoided by applying cyanoacrylate glue after insertion of the stemmed components. Nevertheless, there was inadequate stability of the femur after insertion of the gap defect PEEK implant. This indicated that additional fixation would be required, such as locking screws, internal plating, external fixation or intramedullary wiring.

Mechanical testing and cadaveric implantation indicated some deficiencies within the critical gap defect model. The distal intramedullary model, however, was very easy to perform and there no issues related to femoral instability. Review of similar studies revealed that implants from 3.2 to 5 mm in diameter had been inserted into the intramedullary femoral canal of New Zealand white rabbits (Appendix). This

experiment found that 4 mm diameter rod shaped implants could be inserted into the intramedullary canal 50 – 60 mm from the entry point at the knee using 24-week-old New Zealand male rabbits of approximately three kilograms. The 6 mm diameter nanopatterned PEEK rods provided by Prof Gadegaard could only be implanted into the distal 5-10 mm of the femur, and risked fracturing the femoral condyles. Rabbits with larger bones could potentially be selected by employing a minimum weight criteria of 3.5 kg.[364]

Reaming is often performed to remove cancellous bone when implanting intramedullary devices in human subjects and can lead to the insertion of a larger implant with a more secure press-fit. Examination of the cadaveric bone sections, revealed there was minimal endosteal cancellous bone and so reaming is unlikely to be successful and will risk fracture.

The implants in the intramedullary model would not be directly loaded, but they nevertheless osseointegrate in a manner analogous to stemmed arthroplasty endoprostheses.[367] The intramedullary model allows for the implantation of multiple implants which could exhibit different surfaces (and would improve statistical power) or could be used for different tests (Figure 70). No intramedullary studies have described this method of inserting multiple implants into the intramedullary cavity of a rabbit femur. The concept of testing multiple implants in one subject will risk bioactive influence from adjacent implants, but has been adopted as a standard technique in other animal models.[346]

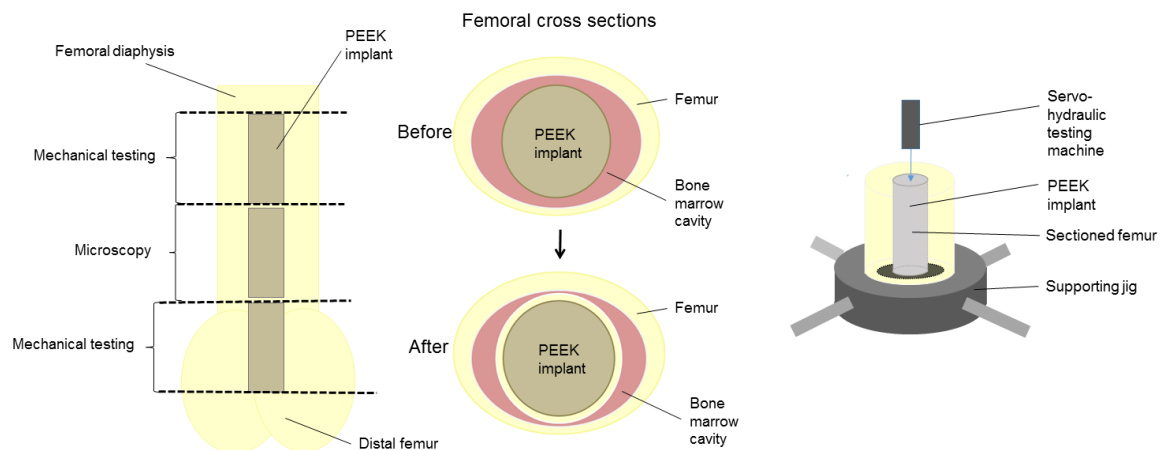


Figure 70. Proposed analysis of retrograde intramedullary model

Schematic demonstrating how the use of multiple implants in rabbit femora would allow the investigator to test endosteal osseointegration using mechanical push-out testing and microscopy. This set-up can also be modified to allow for torsional testing. A notch could be incorporated into the design of the implant to allow insertion a rotating shaft into the flat end of the rod.

Russell and Burch described a set of ethical principles to encourage a humane approach to animal studies.[368] The model proposed here respects the 3 r's of replacement, reduction and refinement as follows:

Replacement

- Considerable *in vitro* analysis using human cells
- Computer modelling will not predict bone growth
- Bioreactors will not support vascularised tissue growth

Reduction

- The minimum number of animals will be used to achieve result
- Multiple test surfaces in one animal will maximise data and statistical power

Refinement

- Peer review of methods will improve quality of study
- This preliminary cadaveric trial will minimise uncertainty

7 General Discussion

This project was ambitious in its approach to translate the in vitro findings of Dalby and Gadegaard into a clinical model to demonstrate the osteogenic capability of nanopatterning in vivo. The use of ordered square, near-square, hexagonal pattern and randomised arrays of nanopits have previously been investigated by Prof Gadegaard and his colleagues. The near-square nanopattern has demonstrated osteogenic capability in PMMA, PC, and PCL and so it was hypothesised that this bioactivity could be translated into other biomaterials.

PEEK is a biomaterial developed for injection moulding and is commonly used to make spinal implants used in intervertebral fusion procedures. Histology from animal studies demonstrates that under normal circumstances PEEK lacks the ability for osteointegration. An exciting prospect and project objective emerged: could injection mould nanopatterning be used to create osteogenic PEEK surfaces and could the technology be developed to pattern orthopaedic implants?

The technology to injection mould nanopattern polymers (including the injection moulding machine and nanopatterned nickel inlays) already existed within our department. As PEEK is specially designed for injection moulding the surfaces were easily and very successfully replicated into PEEK polymer.

The translation of the 25 mm x 25 mm nanopatterned area to an orthopaedic implant, such as a spinal fusion cage, would take significantly more development. Electron beam lithography was used to pattern a larger surface area, but this took over 48 hours, and, as the silicon wafer was sacrificed during subsequent nickel electroplating it made the fabrication process prohibitively expensive. In tandem with this project, step and repeat nanoimprinting using a modified CNC machine was developed by a colleague within our research group that could potentially be used to upscale the nanopattern to larger surface areas.[177]

Methods for nanopatterning injection mould tools were investigated. The use of soft nanoimprint lithography using PDMS stamps was investigated as this would allow transfer from flat onto curved or non-planar surfaces. This was coupled with the use of a sol-gel which could create titanium dioxide nanopillars on the injection mould materials. The sol-gel was susceptible to thermal cracking at thicknesses above 200 nm. Therefore, successful nanopatterning required a polished surface with less than

200 nm between the lowest and highest point. This was achievable using a chemical-mechanical polishing machine on flat surfaces, but non-planar surfaces needed to be polished using hand held tools.

Due to the requirement for annealing at 500°C, P20 tool steel was not suitable as it readily oxidised and destroyed the nanopattern. Aluminium was the easiest material to work with but it deformed when used in the injection moulding machine. Theoretically the presence of alloyed Al and V could cause less predictable results if the material is exposed to reactive ion etching or volatile solvents. As a mould material for use with this titanium dioxide sol-gel CpTi is considered the most suitable. Nanopatterns were successfully transferred onto 2D and non-planar surfaces using flexible PDMS stamps. Although injection mould nanopatterning was achieved using the titanium dioxide nanopatterned inlays, the nanopattern was quickly degraded.

It therefore transpired that the titanium dioxide nanopatterns were not durable enough for injection moulding. As such, the nanopatterned PEEK surfaces were all produced using nickel inlays fabricated by electroplating. At the conception of the project a decision was made to try and explore materials other than nickel for use as an inlay material. The inclusion of orthopaedic biomaterials gave the added benefit of creating nanopatterned surfaces that could potentially be used directly for orthopaedic implants. Future work could adapt the nanofabrication principles described in this project to making nanopatterned moulds with more durable sol-gel nanopatterns such as alumina and zirconia.[176]

The main objective of the project was to determine if the near square (NSQ) nanopattern was osteogenic in PEEK. Ordered square (SQ) and hexagonal (HEX) arrays of nanopits were also investigated as additional objectives to determine if these nanopatterns generated any differential effect on stromal cell cultures when compared to planar and NSQ.

Cell culture on PEEK surfaces was hindered by a lack of cell adhesion. Results were improved in vitro with improvements in cell seeding technique, including the use of a specially designed seeding device. The use of oxygen plasma treatment was also investigated to improve stromal cell adhesion to PEEK surfaces.

The effect of oxygen plasma treatment on surface chemistry, wettability and surface topography was studied. It was initially decided that oxygen plasma treatment was

beneficial to establish stromal cell cultures on PEEK and 120s of oxygen plasma treatment at 0.2 mbar for 120s for used for subsequent experiments. This specific treatment was used as it generated a substantial change in the surface chemistry while causing objectively causing minimal change in the surface nanotopography.

Oxygen plasma treatment was found to increase stromal cell adhesion and prevalence on PEEK surfaces. As such, overall calcium expression (as determined by ARS staining) and phosphate expression (as determined by VK staining) was increased on oxygen plasma treated surfaces. When calcium and phosphate expression was considered relative to cell number on the PEEK surfaces however, calcium and phosphate expression was decreased with the use of oxygen plasma treatment. Furthermore, stromal cells were less prevalent but demonstrated increased relative expression of calcium on NSQ compared to FLAT and SQ PEEK using ARS stain.

As the NSQ nanopattern has osteogenic capabilities on other substrates, priority was given to comparing NSQ with planar surfaces during the PCR experiments in this thesis. The PCR array used in this project was chosen as it provided a useful indication of differentiation cues. This seemed to be the most logical starting point to assess multipotent cell behaviour. With more time, it may have been useful to identify additional osteogenic markers (RUNX2, OCN, BMP2, BMP4, COL1A1 were assessed using the PCR array) at a number of time points on all the available nanopatterns (NSQ, SQ, HEX and RAND) to fully elucidate cell behaviour at a molecular level. Given the problems associated with cell adhesion and underwhelming levels of mineralisation, it was not considered worthwhile to spend large amounts of resources on further PCR experiments.

This finding encapsulated the adhesion-mineralisation paradox that appeared to exist on injection mould nanopatterned PEEK, which results in reduced adhesion and proliferation of stromal cells, but increased osteogenic capability.

In this respect, the NSQ nanopattern does exert a similar effect on PEEK as compared to PMMA, PC and PCL, but the inherent hydrophobic nature of PEEK resists cell adhesion. It is unlikely that nanopatterning of PEEK in isolation would be sufficient to promote osseointegration. The additional use of oxygen plasma treatment is described throughout this thesis, but when considering the results in comparison to those obtained by colleagues using osteogenic media and titanium

nanopatterned surfaces, the PEEK surfaces did not meet the threshold for use in an animal study. Surface modification of PEEK by coating offers the best option for promoting osseointegration of PEEK implants.

As such, titanium nanopatterned surfaces were used in the *in vivo* study of osseointegration described in this thesis. It would have been preferable to use the NSQ nanopatterned PEEK for this experiment, but this was prevented by a pending patent application. The Ti coated SQ and RAND nanopatterned PC surfaces used demonstrated superior bone to implant contact ratios when compared to a commercially available Al_2O_3 grit-blasted, acid-etched titanium surface (Figure). Further work should involve the use of SQ and NSQ nanopatterns and also include mechanical testing.

Involvement in this *in vivo* study revealed a number of potential shortcomings of the animal model in terms of representing orthopaedic application. The fixation of implants to rabbit tibiae has been predominantly been used to investigate osseointegration of surfaces for use in dental applications. This led to the additional development of animal models for the assessment of osseointegration and osteogenesis of non-planar implants.

NSQ nanopatterned PEEK rods were fabricated by Prof Gadegaard, with the potential for use in an *in vivo* study of osseointegration. The method used by Prof Gadegaard involved an adaptation of previous nickel die electroplating and was felt to be very high in cost and resources and not immediately translatable to more complex geometries. Morphometric studies of rabbit cadavers in this project favoured the use of 4 mm diameter rods as these could be implanted into the femoral intramedullary canal to assess endosteal osseointegration. The prototype PEEK implants produced in this project for a critical gap defect model of osteogenesis would require additional orthopaedic stabilisation and is not recommended.

8 Conclusion and Outlook

Osteogenesis by MSC on nanopatterned PEEK was observed to a lesser degree than had been previously been demonstrated with other polymers such as PMMA, PC and PCL. [1, 211, 369] Although bone marrow cells adhered to the PEEK nanopatterns in small numbers, the cells exhibited a more osteogenic phenotype, demonstrated by relative increased in calcium and phosphate expression. Similar trends in cell behaviour were observed in the NSQ, SQ and HEX nanopatterns to previous studies (NSQ is osteogenic, SQ is enables cell proliferation and HEX is non-fouling) but the inherent cytophobicity exhibited by PEEK was difficult to overcome.

Mesenchymal stromal cell culture on PEEK nanopatterns revealed that oxygen plasma treatment increased cell adhesion but mitigated the bioactive effect of nanopatterning. These experiments provide further evidence to support the hypothesis that nanopatterning directs cell behaviour by nanotopographical changes in surface chemistry and surface energy which affect cell adhesion sites. Additionally, PCR has supported the osteogenic effect of NSQ nanopatterning on PEEK and has highlighted a role for modulation of the Notch signalling pathway.

PEEK will continue to be a valuable biomaterial use use as intervertebral fusion cage and bone anchors. It is not suitable for use as a bearing material in high demands joint replacements such as hip and knee, but could be used for lower demand smaller joint replacements in the hands and feet.

Although not suitable for use in high performance injection mould inlays, the titanium dioxide precursor sol-gel can be used to nanopattern orthopaedic implants to promote osseointegration. Furthermore, as demonstrated by the *in vivo* study presented in this thesis, injection mould nanopatterned polymeric implants (such as PEEK) can be modified with an ultra-thin layer of titanium to improve osseointegration.

With a view to further pre-clinical studies of nanopatterned implants, improved *in vivo* models of osseointegration and osteogenesis in rabbits were developed. These will allow the assessment of the next generation of nanopatterned implants and satisfied the UK Home Office requirements for reduction, refinement and replacement of animal models.

9 References

- [1] Dalby MJ, Gadegaard N, Tare R, Andar A, Riehle MO, Herzyk P, et al. The control of human mesenchymal cell differentiation using nanoscale symmetry and disorder. *Nature materials*. 2007;6:997-1003.
- [2] Kurtz SM. Applications of polyaryletheretherketone in spinal implants. In: Kurtz S, editor. *PEEK Biomaterials Handbook*. USA: Elsevier; 2012. p. 201-20.
- [3] Poulsson AHC, Richards RG. Surface modification techniques of polyetheretherketone, including plasma surface treatment. In: Kurtz S, editor. *PEEK Biomaterials Handbook*. USA: Elsevier; 2012. p. 145-61.
- [4] Gadegaard N, Thoms S, Macintyre DS, McGhee K, Gallagher J, Casey B, et al. Arrays of nano-dots for cellular engineering. *Microelectronic Engineering*. 2003;67-68:162-8.
- [5] Kurtz SM, Devine JN. PEEK biomaterials in trauma, orthopedic, and spinal implants. *Biomaterials*. 2007;28:4845-69.
- [6] Brydone AS, Meek D, Maclaine S. Bone grafting, orthopaedic biomaterials, and the clinical need for bone engineering. *Proceedings of the Institution of Mechanical Engineers Part H, Journal of engineering in medicine*. 2010;224:1329-43.
- [7] Gadegaard N, Martines E, Riehle MO, Seunarine K, Wilkinson CDW. Applications of nano-patterning to tissue engineering. *Microelectronic Engineering*. 2006;83:1577-81.
- [8] Abraham CM. A brief historical perspective on dental implants, their surface coatings and treatments. *Open Dent J*. 2014;8:50-5.
- [9] Eynon-Lewis NJ, Ferry D, Pearse MF. Themistocles Gluck: an unrecognised genius. *British Medical Journal*. 1992;305:1534-6.
- [10] Brand RA, Mont MA, Manring MM. Biographical sketch - Themistocle Gluck (1853-1942). *Clinical orthopaedics and related research*. 2011;469:1525-7.
- [11] Bothe RT, Beaton LE, Davenport HA. Reaction of bone to multiple metallic implants. *Surgery, Gynecology and Obstetrics*. 1940;71:598-602.
- [12] National Joint Registry. *National Joint Registry for England & Wales 4th Annual Report*. 2007.

- [13] Brånemark R, Brånemark P-I, Rydevik B, Myers RR. Osseointegration in skeletal reconstruction and rehabilitation. *Journal of Rehabilitation Research and Development*. 2001;38:175-81.
- [14] National Joint Registry Editorial Board and Contributors. 17th Annual Report. 17th ed2020. p. 1-312.
- [15] Tzaphlidou M. Bone architecture: collagen structure and calcium/phosphorus maps. *J Biol Phys*. 2008;34:39-49.
- [16] Frost HM. From Wolff's law to the Utah paradigm: Insights about bone physiology and its clinical applications. *The Anatomical Record*. 2001;262:398-419.
- [17] Mills LA, Simpson, A.H.R.W. In vivo models of bone repair. *JBJS*. 2012.
- [18] Wancket LM. Animal Models for Evaluation of Bone Implants and Devices: Comparative Bone Structure and Common Model Uses. *Veterinary pathology*. 2015;52:842-50.
- [19] Brånemark R, Öhrnell L-O, Skalak R, Carlsson L, Brånemark P-I. Biomechanical characterization of osseointegration: An experimental in vivo investigation in the beagle dog. *Journal of Orthopaedic Research*. 1998;16:61-9.
- [20] Long M, Rack HJ. Titanium alloys in total joint replacement—a materials science perspective. *Biomaterials*. 1998;19:1621-39.
- [21] Furlong RJ, Osborn JF. Fixation of hip prostheses by hydroxyapatite ceramic coatings. *Journal of Bone & Joint Surgery [Br]*. 1991;73:741-5.
- [22] Rajaratnam SS, Jack C, Tavakkolizadeh A, George MD, Fletcher RJ, Hankins M, et al. Long-term results of a hydroxyapatite-coated femoral component in total hip replacement: A 15- to 21-year follow-up study. *Journal of Bone & Joint Surgery [Br]*. 2008;90-B:27-30.
- [23] Lazarinis S, Kärrholm J, Hailer NP. Increased risk of revision of acetabular cups coated with hydroxyapatite. *Acta orthopaedica*. 2010;81:53-9.
- [24] Lazarinis S, Kärrholm J, Hailer NP. Effects of hydroxyapatite coating on survival of an uncemented femoral stem. A Swedish Hip Arthroplasty Register study on 4,772 hips. *Acta orthopaedica*. 2011;82:399-404.
- [25] Paulsen A PA, Johnsen SP, Riis A, Lucht U, Overgaard S. Effect of hydroxyapatite coating on risk of revision after primary total hip arthroplasty in

younger patients: findings from the Danish Hip Arthroplasty Registry. *Acta orthopaedica*. 2007;78:622-8.

[26] Tonino AJ, van der Wal BC, Heyligers IC, Grimm B. Bone remodeling and hydroxyapatite resorption in coated primary hip prostheses. *Clinical orthopaedics and related research*. 2009;467:478-84.

[27] Wong M, Eulenberger J, Schenk R, Hunziker E. Effect of surface topology on the osseointegration of implant materials in trabecular bone. *Journal of biomedical materials research*. 1995;29:1567-75.

[28] Lindahl O. Mechanical properties of dried defatted spongy bone. . *Acta Orthop Scand* 1976;47:11-9.

[29] Burstein A, Reilly D, Martens M. Aging of bone tissue: mechanical properties. *JBJS*. 1976;58:82-6.

[30] Li Y, Yang C, Zhao H, Qu S, Li X, Li Y. New Developments of Ti-Based Alloys for Biomedical Applications. . *Materials (Basel)* 2014;7:1709-800.

[31] Navarro M, Michiardi A, Castano O, Planell JA. Biomaterials in orthopaedics. *Journal of the Royal Society, Interface / the Royal Society*. 2008;5:1137-58.

[32] Van Noort R. Titanium: the implant material of today. *Journal of Materials Science*. 1987;22:3801-11.

[33] Brånemark PI, Breine U, Johansson B, Roylance PJ, Röckert H, Yoffey JM. REGENERATION OF BONE MARROW. *Cells Tissues Organs*. 1964;59:1-46.

[34] Brånemark PI, Breine U, Adell R, Hansson BO, Lindström J, Ohlsson Å. Intra-Osseous Anchorage of Dental Prostheses:I. Experimental Studies. *Scandinavian Journal of Plastic and Reconstructive Surgery*. 1969;3:81-100.

[35] Wen CE, Yamada Y, Shimojima K, Chino Y, Hosokawa H, Mabuchi M. Novel titanium foam for bone tissue engineering. *Journal of materials research*. 2002;17:2633-9.

[36] Lopez-Heredia MA, Sohier J, Gaillard C, Quillard S, Dorget M, Layrolle P. Rapid prototyped porous titanium coated with calcium phosphate as a scaffold for bone tissue engineering. *Biomaterials*. 2008;29:2608-15.

- [37] Oh I-H, Nomura N, Masahashi N, Hanada S. Mechanical properties of porous titanium compacts prepared by powder sintering. *Scripta Materialia*. 2003;49:1197-202.
- [38] Li JP, Li SH, Van Blitterswijk CA, de Groot K. A novel porous Ti6Al4V: Characterization and cell attachment. *Journal of Biomedical Materials Research Part A*. 2005;73A:223-33.
- [39] Li JP, de Wijn JR, Van Blitterswijk CA, de Groot K. Porous Ti6Al4V scaffold directly fabricating by rapid prototyping: Preparation and in vitro experiment. *Biomaterials*. 2006;27:1223-35.
- [40] Choudhary RK, Theruvil B, Taylor GR. First metatarsophalangeal joint arthrodesis: A new technique of internal fixation by using memory compression staples. *The Journal of Foot and Ankle Surgery*. 2004;43:312-7.
- [41] Gotman I, Gutmanas E. Titanium nitride-based coatings on implantable medical devices. *Advanced Biomaterials and Devices in Medicine*. 2014;1:53-73.
- [42] van Hove RP, Sierevelt IN, van Royen BJ, Nolte PA. Titanium-nitride coating of orthopaedic implants: a review of the literature. *BioMed research international*. 2015;2015.
- [43] Hauer G, Leitner L, Ackerl MC, Klim S, Vielgut I, Ehall R, et al. Titanium-nitride coating does not result in a better clinical outcome compared to conventional cobalt-chromium total knee arthroplasty after a long-term follow-up: a propensity score matching analysis. *Coatings*. 2020;10:442.
- [44] de Villiers D, Hothi H, Khatkar H, Meswania J, Blunn G, Skinner J, et al. Lessons from retrievals: retrievals help understand the reason for revision of coated hip arthroplasties. *Proceedings of the Institution of Mechanical Engineers, Part H: Journal of Engineering in Medicine*. 2015;229:804-11.
- [45] Benčina M, Junkar I, Vesel A, Mozetič M, Igljč A. Nanoporous Stainless Steel Materials for Body Implants—Review of Synthesizing Procedures. *Nanomaterials*. 2022;12:2924.
- [46] Posada OM, Tate RJ, Meek RMD, Grant MH. In Vitro Analyses of the Toxicity, Immunological, and Gene Expression Effects of Cobalt-Chromium Alloy Wear Debris and Co Ions Derived from Metal-on-Metal Hip Implants. *Lubricants*. 2015;3:539-68.

- [47] Dawson-Amoah KG, Waddell BS, Prakash R, Alexiades MM. Adverse Reaction to Zirconia in a Modern Total Hip Arthroplasty with Ceramic Head. *Arthroplasty Today*. 2020;6:612-6.e1.
- [48] Depprich R, Zipprich H, Ommerborn M, Mahn E, Lammers L, Handschel J, et al. Osseointegration of zirconia implants: an SEM observation of the bone-implant interface. *Head & face medicine*. 2008;4:25.
- [49] Dawson-Bowling S, Adimonye A, Cohen A, Cottam H, Ritchie J, Fordyce M. MOJE Ceramic Metatarsophalangeal Arthroplasty: Disappointing Clinical Results at Two to Eight Years. *Foot & Ankle International*. 2012;33:560-4.
- [50] Bobyn JD, Stackpool GJ, Hacking SA, Tanzer M, Krygier JJ. Characteristics of bone ingrowth and interface mechanics of a new porous tantalum biomaterial. *Journal of Bone & Joint Surgery [Br]*. 1999;81-B:907-14.
- [51] MN S-P. Evolution of mould arthroplasty of the hip joint. *Journal of Bone & Joint Surgery [Br]*. 1948;30B:59-75.
- [52] Arora M, Chan EK, Gupta S, Diwan AD. Polymethylmethacrylate bone cements and additives: a review of the literature. *World Journal of Orthopaedics*. 2013;4:67-74.
- [53] Scales JT. Paper 13: Arthroplasty of the hip using foreign materials: a history. *Proceedings of the Institution of Mechanical Engineers, Conference Proceedings*. 2006;181:63-84.
- [54] Judet J, Judet R. The use of an artificial femoral head for arthroplasty of the hip joint. *The Journal of Bone & Joint Surgery*. 1950;32-B:166-73.
- [55] Hettfleisch J, Wissenbach R. Forty-year survival of a judet hip prosthesis - a case report. *Journal of Bone & Joint Surgery [Br]*. 1994;76-B:671-2.
- [56] Tennent TD, Eastwood DM. Survival of the Judet hip prosthesis. *Journal of the Royal Society of Medicine*. 1998;91:385-6.
- [57] Kulzer & Co GMBH. Improvements in or relating to the manufacture of surgical protheses. 1936.
- [58] Colquhoun HM, Lewis DF. Production of aromatic polyketones. United Kingdom: Imperial Chemical Industries Ltd.; 1982.

- [59] Kurtz SM. Synthesis and processing of PEEK for surgical implants. In: Kurtz S, editor. PEEK Biomaterials Handbook. USA: Elsevier; 2012. p. 9-22.
- [60] Karrholm J, Anderberg C, Snorrason F, Thanner J, Langeland N, Malachou H. Evaluation of a femoral stem with reduced stiffness. A randomized study with use of radiostereometry and bone densitometry. *J Bone Joint Surg.* 2002;88:1304-14.
- [61] Green S. Compounds and composite materials. In: Kurtz SM, editor. PEEK Biomaterials Handbook. Oxford, United Kingdom: Elsevier; 2012. p. 23-48.
- [62] Toth JM, Wang M, Estes BT, Scifert JL, Seim HB, 3rd, Turner AS. Polyetheretherketone as a biomaterial for spinal applications. *Biomaterials.* 2006;27:324-34.
- [63] Brown T, Bao QB. The use of self-mating PEEK as an alternative bearing material for cervical disc arthroplasty: a comparison of different simulator inputs and tribological environments. *European Spine Journal.* 2012;21:S717-26.
- [64] Lovald S, Kurtz SM. Applications of polyetheretherketone in trauma, arthroscopy, and cranial defect repair. In: Kurtz S, editor. PEEK Biomaterials Handbook. USA: Elsevier; 2012. p. 243-60.
- [65] Kurtz SM, Day J, Ong K. Isoelastic polyaryletheretherketone implants for total joint replacement. In: Kurtz S, editor. PEEK Biomaterials Handbook. USA: Elsevier; 2012. p. 221-42.
- [66] Briem D, Strametz S, Schröder K, Meenen NM, Lehmann W, Linhart W, et al. Response of primary fibroblasts and osteoblasts to plasma treated polyetheretherketone (PEEK) surfaces. *Journal of Materials Science: Materials in Medicine.* 2005;16:671-7.
- [67] Kasemo B, Lausmaa J. Biomaterial and implant surfaces - on the role of cleanliness, contamination, and preparation procedures. *Journal of Biomedical Materials Research Part B: Applied Biomaterials.* 1998;22:145-58.
- [68] Tsougeni K, Vourdas N, Tserepi A, Gogolides E, Cardinaud C. Mechanisms of oxygen plasma nanotexturing of organic polymer surfaces: from stable super hydrophilic to super hydrophobic surfaces. *Langmuir.* 2009;25:11748-59.

- [69] Zhao G, Schwartz Z, Wieland M, Rupp F, Geis-Gerstorfer J, Cochran DL, et al. High surface energy enhances cell response to titanium substrate microstructure. *Journal of Biomedical Materials Research Part A*. 2005;74:49-58.
- [70] Guckenberger DJ, Berthier E, Young EW, Beebe DJ. Induced hydrophobic recovery of oxygen plasma-treated surfaces. *Lab on a chip*. 2012;12:2317-21.
- [71] Reitman M, Jaekel D, Siskey R, Kurtz SM. Morphology and crystalline architecture of polyaryletherketones. In: Kurtz S, editor. *PEEK Biomaterials Handbook*. USA: Elsevier; 2012. p. 49-60.
- [72] Chalmers JM, Gaskin WF, Mackenzie MW. Crystallinity in poly(aryl-etherketone) plaques studied by internal-reflection spectroscopy. *Polymer Bulletin* 1984;11:433-5.
- [73] M. Chalmers J, J. Everall N, Hewitson K, A. Chesters M, Pearson M, Grady A, et al. Fourier transform infrared microscopy: some advances in techniques for characterisation and structure–property elucidations of industrial material. *Analyst*. 1998;123:579-86.
- [74] Fisher J, Reeves EA, Isaac GH, Saum KA, Sanford WM. Comparison of the wear of aged and non-aged ultrahigh molecular weight polyethylene sterilized by gamma irradiation and by gas plasma. *Journal of Materials Science: Materials in Medicine*. 1997;8:375-8.
- [75] Kurtz SM, Muratoglu OK, Evans M, Edidin AA. Advances in the processing, sterilization, and crosslinking of ultra-high molecular weight polyethylene for total joint arthroplasty. *Biomaterials*. 1999;20:1659-88.
- [76] Abdul-Kader AM, Turos A, Radwan RM, Kelany AM. Surface free energy of ultra-high molecular weight polyethylene modified by electron and gamma irradiation. *Applied Surface Science*. 2009;255:7786-90.
- [77] Dalby MJ DSL, Gurav N, Annaz B, Kayser MV, Bonfield W. Optimizing HAPEX topography influences osteoblast response. *Tissue engineering*. 2002;8:453-67.
- [78] Anselme K, Bigerelle M. Topography effects of pure titanium substrates on human osteoblast long-term adhesion. *Acta biomaterialia*. 2005;1:211-22.

- [79] Castellani R, de Ruijter A, Renggli H, Jansen J. Response of rat bone marrow cells to differently roughened titanium discs. *Clinical oral implants research*. 1999;10:369-78.
- [80] ter Brugge PJ, Wolke JGC, Jansen JA. Effect of calcium phosphate coating crystallinity and implant surface roughness on differentiation of rat bone marrow cells. *Journal of biomedical materials research*. 2002;60:70-8.
- [81] Park J, Gemmell C, Davies J. Platelet interactions with titanium: modulation of platelet activity by surface topography. *Biomaterials*. 2001;22:2671-82.
- [82] Di Iorio D, Traini T, Degidi M, Caputi S, Neugebauer J, Piattelli A. Quantitative evaluation of the fibrin clot extension on different implant surfaces: An in vitro study. *Journal of Biomedical Materials Research Part B: Applied Biomaterials*. 2005;74B:636-42.
- [83] Tsapikouni TS, Missirlis YF. Protein–material interactions: from micro-to-nano scale. *Materials Science and Engineering: B*. 2008;152:2-7.
- [84] Pasche S, Vörös J, Griesser HJ, Spencer ND, Textor M. Effects of ionic strength and surface charge on protein adsorption at PEGylated surfaces. *The Journal of Physical Chemistry B*. 2005;109:17545-52.
- [85] Lehnert M, Gorbahn M, Rosin C, Klein M, Köper I, Al-Nawas B, et al. Adsorption and conformation behavior of biotinylated fibronectin on streptavidin-modified TiOX surfaces studied by SPR and AFM. *Langmuir*. 2011;27:7743-51.
- [86] Lin H, Lal R, Clegg DO. Imaging and mapping heparin-binding sites on single fibronectin molecules with atomic force microscopy. *Biochemistry*. 2000;39:3192-6.
- [87] Keselowsky BG, Collard DM, García AJ. Surface chemistry modulates fibronectin conformation and directs integrin binding and specificity to control cell adhesion. *Journal of Biomedical Materials Research Part A: An Official Journal of The Society for Biomaterials, The Japanese Society for Biomaterials, and The Australian Society for Biomaterials and the Korean Society for Biomaterials*. 2003;66:247-59.
- [88] Garcia AJ, Vega MD, Boettiger D. Modulation of cell proliferation and differentiation through substrate-dependent changes in fibronectin conformation. *Molecular biology of the cell*. 1999;10:785-98.

- [89] Rice J, Hunt J, Gallagher J, Hanarp P, Sutherland D, Gold J. Quantitative assessment of the response of primary derived human osteoblasts and macrophages to a range of nanotopography surfaces in a single culture model in vitro. *Biomaterials*. 2003;24:4799-818.
- [90] Cassella J, Barber P, AC. C, Ali S. A Morphometric analysis of osteoid collagen fibril diameter in osteogenesis imperfecta. *Bone*. 1994;15:329-34.
- [91] Hart A, Gadegaard N, Wilkinson CD, Oreffo RO, Dalby MJ. Osteoprogenitor response to low-adhesion nanotopographies originally fabricated by electron beam lithography. *Journal of Materials Science: Materials in Medicine*. 2007;18:1211-8.
- [92] Yang S, Huang FK, Huang J, Chen S, Jakoncic J, Leo-Macias A, et al. Molecular mechanism of fascin function in filopodial formation. *The Journal of biological chemistry*. 2013;288:274-84.
- [93] Vignjevic D, Kojima S, Aratyn Y, Danciu O, Svitkina T, Borisy GG. Role of fascin in filopodial protrusion. *Journal of Cell Biology*. 2006;174:863-75.
- [94] Mendonca G, Mendonca DB, Aragao FJ, Cooper LF. Advancing dental implant surface technology--from micron- to nanotopography. *Biomaterials*. 2008;29:3822-35.
- [95] Kechagia JZ, Ivaska J, Roca-Cusachs P. Integrins as biomechanical sensors of the microenvironment. *Nature Reviews Molecular Cell Biology*. 2019;20:457-73.
- [96] Shattil SJ, Kim C, Ginsberg MH. The final steps of integrin activation: the end game. *Nature Reviews Molecular Cell Biology*. 2010;11:288-300.
- [97] Kanchanawong P, Shtengel G, Pasapera AM, Ramko EB, Davidson MW, Hess HF, et al. Nanoscale architecture of integrin-based cell adhesions. *Nature*. 2010;468:580-4.
- [98] Liu J, Wang Y, Goh WI, Goh H, Baird MA, Ruehland S, et al. Talin determines the nanoscale architecture of focal adhesions. *Proceedings of the National Academy of Sciences*. 2015;112:E4864-E73.
- [99] Elosegui-Artola A, Oria R, Chen Y, Kosmalka A, Pérez-González C, Castro N, et al. Mechanical regulation of a molecular clutch defines force transmission and transduction in response to matrix rigidity. *Nature cell biology*. 2016;18:540-8.

- [100] Biggs MJ, Richards RG, Gadegaard N, Wilkinson CD, Oreffo RO, Dalby MJ. The use of nanoscale topography to modulate the dynamics of adhesion formation in primary osteoblasts and ERK/MAPK signalling in STRO-1+ enriched skeletal stem cells. *Biomaterials*. 2009;30:5094-103.
- [101] Kirby TJ, Lammerding J. Emerging views of the nucleus as a cellular mechanosensor. *Nature cell biology*. 2018;20:373-81.
- [102] Ballestrem C, Erez N, Kirchner J, Kam Z, Bershadsky A, Geiger B. Molecular mapping of tyrosine-phosphorylated protein in focal adhesions using fluorescence resonance energy transfer. *Journal of cell science*. 2006;119:866-75.
- [103] Bershadsky AD, Ballestrem C, Carramusa L, Zilberman Y, Gilquin B, Khochbin S, et al. Assembly and mechanosensory function of focal adhesions: experiments and models. *European journal of cell biology*. 2006;85:165-73.
- [104] Wozniak M, Fausto A, Carron CP, Meyer DM, Hruska KA. Mechanically strained cells of the osteoblast lineage organize their extracellular matrix through unique sites of α v β 3 integrin expression. *Journal of Bone and Mineral Research*. 2000;15:1731-45.
- [105] Gallant ND, Michael KE, García AJ. Cell adhesion strengthening: contributions of adhesive area, integrin binding, and focal adhesion assembly. *Molecular biology of the cell*. 2005;16:4329-40.
- [106] Cohen M JD, Geiger B, Addadi L. Spatial and temporal sequence of events in cell adhesion: from molecular recognition to focal adhesion assembly. *Chembiochem : a European journal of chemical biology*. 2004 5:1393-9.
- [107] Yang W, Han W, He W, Li J, Wang J, Feng H, et al. Surface topography of hydroxyapatite promotes osteogenic differentiation of human bone marrow mesenchymal stem cells. *Materials Science and Engineering: C*. 2016;60:45-53.
- [108] Zhang Y, Gong H, Sun Y, Huang Y, Fan Y. Enhanced osteogenic differentiation of MC3T3-E1 cells on grid-topographic surface and evidence for involvement of YAP mediator. *Journal of Biomedical Materials Research Part A*. 2016;104:1143-52.
- [109] Hwang J-H, Lee D-H, Byun MR, Kim AR, Kim KM, Park JI, et al. Nanotopological plate stimulates osteogenic differentiation through TAZ activation. *Scientific Reports*. 2017;7:3632.

- [110] Qian W, Gong L, Cui X, Zhang Z, Bajpai A, Liu C, et al. Nanotopographic regulation of human mesenchymal stem cell osteogenesis. *ACS applied materials & interfaces*. 2017;9:41794-806.
- [111] Pasapera AM, Schneider IC, Rericha E, Schlaepfer DD, Waterman CM. Myosin II activity regulates vinculin recruitment to focal adhesions through FAK-mediated paxillin phosphorylation. *Journal of Cell Biology*. 2010;188:877-90.
- [112] Lee RT, Lee YC. Affinity enhancement by multivalent lectin–carbohydrate interaction. *Glycoconjugate journal*. 2000;17:543-51.
- [113] Guilluy C, Swaminathan V, Garcia-Mata R, Timothy O'Brien E, Superfine R, Burridge K. The Rho GEFs LARG and GEF-H1 regulate the mechanical response to force on integrins. *Nature cell biology*. 2011;13:722-7.
- [114] Lai C-F, Chaudhary L, Fausto A, Halstead LR, Ory DS, Avioli LV, et al. Erk is essential for growth, differentiation, integrin expression, and cell function in human osteoblastic cells. *Journal of Biological Chemistry*. 2001;276:14443-50.
- [115] Cavalcanti-Adam EA, Micoulet A, Blummel J, Auernheimer J, Kessler H, Spatz JP. Lateral spacing of integrin ligands influences cell spreading and focal adhesion assembly. *European journal of cell biology*. 2006;85:219-24.
- [116] Cavalcanti-Adam EA, Volberg T, Micoulet A, Kessler H, Geiger B, Spatz JP. Cell spreading and focal adhesion dynamics are regulated by spacing of integrin ligands. *Biophysical journal*. 2007;92:2964-74.
- [117] Arnold M, Cavalcanti-Adam EA, Glass R, Blummel J, Eck W, Kantlehner M, et al. Activation of integrin function by nanopatterned adhesive interfaces. *Chemphyschem : a European journal of chemical physics and physical chemistry*. 2004;5:383-8.
- [118] Huang J, Grater SV, Corbellini F, Rinck S, Bock E, Kemkemer R, et al. Impact of order and disorder in RGD nanopatterns on cell adhesion. *Nano letters*. 2009;9:1111-6.
- [119] Patla I, Volberg T, Elad N, Hirschfeld-Warneken V, Grashoff C, Fässler R, et al. Dissecting the molecular architecture of integrin adhesion sites by cryo-electron tomography. *Nature cell biology*. 2010;12:909-15.

- [120] Biggs MJ, Richards RG, Gadegaard N, Wilkinson CD, Dalby MJ. Regulation of implant surface cell adhesion: characterization and quantification of S-phase primary osteoblast adhesions on biomimetic nanoscale substrates. *Journal of Orthopaedic Research*. 2007;25:273-82.
- [121] Sjoström T, Fox N, Su B. Through-mask anodization of titania dot- and pillar-like nanostructures on bulk Ti substrates using a nanoporous anodic alumina mask. *Nanotechnology*. 2009;20:135305.
- [122] Biggs MJ, Richards RG, Gadegaard N, McMurray RJ, Affrossman S, Wilkinson CD, et al. Interactions with nanoscale topography: adhesion quantification and signal transduction in cells of osteogenic and multipotent lineage. *Journal of Biomedical Materials Research Part A*. 2009;91:195-208.
- [123] Pittenger MF, Mackay AM, Beck SC, Jaiswal RK, Douglas R, Mosca JD, et al. Multilineage potential of adult human mesenchymal stem cells. *Science*. 1999;284:143-7.
- [124] Baksh D, Yao R, Tuan RS. Comparison of proliferative and multilineage differentiation potential of human mesenchymal stem cells derived from umbilical cord and bone marrow. *Stem Cells*. 2007;25:1384-92.
- [125] Engler AJ, Sen S, Sweeney HL, Discher DE. Matrix elasticity directs stem cell lineage specification. *Cell*. 2006;126:677-89.
- [126] Arianna S, Mariarosaria M, Dana F, Monia O, Guido C, Giovanni T. Mesenchymal stem cells neuronal differentiation ability: a real perspective for nervous system repair? *Current Stem Cell Research & Therapy*. 2011;6:82-92.
- [127] Dalby MJ, Hart A, Yarwood SJ. The effect of the RACK1 signalling protein on the regulation of cell adhesion and cell contact guidance on nanometric grooves. *Biomaterials*. 2008;29:282-9.
- [128] McBeath R, Pirone DM, Nelson CM, Bhadriraju K, Chen CS. Cell shape, cytoskeletal tension and RhoA regulate stem cell commitment. *Developmental cell*. 2004;6:483-95.
- [129] Kilian KA, Bugarija B, Lahn BT, Mrksich M. Geometric cues for directing the differentiation of mesenchymal stem cells. *Proceedings of the National Academy of Sciences*. 2010;107:4872-7.

- [130] Li JJ, Xie D. Cleavage of focal adhesion kinase (FAK) is essential in adipocyte differentiation. *Biochemical and biophysical research communications*. 2007;357:648-54.
- [131] McMurray RJ, Gadegaard N, Tsimbouri PM, Burgess KV, McNamara LE, Tare R, et al. Nanoscale surfaces for the long term maintenance of mesenchymal stem cell phenotype and multipotency. *Nature materials*. 2011;10:637-44.
- [132] Luo W, Shitaye H, Friedman M, Bennett CN, Miller J, Macdougald OA, et al. Disruption of cell-matrix interactions by heparin enhances mesenchymal progenitor adipocyte differentiation. *Experimental cell research*. 2008;314:3382-91.
- [133] Park J, Bauer S, von der Mark K, Schmuki P. Nanosize and Vitality: TiO₂ Nanotube Diameter Directs Cell Fate. *Nano letters*. 2007;7:1686-91.
- [134] Oh S, Brammer KS, Li YSJ, Teng D, Engler AJ, Chien S, et al. Stem cell fate dictated solely by altered nanotube dimension. *Proceedings of the National Academy of Sciences*. 2009;106:2130-5.
- [135] Wang N, Li H, Lu W, Li J, Wang J, Zhang Z, et al. Effects of TiO₂ nanotubes with different diameters on gene expression and osseointegration of implants in minipigs. *Biomaterials*. 2011;32:6900-11.
- [136] Zhao L, Mei S, Wang W, Chu PK, Zhang Y, Wu Z. Suppressed primary osteoblast functions on nanoporous titania surface. *Journal of Biomedical Materials Research Part A*. 2011;96A:100-7.
- [137] Gongadze E, Kabaso D, Bauer S, Slivnik T, Schmuki P, van Rienen U, et al. Adhesion of osteoblasts to a nanorough titanium implant surface. *International journal of nanomedicine*. 2011;6:1801-16.
- [138] Gulati K, Moon H-J, Li T, Sudheesh Kumar PT, Ivanovski S. Titania nanopores with dual micro-/nano-topography for selective cellular bioactivity. *Materials Science and Engineering: C*. 2018;91:624-30.
- [139] Bjursten LM, Rasmusson L, Oh S, Smith GC, Brammer KS, Jin S. Titanium dioxide nanotubes enhance bone bonding in vivo. *Journal of biomedical materials research Part A*. 2010;92:1218-24.

- [140] Esposito M, Ardebili Y, Worthington HV. Interventions for replacing missing teeth: different types of dental implants. . *Cochrane Database Syst Rev.* 2019;10:CD003815.
- [141] Åstrand P, Engquist B, Dahlgren S, Gröndahl K, Engquist E, Feldmann H. Astra Tech and Brånemark system implants: a 5-year prospective study of marginal bone reactions. *Clinical oral implants research.* 2004;15:413-20.
- [142] Meijer HJA, Raghoobar GM, Batenburg RHK, Vissink A. Mandibular overdentures supported by two Brånemark, IMZ or ITI implants: a ten-year prospective randomized study. *Journal of Clinical Periodontology.* 2009;36:799-806.
- [143] Moberg L-E, Sagulin G-B, Köndell P-Å, Heimdahl A, Gynther GW, Bolin A. Brånemark System® and ITI Dental Implant System® for treatment of mandibular edentulism. *Clinical oral implants research.* 2001;12:450-61.
- [144] Sjöström T, Brydone AS, Meek RDM, Dalby MJ, Su B, McNamara LE. Titanium nanofeaturing for enhanced bioactivity of implanted orthopedic and dental devices. *Nanomedicine : nanotechnology, biology, and medicine.* 2013;8:89-104.
- [145] Abron A, Hopfensperger M, Thompson J, Cooper LF. Evaluation of a predictive model for implant surface topography effects on early osseointegration in the rat tibia model *Journal of Prosthetic Dentistry.* 2001;85:40-6.
- [146] Cooper LF, Zhou Y, Tkebe J, Guo J, Abron A, Holmen A, et al. Fluoride modification effects on osteoblast behavior and bone formation at TiO₂ grit blasted CpTitanium endosseous implants. . *Biomaterials.* 2006;27:926-36.
- [147] Marin C, Granato R, Suzuki M, Gil JN, Piattelli A, Coelho PG. Removal torque and histomorphometric evaluation of bioceramic grit-blasted/acid-etched and dual acid-etched implant surfaces: An experimental study in dogs. *Journal of periodontology.* 2008;79:1942.
- [148] Mendes VC, Moineddin R, Davies JE. The effect of discrete calcium phosphate nanocrystals on bone-bonding to titanium surfaces. *Biomaterials.* 2007;28:4748-55.
- [149] Palmquist A, Emanuelsson L, Branemark R, Thomsen P. Biomechanical, histological and ultrastructural analyses of laser micro- and nano-structured titanium implant after 6 months in rabbit. *Journal of Biomedical Materials Research B Appl Biomater.* 2011;97:289-98.

- [150] Palmquist A, Grandfield K, Norlindh B, Mattsson T, Branemark R, Thomsen P. Bone-titanium oxide interface in humans revealed by transmission electron microscopy and electron tomography. *Journal of the Royal Society, Interface*. 2012;9:396-400.
- [151] Dohan Ehrenfest DM, Vazquez L, Park YJ, Sammartino G, Bernard JP. Identification card and codification of the chemical and morphological characteristics of 14 dental implant surfaces. *The Journal of oral implantology*. 2011;37:525-42.
- [152] Jarmar T, Palmquist A, Branemark R, Hermansson L, Engqvist H, Thomsen P. Characterization of the surface properties of commercially available dental implants using scanning electron microscopy, focused ion beam, and high-resolution transmission electron microscopy. *Clinical implant dentistry and related research*. 2008;10:11-22.
- [153] Kang SH, Cho SA. Comparison of removal torques for laser-treated titanium implants with anodized implants. *The Journal of craniofacial surgery*. 2011;22:1491-5.
- [154] Choi JY, Lee HJ, Jang JU, Yeo IS. Comparison between bioactive fluoride modified and bioinert anodically oxidized implant surfaces in early bone response using rabbit tibia model. *Implant dentistry*. 2012;21:124-8.
- [155] Orsini G, Piattelli M, Scarano A, Petrone G, Kenealy J, Piattelli A, et al. Randomized, controlled histologic and histomorphometric evaluation of implants with nanometer-scale calcium phosphate added to the dual acid-etched surface in the human posterior maxilla. *Journal of periodontology*. 2007;78:209-18.
- [156] Goené RJ, Testori T, Trisi P. Influence of a nanometer-scale surface enhancement on de novo bone formation on titanium implants: a histomorphometric study in human maxillae. *Int J Periodontics Restorative Dent*. 2007;3:211-9.
- [157] Wennerberg A, Svanborg LM, Berner S, Andersson M. Spontaneously formed nanostructures on titanium surfaces. *Clinical oral implants research*. 2013;24:203-9.
- [158] Wennerberg A, Jimbo R, Stübinger S, Obrecht M, Dard M, Berner S. Nanostructures and hydrophilicity influence osseointegration: a biomechanical study in the rabbit tibia. *Clinical oral implants research*. 2014;25:1041-50.

- [159] Bornstein MM, Valderrama P, Jones AA, Wilson TG, Seibl R, Cochran DL. Bone apposition around two different sandblasted and acid-etched titanium implant surfaces: a histomorphometric study in canine mandibles. *Clinical oral implants research*. 2008;19:233-41.
- [160] Stavropoulos A, Sandgren R, Bellon B, Sculean A, Pippenger BE. Greater Osseointegration Potential with Nanostructured Surfaces on TiZr: Accelerated vs. Real-Time Ageing. *Materials (Basel)* 2021;14:1678.
- [161] Tsuchiya H, Suzumura T, Terada Y, Fujimoto S. Formation of self-organized pores on type 316 stainless steel in organic solvents. *Electrochimica Acta*. 2012;82:333-8.
- [162] Tsuchiya H. Formation of Self-Organized Pore Arrays on Metallic Substrates by Anodization and their Applications. *Materials Science Forum*. 2014;783-786:2034-9.
- [163] Pan H-A, Liang J-Y, Hung Y-C, Lee C-H, Chiou J-C, Huang GS. The spatial and temporal control of cell migration by nanoporous surfaces through the regulation of ERK and integrins in fibroblasts. *Biomaterials*. 2013;34:841-53.
- [164] Ban G-H, Rungraeng N, Li Y, Jun S. Nanoporous Stainless Steel Surfaces for Anti-Bacterial Adhesion Performances. *Transactions of the ASABE*. 2018;61:1175-9.
- [165] Bae I, Lim K-S, Park J-K, Song JH, Oh S-H, Kim J-W, et al. Evaluation of cellular response and drug delivery efficacy of nanoporous stainless steel material. *Biomaterials Research*. 2021;25:30.
- [166] Farrag HH, Sayed SY, Allam NK, Mohammad AM. Emerging nanoporous anodized stainless steel for hydrogen production from solar water splitting. *Journal of Cleaner Production*. 2020;274:122826.
- [167] Rodriguez-Contreras A, Guadarrama Bello D, Flynn S, Variola F, Wuest JD, Nanci A. Chemical nanocavitation of surfaces to enhance the utility of stainless steel as a medical material. *Colloids and Surfaces B: Biointerfaces*. 2018;161:677-87.
- [168] van Noort R. The future of dental devices is digital. *Dental Materials*. 2012;28:3-12.

- [169] Atzeni E, Iuliano L, Minetola P, Salmi A. Redesign and cost estimation of rapid manufactured plastic parts. *Rapid Prototyping Journal*. 2010;16:308-17.
- [170] Gadegaard N, Mosler S, Larsen NB. Biomimetic polymer nanostructures by injection molding. *Macromolecular Materials and Engineering*. 2003;288:76-83.
- [171] Vieu C, Carcenac F, Pépin A, Chen Y, Mejias M, Lebib A, et al. Electron beam lithography: resolution limits and applications. *Applied Surface Science*. 2000;164:111-7.
- [172] Christenson EM, Anseth KS, van den Beucken JJ, Chan CK, Ercan B, Jansen JA, et al. Nanobiomaterial applications in orthopedics. *Journal of Orthopaedic Research*. 2007;25:11-22.
- [173] Chou SY KP, Renstrom PJ. Nanoimprint lithography. *Journal of Vacuum Science & Technology B, Nanotechnology and Microelectronics: Materials, Processing, Measurement, and Phenomena*. 1996;14:4129.
- [174] Richmond DA, Zhang Q, Cao G, Weiss DN. Pressureless nanoimprinting of anatase TiO₂ precursor films. *Journal of Vacuum Science & Technology B: Microelectronics and Nanometer Structures*. 2011;29:021603.
- [175] Yoon K-M, Yang K-Y, Lee H. Fabrication of polycrystalline TiO₂ nanopatterns by TiO₂ sol base imprint lithography. *Thin Solid Films*. 2009;518:126-9.
- [176] Greer AIM, Lim TS, Brydone AS, Gadegaard NJ. Mechanical compatibility of sol-gel annealing with titanium for orthopaedic prostheses. *Journal of Materials Science: Materials in Medicine*. 2016;27:21.
- [177] Greer AI, Della-Rosa B, Khokhar AZ, Gadegaard N. Step-and-repeat nanoimprint-, photo- and laser lithography from one customised CNC machine. *Nanoscale research letters*. 2016;11:129.
- [178] Mata A, Fleischman AJ, Shuvo R. Characterization of polydimethylsiloxane (PDMS) properties for biomedical micro/nanosystems. *Biomedical microdevices*. 2005;7:281-93.
- [179] Auzelyte V, Flauraud V, Cadarso VJ, Kiefer T, Brugger J. Biomimetic soft lithography on curved nanostructured surfaces. *Microelectronic Engineering*. 2012;97:269-71.

- [180] Farshchian B, Amirsadeghi A, Hurst SM, Wu J, Lee J, Park S. Soft UV-nanoimprint lithography on non-planar surfaces. *Microelectronic Engineering*. 2011;88:3287-92.
- [181] Farshchian B, Amirsadeghi A, Hurst SM, Kim J, Park S. Deformation behavior in 3D molding: experimental and simulation studies. *Journal of Micromechanics and Microengineering*. 2012;22:115027.
- [182] Choi WM, Park OO. The fabrication of submicron patterns on curved substrates using a polydimethylsiloxane film mould. *Nanotechnology*. 2004;15:1767-70.
- [183] Cech J. Nano-patterning of tools for replication of non-planar polymer surfaces. PhD Thesis: Denmark Technical University; 2013.
- [184] Gadegaard N. Biomimetic polymer nanostructures by injection moulding. *Macromolecular Materials and Engineering*. 2003;288:76-83.
- [185] Greer AIM, Della-Rosa B, Khokhar AZ, Gadegaard N. Step-and-Repeat Nanoimprint-, Photo- and Laser Lithography from One Customised CNC Machine. *Nanoscale research letters*. 2016;11:129.
- [186] McMurray RJ, Gadegaard N, Tsimbouri PM, Burgess KV, McNamara LE, Tare R, et al. Nanoscale surfaces for the long-term maintenance of mesenchymal stem cell phenotype and multipotency. *Nature Materials Supplementary Information*. 2011;10:1-23.
- [187] Okawa S, Watanabe K. Chemical mechanical polishing of titanium with colloidal silica containing hydrogen peroxide — mirror polishing and surface properties. *Dental Materials Journal*. 2009;28:68-74.
- [188] Sivanandini M, Dhama SS, Pabla DS. Chemical mechanical polishing by colloidal silica slurry. *International Journal of Engineering Research and Applications*. 2013;3:1337-45.
- [189] Stormonth-Darling JM. Fabrication of difficult nanostructures by injection moulding: University of Glasgow; 2013.
- [190] Kametsky L, Jones TR, Fraser A, Bray M-A, Logan DJ, Madden KL, et al. Improved structure, function and compatibility for CellProfiler: modular high-throughput image analysis software. *Bioinformatics*. 2011;27:1179-80.

- [191] Nečas D, Klapetek P. Gwyddion: an open-source software for SPM data analysis. *Central European Journal of Physics*. 2012;10:181-8.
- [192] Schneider CA, Rasband WS, Eliceiri KW. NIH Image to ImageJ: 25 years of image analysis. *Nature methods*. 2012;9:671-5.
- [193] Covestro. Makrolon OD2015 datasheet. 2018:1-3.
- [194] Invibio Biomaterial Solutions. PEEK Optima Natural: typical material properties. 2013:1-2.
- [195] Horie T. Horie U.S.A. Titanium Surface Engineering. 2018.
- [196] Campbell T, Kalia RK, Nakano A, Vashishta P. Dynamics of oxidation of aluminum nanoclusters using variable charge molecular dynamics stimulation on parallel computers. *Physical review letters*. 1999;82:4866-9.
- [197] Greer AIM, Seunarine K, Khokhar AZ, MacLaren I, Brydone AS, Moran DAJ, et al. Increased efficiency of direct nanoimprinting on planar and curved bulk titanium through surface modification. *Microelectronic Engineering*. 2013;112:67-73.
- [198] Stormonth-Darling JM, Gadegaard N. Injection moulding difficult nanopatterns with hybrid polymer inlays. *Macromolecular Materials and Engineering*. 2012;297:1075-80.
- [199] Toth JM. Biocompatibility of polyaryletheretherketone polymers. In: Kurtz S, editor. *PEEK Biomaterials Handbook*. USA: Elsevier; 2012. p. 81-92.
- [200] Gadegaard N, Dalby MJ, Martines E, Seunarine K, Riehle MO, Curtis ASG, et al. Nano patterned surfaces for biomaterial applications. *Advances in Science and Technology*. 2006;53:107-15.
- [201] Nguyen HX, Ishida H. Molecular analysis of the crystallization behavior of poly(aryl-ether-ether-ketone). *Journal of Polymer Science Part B: Polymer Physics*. 1986;24:1079-91.
- [202] Jonas A, Legras R, Issi JP. Differential scanning calorimetry and infra-red crystallinity determinations of poly(aryl ether ether ketone). *Polymer*. 1991;32:3364-70.
- [203] Cassie ABD, Baxter S. Wettability of porous surfaces. *Transactions of the Faraday Society*. 1944;40:546.

- [204] Wenzel RN. Resistance of solid surfaces to wetting by water. *Industrial and Engineering Chemistry*. 1936;28:988-94.
- [205] Martines E, Seunarine K, Morgan H, Gadegaard N, Wilkinson CDW, Riehle M. Air-trapping on biocompatible nanopatterns. *Langmuir*. 2006;22:11230-3.
- [206] Gao L, McCarthy TJ. How Wenzel and Cassie were wrong. *Langmuir*. 2007;23:3762-5.
- [207] Lipowsky R, Lenz P, Swain PS. Wetting and dewetting of structured and imprinted surfaces. *Colloids and Surfaces A: Physicochemical and Engineering Aspects*. 2000;161:3-22.
- [208] Bonn D, Eggers J, Indekeu J, Meunier J, Rolley E. Wetting and spreading. *Reviews of Modern Physics*. 2009;81:739-805.
- [209] Cole KC, Casella IG. Fourier transform infra-red spectroscopic study of thermal degradation in poly(ether ether ketone)-carbon composites. *Polymer*. 1993;34:740-5.
- [210] Dalby MJ, McCloy D, Robertson M, Wilkinson CD, Oreffo RO. Osteoprogenitor response to defined topographies with nanoscale depths. *Biomaterials*. 2006;27:1306-15.
- [211] Yang J, McNamara LE, Gadegaard N, Alakpa EV, Burgess KV, Meek RMD, et al. Nanotopographical induction of osteogenesis through adhesion, bone morphogenic protein cosignaling, and regulation of MicroRNAs. *ACS Nano*. 2014;8:9941-53.
- [212] Lee LCY, Gadegaard N, de Andrés MC, Turner L-A, Burgess KV, Yarwood SJ, et al. Nanotopography controls cell cycle changes involved with skeletal stem cell self-renewal and multipotency. *Biomaterials*. 2017;116:10-20.
- [213] Althaus J, Padeste C, Köser J, Pielers U, Peters K, B. M. Nanostructuring polyetheretherketone for medical implants. *European Journal of Nanomedicine*. 2012;4:7-15.
- [214] Puchtler H, Meloan SN, Terry MS. On the history and mechanism of alizarin and alizarin red S stains for calcium. *Journal of Histochemistry & Cytochemistry*. 1969;17:110-24.

- [215] Puchtler H, Meloan SN. Demonstration of phosphates in calcium deposits: a modification of von Kossa's reaction. *Histochemistry*. 1978;56:177-85.
- [216] Carpenter AE, Jones TR, Lamprecht MR, Clarke C, Kang IH, Friman O, et al. CellProfiler: image analysis software for identifying and quantifying cell phenotypes. *Genome Biology*. 2006;7:R100.
- [217] Lamprecht M, Sabatini D, Carpenter A. CellProfiler: free, versatile software for automated biological image analysis. *Biotechniques*. 2007;42:71-5.
- [218] Kamentsky L, Jones T, Fraser A, Bray M, Logan D, Madden K, et al. Improved structure, function, and compatibility for CellProfiler: modular high-throughput image analysis software. *Bioinformatics*. 2011;27:1179-80.
- [219] Promocell. Mesenchymal Stem Cells. Instruction Manual. Promocell Company Literature. Downloaded 2012.
- [220] Hu J, Zeng B, Jiang X, Hu L, Meng Y, Zhu Y, et al. The expression of marker for endometrial stem cell and fibrosis was increased in intrauterine adhesions. *Int J Clin Exp Pathol*. 2015;8:1525-34.
- [221] Bonewald LF, Harris SE, Rosser J, Dallas MR, Dallas SL, Camacho NP, et al. Von Kossa staining alone is not sufficient to confirm that mineralization in vitro represents bone formation. *Calcified tissue international*. 2003;72:537-47.
- [222] Lawson C, Lim S-T, Uryu S, Chen XL, Calderwood DA, Schlaepfer DD. FAK promotes recruitment of talin to nascent adhesions to control cell motility. *Journal of Cell Biology*. 2012;196:223-32.
- [223] Ngandu Mpoyi E, Cantini M, Reynolds PM, Gadegaard N, Dalby MJ, Salmerón-Sánchez M. Protein adsorption as a key mediator in the nanotopographical control of cell behavior. *ACS Nano*. 2016;10:6638-47.
- [224] Dominici M, Le Blanc K, Mueller I, Slaper-Cortenbach I, Marini F, Krause D, et al. Minimal criteria for defining multipotent mesenchymal stromal cells. The International Society for Cellular Therapy position statement. *Cytotherapy*. 2006;8:315-7.
- [225] Mafi P, Hindocha S, Mafi R, Griffin M, Khan WS. Adult mesenchymal stem cells and cell surface characterization: a systematic review of the literature. *The Open Orthopaedics Journal*. 2011;5:253-60.

- [226] Huang GTJ, Gronthos S, Shi S. Mesenchymal stem cells derived from dental tissues vs. those from other sources: their biology and role in regenerative medicine. *Journal of Dental Research*. 2009;88:792-806.
- [227] Mao JJ, Prockop DJ. Stem cells in the face: tooth regeneration and beyond. *Cell stem cell*. 2012;11:291-301.
- [228] Brinkhof B, Zhang B, Cui Z, Ye H, Wang H. ALCAM (CD166) as a gene expression marker for human mesenchymal stromal cell characterisation. *Gene X*. 2020;5:100031-.
- [229] Yu K-R, Yang S-R, Jung J-W, Kim H, Ko K, Han DW, et al. CD49f enhances multipotency and maintains stemness through the direct regulation of OCT4 and SOX2. *Stem Cells*. 2012;30:876-87.
- [230] Lv F-J, Tuan RS, Cheung KMC, Leung VYL. Concise review: the surface markers and identity of human mesenchymal stem cells. *Stem Cells*. 2014;32:1408-19.
- [231] Pinho S, Lacombe J, Hanoun M, Mizoguchi T, Bruns I, Kunisaki Y, et al. PDGFR α and CD51 mark human nestin⁺ sphere-forming mesenchymal stem cells capable of hematopoietic progenitor cell expansion. *J Exp Med*. 2013;210:1351-67.
- [232] Mareschi K, Ferrero I, Rustichelli D, Aschero S, Gammaitoni L, Aglietta M, et al. Expansion of mesenchymal stem cells isolated from pediatric and adult donor bone marrow. *Journal of cellular biochemistry*. 2006;97:744-54.
- [233] Chitteti BR, Cheng Y-H, Kacena MA, Srour EF. Hierarchical organization of osteoblasts reveals the significant role of CD166 in hematopoietic stem cell maintenance and function. *Bone*. 2013;54:58-67.
- [234] Radtke S, Görgens A, Kordelas L, Schmidt M, Kimmig KR, Königer A, et al. CD133 allows elaborated discrimination and quantification of haematopoietic progenitor subsets in human haematopoietic stem cell transplants. *British journal of haematology*. 2015;169:868-78.
- [235] Gerber HP, Malik AK, Solar GP, Sherman D, Liang XH, Meng G, et al. VEGF regulates haematopoietic stem cell survival by an internal autocrine loop mechanism. *Nature*. 2002;417:954-8.

- [236] Covas DT, Panepucci RA, Fontes AM, Silva WA, Orellana MD, Freitas MCC, et al. Multipotent mesenchymal stromal cells obtained from diverse human tissues share functional properties and gene-expression profile with CD146+ perivascular cells and fibroblasts. *Experimental Hematology*. 2008;36:642-54.
- [237] Russell KC, Phinney DG, Lacey MR, Barrilleaux BL, Meyertholen KE, O'Connor KC. In vitro high-capacity assay to quantify the clonal heterogeneity in trilineage potential of mesenchymal stem cells reveals a complex hierarchy of lineage commitment. *Stem Cells*. 2010;28:788-98.
- [238] Tormin A, Li O, Brune JC, Walsh S, Schütz B, Ehinger M, et al. CD146 expression on primary nonhematopoietic bone marrow stem cells is correlated with in situ localization. *Blood*. 2011;117:5067-77.
- [239] Wagegg M, Gaber T, Lohanatha FL, Hahne M, Strehl C, Fangradt M, et al. Hypoxia promotes osteogenesis but suppresses adipogenesis of human mesenchymal stromal cells in a hypoxia-inducible factor-1 dependent manner. *PLoS one*. 2012;7:e46483.
- [240] Mayer H, Bertram H, Lindenmaier W, Korff T, Weber H, Weich H. Vascular endothelial growth factor (VEGF-A) expression in human mesenchymal stem cells: Autocrine and paracrine role on osteoblastic and endothelial differentiation. *Journal of cellular biochemistry*. 2005;95:827-39.
- [241] Yang Y-Q, Tan Y-Y, Wong R, Wenden A, Zhang L-K, Rabie ABM. The role of vascular endothelial growth factor in ossification. *International Journal of Oral Science*. 2012;4:64-8.
- [242] Shalaby F, Rossant J, Yamaguchi TP, Gertsenstein M, Wu X-F, Breitman ML, et al. Failure of blood-island formation and vasculogenesis in Flk-1-deficient mice. *Nature*. 1995;376:62-6.
- [243] Jacobsen KA, Al-Aql ZS, Wan C, Fitch JL, Stapleton SN, Mason ZD, et al. Bone formation during distraction osteogenesis is dependent on both VEGFR1 and VEGFR2 signaling. *Journal of Bone and Mineral Research*. 2008;23:596-609.
- [244] Liu Y, Berendsen AD, Jia S, Lotinun S, Baron R, Ferrara N, et al. Intracellular VEGF regulates the balance between osteoblast and adipocyte differentiation. *J Clin Invest*. 2012;122:3101-13.

- [245] Hu K, Olsen BR. Osteoblast-derived VEGF regulates osteoblast differentiation and bone formation during bone repair. *J Clin Invest*. 2016;126:509-26.
- [246] Arumugam B, Balagangadharan K, Selvamurugan N. Syringic acid, a phenolic acid, promotes osteoblast differentiation by stimulation of Runx2 expression and targeting of Smad7 by miR-21 in mouse mesenchymal stem cells. *J Cell Commun Signal*. 2018;12:561-73.
- [247] Kent D, Copley M, Benz C, Dykstra B, Bowie M, Eaves C. Regulation of hematopoietic stem cells by the steel factor/KIT signaling pathway. *Clinical Cancer Research*. 2008;14:1926-30.
- [248] Williams RL, Hilton DJ, Pease S, Willson TA, Stewart CL, Gearing DP, et al. Myeloid leukaemia inhibitory factor maintains the developmental potential of embryonic stem cells. *Nature*. 1988;336:684-7.
- [249] Zhao Q, Wang X-Y, Yu X-X, Zhai Y-X, He X, Wu S, et al. Expression of human telomerase reverse transcriptase mediates the senescence of mesenchymal stem cells through the PI3K/AKT signaling pathway. *International Journal of Molecular Medicine*. 2015;36:857-64.
- [250] Saeed H, Qiu W, Li C, Flyvbjerg A, Abdallah BM, Kassem M. Telomerase activity promotes osteoblast differentiation by modulating IGF-signaling pathway. *Biogerontology*. 2015;16:733-45.
- [251] Xie L, Zeng X, Hu J, Chen Q. Characterization of nestin, a selective marker for bone marrow derived mesenchymal stem cells. *Stem cells international*. 2015;2015:762098-.
- [252] Wong A, Ghassemi E, Yellowley CE. Nestin expression in mesenchymal stromal cells: regulation by hypoxia and osteogenesis. *BMC Vet Res*. 2014;10:173-.
- [253] Liu TM, Wu YN, Guo XM, Hui JHP, Lee EH, Lim B. Effects of ectopic Nanog and Oct4 overexpression on mesenchymal stem cells. *Stem cells and development*. 2009;18:1013-22.
- [254] Riekstina U, Cakstina I, Parfejevs V, Hoogduijn M, Jankovskis G, Muiznieks I, et al. Embryonic stem cell marker expression pattern in human mesenchymal stem Cells derived from bone marrow, adipose tissue, heart and dermis. *Stem Cell Reviews and Reports*. 2009;5:378-86.

- [255] Han S-M, Han S-H, Coh Y-R, Jang G, Chan Ra J, Kang S-K, et al. Enhanced proliferation and differentiation of Oct4- and Sox2-overexpressing human adipose tissue mesenchymal stem cells. *Experimental & molecular medicine*. 2014;46:e101-e.
- [256] Simandi Z, Horvath A, Wright LC, Cuaranta-Monroy I, De Luca I, Karolyi K, et al. OCT4 Acts as an Integrator of Pluripotency and Signal-Induced Differentiation. *Mol Cell* 2016;63:647-61.
- [257] Ben-Shushan E, Thompson JR, Gudas LJ, Bergman Y. Rex-1, a gene encoding a transcription factor expressed in the early embryo, is regulated via Oct-3/4 and Oct-6 binding to an octamer site and a novel protein, Rox-1, binding to an adjacent site. *Molecular and Cellular Biology*. 1998;18:1866-78.
- [258] Bhandari DR, Seo K-W, Roh K-H, Jung J-W, Kang S-K, Kang K-S. REX-1 expression and p38 MAPK activation status can determine proliferation/differentiation fates in human mesenchymal stem cells. *PloS one*. 2010;5:e10493.
- [259] Shi G, Jin Y. Role of Oct4 in maintaining and regaining stem cell pluripotency. *Stem Cell Research & Therapy*. 2010;1:39.
- [260] Park SB, Seo KW, So AY, Seo MS, Yu KR, Kang SK, et al. SOX2 has a crucial role in the lineage determination and proliferation of mesenchymal stem cells through Dickkopf-1 and c-MYC. *Cell Death & Differentiation*. 2011;19:534.
- [261] Blokzijl A, Dahlqvist C, Reissmann E, Falk A, Moliner A, Lendahl U, et al. Cross-talk between the Notch and TGF- β signaling pathways mediated by interaction of the Notch intracellular domain with Smad3. *Journal of Cell Biology*. 2003;163:723-8.
- [262] Zamurovic N, Cappellen D, Rohner D, Susa M. Coordinated activation of Notch, Wnt, and transforming growth factor- β signaling pathways in bone morphogenic protein 2-induced osteogenesis. *Journal of Biological Chemistry*. 2004;279:37704-15.
- [263] Suh JH, Lee HW, Lee J-W, Kim JB. Hes1 stimulates transcriptional activity of Runx2 by increasing protein stabilization during osteoblast differentiation. *Biochemical and biophysical research communications*. 2008;367:97-102.

- [264] Hardingham TE, Oldershaw RA, Tew SR. Cartilage, SOX9 and Notch signals in chondrogenesis. *Journal of anatomy*. 2006;209:469-80.
- [265] Engin F, Yao Z, Yang T, Zhou G, Bertin T, Jiang MM, et al. Dimorphic effects of Notch signaling in bone homeostasis. *Nature Medicine*. 2008;14:299-305.
- [266] Lawal RA, Zhou X, Batey K, Hoffman CM, Georger MA, Radtke F, et al. The Notch ligand Jagged1 regulates the osteoblastic lineage by maintaining the osteoprogenitor pool. *Journal of Bone and Mineral Research*. 2017;32:1320-31.
- [267] Youngstrom DW, Dishowitz MI, Bales CB, Carr E, Mutyaba PL, Kozloff KM, et al. Jagged1 expression by osteoblast-lineage cells regulates trabecular bone mass and periosteal expansion in mice. *Bone*. 2016;91:64-74.
- [268] Oda T, Elkahoun AG, Pike BL, Okajima K, Krantz ID, Genin A, et al. Mutations in the human Jagged1 gene are responsible for Alagille syndrome. *Nature Genetics*. 1997;16:235-42.
- [269] Wang H, Jiang Z, Zhang J, Xie Z, Wang Y, Yang G. Enhanced osteogenic differentiation of rat bone marrow mesenchymal stem cells on titanium substrates by inhibiting Notch3. *Archives of Oral Biology*. 2017;80:34-40.
- [270] Calciolari E, Hamlet S, Ivanovski S, Donos N. Pro-osteogenic properties of hydrophilic and hydrophobic titanium surfaces: Crosstalk between signalling pathways in in vivo models. *Journal of Periodontal Research*. 2018;53:598-609.
- [271] Souza PG, Adolpho LF, Lopes HB, Weffort D, Souza ATP, Oliveira FS, et al. Effects of Modulation of the Hedgehog and Notch Signaling Pathways on Osteoblast Differentiation Induced by Titanium with Nanotopography. *Journal of Functional Biomaterials*. 2023;14:79.
- [272] Dishowitz MI, Terkhorn SP, Bostic SA, Hankenson KD. Notch signaling components are upregulated during both endochondral and intramembranous bone regeneration. *Journal of Orthopaedic Research*. 2012;30:296-303.
- [273] Andrae J, Gallini R, Bertsholtz C. Role of platelet-derived growth factors in physiology and medicine. *Genes & Development*. 2008;22:1276-312.
- [274] James MF, Beauchamp RL, Manchanda N, Kazlauskas A, Ramesh V. A NHERF binding site links the β PDGFR to the cytoskeleton and regulates cell spreading and migration. *Journal of cell science*. 2004;117:2951-61.

- [275] Trojanowska M. Role of PDGF in fibrotic diseases and systemic sclerosis. *Rheumatology*. 2008;47:v2-v4.
- [276] Chang KK, Yoon C, Yi BC, Tap WD, Simon MC, Yoon SS. Platelet-derived growth factor receptor- α and - β promote cancer stem cell phenotypes in sarcomas. *Oncogenesis*. 2018;7:47.
- [277] Agarwal R, Williams K, Umscheid CA, Welch WC. Osteoinductive bone graft substitutes for lumbar fusion: a systematic review. *Journal of Neurosurgery*. 2009;11:729-40.
- [278] Lavery K, Hawley S, Swain P, Rooney R, Falb D, Alaoui-Ismaili MH. New insights into BMP-7 mediated osteoblastic differentiation of primary human mesenchymal stem cells. *Bone*. 2009;45:27-41.
- [279] Bai X, Li G, Zhao C, Duan H, Qu F. BMP7 induces the differentiation of bone marrow-derived mesenchymal cells into chondrocytes. *Medical & biological engineering & computing*. 2011;49:687-92.
- [280] Neumann K, Endres M, Ringe J, Flath B, Manz R, Häupl T, et al. BMP7 promotes adipogenic but not osteo-/chondrogenic differentiation of adult human bone marrow-derived stem cells in high-density micro-mass culture. *Journal of cellular biochemistry*. 2007;102:626-37.
- [281] Knippenberg M, Helder MN, Zandieh Doulabi B, Wuisman PIJM, Klein-Nulend J. Osteogenesis versus chondrogenesis by BMP-2 and BMP-7 in adipose stem cells. *Biochemical and biophysical research communications*. 2006;342:902-8.
- [282] Neumann K, Endres M, Ringe J, Flath B, Manz R, Häupl T, et al. BMP7 promotes adipogenic but not osteo-/chondrogenic differentiation of adult human bone marrow-derived stem cells in high-density micro-mass culture. *Journal of cellular biochemistry*. 2007;102:626-37.
- [283] Polinkovsky A, Robin NH, Thomas JT, Irons M, Lynn A, Goodman FR, et al. Mutations in CDMP1 cause autosomal dominant brachydactyly type C. *Nature Genetics*. 1997;17:18.
- [284] Thomas JT, Kilpatrick MW, Lin K, Erlacher L, Lembessis P, Costa T, et al. Disruption of human limb morphogenesis by a dominant negative mutation in CDMP1. *Nature Genetics*. 1997;17:58.

- [285] Settle SH, Rountree RB, Sinha A, Thacker A, Higgins K, Kingsley DM. Multiple joint and skeletal patterning defects caused by single and double mutations in the mouse *Gdf6* and *Gdf5* genes. *Developmental biology*. 2003;254:116-30.
- [286] Chang C, Hemmati-Brivanlou A. *Xenopus* GDF6, a new antagonist of noggin and a partner of BMPs. *Development*. 1999;126:3347-57.
- [287] Tsimbouri P, Gadegaard N, Burgess K, White K, Reynolds P, Herzyk P, et al. Nanotopographical effects on mesenchymal stem cell morphology and phenotype. *Journal of cellular biochemistry*. 2014;115:380-90.
- [288] Kollmer M, Buhrman JS, Zhang Y, Gemeinhart RA. Markers are shared between adipogenic and osteogenic differentiated mesenchymal stem cells. *J Dev Biol Tissue Eng*. 2013;5:18-25.
- [289] Barry F, Boynton RE, Liu B, Murphy JM. Chondrogenic differentiation of mesenchymal stem cells from bone marrow: differentiation-dependent gene expression of matrix components. *Experimental cell research*. 2001;268:189-200.
- [290] Jakob M, Démarteau O, Schäfer D, Hintermann B, Dick W, Heberer M, et al. Specific growth factors during the expansion and redifferentiation of adult human articular chondrocytes enhance chondrogenesis and cartilaginous tissue formation in vitro. *Journal of cellular biochemistry*. 2001;81:368-77.
- [291] Karlsson C, Brantsing C, Svensson T, Brisby H, Asp J, Tallheden T, et al. Differentiation of human mesenchymal stem cells and articular chondrocytes: Analysis of chondrogenic potential and expression pattern of differentiation-related transcription factors. *Journal of Orthopaedic Research*. 2007;25:152-63.
- [292] Takarada T, Nakazato R, Tsuchikane A, Fujikawa K, Iezaki T, Yoneda Y, et al. Genetic analysis of *Runx2* function during intramembranous ossification. *Development*. 2016;143:211.
- [293] Otto F, Thornell A, Crompton T, Denzel A, Gilmour K, Rosewell I, et al. *Cbfa1*, a candidate gene for cleidocranial dysplasia syndrome, is essential for osteoblast differentiation and bone development. *Cell*. 1997;89:765-71.
- [294] Komori T, Yagi H, Nomura S, Yamaguchi A, Sasaki K, Deguchi K, et al. Targeted disruption of *Cbfa1* results in a complete lack of bone formation owing to maturational arrest of osteoblasts *Cell*. 1997;89:755-64.

- [295] Levanon D, Negreanu V, Bernstein Y, Bar-Am I, Avivi L, Groner Y. AML1, AML2, and AML3, the human members of the runt domain gene-family: cDNA structure, expression, and chromosomal localization. *Genomics*. 1994;23:425-32.
- [296] Mundlos S, Otto F, Mundlos C, Mulliken JB, Aylsworth AS, Albright S, et al. Mutations involving the transcription factor CBFA1 cause cleidocranial dysplasia. *Cell*. 1997;89:773-9.
- [297] Ducy P, Zhang R, Geoffroy V, Ridall AL, Karsenty G. *Osf2-Cbfa1*: a transcriptional activator of osteoclast differentiation. *Cell*. 1997;89:747-54.
- [298] Ducy P, Karsenty G. Two distinct osteoblast-specific cis-acting elements control expression of a mouse osteocalcin gene. *Molecular and Cellular Biology*. 1995;15:1858-69.
- [299] Geoffroy V, Kneissel M, Fournier B, Boyde A, Matthias P. High bone resorption in adult aging transgenic mice overexpressing *cbfa1/runx2* in cells of the osteoblastic lineage. *Molecular and Cellular Biology*. 2002;22:6222-33.
- [300] Maruyama Z, Yoshida CA, Furuichi T, Amizuka N, Ito M, Fukuyama R, et al. *Runx2* determines bone maturity and turnover rate in postnatal bone development and is involved in bone loss in estrogen deficiency. *Developmental Dynamics*. 2007;236:1876-90.
- [301] Liu W, Toyosawa S, Furuichi T, Kanatani N, Yoshida C, Liu Y, et al. Overexpression of *Cbfa1* in osteoblasts inhibits osteoblast maturation and causes osteopenia with multiple fractures. *Journal of Cell Biology*. 2001;155:157-66.
- [302] Arvidson K, Abdallah BM, Applegate LA, Baldini N, Cenni E, Gomez-Barrena E, et al. Bone regeneration and stem cells. *Journal of cellular and molecular medicine*. 2011;15:718-46.
- [303] Zhu H, Kavsak P, Abdollah S, Wrana JL, Thomsen GH. A SMAD ubiquitin ligase targets the BMP pathway and affects embryonic pattern formation. *Nature*. 1999;400:687.
- [304] Zhu H, Kavsak P, Abdollah S, Wrana JL, Thomsen GH. A SMAD ubiquitin ligase targets the BMP pathway and affects embryonic pattern formation. *Nature*. 1999;400:687-93.

- [305] Shen R, Chen M, Wang Y-J, Kaneki H, Xing L, O'Keefe RJ, et al. Smad6 interacts with Runx2 and mediates Smad ubiquitin regulatory factor 1-induced Runx2 degradation. *Journal of Biological Chemistry*. 2006;281:3569-76.
- [306] Lu K, Yin X, Weng T, Xi S, Li L, Xing G, et al. Targeting WW domains linker of HECT-type ubiquitin ligase Smurf1 for activation by CKIP-1. *Nature cell biology*. 2008;10:994-1002.
- [307] Yamashita M, Ying S-X, Zhang G-m, Li C, Cheng SY, Deng C-x, et al. Ubiquitin ligase Smurf1 controls osteoblast activity and bone homeostasis by targeting MEKK2 for degradation. *Cell*. 2005;121:101-13.
- [308] Shimazu J, Wei J, Karsenty G. Smurf1 Inhibits Osteoblast Differentiation, Bone Formation, and Glucose Homeostasis through Serine 148. *Cell reports*. 2016;15:27-35.
- [309] Zhao M, Qiao M, Harris SE, Oyajobi BO, Mundy GR, Chen D. Smurf1 inhibits osteoblast differentiation and bone formation in vitro and in vivo. *Journal of Biological Chemistry*. 2004;279:12854-9.
- [310] Lin X, Liang M, Feng X-H. Smurf2 Is a ubiquitin E3 ligase mediating proteasome-dependent degradation of Smad2 in transforming growth factor-beta signaling. *Journal of Biological Chemistry*. 2000;275:36818-22.
- [311] Zhang Y, Chang C, Gehling DJ, Hemmati-Brivanlou A, Derynck R. Regulation of Smad degradation and activity by Smurf2, an E3 ubiquitin ligase. *Proceedings of the National Academy of Sciences*. 2001;98:974-9.
- [312] Luzzi E, Marini F, Sala SC, Tognarini I, Galli G, Brandi ML. Osteogenic Differentiation of Human Adipose Tissue-Derived Stem Cells Is Modulated by the miR-26a Targeting of the SMAD1 Transcription Factor. *Journal of Bone and Mineral Research*. 2008;23:287-95.
- [313] Fujii M, Takeda K, Imamura T, Aoki H, Sampath TK, Enomoto S, et al. Roles of bone morphogenetic protein type I receptors and Smad proteins in osteoblast and chondroblast differentiation. *Molecular biology of the cell*. 1999;10:3801-13.
- [314] Lee KS, Kim HJ, Li QL, Chi XZ, Ueta C, Komori T, et al. Runx2 is a common target of transforming growth factor beta1 and bone morphogenetic protein 2, and cooperation between Runx2 and Smad5 in the pluripotent mesenchymal precursor cell line C2C12. *Molecular and Cellular Biology*. 2000;20:8783-92.

- [315] Yamamoto N, Akiyama S, Katagiri T, Namiki M, Kurokawa T, Suda T. Smad1 and Smad5 act downstream of intracellular signalings of BMP-2 that inhibits myogenic differentiation and induces osteoblast differentiation in C2C12 myoblasts. *Biochemical and biophysical research communications*. 1997;238:574-80.
- [316] Jeon E-J, Lee K-Y, Choi N-S, Lee M-H, Kim H-N, Jin Y-H, et al. Bone morphogenetic protein-2 stimulates Runx2 acetylation. *Journal of Biological Chemistry*. 2006;281:16502-11.
- [317] Drissi H, Luc Q, Shakoory R, Chuva De Sousa Lopes S, Choi J-Y, Terry A, et al. Transcriptional autoregulation of the bone related CBFA1/RUNX2 gene. *Journal of Cell Physiology*. 2000;184:341-50.
- [318] Cheng H, Jiang W, Phillips FM, Haydon RC, Peng Y, Zhou L, et al. Osteogenic activity of the fourteen types of human bone morphogenetic proteins (BMPs). *Journal of Bone & Joint Surgery [Am]*. 2003;85.
- [319] Schmitt B, Ringe J, Häupl T, Notter M, Manz R, Burmester G-R, et al. BMP2 initiates chondrogenic lineage development of adult human mesenchymal stem cells in high-density culture. *Differentiation*. 2003;71:567-77.
- [320] Kwon S-H, Lee T-J, Park J, Hwang J-E, Jin M, Jang H-K, et al. Modulation of BMP-2-induced chondrogenic versus osteogenic differentiation of human mesenchymal stem cells by cell-specific extracellular matrices. *Tissue Engineering: Part A*. 2013;19:49-58.
- [321] Schwartz Z, Simon BJ, Duran MA, Barabino G, Chaudhri R, Boyan BD. Pulsed electromagnetic fields enhance BMP-2 dependent osteoblastic differentiation of human mesenchymal stem cells. *Journal of Orthopaedic Research*. 2008;26:1250-5.
- [322] Dimar JR, Glassman SD, Burkus KJ, Carreon LY. Clinical outcomes and fusion success at 2 years of single-level instrumented posterolateral fusions with recombinant human bone morphogenetic protein-2/compression resistant matrix versus iliac crest bone graft. *Spine*. 2006;31:2534-9.
- [323] Garrison KR, Shemilt I, Donell S, Ryder JJ, Mugford M, Harvey I, et al. Bone morphogenetic protein (BMP) for fracture healing in adults. *Cochrane Database of Systematic Reviews*. 2010.

- [324] Carragee EJ, Hurwitz EL, Weiner BK. A critical review of recombinant human bone morphogenetic protein-2 trials in spinal surgery: emerging safety concerns and lessons learned. *The spine journal*. 2011;11:471-91.
- [325] Mroz TE, Wang JC, Hashimoto R, Norvell DC. Complications Related to Osteobiologics Use in Spine Surgery: A Systematic Review. *Spine*. 2010;35:S86-104.
- [326] Irie K, Alpaslan C, Takahashi K, Kondo Y, Izumi N, Sakakura Y, et al. Osteoclast differentiation in ectopic bone formation induced by recombinant human bone morphogenetic protein 2 (rhBMP-2). *Journal of bone and mineral metabolism*. 2003;21:363-9.
- [327] Broege A, Pham L, Jensen ED, Emery A, Huang T-H, Stemig M, et al. Bone morphogenetic proteins signal via SMAD and mitogen-activated protein (MAP) kinase pathways at distinct times during osteoclastogenesis. *The Journal of biological chemistry*. 2013;288:37230-40.
- [328] Fajas L, Auboeuf D, Raspé E, Schoonjans K, Lefebvre AM, Saladin R, et al. The organization, promoter analysis, and expression of the human PPARgamma gene. *The Journal of biological chemistry*. 1997;272:18779–89.
- [329] Jeon MJ, Kim JA, Kwon SH, Kim SW, Park KS, Park S-W, et al. Activation of peroxisome proliferator-activated receptor-gamma inhibits the Runx2-mediated transcription of osteocalcin in osteoblasts. *Journal of Biological Chemistry*. 2003;278:23270-7.
- [330] Lecka-Czernik B, Gubrij I, Moerman EJ, Kajkenova O, Lipschitz DA, Manolagas SC, et al. Inhibition of *Osf2/Cbfa1* expression and terminal osteoblast differentiation by PPARgamma2. *Journal of cellular biochemistry*. 1999;74:357- 71.
- [331] Biggs MJ, Richards RG, Dalby MJ. Nanotopographical modification: a regulator of cellular function through focal adhesions. *Nanomedicine : nanotechnology, biology, and medicine*. 2010;6:619-33.
- [332] Takada Y, Ye X, Simon S. The integrins. *Genome Biology*. 2007;8:215.
- [333] Fässler R, Meyer M. Consequences of lack of beta 1 integrin gene expression in mice. *Genes & Development*. 1995;9:1896-908.

- [334] Aszodi A, Hunziker EB, Brakebusch C, Fässler R. Beta1 integrins regulate chondrocyte rotation, G1 progression, and cytokinesis. *Genes & Development*. 2003;17:2465-79.
- [335] Villa-Diaz LG, Kim JK, Laperle A, Palecek SP, Krebsbach PH. Inhibition of focal adhesion kinase signaling by integrin $\alpha 6 \beta 1$ supports human pluripotent stem cell self-renewal. *Stem Cells*. 2016;34:1753-64.
- [336] Rouahi M, Champion E, Hardouin P, Anselme K. Quantitative kinetic analysis of gene expression during human osteoblastic adhesion on orthopaedic biomaterials. *Biomaterials*. 2006;27:2829-44.
- [337] Biggs MJ, Dalby MJ. Focal adhesions in osteoneogenesis. *Proceedings of the Institution of Mechanical Engineers H*. 2010;224:1441-53.
- [338] Kim J-B, Leucht P, Luppen CA, Park YJ, Beggs HE, Damsky CH, et al. Reconciling the roles of FAK in osteoblast differentiation, osteoclast remodeling, and bone regeneration. *Bone*. 2007;41:39-51.
- [339] Schaller MD, Borgman CA, Cobb BS, Vines RR, Reynolds AB, Parsons JT. pp125FAK a structurally distinctive protein-tyrosine kinase associated with focal adhesions. *Proceedings of the National Academy of Sciences*. 1992;89:5192-6.
- [340] Harburger DS, Calderwood DA. Integrin signalling at a glance. *Journal of cell science*. 2009;122:159-63.
- [341] Holt G, Murnaghan C, Reilly J, Meek RM. The biology of aseptic osteolysis. *Clinical orthopaedics and related research*. 2007;460:240-52.
- [342] Sundfeldt M, Carlsson LV, Johansson CB, Thomsen P, Gretzer C. Aseptic loosening, not only a question of wear: a review of different theories. *Acta orthopaedica*. 2006;77:177-97.
- [343] Rønold HJ, Ellingsen JE. Effect of micro-roughness produced by TiO₂ blasting-tensile testing of bone attachment by using coin-shaped implants. *Biomaterials*. 2002;23:4211-9.
- [344] Rønold HJ, Ellingsen JE. The use of a coin shaped implant for direct in situ measurement of attachment strength for osseointegrating biomaterial surfaces. *Biomaterials*. 2002;23:2201–9.

- [345] Rønold HJ, Ellingsen JE, Lyngstadaas SP. Tensile force testing of optimized coin-shaped titanium implant attachment kinetics in the rabbit tibiae. *Journal of Materials Science: Materials in Medicine* 2003;14:843–9.
- [346] Prodanov L, Lamers E, Wolke J, Huiberts R, Jansen JA, Walboomers XF. In vivo comparison between laser-treated and grit blasted/acid etched titanium. *Clinical oral implants research*. 2014;25:234-9.
- [347] Prodanov L, te Riet J, Lamers E, Domanski M, Luttge R, van Loon JJ, et al. The interaction between nanoscale surface features and mechanical loading and its effect on osteoblast-like cells behavior. *Biomaterials*. 2010;31:7758-65.
- [348] Schneider CA, Rasband WS, Eliceiri KW. NIH Image to ImageJ: 25 years of image analysis. *Nature methods*. 2012;9:671-5.
- [349] AZO Materials. Polycarbonate Properties - Supplier Data by Goodfellow Cambridge Ltd., Huntingdon, UK.
- [350] Ni GX, Choy YS, Lu WW, Ngan AHW, Chiu KY, Li ZY, et al. Nano-mechanics of bone and bioactive bone cement interfaces in a load-bearing model. *Biomaterials*. 2006;27:1963-70.
- [351] Isaksson H, Nagao S, Małkiewicz M, Julkunen P, Nowak R, Jurvelin JS. Precision of nanoindentation protocols for measurement of viscoelasticity in cortical and trabecular bone. *Journal of biomechanics*. 2010;43:2410-7.
- [352] Akhavan S, Matthiesen MM, Schulte L, Penoyar T, Kraay MJ, Rimnac CM, et al. Clinical and histologic results related to a low-modulus composite total hip replacement stem. *Journal of Bone & Joint Surgery [Am]*. 2006;88:1308-14.
- [353] Giannoudis PV, Einhorn TA, Marsh D. Fracture healing: the diamond concept. *Injury*. 2007;38:S3-S6.
- [354] Shalabi MM, Gortemaker A, Van't Hof MA, Jansen JA, Creugers NH. Implant surface roughness and bone healing: a systematic review. *Journal of Dental Research* 2006;85:496-500.
- [355] McNamara LE, Sjostrom T, Burgess KE, Kim JJ, Liu E, Gordonov S, et al. Skeletal stem cell physiology on functionally distinct titania nanotopographies. *Biomaterials*. 2011;32:7403-10.

- [356] Mathieu V, Fukui K, Matsukawa M, Kawabe M, Vayron R, Soffer E, et al. Micro-brillouin scattering measurements in mature and newly formed bone tissue surrounding an implant. *Journal of Biomechanical Engineering*. 2011;133:021006--6.
- [357] Ellingsen JE, Johansson CB, Wennerberg A, Holmén A. Improved retention and bone-to-implant contact with fluoride-modified titanium Implants. *International Journal of Oral & Maxillofacial Implants*. 2004;19:659-66.
- [358] Mathieu V, Vayron R, Soffer E, Anagnostou F, Haïat G. Influence of healing time on the ultrasonic response of the bone-implant interface. *Ultrasound in Medicine & Biology*. 2012;38:611-8.
- [359] Pazzaglia UE, Bonaspetti G, Ranchetti F, Bettinsoli P. A model of the intracortical vascular system of long bones and of its organization: an experimental study in rabbit femur and tibia. *Journal of anatomy*. 2008;213:183-93.
- [360] Mosekilde L, Kragstrup J, Richards A. Compressive strength, ash weight, and volume of vertebral trabecular bone in experimental fluorosis in pigs. *Calcified tissue international*. 1987;40:318-22.
- [361] Aerssens J, Boonen S, Lowet G, Dequeker J. Interspecies differences in bone composition, density, and quality: potential implications for in vivo bone research. *Endocrinology*. 1998;139:663-70.
- [362] Hillier ML, Bell LS. Differentiating human bone from animal bone: a review of histological methods. *Journal of Forensic Science*. 2007;52:249-63.
- [363] Reichert JC, Epari DR, Wullschleger ME, Saifzadeh S, Steck R, Lienau J, et al. Establishment of a pre-clinical ovine model for tibial segmental bone defect repair by applying bone tissue engineering strategies. *Tissue Engineering: Part B*. 2010;16:93-105.
- [364] Feighan JE, Goldberg VM, Davy D, Parr JA, Stevenson S. The influence of surface-blasting on the incorporation of titanium-alloy implants in a rabbit intramedullary model. *The Journal of Bone and Joint Surgery*. 1995;77-A:1380-95.
- [365] Handal JA, John TK, Goldstein DT, Khurana JS, Saing M, Braitman LE, et al. Effect of atorvastatin on the cortical bones of corticosteroid treated rabbits. *Journal of Orthopaedic Research*. 2012;30:872-6.

- [366] Barron HW, McBride M, Martinez-Jimenez D, Foutz T, Divers S, Budsberg S. Comparison of two methods of long bone fracture repair in rabbits. *Journal of Exotic Pet Medicine*. 2010;19:183-8.
- [367] Bretschneider H, Mettelsiefen J, Rentsch C, Gelinsky M, Link HD, Günther K-P, et al. Evaluation of topographical and chemical modified TiAl6V4 implant surfaces in a weight-bearing intramedullary femur model in rabbit. *Journal of Biomedical Materials Research Part B: Applied Biomaterials*. 2020;108:1117-28.
- [368] Tannenbaum J, Bennett BT. Russell and Burch's 3Rs then and now: the need for clarity in definition and purpose. *J Am Assoc Lab Anim Sci*. 2015;54:120-32.
- [369] Kantawong F, Burchmore R, Gadegaard N, Oreffo RO, Dalby MJ. Proteomic analysis of human osteoprogenitor response to disordered nanotopography. *Journal of the Royal Society, Interface / the Royal Society*. 2009;6:1075-86.
- [370] Ueda K, Clark DP, Chen CJ, Roninson IB, Gottesman MM, Pastan I. The human multidrug resistance (MDR1) gene. cDNA cloning and transcription initiation. *Journal of Biological Chemistry*. 1987;262:505-8.
- [371] Nagamoto T, Eguchi G, Beebe DC. Alpha-smooth muscle actin expression in cultured lens epithelial cells. *Investigative Ophthalmology & Visual Science*. 2000;41:1122-9.
- [372] Look AT, Ashmun RA, Shapiro LH, Peiper SC. Human myeloid plasma membrane glycoprotein CD13 (gp150) is identical to aminopeptidase N. *J Clin Invest*. 1989;83:1299-307.
- [373] Gerasimou A, Ramella R, Brero A, Boero O, Sheiban I, Levi R, et al. Homing of annexin-labeled stem cells to apoptotic cells. *Cellular & molecular biology letters*. 2009;14:100-12.
- [374] Leschik J, Eckenstaler R, Nieweg K, Lichtenecker P, Brigadski T, Gottmann K, et al. Embryonic stem cells stably expressing BDNF-GFP exhibit a BDNF-release-dependent enhancement of neuronal differentiation. *Journal of cell science*. 2013;126:5062-73.
- [375] Tsao Y-T, Huang Y-J, Wu H-H, Liu Y-A, Liu Y-S, Lee OK. Osteocalcin mediates biomineralization during osteogenic maturation in human mesenchymal stromal cells. *Int J Mol Sci*. 2017;18:159.

- [376] Berasi SP, Varadarajan U, Archambault J, Cain M, Souza TA, Abouzeid A, et al. Divergent activities of osteogenic BMP2, and tenogenic BMP12 and BMP13 independent of receptor binding affinities. *Growth Factors*. 2011;29:128-39.
- [377] Mizrahi O, Sheyn D, Tawackoli W, Kallai I, Oh A, Su S, et al. BMP-6 is more efficient in bone formation than BMP-2 when overexpressed in mesenchymal stem cells. *Gene Therapy*. 2013;20:370-7.
- [378] Zhu W, Kim J, Cheng C, Rawlins BA, Boachie-Adjei O, Crystal RG, et al. Noggin regulation of bone morphogenetic protein (BMP) 2/7 heterodimer activity in vitro. *Bone*. 2006;39:61-71.
- [379] Deotare U, Al-Dawsari G, Couban S, Lipton JH. G-CSF-primed bone marrow as a source of stem cells for allografting: revisiting the concept. *Bone marrow transplantation*. 2015;50:1150-6.
- [380] Müller-Deubert S, Seefried L, Krug M, Jakob F, Ebert R. Epidermal growth factor as a mechanosensitizer in human bone marrow stromal cells. *Stem Cell Research*. 2017;24:69-76.
- [381] Schuldiner M, Yanuka O, Itskovitz-Eldor J, Melton DA, Benvenisty N. Effects of eight growth factors on the differentiation of cells derived from human embryonic stem cells. *Proceedings of the National Academy of Sciences*. 2000;97:11307-12.
- [382] Lee T-J, Jang J, Kang S, Jin M, Shin H, Kim D-W, et al. Enhancement of osteogenic and chondrogenic differentiation of human embryonic stem cells by mesodermal lineage induction with BMP-4 and FGF2 treatment. *Biochemical and biophysical research communications*. 2013;430:793-7.
- [383] Corre J, Labat E, Espagnolle N, Hébraud B, Avet-Loiseau H, Roussel M, et al. Bioactivity and prognostic significance of growth differentiation factor GDF15 secreted by bone marrow mesenchymal stem cells in multiple myeloma. *Cancer Research*. 2012;72:1395-406.
- [384] Coleman CM, Vaughan EE, Browe DC, Mooney E, Howard L, Barry F. Growth differentiation factor-5 enhances in vitro mesenchymal stromal cell chondrogenesis and hypertrophy. *Stem cells and development*. 2013;22:1968-76.
- [385] Howard M, Tuan RS, Wallis GA. The function and interrelationship between GDF5 and ERG-010 during chondrogenesis in vitro. *In Vitro Cellular & Developmental Biology - Animal*. 2016;52:182-92.

- [386] Mikic B. Multiple effects of GDF-5 deficiency on skeletal tissues: Implications for therapeutic bioengineering. *Annals of biomedical engineering*. 2004;32:466-76.
- [387] Hisamatsu D, Ohno-Oishi M, Nakamura S, Mabuchi Y, Naka-Kaneda H. Growth differentiation factor 6 derived from mesenchymal stem/stromal cells reduces age-related functional deterioration in multiple tissues. *Aging (Albany NY)*. 2016;8:1259-75.
- [388] Lee JY, Zhou Z, Taub PJ, Ramcharan M, Li Y, Akinbiyi T, et al. BMP-12 treatment of adult mesenchymal stem cells in vitro augments tendon-like tissue formation and defect repair in vivo. *PloS one*. 2011;6:e17531.
- [389] Mizuno M, Katano H, Mabuchi Y, Ogata Y, Ichinose S, Fujii S, et al. Specific markers and properties of synovial mesenchymal stem cells in the surface, stromal, and perivascular regions. *Stem Cell Research & Therapy*. 2018;9:123.
- [390] Gronthos S, Franklin DM, Leddy HA, Robey PG, Storms RW, Gimble JM. Surface protein characterization of human adipose tissue-derived stromal cells. *Journal of Cell Physiology*. 2001;189:54-63.
- [391] Ren G, Zhao X, Zhang L, Zhang J, L'Huillier A, Ling W, et al. Inflammatory cytokine-induced intercellular adhesion molecule-1 and vascular cell adhesion molecule-1 in mesenchymal stem cells are critical for immunosuppression. *The Journal of Immunology*. 2010;184:2321-8.
- [392] Sonomoto K, Yamaoka K, Oshita K, Fukuyo S, Zhang X, Nakano K, et al. Interleukin-1 β induces differentiation of human mesenchymal stem cells into osteoblasts via the Wnt-5a/receptor tyrosine kinase-like orphan receptor 2 pathway. *Arthritis & Rheumatism*. 2012;64:3355-63.
- [393] Xie Z, Tang Sa, Ye G, Wang P, Li J, Liu W, et al. Interleukin-6/interleukin-6 receptor complex promotes osteogenic differentiation of bone marrow-derived mesenchymal stem cells. *Stem Cell Research & Therapy*. 2018;9:13.
- [394] Nieto-Nicolau N, de la Torre RM, Fariñas O, Savio A, Vilarrodona A, Casaroli-Marano RP. Extrinsic modulation of integrin α 6 and progenitor cell behavior in mesenchymal stem cells. *Stem Cell Research*. 2020;47:101899.
- [395] Brafman DA, Phung C, Kumar N, Willert K. Regulation of endodermal differentiation of human embryonic stem cells through integrin-ECM interactions. *Cell Death & Differentiation*. 2013;20:369-81.

- [396] Collin M, Bigley V. Human dendritic cell subsets: an update. *Immunology*. 2018;154:3-20.
- [397] Brunner M, Mandier N, Gautier T, Chevalier G, Ribba A-S, Guardiola P, et al. β 1 integrins mediate the BMP2 dependent transcriptional control of osteoblast differentiation and osteogenesis. *PLoS one*. 2018;13:e0196021.
- [398] Diao Y, Ma Q, Cui F, Zhong Y. Human umbilical cord mesenchymal stem cells: Osteogenesis in vivo as seed cells for bone tissue engineering. *Journal of Biomedical Materials Research Part A*. 2009;91A:123-31.
- [399] Harkness L, Zaher W, Ditzel N, Isa A, Kassem M. CD146/MCAM defines functionality of human bone marrow stromal stem cell populations. *Stem Cell Research & Therapy*. 2016;7:4-.
- [400] Quirici N, Soligo D, Bossolasco P, Servida F, Lumini C, Deliliers GL. Isolation of bone marrow mesenchymal stem cells by anti-nerve growth factor receptor antibodies. *Experimental Hematology*. 2002;30:783-91.
- [401] Bradaschia-Correa V, Josephson AM, Egol AJ, Mizrahi MM, Leclerc K, Huo J, et al. Ecto-5'-nucleotidase (CD73) regulates bone formation and remodeling during intramembranous bone repair in aging mice. *Tissue and Cell*. 2017;49:545-51.
- [402] Ohishi K, Inoue N, Kinoshita T. PIG-S and PIG-T, essential for GPI anchor attachment to proteins, form a complex with GAA1 and GPI8. *The EMBO Journal*. 2001;20:4088-98.
- [403] Niwa H, Miyazaki J-i, Smith AG. Quantitative expression of Oct-3/4 defines differentiation, dedifferentiation or self-renewal of ES cells. *Nature Genetics*. 2000;24:372-6.
- [404] Heo JS, Choi Y, Kim H-S, Kim HO. Comparison of molecular profiles of human mesenchymal stem cells derived from bone marrow, umbilical cord blood, placenta and adipose tissue. *International Journal of Molecular Medicine*. 2016;37:115-25.
- [405] Irollo E, Pirozzi G. CD133: to be or not to be, is this the real question? *Am J Transl Res*. 2013;5:563-81.
- [406] Guan J-L. Role of focal adhesion kinase in integrin signaling. *The International Journal of Biochemistry & Cell Biology*. 1997;29:1085-96.

- [407] Ying S-X, Hussain ZJ, Zhang YE. Smurf1 facilitates myogenic differentiation and antagonizes the bone morphogenetic protein-2-induced osteoblast conversion by targeting Smad5 for degradation. *Journal of Biological Chemistry*. 2003;278:39029-36.
- [408] Bischoff DS, Makhijani NS, Yamaguchi DT. Constitutive expression of human telomerase enhances the proliferation potential of human mesenchymal stem cells. *Biores Open Access*. 2012;1:273-9.
- [409] Liu F, Akiyama Y, Tai S, Maruyama K, Kawaguchi Y, Muramatsu K, et al. Changes in the expression of CD106, osteogenic genes, and transcription factors involved in the osteogenic differentiation of human bone marrow mesenchymal stem cells. *Journal of bone and mineral metabolism*. 2008;26:312.
- [410] Fukiage K, Aoyama T, Shibata KR, Otsuka S, Furu M, Kohno Y, et al. Expression of vascular cell adhesion molecule-1 indicates the differentiation potential of human bone marrow stromal cells. *Biochemical and biophysical research communications*. 2008;365:406-12.
- [411] Quarto N, Behr B, Longaker MT. Opposite spectrum of activity of canonical Wnt signaling in the osteogenic context of undifferentiated and differentiated mesenchymal cells: implications for tissue engineering. *Tissue Engineering: Part A*. 2010;16:3185-97.
- [412] Shi W, Wang H, Pan G, Geng Y, Guo Y, Pei D. Regulation of the Pluripotency Marker Rex-1 by Nanog and Sox2*. *Journal of Biological Chemistry*. 2006;281:23319-25.
- [413] Concannon MJ, Boschert MT, Puckett CL. Bone induction using demineralized bone in the rabbit femur: A long-term study. *Plastic and reconstructive surgery*. 1997;99.
- [414] Inui K, Maeda M, Sano A, Fujioka K, Yutani Y, Sakawa A, et al. Local application of basic fibroblast growth factor minipellet induces the healing of segmental bony defects in rabbits. *Calcified tissue international*. 1998;63:490-5.
- [415] Fujibayashi S, Kim H-M, Neo M, Uchida M, Kokubo T, Nakamura T. Repair of segmental long bone defect in rabbit femur using bioactive titanium cylindrical mesh cage. *Biomaterials*. 2003;24:3445-51.

- [416] Fiakov JA, Holy CE, Shoichet MS, Davies JE. In vivo bone engineering in a rabbit femur. *The Journal of craniofacial surgery*. 2003;14:324-32.
- [417] Nunotani Y, Abe M, Shirai H, Otsuka H. Efficacy of rhBMP-2 during distraction osteogenesis. *Journal of Orthopedic Science*. 2005;10:529-33.
- [418] Yoneda M, Terai H, Imai Y, Okada T, Nozaki K, Inoue H, et al. Repair of an intercalated long bone defect with a synthetic biodegradable bone-inducing implant. *Biomaterials*. 2005;26:5145-52.
- [419] Gil-Albarova J, Salinas AJ, Bueno-Lozano AL, Roman J, Aldini-Nicolo N, Garcia-Barea A, et al. The in vivo behaviour of a sol-gel glass and a glass-ceramic during critical diaphyseal bone defects healing. *Biomaterials*. 2005;26:4374-82.
- [420] Yoon SJ, Park KS, Kim MS, Rhee JM, Khang G, Lee HB. Repair of diaphyseal bone defects with calcitriol-loaded PLGA scaffolds and marrow stromal cells. *Tissue engineering*. 2007;13:1125-33.
- [421] Sarahrudi K, Mousavi M, Grossschmidt K, Sela N, Konig F, Vecsei V, et al. The impact of colony-stimulating factor-1 on fracture healing: an experimental study. *Journal of Orthopaedic Research*. 2009;27:36-41.
- [422] Wang L, Fan H, Zhang ZY, Lou AJ, Pei GX, Jiang S, et al. Osteogenesis and angiogenesis of tissue-engineered bone constructed by prevascularized β -tricalcium phosphate scaffold and mesenchymal stem cells. *Biomaterials*. 2010;31:9452-61.
- [423] Collier JP, Colligan GA, Brown SA. Bone ingrowth into dynamically loaded porous-coated intramedullary nails. *Journal of biomedical materials research*. 1976;10:485-92.
- [424] Simpson AH, Williams PE, Kyberd P, Goldspink G, Kenwright J. The response of muscle to leg lengthening. *Journal of Bone & Joint Surgery [Br]*. 1995;77:630-6.
- [425] Brownlow HC, Simpson AHRW. Metabolic activity of a new atrophic nonunion model in rabbits. *Journal of Orthopaedic Research*. 2000;18:438-42.
- [426] Tobita K, Ohnishi I, Matsumoto T, Ohashi S, Bessho M, Kaneko M, et al. Effect of low-intensity pulsed ultrasound stimulation on callus remodelling in a gap-healing model: evaluation by bone morphometry using three-dimensional quantitative micro-CT. *Journal of Bone & Joint Surgery [Br]*. 2011;93:525-30.

- [427] Li G, Bouxsein ML, Luppen C, Li XJ, Wood M, Seeherman HJ, et al. Bone consolidation is enhanced by rhBMP-2 in a rabbit model of distraction osteogenesis. *Journal of Orthopaedic Research*. 2002;20:779-88.
- [428] Manninen MJ, Pohjonen T. Intramedullary nailing of the cortical bone osteotomies in rabbits with self-reinforced poly-L-lactide rods manufactured by the fibrillation method. *Biomaterials*. 1993;14:305-12.
- [429] Hing KA, Best SM, Tanner KE, Bonfield W. Biomechanical assessment of bone ingrowth in porous hydroxyapatite. *Journal of Materials Science: Materials in Medicine*. 1997;8:731-6.
- [430] D'Lima DD, Lemperle SM, Chen PC, Holmes RE, Colwell CWJ. Bone response to implant surface morphology. *Journal of Arthroplasty*. 1998;13:928-34.
- [431] Kettunen J, Mäkelä A, Miettinen H, Nevalainen T, Heikkilä M, Törmälä P, et al. Fixation of distal femoral osteotomy with an intramedullary rod: Early failure of carbon fibre composite implant in rabbits. *Journal of Biomaterials Science, Polymer Edition*. 1999;10:715-28.
- [432] Kettunen J, Mäkelä A, Miettinen H, Nevalainen T, Pohjonen T, Suokas E, et al. The fixation properties of carbon fiber-reinforced liquid crystalline polymer implant in bone: an experimental study in rabbits. *Journal of biomedical materials research*. 2001;56:137-43.
- [433] Saikku-Bäckström A, Tulamo RM, Räihä JE, Kellomäki M, Toivonen T, Törmälä P, et al. Intramedullary fixation of cortical bone osteotomies with absorbable self-reinforced fibrillated poly-96L/4D-lactide (SR-PLA96) rods in rabbits. *Biomaterials*. 2000;22:33-43.
- [434] Stewart M, Welter JF, Goldberg VM. Effect of hydroxyapatite/tricalcium-phosphate coating on osseointegration of plasma-sprayed titanium alloy implants. *Journal of Biomedical Materials Research Part A*. 2004;69A:1-10.
- [435] Dimitrievska S, Whitfield J, Hacking SA, Bureau MN. Novel carbon fiber composite for hip replacement with improved in vitro and in vivo osseointegration. *Journal of Biomedical Materials Research Part A*. 2009;91A:37-51.
- [436] Lakstein D, Kopelovitch W, Barkay Z, Bahaa M, Hendel D, Eliaz N. Enhanced osseointegration of grit-blasted, NaOH-treated and electrochemically

hydroxyapatite-coated Ti-6Al-4V implants in rabbits. *Acta biomaterialia*. 2009;5:2258-69.

[437] Hermida JC, Bergula A, Dimaano F, Hawkins M, Colwell CW, Jr., D'Lima DD. An in vivo evaluation of bone response to three implant surfaces using a rabbit intramedullary rod model. *Journal of orthopaedic surgery and research*. 2010;5:57.

[438] Aydin N, Bezer M. The effect of an intramedullary implant with a static magnetic field on the healing of the osteotomised rabbit femur. *International orthopaedics*. 2011;35:135-41.

[439] Guo Y, Chen D, Cheng M, Lu W, Wang L, Zhang X. The bone tissue compatibility of a new Ti₃₅Nb₂Ta₃Zr alloy with a low Young's modulus. *International Journal of Molecular Medicine*. 2013;31:689-97.

10Appendix

Table 13. Elemental analysis of oxygen plasma treated PEEK

Binding state (at. %)		O	C		C-C/C-H	C-O	C=O	π - π^*
Measured energy range (eV)		233.0- 234.5	284.0- 287.0		284.6- 285.0	286.4- 287.0	287.4- 288.4	292
Duration of plasma treatment (s)	Days since plasma treatment							
0	0	12.9	87.2		54.7	21.3	16.1	7.9
30	0	19.9	80.1		48.2	19.4	24.6	7.8
60	0	21.9	78.1		45.9	17.6	28.1	8.5
120	0	22.2	77.8		47.6	17.7	27.8	6.9
300	0	26.8	73.2		47.3	18.2	30.6	3.9
600	0	30.0	70.0		40.8	20.2	36.0	3.0
0	42	12.9	87.2		52.4	21.2	17.6	8.7
30	42	16.0	84.0		49.0	18.9	23.6	8.5
60	42	17.5	82.5		45.6	20.1	25.3	9.0
120	42	18.6	81.4		46.8	18.1	27.2	7.9
300	42	23.6	76.5		44.6	15.5	31.4	8.6
600	42	26.2	73.8		41.2	26.2	27.3	5.4
0	364	10.9	88.8					
120	364	14.6	84.1					
300	364	16.0	82.9					
600	364	18.1	80.6					

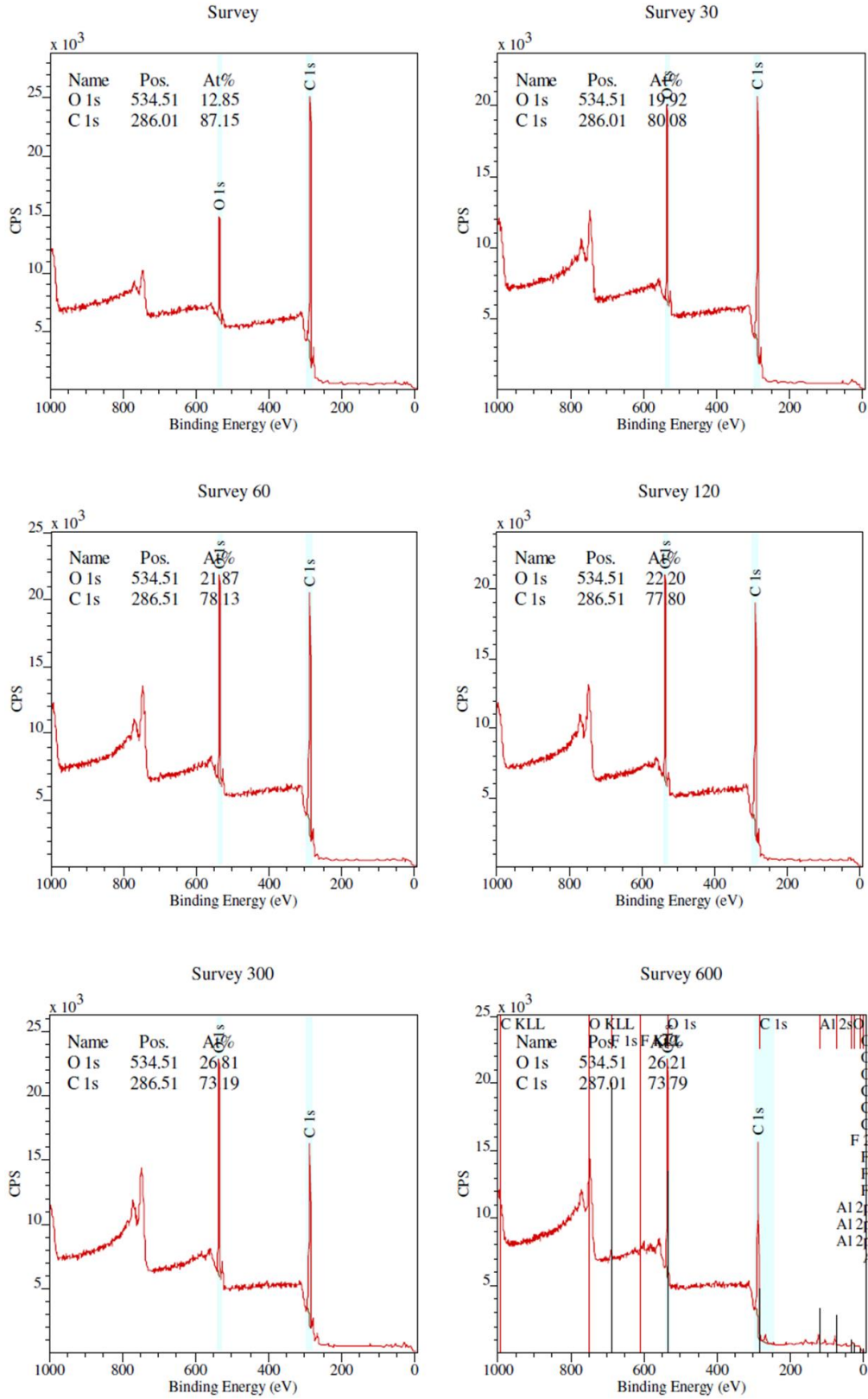


Figure 71. XPS survey scan of PEEK, 0 days after plasma treatment

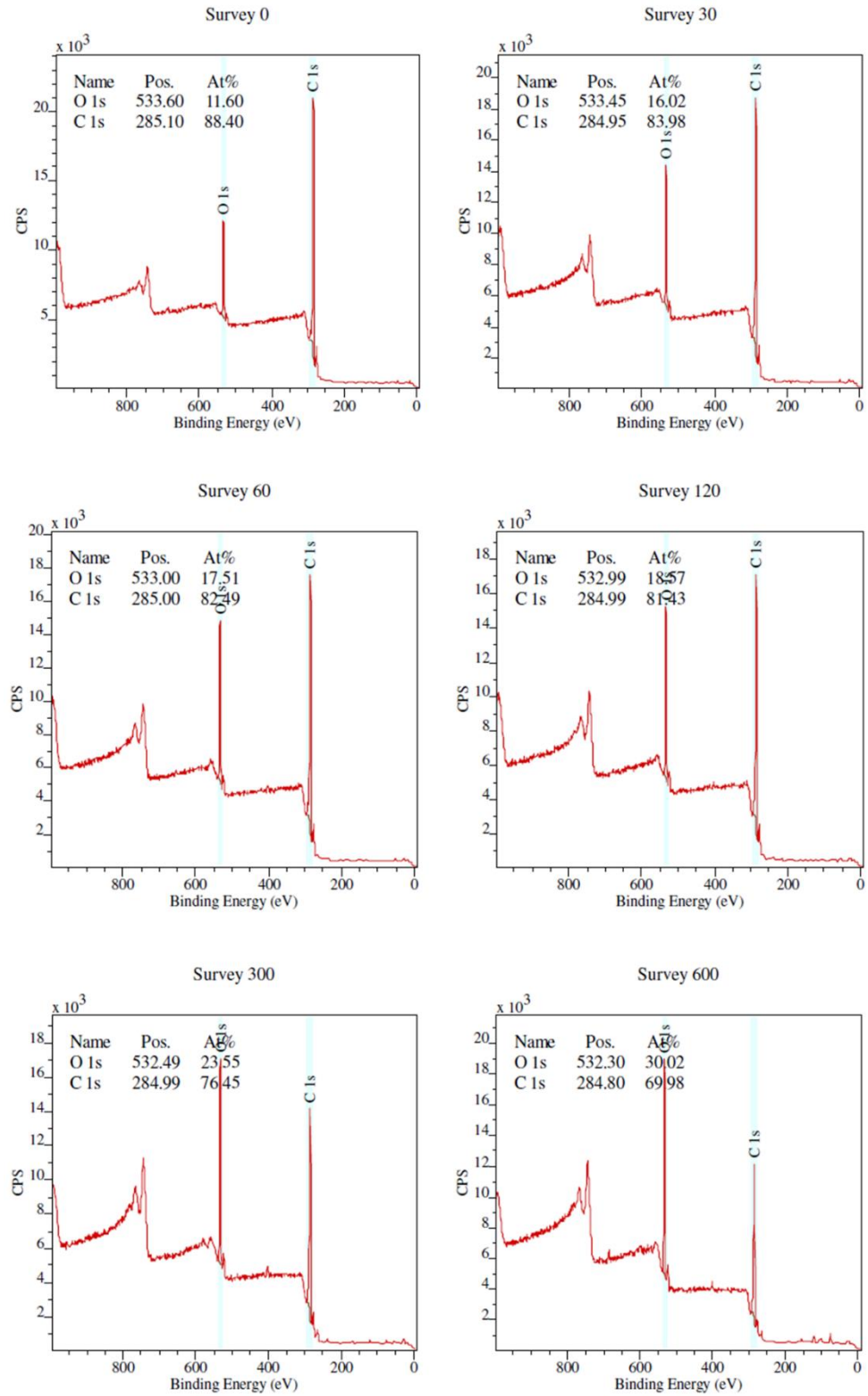


Figure 72. XPS survey scans of PEEK, 6 weeks after plasma treatment

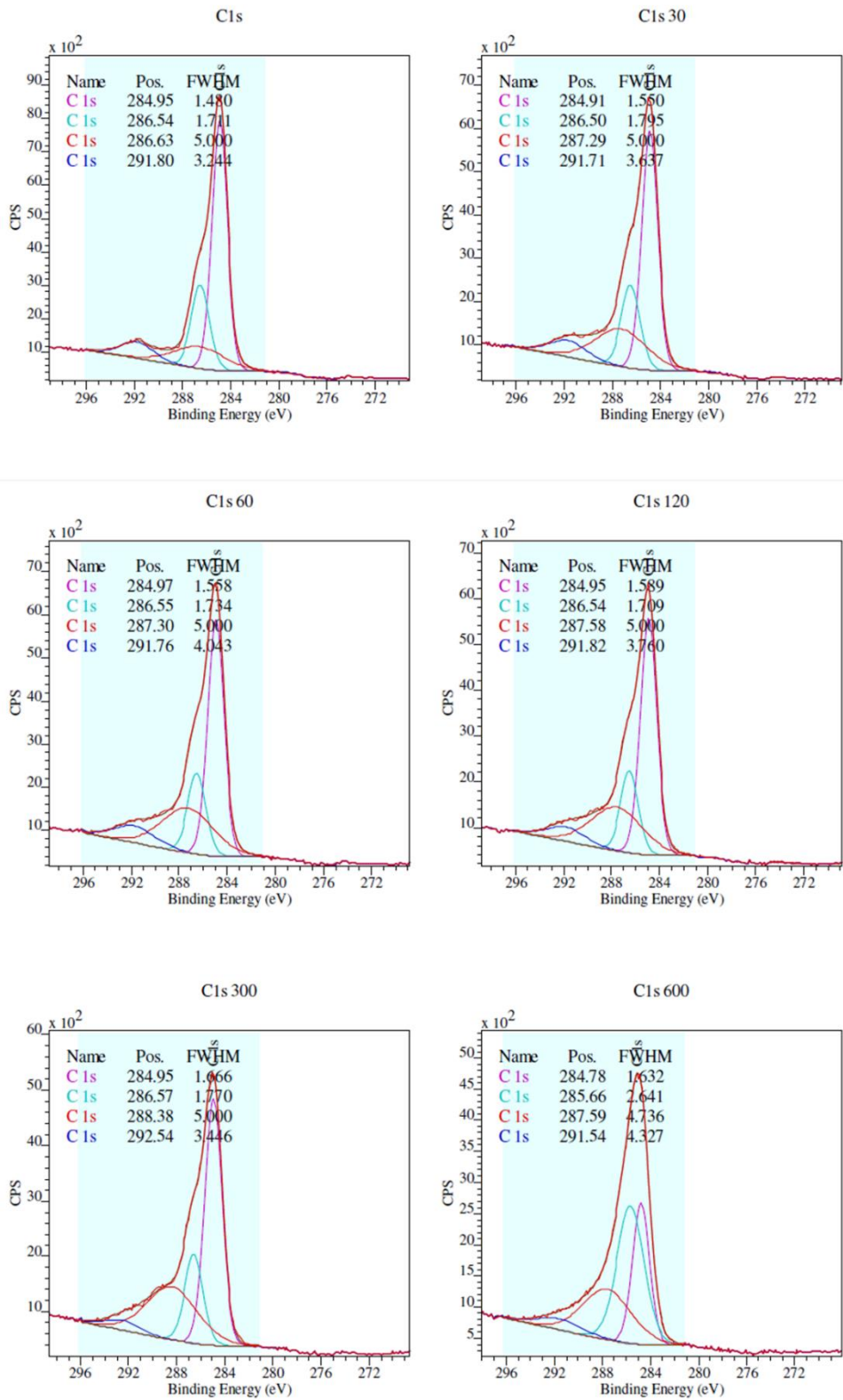


Figure 73. Curve fitting XPS spectra for PEEK, 0 days after O₂ plasma treatment

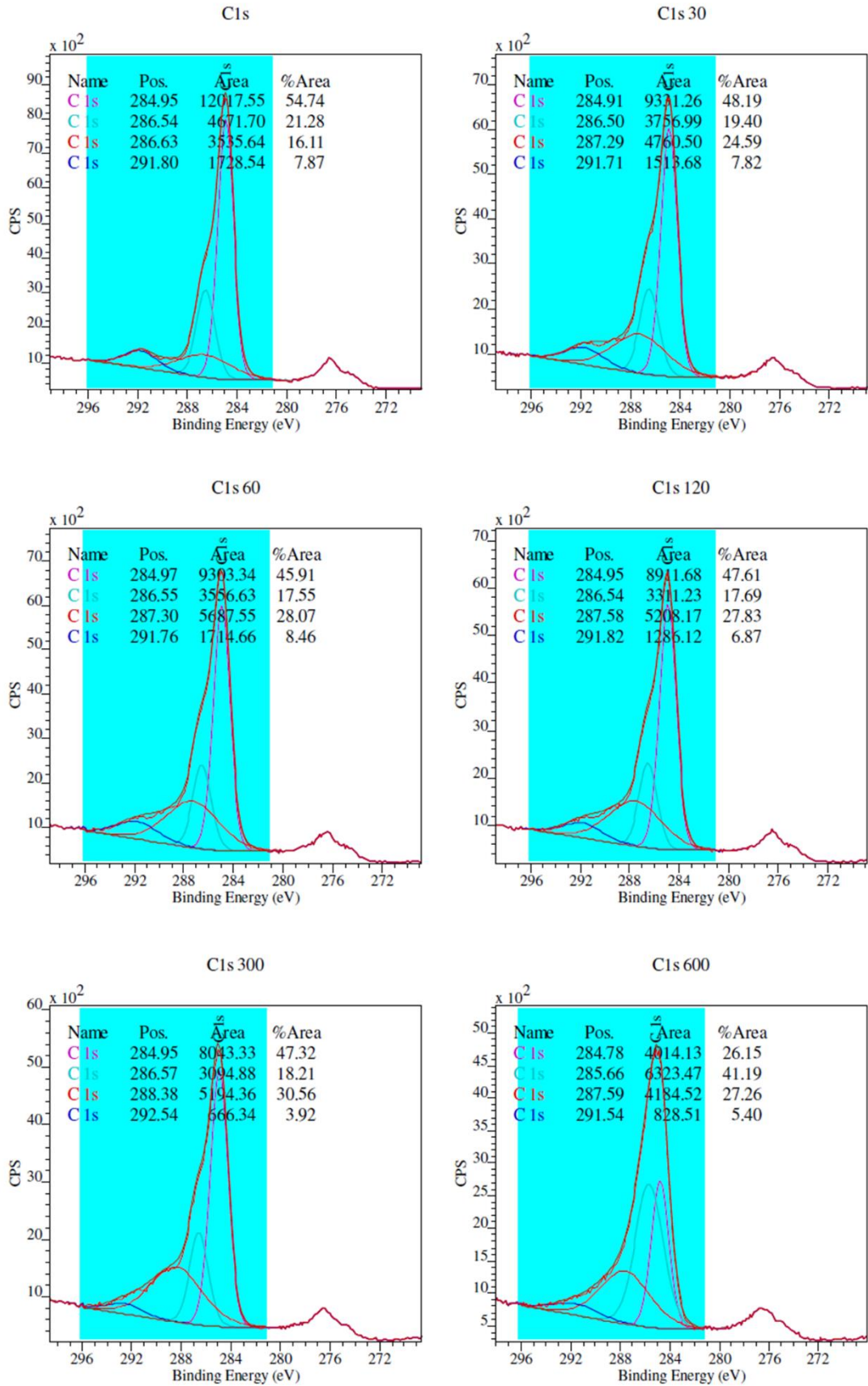


Figure 74. Narrow scan XPS spectra for PEEK, 0 days after O₂ plasma treatment

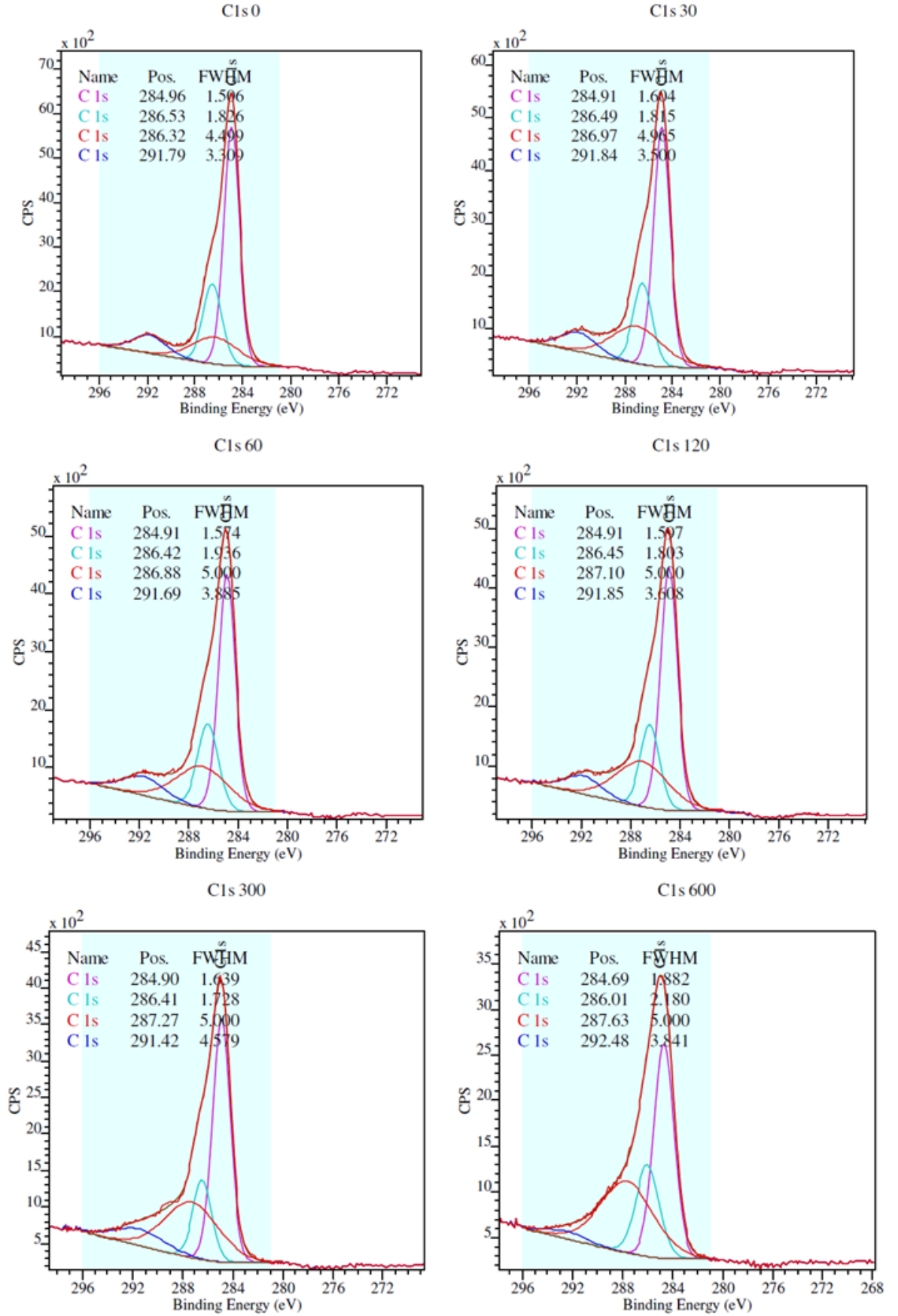


Figure 75. Curve fitting XPS spectra for PEEK, 6 weeks after O_2 plasma treatment

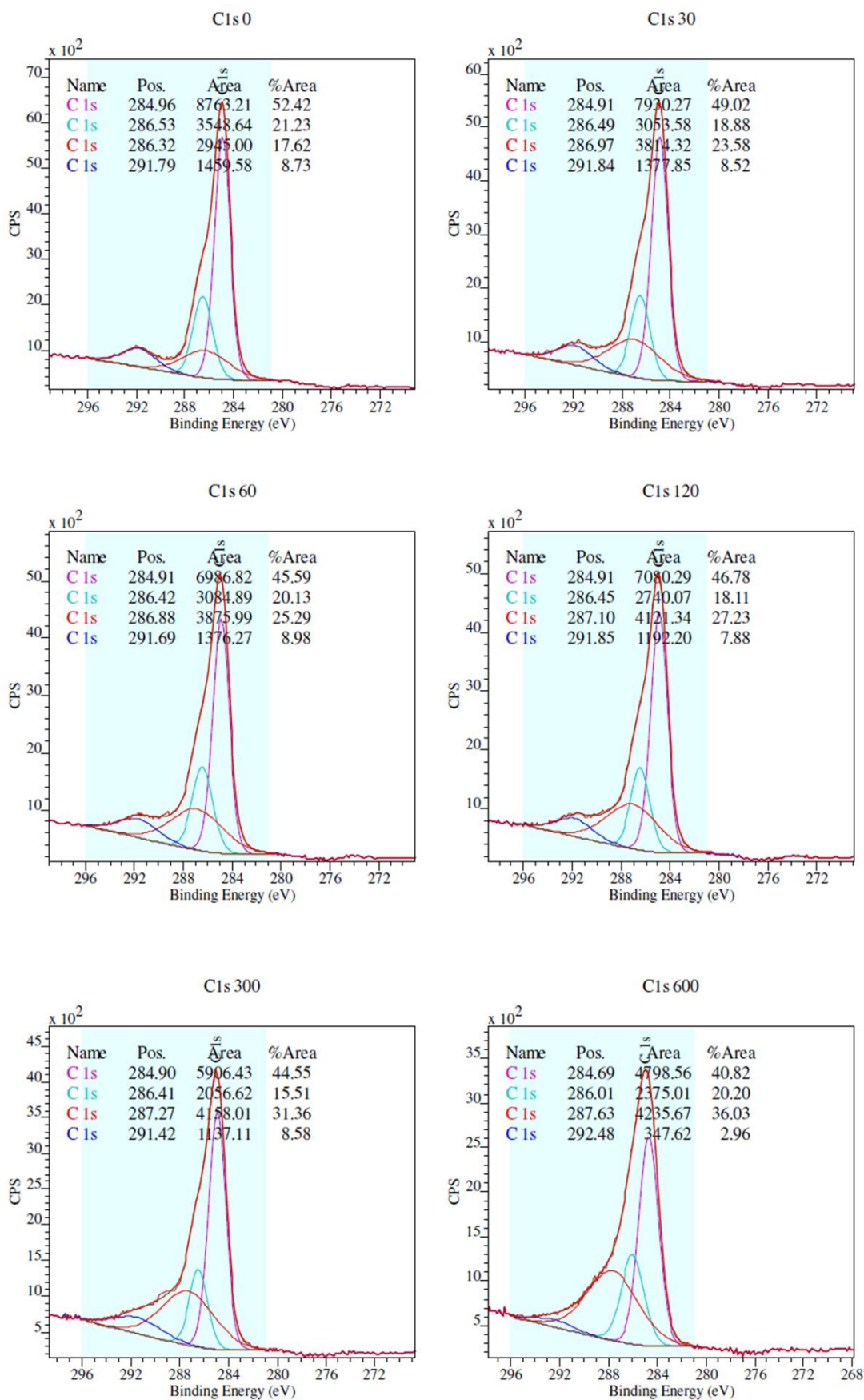


Figure 76. Narrow scan XPS spectra for PEEK, 6 weeks after O₂ plasma treatment

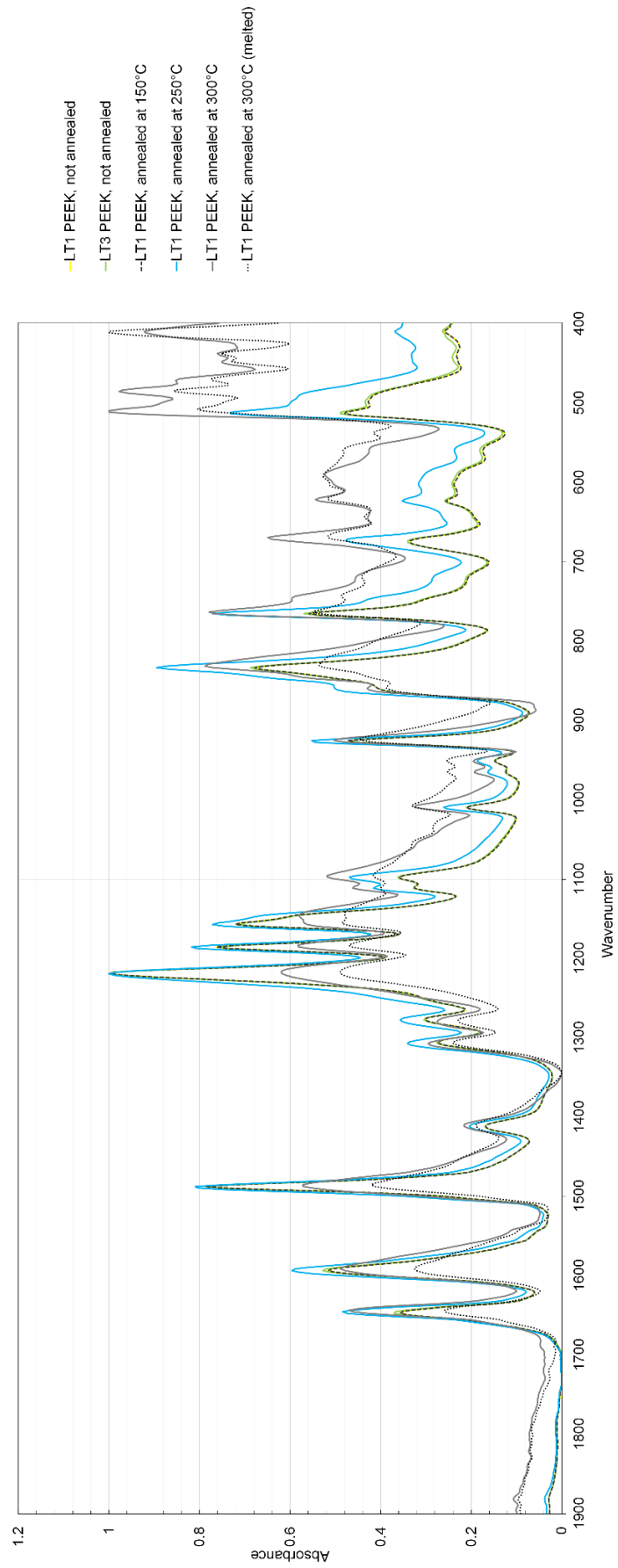


Figure 77. FTIR analysis of injection moulded and annealed PEEK

Table 14. Gene reference table for PCR array

	<i>Gene</i>	<i>Unigene/ GenBank</i>	<i>Transcribed protein (and aliases)</i>	<i>Ref.</i>
A01	<i>ABCB1</i>	Hs.489033 NM_000927	<i>Permeability-glycoprotein 1 (P-gp or Pgp); Multidrug resistance protein 1 (MDR1); ATP-binding cassette sub-family B member 1; Cluster of differentiation 243 (CD243)</i>	[370]
A02	<i>ACTA2</i>	Hs.500483 NM_001613	<i>Alpha-actin-2; Aortic smooth muscle; Alpha smooth muscle actin;</i>	[371]
A03	<i>ALCAM</i>	Hs.591293 NM_001627	<i>Activate leucocyte cell adhesion molecule; Cluster of differentiation 166 (CD166)</i>	[228]
A04	<i>ANPEP</i>	Hs.1239 NM_001150	<i>Alanyl aminopeptidase (AAP); Aminopeptidase N; Human myeloid plasma membrane glycoprotein (gp150) Cluster of differentiation 13 (CD13)</i>	[372]
A05	<i>ANXA5</i>	Hs.480653 NM_001154	<i>Annexin A5; Annexin V</i>	[373]
A06	<i>BDNF</i>	Hs.502182 NM_001709	<i>Brain derived neurotrophic factor; Abineurin</i>	[374]
A07	<i>BGLAP</i>	Hs.654541 NM_199173	<i>γ-bone gamma-carboxyglutamic acid-containing protein; Osteocalcin (OCN)</i>	[375]
A08	<i>BMP2</i>	Hs.73853 NM_001200	<i>Bone morphogenetic protein 2</i>	[376]
A09	<i>BMP4</i>	Hs.68879 NM_130851	<i>Bone morphogenetic protein 4</i>	
A10	<i>BMP6</i>	Hs.285671 NM_001718	<i>Bone morphogenetic protein 6</i>	[377]
A11	<i>BMP7</i>	Hs.473163 NM_001719	<i>Bone morphogenetic protein 7; Osteogenic protein 1</i>	[278, 378]
A12	<i>CASP3</i>	Hs.141125 NM_004346	<i>Cysteine-aspartic acid protease 3</i>	
B01	<i>CD44</i>	Hs.502328 NM_000610	<i>Homing cell adhesion molecule (HCAM); Phagocytic glycoprotein (Pgp-1); Cluster of differentiation 44</i>	[225]
B02	<i>COL1A1</i>	Hs.172928 NM_000088	<i>Collagen type 1, sub-unit alpha 1</i>	
B03	<i>CSF2</i>	Hs.1349 NM_000758	<i>Granulocyte-macrophage colony stimulating factor (GM-CSF); Colony stimulating factor 2</i>	
B04	<i>CSF3</i>	Hs.2233 NM_000759	<i>Colony stimulating factor 3; Granulocyte colony stimulating factor (G-CSF)</i>	[379]
B05	<i>CTNNB1</i>	Hs.476018 NM_001904	<i>Catenin (Cadherin Associated Protein) Beta 1</i>	
B06	<i>EGF</i>	Hs.419815 NM_001963	<i>Epidermal growth factor; Human epidermal growth factor receptor 1 (HER1); Receptor tyrosine-protein kinase ErBb-1</i>	[380, 381]

B07	ENG	Hs.76753 NM_000118	Endoglin Cluster of differentiation 105 (CD105)	
B08	ERBB2	Hs.446352 NM_004448	Proto-oncogene Neu; Receptor tyrosine-protein kinase ErbB-2; Human epidermal growth factor receptor 2 (HER2); Cluster of differentiation 340 (CD340)	
B09	FGF10	Hs.664499 NM_004465	Fibroblast growth factor 10	
B10	FGF2	Hs.284244 NM_002006	Basic fibroblast growth factor	[382]
B11	FUT1	Hs.69747 NM_000148	Galactoside 2-alpha-L-fucosyltransferase 1	
B12	FUT4	Hs.390420 NM_002033	Fucosyltransferase 4 (alpha (1,3); Fucosyltransferase, myeloid-specific)	
C01	FZD9	Hs.647029 NM_003508	Frizzled-9; Cluster of differentiation 349 (CD349)	
C02	GDF15	Hs.616962 NM_004864	Growth/differentiation factor 15; Macrophage inhibitory cytokine-1; Placental transforming growth factor beta	[383]
C03	GDF5	Hs.1573 NM_000557	Growth/differentiation factor 5; Bone morphogenetic protein 14; Cartilage derived morphogenic protein 1	[384-386]
C04	GDF6	Hs.492277 NM_001001557	Growth/differentiation factor 6; Bone morphogenetic protein 13	[387]
C05	GDF7	Hs.447688 NM_182828	Growth/differentiation factor 7	[388]
C06	GTF3A	Hs.445977 NM_002097	General transcription factor IIIa	[389]
C07	HAT1	Hs.632532 NM_003642	Histone acetyltransferase 1	
C08	HDAC1	Hs.88556 NM_004964	Histone deacetylase 1	
C09	HGF	Hs.396530 NM_000601	Hepatocyte growth factor	
C10	HNF1A	Hs.654455 NM_000545	Hepatocyte nuclear factor 1 homeobox A	
C11	ICAM1	Hs.643447 NM_000201	Intercellular adhesion molecule 1; Cluster of differentiation 54 (CD54)	[390, 391]
C12	IFNG	Hs.856 NM_000619	Interferon gamma	
D01	IGF1	Hs.160562 NM_000618	Insulin-like growth factor 1	
D02	IL1B	Hs.193717 NM_000572	Interleukin 1 beta; Leukocytic pyrogen; Leukocytic endogenous mediator; Mononuclear cell factor; Lymphocyte activating factor	[392]
D03	IL6	Hs.126256 NM_000576	Interleukin 6	[393]
D04	IL10	Hs.654458 NM_000600	Interleukin 10; Human cytokine synthesis inhibitory factor (CSIF)	

D05	INS	Hs.654579 NM_000207	Insulin hormone	
D06	ITGA6	Hs.133397 NM_000210	Integrin sub-unit alpha 6; Very Late Activation Protein, 6; Cluster of differentiation 49 (CD49)	[229, 335, 394]
D07	ITGAV	Hs.436873 NM_002210	Integrin sub-unit alpha V; Vitronectin receptor alpha; Cluster of differentiation 51 (CD51)	[395]
D08	ITGAX	Hs.248472 NM_000887	Integrin sub-unit alpha X; Cluster of differentiation 11c (CD11c)	[396]
D09	ITGB1	Hs.643813 NM_002211	Integrin sub-unit beta 1; Very late activation protein, beta; Fibronectin receptor subunit beta; Cluster of differentiation 29 (CD29)	[397]
D10	JAG1	Hs.728907 NM_000214	Jagged-1 Cluster of differentiation 339 (CD339)	
D11	KAT2B	Hs.533055 NM_003884	K(lysine) acetyltransferase 2B; P300/CBP-associated factor (PCAF)	
D12	KDR	Hs.479756 NM_002253	Kinase insert domain receptor; Vascular endothelial growth factor receptor 2 (VEGFR2); Fetal liver kinase 1; Cluster of differentiation 309 (CD309)	
E01	KITLG	Hs.1048 NM_003994	Stem cell factor (SCF); KIT-ligand	[398] [247]
E02	LIF	Hs.2250 NM_002309	Leukemia inhibitory factor; Myeloid leukaemia inhibitory factor	[248]
E03	MCAM	Hs.599039 NM_006500	Melanoma cell adhesion molecule; Cell surface glycoprotein Muc18; Cluster of differentiation 146 (CD146)	[236, 237, 399]
E04	MMP2	Hs.513617 NM_004530	Matrix metalloproteinase 2; Gelatinase 2; Collagenase type 4	
E05	NES	Hs.527971 NM_006617	Neuroectodermal stem cell marker	[231, 251, 252]
E06	NGFR	Hs.415768 NM_002507	Low-affinity nerve growth factor receptor (α -LNGFR); Cluster of differentiation 271 (CD271)	[400]
E07	NOTCH1	Hs.495473 NM_017617	Notch homolog 1	
E08	NT5E	Hs.153952 NM_002526	Ecto-5'-nucleotidase (5'-NT); Cluster of differentiation 73 (CD73)	[401]
E09	NUDT6	Hs.558459 NM_007083	Nudix (nucleoside diphosphate linked moiety X)-type motif 6; Fibroblast Growth Factor 2 antisense gene (FGF-1)	
E10	PDGFRB	Hs.509067 NM_002609	Platelet derived growth factor receptor beta; Cluster of differentiation 140b (CD140b)	

E11	PIGS	Hs.462550 NM_033198	Phosphatidylinositol glycan anchor biosynthesis, class S	[402]
E12	POU5F1	Hs.249184 NM_002701	POU domain, class 5, transcription factor 1; Octamer-binding transcription factor 4 (Oct-4)	[259, 403]
F01	PPARG	Hs.162646 NM_015869	Peroxisome proliferator-activated receptor gamma; Glitazone receptor;	[404]
F02	PROM1	Hs.614734 NM_006017	Prominin-1; Cluster of differentiation 133 (CD133)	[405]
F03	PTPRC	Hs.395482 NM_005607	Protein tyrosine phosphatase receptor type C	
F04	PTK2	Hs.654514 NM_002838	Protein tyrosine kinase 2; Focal adhesion kinase (FAK)	[406]
F05	RHOA	Hs.247077 NM_001664	Rhomboid homolog transforming protein A	[128]
F06	RUNX2	Hs.535845 NM_004348	Runt-related transcription factor 2; Core-binding factor sub-unit alpha 1; Osteoblast specific transformation factor 1	[211]
F07	SLC17A5	Hs.597422 NM_012434	Solute carrier family 17 (anion/sugar transporter), member 5	
F08	SMAD4	Hs.75862 NM_005359	Small mothers against decapentaplegic homolog 4	
F09	SMURF1	Hs.189329 NM_020429	SMAD ubiquitin regulatory factor 1	[308, 407]
F10	SMURF2	Hs.705442 NM_022739	SMAD ubiquitin regulatory factor 2	
F11	SOX2	Hs.518438 NM_003106	Sex determining region Y-box 2	
F12	SOX9	Hs.647409 NM_000346	Sex determining region Y-box 9	
G01	TBX5	Hs.381715 NM_181486	T-box transcription factor 5	
G02	TERT	Hs.492203 NM_198253	Telomerase reverse transcriptase	[408] [173, 174]
G03	TGFB1	Hs.645227 NM_000660	Transforming growth factor, beta 1	
G04	TGFB3	Hs.592317 NM_003239	Transforming growth factor, beta 3	
G05	THY1	Hs.644697 NM_006288	Thymocyte-1 surface antigen; Cluster of differentiation 90 (CD90)	
G06	TNF	Hs.241570 NM_000594	Tumor necrosis factor	
G07	VCAM1	Hs.109225 NM_001078	Vascular cell adhesion molecule; Cluster of differentiation 106 (CD106)	[409, 410]
G08	VEGFA	Hs.73793 NM_003376	Vascular endothelial growth factor A	[240, 244]
G09	VIM	Hs.642813 NM_003380	Vimentin	
G10	VWF	Hs.440848 NM_000552	Von Willebrand factor homolog	
G11	WNT3A	Hs.336930 NM_033131	Wingless-Integrated homolog protein 3a	[411]
G12	ZFP42	Hs.335787 NM_174900	Zinc finger protein-42; Reduced expression 1 (Rex-1)	[258, 412]

Table 15. Gap defect studies in rabbit femora

<i>Study</i>	<i>Operation</i>	<i>Stabilisation</i>
<i>Concannon et al. [413] USA 1997</i>	<i>10 mm resection, periosteum excised*</i>	<i>Internal plate fixation (4 screws) Cerclage cables</i>
<i>Inui et al. [414] Japan 1998</i>	<i>10 mm resection, periosteum excised*</i>	<i>External fixation</i>
<i>Fujibayashi et al. [415] Japan 2003</i>	<i>10 mm resection, periosteum retained</i>	<i>Ti mesh cage (10 mm x 6.5 mm x 8 mm) 3 x Ti intramedullary wires (2 x 1.8 mm & 1 x 2.0 mm)</i>
<i>Fiakov et al. [416] Canada 2003</i>	<i>12 mm resection, periosteum excised and stripped</i>	<i>Internal plate fixation (6 screws)</i>
<i>Nunotani et al. [417] Japan 2005</i>	<i>Osteotomy and lengthening</i>	<i>External fixation</i>
<i>Yoneda et al. [418] Japan 2005</i>	<i>15 mm resection, periosteum excised*</i>	<i>External fixation (4 screws)</i>
<i>Gil-Albarova et al. [419] Spain 2005</i>	<i>15 mm resection, periosteum excised*</i>	<i>Internal plate fixation (4 screws) 1 x 2mm intramedullary wire</i>
<i>Yoon et al. [420] South Korea 2007</i>	<i>15 mm resection, periosteum excised*</i>	<i>External fixation (4 screws)</i>
<i>Sarahrudi et al. [421] Austria 2009</i>	<i>5 mm resection, periosteum retained</i>	<i>Internal plate fixation (6 screws)</i>
<i>Wang et al. [422] China 2010</i>	<i>15 mm resection, periosteum excised*</i>	<i>Internal plate fixation (4 screws) 2 x cerclage cables</i>

* Critical gap defects i.e., control subjects did not heal osseous defect

Table 16. Gap defect studies in rabbit tibiae

<i>Study</i>	<i>Operation</i>	<i>Stabilisation</i>
<i>Collier et al.[423] USA 1976</i>	<i>10 mm resection, periosteum excised, silastic spacer</i>	<i>Vitallium intramedullary nail</i>
<i>Simpson et al. [424] UK 1998</i>	<i>Osteotomy and lengthening</i>	<i>External fixation</i>
<i>Brownlow & Simpson [425] UK 2000</i>	<i>2 mm resection, periosteum excised and stripped</i>	<i>External fixation</i>
<i>Tobita et al. [426] Japan 2001</i>	<i>2 mm resection, periosteum excised</i>	<i>External fixation</i>
<i>Li et al. [427] UK 2002</i>	<i>10 mm resection, periosteum excised, acute shortening and 20 mm lengthening</i>	<i>External fixation</i>

Table 17. Distal femoral and intramedullary implant studies in rabbits

<i>Study</i>	<i>Operation</i>	<i>Implant</i>
<i>Manninen et al. [428] Finland 1993</i>	<i>Intramedullary insertion Distal femoral osteotomy</i>	<i>PLLA rod 70 mm long - cut to fit 4.6 mm diameter</i>
<i>Feighan et al. [364] USA 1995</i>	<i>Intramedullary insertion No osteotomy</i>	<i>Titanium rod 25 mm long 5 mm diameter</i>
<i>Hing et al. [429] UK 1997</i>	<i>Distal femoral plug</i>	<i>HA plug 6.55 mm long 4.5 mm diameter</i>
<i>D'Lima et al. [430] USA 1998</i>	<i>Intramedullary insertion No osteotomy</i>	<i>Titanium rod 25 mm long 5 mm diameter</i>
<i>Kettunen et al. [431, 432] Finland 1999/2001</i>	<i>Intramedullary insertion Distal femoral osteotomy</i>	<i>Carbon fibre / polymer rod 50 mm long 3.2 mm diameter</i>
<i>Saikkun-Backstrom et al.[433] Finland 2000</i>	<i>Intramedullary insertion Femoral shaft osteotomy</i>	<i>PLLA rod 50-60 mm long 4.5 mm diameter</i>
<i>Stewart et al.[434] USA 2004</i>	<i>Intramedullary insertion No osteotomy</i>	<i>Titanium rod 25 mm long 4.9 mm diameter</i>
<i>Dimitrievska et al.[435] Canada 2009</i>	<i>Intramedullary insertion No osteotomy</i>	<i>Ti-6Al-4V / HA coated rods 10 mm long 3.2 mm diameter</i>
<i>Lakstein et al. [436] Israel 2009</i>	<i>Intramedullary insertion No osteotomy</i>	<i>Ti-6Al-4V rod 25 mm long 4.76 mm diameter</i>
<i>Hermida et al. [437] USA 2010</i>	<i>Intramedullary insertion No osteotomy</i>	<i>Titanium rod 25 mm long 5 mm diameter</i>
<i>Aydin et al.[438] Turkey 2011</i>	<i>Intramedullary insertion Femoral shaft osteotomy</i>	<i>Steel rod 55 mm long 4 mm diameter</i>
<i>Guo et al. [439] China 2013</i>	<i>Intramedullary insertion No osteotomy</i>	<i>Ti alloy rod 25 mm long 4.5 mm diameter</i>
<i>Bretschneider et al. [367] Germany 2020</i>	<i>Intramedullary insertion No osteotomy</i>	<i>Ti-6Al-4V rod 25 mm long 4.5 mm diameter</i>